UNIVERSIDAD DE NAVARRA

ESCUELA SUPERIOR DE INGENIEROS



Novel amorphous and nanocrystalline Fe-based soft magnetic powders produced by gas atomisation

Dissertation

Submitted for the Degree of Doctor of Philosophy at University of Navarra by

Kenny Lynn Alvarez Chavez

Under the supervision of

José Manuel Martín

&

Julián Maria González

Donostia-San Sebastián, July 2020

"Si la oportunidad no
llama a tu puerta,
construye una puerta"

Milton Berle

"Life is not a problem to be
solved, but a reality
to be experienced."

Søren Kierkegaard

Acknowledgment-Agradecimientos

En primer lugar, me gustaría agradecer al CEIT y TECNUN-Universidad de Navarra- por recibirme en sus instalaciones y proporcionarme tanta gente capacitada para desarrollar mi tesis doctoral. A Becas Chile por la financiación y a la Pontificia Universidad Católica de Valparaíso (PUCV), por apostar en mi formación como doctor.

Quiero agradecer enormemente a mi director José Manuel Martín por todo el apoyo entregado todos estos años y por guiarme en mis primeros pasos como investigador. Por esas largas conversaciones (a veces discusiones) científicas que siempre me dejaban inquietante y pensativo para dar el siguiente paso. A mi codirector Julián González, que con su sabiduría en magnetismo me guio hacia una física que era prácticamente desconocida para mí, y agradecer también sus palabras de aliento y de "te va a quedar una tesis muy bonita".

Agradecer también al Departamento de Materiales y Fabricación, especialmente al grupo de Polvos, más bien conocido hoy en día como FAPL. A Paco Castro que fue clave en el inicio y desarrollo del proyecto, a Iñigo Iturriza por su carisma y apoyo en todo momento, a todos los técnicos que, de una u otra forma, directa o indirectamente, contribuyeron con esta tesis en gran manera. A Iñigo Andueza, un grande, siempre solucionando problemas y sacándonos de apuros, a Unai Pascual, siempre dispuesto a atomizar y ayudar y como no, a Itziar Morán, que me enseñó qué no hay que hacer para obtener esos bellos surcos en mis muestras.

Como no mencionar a mi familia, que a pesar de los kilómetros y el océano que nos separan, siempre han sido un pilar fundamental en todo este proceso. A mi hermano Luis, que siempre ha estado ahí para charlar y aconsejar, a mi madre por su incansable preocupación, a mi padre por sus llamadas de aliento, a mis otros hermanos y hermanas por todo su apoyo. A mi tía por sus maravillosas recetas, y por supuesto, agradecer a la persona que me ha dejado un ejemplo de vida, Tata mil gracias al cielo por tu enseñanza y por ser como un padre en el momento que más lo necesitaba.

A mi mejor amigo Rodrigo, siempre dispuesto a escuchar y dar palabras de aliento, el mejor solucionando problemas.

I would like to thank Tyndall National Institute for admitting me in its facilities. Thanks to Paul for accepting my application, Zoran for teaching me how to use the instruments, Ansar for his enormous help in analysing all

the results and contribution to each paper, and of course, my dear friend Hasan, thanks for everything, you are a great person and I will be always grateful for contacting me and starting our collaboration. Thanks to my lunch friends, Natalia, Yuliya, Aman, Eimear and Tim, for welcoming me into the group, we had many funny moments, especially with my English misunderstandings.

Y ahora la parte difícil, a mis compañer@s y amig@s del CEIT con los cuales compartí tantas cosas, cafés, comidas, cenas en el txoko, etc. A los del despacho 311: Unai, Xabi, Jazmina, Andrea y Luna, que alegraban esos cafés por las mañanas con interesantes conversaciones, Mari, Bea y Maitane, las inseparables, gracias por los bellos momentos vividos y por la paciencia que han tenido con este chileno, especialmente a Mari, mil gracias por escuchar mis historias de telenovelas venezolanas y aconsejarme. A los de mi primer despacho: JonPe siempre en su mundo, Ernesto siempre enterado de todo, una gran persona a quien agradezco que me guiara en mis primeros pasos en el CEIT, Carlota una chica encantadora que con su alegría puede subirle el ánimo a cualquiera, Gorkita, tan especial, sensible y directo, a quien voy a echar mucho de menos, Neri, un ejemplo de vida, mi amiga, mi confidente, la que me levantaba cuando me estaba cayendo y a la que le debo gran parte de esta tesis doctoral, su simpatía hacía que cada problema se esfumara.

Agradecer a los de la pradera, en donde acogieron con alegría a este chileno: David y Julia, han llegado a un muy buen sitio, Gotzi por su entusiasmo y por ser única, Karmentxu por siempre saber cómo solucionar los problemas con el Word, Idoia la rubia de la pradera, tu no hagas caso que tus idoiadas molan, Ernesto, si otra vez lo tuve que aguantar, o el a mí, Miren, un tiro al aire, sin filtro, con quien la risa y el entretenimiento están asegurados, te dije que el pádel molaba, a que si?, Nerea B., infinitas gracias por tu gran ayuda, tu paciencia y dedicación son de imitar, te prometo que te dejaré un audio que diga “fóforo”, y por último, a la pollito, aunque dejó el nido y voló cuando su mentora se fue, Aintzane, mi compañera de mesa, infinitas gracias por tanto, por aguantarme, por enseñarme como son las vascas (simpáticas selectivas), por tu sonrisa, sobre todo en los momentos más difíciles, por tus canciones que me sacaban de mi bucle de radio chilena, por todos los detalles y esas travesurillas de ir a buscar galletas Gullón.

Infine, vorrei ringraziare alla mia ragazza Illy, la mia compagna di vita, grazie mille per la pazienza che hai avuto con me, per avermi ascoltato in tempi difficili, per la tua capacita di essere come tu sei senza complessi, per essere felice di cose molto picole, per il cibo buonisimo che solo tu sai come prepararlo, dirò sempre che la cosa più bella che Donosti mi ha portato, sei stata tu.

Abstract

Industry is currently facing increasing challenges related to resources and the environment, and some sectors have been going to great lengths to control them. Two of the biggest concerns are using material more efficiently while simultaneously reducing the amount of energy consumed and the amount of pollutant gases emitted. Within this context, soft magnetic materials have been broadly studied because they are widespread in many industrial sectors and can be found in numerous applications. In fact, this group of materials comprise about 40 % of the total market of magnetic materials and they are present in electrical and electronic devices, telecommunication industry, energy conversion and transportation, and the automotive sector, among other uses. In the last decade, the electrical and electronic industry has exponentially increased its production due to the massive use of technological devices and the worldwide tendency to be fully connected, triggering a high demand for soft magnetic materials. This high demand, together with a tendency to miniaturise devices, have led researchers and industries to search for novel and more efficient soft magnetic materials.

Fe-based amorphous and nanocrystalline alloys are one of the major soft magnetic materials, because they exhibit superior soft magnetic properties, including high saturation magnetisation, extremely low coercivity and excellent power loss performance. However, the preparation of Fe-based amorphous materials is challenging; it consists of a rapid solidification process, requiring in some cases cooling rates higher than 10^4 K/s. For that reason, for many years the main fabrication process has been, and is still, the well-known melt-spinning process. This process produces thin ribbons that are extensively used to manufacture electronic devices, as well as other components. Nevertheless, there are some difficulties that must be addressed; the geometry of thin ribbons makes it difficult the manufacturing of finished or semi-finished part, especially when complex geometry is required. This problem has led several researchers to explore novel materials and new fabrication processes. One of the promising technologies that has been recently used to produce amorphous materials is the gas atomisation process. Gas atomisation is a mass production process that turns a metallic molten stream into small droplets, which later solidify in a spherical form. The high cooling rates achieved during the solidification process, the elevated production rates and the product characteristics make this process a very attractive way to produce amorphous materials. In fact, it is now being considered as a substitute for melt-spinning in some applications.

In order to address the problem described above and increase the knowledge in this field, this thesis presents interesting results with regard to the production of novel Fe-based amorphous alloys. Based on amorphous forming ability studies, various amorphous Fe-based compositions are produced by gas atomisation. The as-quenched powders are submitted to different heat treatments in order to study relaxation and crystallisation phenomena. In addition, after optimising the annealing process, the as-quenched, relaxed and nanocrystalline powders are used as raw materials in the manufacturing of soft magnetic cores, which are characterised in their working conditions.

The as-quenched powders exhibit excellent soft magnetic properties, which are further improved by proper heat treatments. The soft magnetic cores reveal extraordinary behaviour at high-frequency, which in other words means that the power loss at high-frequency is comparatively lower than for other reported materials. Furthermore, the analysis of the results allow the author of this thesis to establish three conditions for the formation of amorphous structure of Fe-Si-B alloys. All these results are presented and proposed with the aim of considering gas atomisation as an excellent alternative to produce amorphous materials.

Appended Papers

This thesis is presented in the paper format and the following papers have been published or submitted by the author.

Paper A

K. L. Alvarez, J. M. Martín, M. Ipatov, J. Gonzalez, Soft magnetic amorphous alloys (Fe-rich) obtained by gas atomisation technique, J. Alloys Compd. 735 (2018) 2646–2652.

Paper B

K. L. Alvarez, J. M. Martin, M. Ipatov, L. Dominguez, J. Gonzalez, "Magnetic properties of annealed amorphous $Fe_{72.5}Si_{12.5}B_{15}$ alloy obtained by gas atomization technique," IEEE Trans. Magn. 54 (2018) 2002405.

Paper C

Kenny L. Alvarez, J.M. Martín, N. Burgos, M. Ipatov, L. Domínguez, J. González, "Structural and magnetic properties of amorphous and nanocrystalline Fe–Si–B–P–Nb–Cu alloys produced by gas atomization," J. Alloys Compd. 810 (2019) 151754.

Paper D

Kenny L. Alvarez, H. A. Baghbaderani, J. M. Martín, N. Burgos, M. Ipatov, Z. Pavlovic, P. McCloskey, A. Masood, J. Gonzalez, Novel Fe-based amorphous and nanocrystalline powder cores for high-frequency power conversion, J. Magn. Magn. Mater 501 (2020) 166457.

Paper E

Kenny L. Alvarez, José Manuel Martín, Nerea Burgos, Mihail Ipatov, Lourdes Domínguez, Julián González, Coercivity and magnetic anisotropy of $(Fe_{0.76}Si_{0.09}B_{0.10}P_{0.05})_{97.5}Nb_{2.0}Cu_{0.5}$ amorphous and nanocrystalline alloy produced by gas atomization process, Nanomaterials 10(5) (2020) 884.

Paper F

Kenny L. Alvarez, H. Ahmadian Baghbaderani, J. M. Martín, N. Burgos, P. McCloskey, J. Gonzalez, A. Masood, Novel methodology to predict amorphisation capability of Fe-Si-B soft magnetic powders. In preparation.

CRediT Authorship Contribution Statement

All the appended papers are directly related to this thesis and were prepared in collaboration with co-authors. The work carried out in each paper has been jointly planned by the authors and the contribution of each one is listed below.

Kenny L. Alvarez (author of this thesis)

The author of this thesis collaborated in planning the atomised compositions. He conducted the entire characterisation process of the powders:

i. Structural characterisation by X-ray diffraction.

ii. Thermal characterisation by differential scanning calorimetry.

iii. Powder properties by density and particle size measurements.

iv. Sample preparation by focused ion beam microscopy (FIB), mounting, polishing and etching.

v. Morphology and microstructure observations by secondary electron microscopy (SEM) and transmission electron microscopy (TEM).

He also conducted the heat treatments and participated in analysing the results. He carried out the powder preparation and consolidation by compression moulding and core loss measurements at different frequency, in close collaboration with other authors. All the papers appended to this thesis were partially or fully written by the author of this thesis.

J.M. Martín

J.M Martín planned and supervised the powder production by gas atomisation, collaborated in planning the compositions and supervised the powder characterisation and heat treatment carried out by the author of this thesis. He also participated in analysing the results and writing the manuscripts.

J. Gonzalez

J. Gonzalez participated in planning the compositions and magnetic measurements, as well as analysing the results of the DC-magnetic properties. He also wrote the first drafts of **Papers A-C** and **E.**

H. A. Baghbaderani

H.A. Baghbaderani contributed to plan and carry out the measurements of the AC-magnetic properties, as well as analyse the results and write the manuscripts of **Paper D** and **F.** He also conducted the thermodynamic modelling of **Paper F.**

A. Masood

A. Masood collaborated in designing the measurements of the AC-magnetic properties, analysing the results and writing the manuscript of **Paper D** and **F.** He also contributed to define the amorphisation criteria reported in **Paper F.**

N. Burgos

N. Burgos conducted the advanced structural measurements by X-ray diffraction and Rietveld method, and collaborated in analysing the results of **Papers C-F.** She also taught to the author of this thesis to prepare the powder samples to be consolidated by compression moulding.

Z. Pavlovic

Z. Pavlovic taught to the author of this thesis to carry out the measurements of the AC-magnetic properties. He also collaborated in conducting the measurements and analysing the results.

M. Ipatov

M. Ipatov conducted the measurements of the DC-magnetic properties.

P. McCloskey

P. McCloskey facilitated the AC-magnetic equipment and collaborated in writing the manuscript of **Paper D** and **F.**

L. Dominguez

L. Dominguez collaborated in analysing the results and writing the manuscripts of **Papers B-C** and **E.**

Contributions to other Papers

The author of this thesis has also contributed to the following papers.

Paper G

Hasan Ahmandian Baghbaderani, Ansar Masood, Zoran Pavlovic, **Kenny L. Alvarez**, Cian O'Mathúna, Paul McCloskey, Plamen Stamenov, On the mechanisms limiting power loss in amorphous CoFeB-based melt-spun ribbons, J. Magn. Magn. Mater. 502 (2020) 166535.

Paper H

Ansar Masood, H. A. Baghbaderani, **K. L. Alvarez**, J. M. Blanco, Z. Pavlovic, V. Ström, P. Stamenov, C. O. Mathuna, P. McCloskey, High-frequency power loss mechanisms in ultra-thin amorphous ribbons, submitted to J. Magn. Magn. Mater (2020). Under review.

Contributions to Conferences

The author of this thesis has contributed to the following conferences.

Posters

Kenny L. Alvarez*, J. M. Martín, M. Ipatov, J. González, "Soft magnetic amorphous alloys (Fe-rich) obtained by gas atomization technique," *24th ISMANAM 2017*, 18th to 23rd of June 2017, Donostia-San Sebastián, Spain.

Kenny. L. Alvarez, H. A. Baghbaderani, J. M. Martín, N. Burgos, M. Ipatov, A. Masood*, Z. Pavlovic, P. McCloskey, J. Gonzalez, "Novel Fe-based amorphous and nanocrystalline powder cores for high-frequency power conversion," *24th Soft Magnetic Materials Conference*, 4th to 7th of September 2019, Poznań, Poland.

Oral presentations

Kenny L. Álvarez*, J. M. Martín, J. González, "Caracterización magnética y microstructural de polvos metálicos de Fe-Si-B producidos mediante atomización con gas," *VI Congreso Nacional de Pulvimetalurgia y I Congreso Iberoamericano de Pulvimetalurgia*, 7th to 9th of June 2017, Ciudad Real, Spain.

Kenny L. Álvarez*, J. M. Martín, J. González, "Producción y caracterización de polvos metálicos de Fe-Si-B obtenidos mediante atomización con gas," *13th Congreso Iberoamericano de Ingeniería Mecánica*, 23rd to 26th of October 2017, Lisbon, Portugal.

K. L. Alvarez, J. M. Martín*, M. Ipatov, L. Dominguez, J. Gonzalez, "Magnetic Properties of Annealed Amorphous Alloys (Fe-rich) Obtained by Gas Atomization Technique," *INTERMAG 2018*, 28th to 27th of April 2018, Singapore.

A. Masood*, H. A. Baghbaderani, **K. Alvarez**, Z. Pavlovic, V. Ström, P. Stamenov, P. McCloskey, C. Ó. Mathúna, "Amorphous metals on the move: making amorphous metal ribbons suitable for high-frequency applications," *24th Soft Magnetic Materials Conference*, 4th to 7th of September 2019, Poznań, Poland.

* Corresponding author.

Kenny. L. Alvarez, José M. Martín*, M. Ipatov, L. Domínguez, J. Gonzalez, "Effect of Composition and Particle Size on the Soft Magnetic Character of Fe-Rich Amorphous Alloys Obtained by Gas Atomization," *EuroPM2019*, 13th to 16th of October 2019, Maastricht, The Netherlands.

* Corresponding author.

Index

Table of Contents

1 Introduction 1

2 Literature Review 5

2.1 Magnetism and Magnetic Materials 5

2.1.1 Magnetic materials 5

2.1.2 Magnetisation process in ferromagnetic materials 7

2.1.3 Magnetic properties 9

2.1.4 Soft magnetic materials 11

2.1.5 Applications and soft magnetic composites 15

2.2 Amorphous and Nanocrystalline Materials 18

2.2.1 Amorphous materials 18

2.2.2 Amorphous forming ability 21

2.2.3 Nanocrystalline materials based on Fe-Si-B alloys 24

2.3 Powder Metallurgy 26

2.3.1 Basis of powder metallurgy 26

2.3.2 Powder properties 28

2.3.3 Gas atomisation process 30

3 Appended Paper Details 33

3.1 Work Methodology 33

3.1.1 Material production 34

3.1.2 Material characterisation 34

3.1.3 Powder consolidation 35
3.2 Journal Information 36
3.2.1 Journal of Alloys and Compounds 36
3.2.2 IEEE Transactions on Magnetics 36
3.2.3 Journal of Magnetism and Magnetic Materials 37
3.2.4 Nanomaterials 38
3.3 Appended Papers 39
Paper A 39
Paper B 40
Paper C 40
Paper D 42
Paper E 43
Paper F 44
3.4 Discussion 46
4 Conclusions and Future Work 49
5 References 53
5.1 Reference Statistics 53
5.1.1 Most cited Journals 53
5.1.2 Most cited Authors 54
5.1.3 Number of references for range of years 54
5.2 Reference List 54

Appendix I: Appended Papers

Papers A to F

Appendix II: Contribution to other Papers

Papers G to H

Chapter 1

Introduction

The great demand for magnetic materials has increased in the last few years due to the necessity of reducing energy consumption and the greenhouse gas effect. In fact, the search for more efficient magnetic materials has been the main topic of most of the publications in this field. Since the oxide of iron, magnetite (Fe_3O_4), was discovered in the antiquity, many advances in technology have made it possible to improve the performance of these materials. This has been achieved by the acquisition of purer raw materials, the optimisation of production processes and the discovery of new magnetic alloys and compounds. Despite all these advances, there is still a lack of knowledge and a need to improve the performance of these materials even further, and these gaps need to be addressed.

Magnetic materials are essential for our lives; they are present in electronic devices, automobiles, communication systems, electricity generation and transportation, etc. There is great concern about the use of magnetic materials due to the exponential increase in demand and strict

requirements. Magnetic materials can be roughly divided into three categories: hard magnetic, magnetic recording and soft magnetic materials. This thesis only focuses on the study of soft magnetic materials; therefore, this kind of material will be discussed in more detail throughout this document.

Soft magnetic materials comprise forty percent of the whole market of magnetic materials. Because of this, much effort has been made over time to improve material performance and manufacturing processes; the search for new compositions to be used as soft magnetic materials, as well as new alternatives to produce them, have been the two main concerns of researchers and companies. Today, everything tends towards miniaturisation, which means that one material must have the same (or better) behaviour with smaller dimensions (or mass), under certain conditions. This has led to significant component downsizing in many industrial sectors.

Within this context, one of the most important milestones was the discovery of amorphous and nanocrystalline metallic materials and their use as soft magnets. It has been widely demonstrated that these materials exhibit an excellent combination of soft magnetic properties (i.e., ultra-low coercivity, high magnetisation saturation, low magnetostriction and low power loss), as well as exceptional mechanical and corrosion resistance. The question now is how amorphous and nanocrystalline materials are produced. The production of these materials involves the synthesis of a non-crystalline structure by a rapid solidification process, for example. Then, through further heat treatments, the amorphous structure partially transforms into crystalline. It sounds easy, but in practice, it is much harder to achieve. In order to attain the excellent soft magnetic properties, it is essential that the material has at least the following constituents: a ferromagnetic element (usually Fe, Co or Ni), an amorphous former element (B, P, C, etc.), a nucleating element (usually Cu) and a grain growth inhibitor (Nb). Other elements are also added with the aim of having special properties, as is the case of using Si to increase electric resistivity.

The main fabrication process has been, and is still, the well-known melt spinning process, which produces thin ribbons by rapid quenching the melt and achieves cooling rates as high as 10^6 K/s. The thicknesses of the solidified ribbons are usually between 10 - 50 μm and their width is between 1 and 50 mm. There is a large amount of different materials that have been produced using this process, and due to technological developments, the production rates have reached large numbers, turning this process into a mass production technique. Despite this, this process has some drawbacks

that must be taken into account. The main challenge is usually related to the post-processing and/or component manufacturing; ribbons are very long in length, extremely thin in thickness and brittle, and all these characteristics make them unsuitable for use as a raw material, for instance, for the fabrication of finished or semi-finished parts. Occasionally, it is necessary to perform further processes, thus considerably increasing manufacturing costs.

For that reason, over the last decade, the search for novel rapid solidification processes to produce amorphous materials has intensified. In this regard, gas atomisation has emerged as a promising process for the production of amorphous materials. Gas atomisation is a mass production process that produces powder from the melt by a high velocity gas flow. The advantage of this process is that the powder can be used as raw material for the manufacturing of finished or semi-finished parts by certain powder metallurgy processes, thereby reducing post-processing and, consequently, production costs. This process is not new; it has been used since the twentieth century. However, its use as a way to produce amorphous powders started to be successful only a few decades ago. Even though the typical average cooling rates in gas atomisation are lower than in melt spinning (10^4 – 10^5 K/s), the discovery of materials with higher amorphous forming ability has made it possible to synthesise numerous metallic alloys as fully amorphous, turning this process into an attractive alternative.

Within this theoretical framework, CEIT has decided to start a new research line that addresses the problems outlined above. The internal project is called 'SOFTMAG'; it started as an idea and has ended up in a doctoral thesis whose results have been published in scientific journals and presented national and international academic conferences. Furthermore, the experience acquired during these four years has made it possible to expand the network of contacts and start new projects with both academy and industry.

The main objective of the SOFTMAG project is to use the well-known gas atomisation process to produce amorphous and nanocrystalline Fe-based soft magnetic powders that have competitive soft magnetic properties for use in high-frequency applications. In order to achieve this objective, the work is divided into different steps, each one with its own objective:

Objective 1: To design compositions based on the ternary Fe-Si-B system to be synthesised as amorphous by gas atomisation. This involves taking into account the expected soft magnetic properties and amorphous forming ability. Next, the designed compositions must be gas-atomised using

the most extreme conditions during the process (i.e., highest gas pressure, highest melt temperature and He as atomising gas), obtaining in this way amorphous particles.

Objective 2: To produce nanocrystalline powders by carrying out proper heat treatments on the amorphous precursor. As a target, the phase of nanocrystals must be based on Fe(Si), the crystal size shall be below 20 nm and the crystals shall be homogeneously distributed in the amorphous matrix. It is expected that these powders possess excellent soft magnetic properties.

Objective 3: To use the amorphous and nanocrystalline powders to fabricate soft magnetic cores. The powder will be mixed with an epoxy resin, and the cores will be consolidated in a toroidal shape by the compression moulding process. Then, the cores will be tested in real working conditions in order to characterise their possible behaviour and applications.

This thesis is divided into five chapters and two appendices. The first chapter corresponds to this introduction. In the second chapter, the background of the three main areas of the present thesis—magnetic materials, amorphous and nanocrystalline materials and powder metallurgy—will be reviewed and discussed. The third chapter describes details about the appended papers, i.e., work methodology, journal information, a brief explanation of the papers and the discussion of the main results. Finally, the last two chapters present conclusions and future work, and references, respectively. The appendices I and II consist of all the papers presented in this thesis, as they have been published or submitted, and the contribution of the author of this thesis to other papers, respectively.

Chapter 2

Literature Review

2.1 Magnetism and Magnetic Materials

2.1.1 Magnetic materials

The magnetic phenomenon was first observed in the ancient world, when people noticed the attraction of two materials. People from Sumer, ancient Greece and China were familiar with the iron oxide Fe_3O_4, mostly known as magnetite. The name magnetite was adopted because of the greatest ancient deposits were found in the district of Magnesia, in present-day Turkey. The first known application of lodestone (rock rich in magnetite) was a device called 'South pointer': a spoon made of a chunk of lodestone that was placed in a base, so that its handle aligned with the Earth magnetic field [1]. The next great milestones were the discoveries of Zheng Gongliang in 1064, who observed that iron could be magnetised after quenching it from red heat, and the invention of the compass by Shen Kua around 1088, who saw how a suspended steel needle previously magnetised

aligned with the Earth field. This led to the beginning of the guided ocean voyages, which led to discovery expeditions of China to Africa (in 1433 by Cheng Ho) and Europeans to America (in 1492 by Cristopher Columbus) [2].

After a few centuries, William Gilbert carried out the first known magnetic scientific study. He published a book in the 1600s with his theory that the Earth itself was a great magnet. Subsequent discoveries in the 17th and 18th centuries led to the invention of the horseshoe magnet by the Swiss Daniel Bernoulli. From this period, experimental discoveries such as the connection between electricity and magnetism by Hans-Christian Oesterd, the equivalence of a current-carrying coil with a magnet by André-Marie Ampère and Dominique-François Arago, and the electromagnetic induction by Michael Faraday launched the electromagnetic revolution. All these works allowed James Clerk Maxwell to relate electricity, magnetism and light in 1864, formulating the very well-known Maxwell's equations. These novel concepts made possible to establish that a magnetic material placed inside a coil can be magnetised by applying an electrical current. The vector direction of the induced magnetic field will follow the right-hand rule and will be directly related with the applied electrical current.

The basis of magnetism comes from the magnetic moment generated by the electrons from two different contributions: the orbital motion around the nucleus and electron spin. Every contribution is represented by vector whose magnitude and direction contribute to the total magnetic moment. The contribution from the orbital motion may be linked to a current in a loop of wire without any resistance, and has its direction perpendicular to the orbital plane. The contribution from the electron spin comes from the magnetic moment produced by the electron rotation in its own axis. This magnetic moment is generated by the array of tiny current loops produced by the electron charge and causes the appearance of two different poles aligned to the rotation axis [3]. The magnetisation process in magnetic materials is governed by rotation of the net magnetic moments from each atom. When an external magnetic field (H) is applied to a material, the response will depend on the material atomic dipole configuration [4,5].

Materials can be mainly classified into three categories: diamagnetic, paramagnetic and ferromagnetic. They differentiate between them because of their response when an external H field is applied. This thesis focuses on the study of ferromagnetic materials; therefore, more details about this kind of materials will be found in the following sections.

2.1.2 Magnetisation process in ferromagnetic materials

Below a certain temperature called Curie temperature (T_C), ferromagnetic materials are composed of small volumes in which the magnetic dipoles are aligned in the same direction. These volumes are called domains. Each domain is separated from the surrounding ones by a domain boundary or domain wall and, normally, they are microscopic in size. In polycrystalline materials, there may exist more than one domain within one crystal; therefore, on a macroscopic scale, one can find a large amount of domains.

If a ferromagnetic material is exposed to an external H field, the domains that are oriented in a direction favourable to H will grow at the expense of those that are unfavourable oriented. This change will provoke a gradual change in domain shape and size. Consequently, the magnetisation process can be understood in terms of domain wall motion and/or domain rotation. This process continues until the macroscopic material becomes a single domain oriented along H at an external field called magnetic anisotropy field (H_K), reaching in this way the magnetisation saturation (M_S, point 1 in Figure 2.1.2-1).

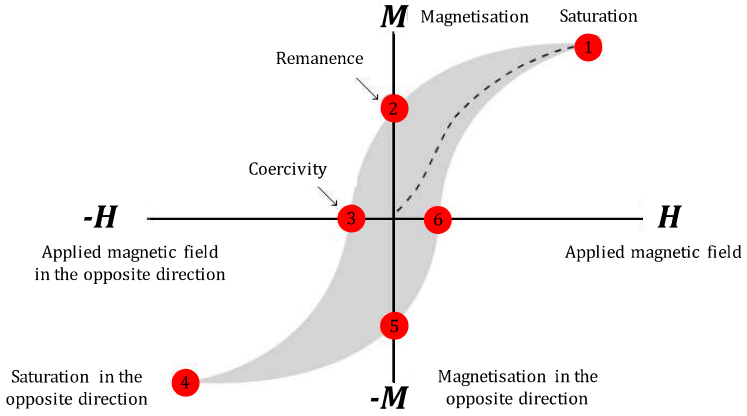

Figure 2.1.2-1. Magnetisation process and hysteresis loop of ferromagnetic materials.

From the saturation state (point 1 in Figure 2.1.2-1), as the external H is reduced, the curve does not repeat its original path. First, there is a rotation of the single domain. Next, domains having magnetic moments aligned with the new field direction form and grow at the expense of the former domains. The resistance to this movement of domain walls provokes a lag of M with H, or the hysteresis. When the H field reaches zero (point 2 in Figure 2.1.2-1), there exists a residual magnetisation called remanence (M_r),

in which the material remains magnetised in the absence of an external H. The magnitude of M_r will depend on the material characteristics.

In order to reduce the magnetisation within the material until zero, an external magnetic field in a direction opposite to that of the original field is applied, called coercivity -H_C (point 3 in Figure 2.1.2-1). If the strength of the external opposite magnetic field increases, the material will reach the opposite saturation (-M_S, point 4 in Figure 2.1.2-1) by the same domain rotation and/or wall motion process. A second reversal of the field to the point of the initial saturation will complete the symmetrical hysteresis loop and yield both, a negative remanence and a positive coercivity (point 5 and 6 in Figure 2.1.2-1).

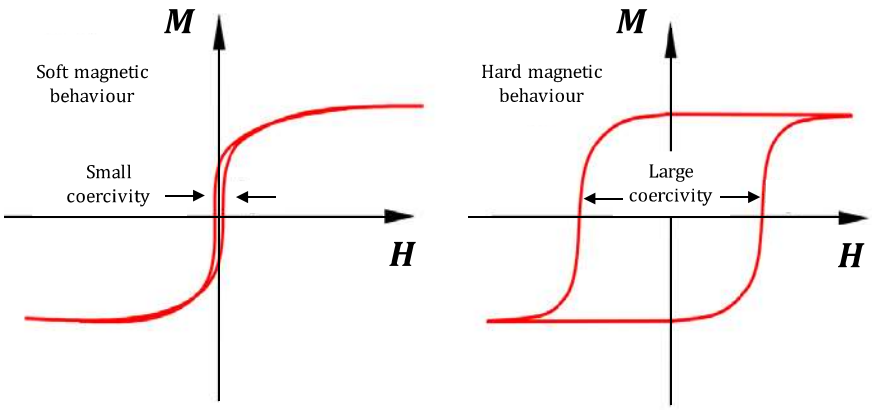

Figure 2.1.2-2. Hysteresis loops of soft (left) and hard (right) magnetic materials.

From the hysteresis loop characteristics, two main groups of materials can be identified: hard and soft magnetic materials. Figure 2.1.2-2 graphically depicts the differences in the hysteresis loop of both. Two main differences can be observed; hard magnetic materials possess a very large H_C compared to soft magnetic materials and M_r is comparatively higher, and, consequently, the area of the hysteresis loop is larger. This means that the magnetic energy stored within the material is very high and, in order to demagnetise the material, a strong opposite magnetic field must be applied. Due to these characteristics, hard magnetic materials are used as permanent magnets in several applications [6,7]. Conversely, the low H_C and power loss (P) exhibited by soft magnetic materials makes them unique to be used in several other applications, such as AC applications, high-frequency, power converters, etc. [8].

2.1.3 Magnetic properties

The classical explanation [1,4,5] of magnetic properties usually starts with a *H* field generated by a cylindrical coil (or solenoid), consisting of *N* closely equally spaced turns, having a length *l* and carrying a current of magnitude *I*. Thus, the magnetic field *H* generated by the coil can be expressed as:

$$H = \frac{NI}{l} \qquad \text{2.1.3-1}$$

Within the coil, a magnetic field is induced denoted by *B* (also called magnetic flux density). The magnetic field strength and flux density are related according to the following expression:

$$B = \mu H \qquad \text{2.1.3-2}$$

The parameter μ is the permeability, which is a property of the specific medium through which the *H* field passes and in which *B* is measured. The same expression can be written if the coil is in vacuum (i.e., without the presence of any material):

$$B_0 = \mu_0 H \qquad \text{2.1.3-3}$$

where μ_0 is the permeability of vacuum, which has a value of $4\pi \times 10^{-7}$ H/m.

In order to describe the magnetic properties of solids, a parameter called relative permeability μ_r may be used. This parameter is calculated by the ratio of the material permeability μ to the permeability of vacuum μ_0:

$$\mu_r = \frac{\mu}{\mu_0} \qquad \text{2.1.3-4}$$

μ_r is dimensionless and provides a measure of the degree up to which the material can be magnetised or how ease a *B* field can be induced in the presence of an external *H* field.

The magnetisation *M* can be related with the applied field *H*, the vacuum permeability μ_0 and the magnetic flux density *B*, by the following expression:

$$B = \mu_0(H + M) \qquad \text{2.1.3-5}$$

All these equations make possible to introduce another dimensionless magnetic property called magnetic susceptibility χ_m expressed as:

$$\chi_m = \frac{M}{H} = \mu_r - 1 \qquad \text{2.1.3-6}$$

In soft magnetic materials, there are also other properties to take into account: the magnetic anisotropy field (H_K) and the power loss (P).

The magnetic anisotropy represents the variation of the internal energy when the magnetisation vector is rotated out of the direction of spontaneous magnetisation. This parameter is also defined as a hindrance to the domain wall motion or domain rotation, which provokes a delay in the magnetic saturation. A given material can have a favourable and unfavourable direction of magnetisation, which are called easy and hard axis of magnetisation, respectively. The directional dependence of magnetisation is usually caused by the combination of three different anisotropy sources: magnetocrystalline, magnetoelastic and shape anisotropy. Magnetocrystalline anisotropy mainly comes from the spin-orbit coupling, which couples the spin moments to the crystal lattice by means of orbital electrons. Magnetoelastic anisotropy generates due to the strain existing in the material structure; the presence of strain alters the interaction energy and the domain structure changes by reorienting its domain vector. Conversely, shape anisotropy is due to the appearance of poles on the top and bottom surfaces of a finite element; these magnetic poles generate an internal field opposing to the external H, reducing in this way B. This opposite field is called demagnetising field (H_d) [1,5,9].

Crystalline materials possess easy and hard directions of magnetisation, according to its crystal structure. For instance, iron bcc crystal structure has an easy axis in the ⟨100⟩ direction and hard axis in ⟨111⟩ direction. This means that if an external H field is applied to a material with crystals oriented in the direction ⟨100⟩, the energy required to magnetise it along this preferred orientation will be smaller than when the crystals are randomly oriented (or oriented in the hard direction ⟨111⟩) [10].

The magnetic anisotropy can be generally quantified by a parameter called anisotropy field (H_K). H_K corresponds to the field required to make $M = M_S$ and can be related with M_S by the following simplified equation:

$$H_K = \frac{2K_u}{\mu_0 M_S} \qquad 2.1.3\text{-}7$$

where K_u is the anisotropy constant. If only perpendicular anisotropies are considered, the average H_K ($<H_K>$) can be estimated by calculating the distribution of the anisotropy field (P[H_K]) from the hysteresis loop [11,12].

Regarding the power loss (P, sometimes-called energy loss W or core loss P_C), this property corresponds to the energy dissipated during the magnetisation-demagnetisation process, usually under AC conditions. The total power loss (P_T) has mainly three different contributions: the hysteresis loss (P_h), eddy current loss (P_{ec}) and anomalous loss (P_{an}, or excess loss P_{exc}) [13–15]. P_T can be expressed as the sum of each contribution:

$$P_T = P_h + P_{ec} + P_{an} \qquad 2.1.3\text{-}8$$

P_h corresponds to the energy dissipated by the hysteresis effect, and can be calculated by the area of the hysteresis loop. P_{ec} phenomenon can be explained considering the operation of a transformer; when an AC-electrical current is applied to the primary coil of a transformer, a magnetic flux is induced. This alternating flux induces an electromagnetic force (emf), not only in the secondary coil, but also in the core itself. If the core is a conductor, this internal emf will cause eddy currents. Eddy currents oppose to the main field and are not desired, not only because they decrease the field, but also because they produce heat [1,2]. This kind of loss becomes important at high frequencies (>100 kHz) and is mainly dependent on the material thickness and resistivity. P_{an} originates from localized eddy currents around moving domain walls under the driving action of an external magnetic field and it can be reduced by changing the dominantly magnetisation process from domain wall motion to coherent rotation of domains.

2.1.4 Soft magnetic materials

When the magnetisation process in ferromagnetic materials (produced by domain wall motion and/or domain rotation) occurs in a weak field and H_C takes values below the 10^3 A/m (~13 Oe), the material is called soft magnetic [5]. This is well represented by Figure 2.1.2-2 (left), where a representative hysteresis loop of a soft magnetic material is shown. There

are several application in which soft magnetic materials can be used, for instance: power generation, condition, transfer and conversion; electric machines; power electronics; sensors, or electromagnetic interference (EMI) shielding, among others.

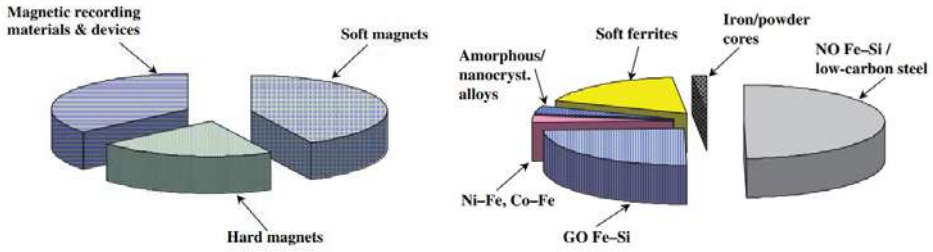

Figure 2.1.4-1. Global market of magnetic materials (left) and distribution of the production of soft magnetic materials (right) [8].

Soft magnetic materials cover a large proportion of the global market of magnetic materials (~40%), with a value around € 20 billion in the year 2015 and an annual growth rate around 5% [8]. A major share of the market is covered by the grain-oriented (GO) and non-oriented (NO) electrical steels [2,8]. Figure 2.1.4-1 depicts the global market distribution and the distribution detail of soft magnetic materials. As can be seen, the production of soft magnetic material is governed by the classical Fe-Si steel (NO or GO). The soft ferrites take the next largest portion of the whole market (shown in yellow). The rest is shared by Fe-, Co- and Ni-based alloys; amorphous/nanocrystalline alloys, and iron/powder cores.

Nowadays, the search for new materials with better soft magnetic properties is still an issue of interest for many researchers due to the tendency to miniaturise devices and reduce both energy consumption and production costs. For example, in a transformer, an increase of 1.5% in energy efficiency implies a direct saving of 240×10^9 kW·h [1], which is equivalent to $12 billion/yr for an electricity price of $0.05/kW·h [16].

There are several kinds of soft magnetic materials; most of them are based on iron (Fe), nickel (Ni) and cobalt (Co). The classical, and one of the most studied, soft magnetic material is the iron-silicon (Fe-Si) alloy, which was discovered when the scientist Robert A. Hadfield added Si to pure Fe and saw how the permeability and resistivity were dramatically increased, while decreasing the coercivity [17]. After this breakthrough, further investigations conducted other researchers to find that adding 6.5 wt % of Si to pure Fe produced the best electrical and magnetic properties [18,19]. The high M_S and relatively low cost make Fe-Si alloys suitable for transformers and electrical machines. However, despite these benefits, the

low electrical resistivity makes silicon steels unsuitable at high-frequency due to the high eddy loss [20]. Other typical commercially available soft magnetic materials are [21]: pure Fe, low-carbon steel, Fe-based powders, Permalloy (Fe-Ni) or Molypermalloy (Fe-Ni-Mo), Permendur or Hiperco (Fe-Co-V), MnZn or NiZn ferrites and Sendust (Fe-Si-Al), among others. A common feature of all these materials is that they possess a crystalline structure. Conversely, discoveries in the last sixty years have shown that amorphous and nanocrystalline materials exhibit an excellent soft magnetic behaviour. These materials are usually based on Fe and Co, and some of them can be found in the market with commercial names as: METGLAS [22], NANOPERM [23], FINEMET [24,25], VITROVAC [26], VITROPERM [27], HITPERM [28] and NANOMET [29].

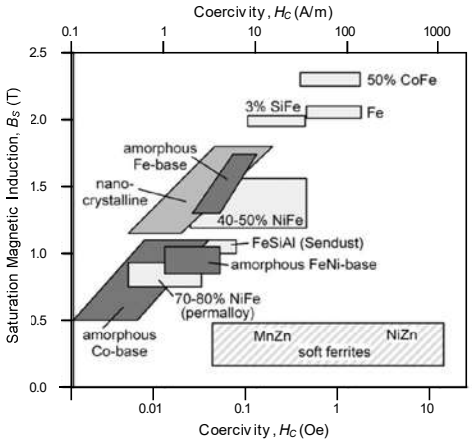

Figure 2.1.4-2. Comparison of various soft magnetic materials. Magnetic behaviour in various ranges of saturation magnetic induction (B_S) and coercivity (H_C) (adapted from Ref. [30,31]).

Regarding the magnetic properties, beside the low H_C, soft magnets are known to have high μ and B_S. Figure 2.1.4-2 and Figure 2.1.4-3 show a summary of the most important magnetic properties of soft magnetic materials. As can be seen, depending on the composition and structure, H_C can take values as low as ~1 A/m (~0.1 Oe) and the effective permeability (μ_e) as large as 2×10^5. Furthermore, B_S will depend mainly on the amount of ferromagnetic material (Fe, Ni or Co) and the structural character (crystalline, nanocrystalline or amorphous, see Ref. [2]).

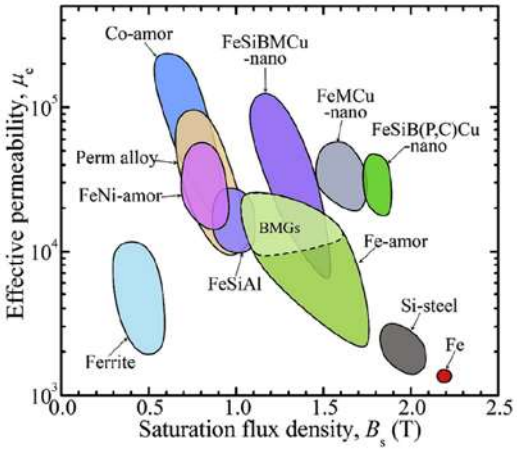

Figure 2.1.4-3. Relationship between effective permeability (μ_e, at 1 kHz) and saturation magnetic induction (B_S) for different soft magnetic materials [32,33].

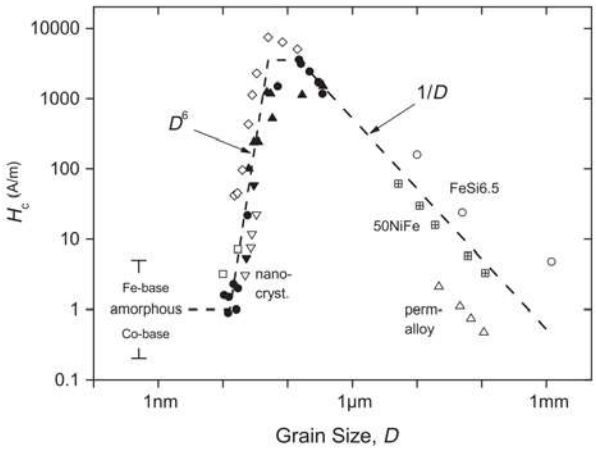

Figure 2.1.4-4. Coercivity (H_C) vs grain size (D) for various soft magnetic materials [34].

There have been several studies about H_C in soft magnetic materials, and how this property changes with the structural character. One of the most complete works, which summarises many investigations, was carried out by Herzer [30,35], who developed a relation between H_C and the material grain size (D). The $1/D$ dependence of coercivity for large grain size reflects the conventional rule that very low coercivity can be achieved by increasing the grain size. This rule is valid only for gran size larger than ~100 nm. On the contrary, decreasing the grain size from 100 nm will provoke a sudden decrease in H_C, turning its dependence into D^6. This drop can lead to extremely small values of H_C (~1 A/m) in nanocrystalline structures (for crystal size $\lesssim$20 nm) and amorphous materials. The extremely low coercivity in amorphous materials was first explained by Alben et al. [36] by

the *Random Anisotropy Model* (RAM). This model was later extended to nanocrystalline materials by Herzer [34] (for crystal size smaller than the ferromagnetic correlation exchange length, L_{ex}), where it was found that the local magnetocrystalline anisotropies of the crystals embedded in an amorphous structure are randomly averaged out when the ferromagnetic correlation exchange length is larger than *D.* The best magnetic properties are achieved in materials that possess a nanocrystalline structure of a soft magnetic phase of about 70–80% (wt. %) embedded homogeneously in an amorphous matrix.

Additionally, it is well-known that H_C is controlled by the process of magnetisation reversal, which mainly depends on domain wall motion. The movement of domain walls depends on many factors such us strain, exchange interactions, demagnetising effects, and structural and surface heterogeneities. For Fe-based amorphous melt-spun ribbons, the contribution of surface roughness has been estimated as 0.5 A/m, being this the limiting factor for H_C in this kind of samples [37,38].

Despite that RAM has demonstrated to be a good approach to explain H_C of amorphous and nanocrystalline materials, the presence of dipole effects on the surface of nanocrystals (surrounded by an amorphous matrix) and particles (for powder samples) makes RAM inaccurate. This suggests that new models should be formulated in the future that consider also these phenomena.

2.1.5 Applications and soft magnetic composites

Soft magnetic materials can be used in both DC- and AC-applications. In DC-applications, also called static applications, it is required that the material possesses high magnetic flux density (B_m) and μ, and low H_C. In AC-applications, the most important requirement is that the material has the minimum possible power loss (P), though the aforementioned properties should remain in certain values as well [16]. Figure 2.1.5-1 exhibits some of the most known soft magnetic materials, as well as the main applications and requirements in working conditions. For high operating frequency, the main requirement is the fast response of the material at a given excitation field; in other words, the material is intended to be highly efficient. On the contrary, for low operating frequency, a high flux density is needed to attain high outputs; in this way, the components can be reduced in size while keeping the electromagnetic performance.

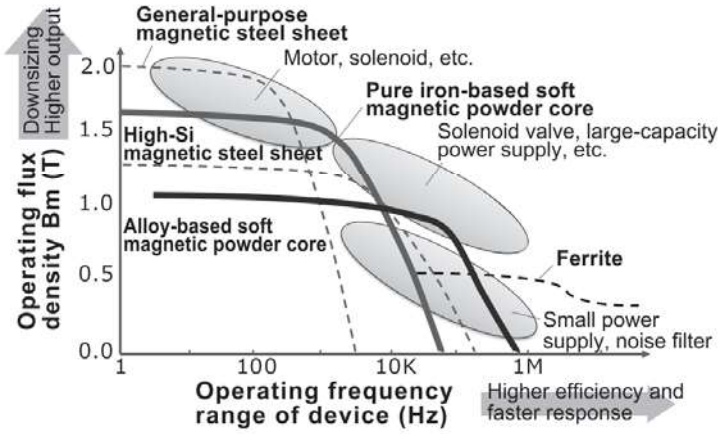

Figure 2.1.5-1. Operating frequency (f) and flux density (B_m) range for various soft magnetic materials [39].

Soft magnetic materials have been classified into different categories according to their operating frequency (see TABLE 2.1.5-I). For static applications (i.e., f <1 Hz), materials such as soft iron, Fe-Co (Permendur) and Ni-Fe (Permalloy) are mostly used. The main applications of these materials are electromagnets and relays. When the operating f exceeds 1 Hz, we speak of AC-applications. AC-applications can be divided into 4 main groups, depending on the range of operating frequency: low frequency (1 Hz–1 kHz), audio-frequency (100 Hz–100 kHz), radio-frequency (100 kHz–1000 MHz) and microwave (f >1 GHz). For low-frequency, Si steel and crystalline soft magnetic materials are preferred; for audio-frequency, amorphous and nanocrystalline are the most suitable, and for radio-frequency and microwave, ferrites are widely used.

TABLE 2.1.5-I. Frequency classification of soft magnetic materials and their applications [2].

Frequency	Materials	Applications
Static <1 Hz	Soft iron, Fe–Co (permendur) Ni–Fe (permalloy)	Electromagnets, relays
Low frequency 1 Hz–1 kHz	Si steel, permalloy, finmet, magnetic glasses	Transformers, motors, generators
Audio-frequency 100 Hz–100 kHz	Permalloy foils, finmet, magnetic glasses, Fe–Si–Al powder (sendust) Mn–Zn ferrite	Inductors, transformers for switched mode power supplies, TV flyback transformers
Radio-frequency 0.1–1000 MHz	Mn–Zn ferrite, Ni–Zn ferrite	Inductors, antenna rods
Microwave >1 GHz	YIG, Li ferrite	Microwave isolators, circulators, phase shifters, filters

The need for new materials with superior soft magnetic performance has led researchers to develop a novel group of materials, the so-called *Soft Magnetic Composites* (SMCs). This group of materials has emerged to aid in

improving the efficiency and reducing weight and costs. SMCs consist of micrometre-scale particles (most often Fe, but sometimes alloys such as Fe-P, Fe-Si, Fe-Co or Fe-Ni-Mo, among others), mixed with an organic or inorganic material as coating and/or bonding agent. The powder coating acts as electrical insulator between particles with the aim of reducing power loss and, therefore, improving the device performance at high-frequency [40,41]. Due to these characteristics, crystalline ferromagnetic powders have shown a great potential for the manufacturing of low/radio-frequency devices.

Two important aspects to take into account are the powder production and SMC preparation. The search for the optimum process to produce powders and manufacture components has been a topic of great interest for many researchers and companies. Most of the developments have been focused on device preparation (for example, cores) from gas/water atomised or mechanically alloyed (MA) powders by some powder metallurgy consolidation processes, such as *compression moulding*, *cold pressing*, *spark plasma sintering*, *hot pressing*, etc. [42–44].

The particle size in SMCs has an important effect on the final magnetic properties. It has been reported that the coercivity is inversely proportional to the particle size in crystalline particles; smaller particles have an unfavourable surface to volume ratio compared to larger ones, together with an increased number of particle boundaries and defects, which hinder the magnetisation process by pinning domain walls [45]. In addition, the use of particles and, therefore, the presence of free surfaces in SMCs, enhances the *demagnetising field*. During the magnetisation process of particles, poles are induced on the particle surfaces. Hence, the field necessary to magnetise the composite increases and, consequently, μ becomes smaller. The demagnetising effect increases as the particle size decreases and becomes more important when the particles are mostly spherical [46]. It has been demonstrated that this phenomenon can be reduced by changing the powder morphology and heat treating the powders [46–48].

As opposed to crystalline particles, amorphous and nanocrystalline particles exhibit lower H_C when they are smaller, so they may have a promising future in SMCs, especially for radio/microwave frequency applications. Since the first amorphous powder was produced by *atomisation* many years ago, and due to the excellent performance exhibited at high-frequency [49], they have turned into the best alternative in many electromagnetic applications [27,50]. Several amorphous compositions have been developed and produced by gas atomisation, most of which are

based on the ternary FeSiB system. Recent studies have revealed the excellent power loss performance of gas-atomised alloys of FeSiBP [51], FeSiBPCu [52] and FeSiBNbCu [53]. It has also been demonstrated that further treatments, such as magnetic annealing, significantly improve the power loss performance [54] and slightly improve μ [55].

The high-frequency (>100 kHz) performance of amorphous and nanocrystalline SMCs is due to the use of both small particles and an insulating layer. As is well-known, one of the main contributor to P_T at high-frequency is eddy current loss. Eddy currents in SMCs follow two different paths: inter-particle and intra-particle. Inter-particle eddy currents can be considerably reduced by insulating each particle, whereas intra-particle eddy currents are reduced by decreasing the particle size [13].

The advantages of using amorphous and nanocrystalline soft magnetic powders for high-frequency applications are more than noticeable, but the production is still challenging and many efforts must be done in order to increase the yield.

2.2 Amorphous and Nanocrystalline Materials

2.2.1 Amorphous materials

The first known non-crystalline metallic material was reported by Duwez et al. [56], who achieved the production of non-crystalline silver-copper alloys. The presence of only one broad and diffuse peak in the *X-ray Diffraction* (XRD) pattern confirmed that the material was non-crystalline, which was later corroborated by *Transmission Electron Microscopy* (TEM). After this breakthrough in the 60s, thousands of different alloys have been prepared with a non-crystalline structure by different processes.

As is well known in the classical nucleation and growth theory, when a metallic material is cooled down from the liquid stare, since the free energy associated with the crystalline structure of the solid is smaller than the free energy of the liquid, nuclei will appear at the nucleation sites (see line 1 in Figure 2.2.1-1(a)). These small embryos will growth if their radii overtake the critical radius at the maximum total free energy change (ΔG) and will transform into crystals [57]. Nevertheless, if the material is cooled down swiftly, exceeding the critical cooling rate (R_C), the crystallisation will be suppressed and a non-crystalline structure will form (see line 2 in Figure 2.2.1-1(a)). The other way to produce non-crystalline metallic materials is by solid-state amorphisation [58], but it will not be discussed in this thesis.

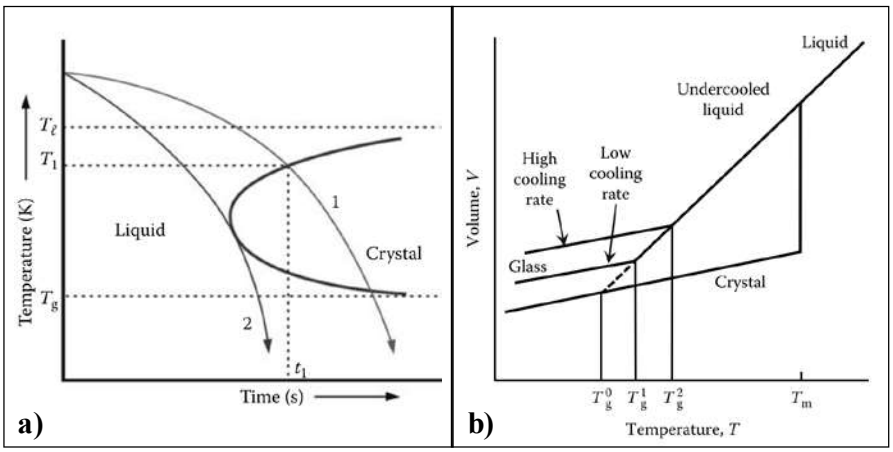

Figure 2.2.1-1. a) Schematic representation of a diagram Time-Temperature-Transformation (TTT) showing two different cooling rates (lines 1 and 2), and b) variation of the volume with temperature during the material cooling [59].

Cooling down a metal from the liquid state provokes a reduction of the specific volume. When the temperature reaches the solidification/melting point (T_m), a sharp drop in the specific volume of the material is observed, until it reaches the value of the equivalent crystalline solid (see Figure 2.2.1-1(b)). Further decrease in temperature results in a slight decrease in the specific volume. When materials are cooled down below T_m, the melt maintains its non-crystalline state as an undercooled (or supercooled) liquid in a certain range of temperature before the crystallisation begins. If the metal possesses a wide undercooled (or supercooled) liquid region, the liquid achieves such a high viscosity that gets *frozen-in*, becoming a glass at the glass transition temperature (T_g), when the viscosity reaches 10^{12} Pa·s. This supercooled liquid region depends on several factors such as material viscosity, cooling rate, interfacial energy between liquid and crystal, type of nucleation, etc. [59].

There is a group of non-crystalline materials that possess a narrow supercooled liquid region and do not reveal a glass transition, or at least it cannot be easily observed; these materials are usually called *amorphous* instead of *glasses*. Many different definitions have been formulated to explain the difference between *glass* and *amorphous*, which have led researchers to use these two terms interchangeably. Inoue et al. has explained that a *glass* is any non-crystalline solid obtained by continuous cooling from the liquid state, whereas *amorphous* is that one obtained by other process (for example, solid-state amorphisation) [59]. On the other hand, Gupta has formulated another explanation based on structural and thermal properties: a non-crystalline solid is a *glass* if the short-range order

of the freeze-in solid below glass transition and that of the delivering melt are the same. However, if the short range order is not the same as in the melt precursor, the non-crystalline solid is called *amorphous* [60,61]. Even though these definitions are scientifically supported, there still exist a confusion and almost each researcher assumes its own criteria. In the case of this work, it has been adopted that a non-crystalline material that reveals a glass transition upon heating and/or cooling is a *glass*, and that one that does not exhibit this glass transition is *amorphous*. As most of the materials produced in this thesis do not reveal a glass transition, it will be used the term *amorphous* instead of *glass* throughout this work.

Amorphous materials can be classified into three categories: the transition metal-metalloid (TM-M) alloys, the rare earth-transition metal (RE-TM) alloys and the transition metal-zirconium or hafnium (TM-Zr-Hf) alloys. TM-M alloys are typically composed of about 80 % of Fe, Co or Ni, and the remainder corresponds to carbon, boron, silicon, phosphorous or aluminium. These kind of materials are usually produced by quenching from the liquid state by rapid solidification process (RSP), being the presence of metalloids helpful to lower the liquidus temperature (T_l) and favour the amorphous structure, although their presence also alters the magnetic, mechanical and electrical properties [62]. This work involves the use of only TM-M alloys, therefore, the other two types of amorphous material will not be discussed.

There exist many applications where amorphous materials can be used, i.e.: electronic devices, sporting goods, automobile components, structural parts, magnetic components, etc. This versatility comes from their superior properties such as corrosion resistance, soft magnetic properties and mechanical strength, among others [63]. For many years, the search for new amorphous materials has been a big challenge, since not all materials can be synthesised in the amorphous state by RSP. Before producing amorphous materials, it is required to design the precise composition. The material must have the ability to retain the amorphous structure when it is cooled down at the cooling rate that is characteristic of the selected RSP. This implies that the material must have a large supercooled liquid region (ΔTx), so that the amorphous structure is thermally stable at low temperature [59]. In some materials, the composition is modified adding amorphous forming elements, for example. The ability to form an amorphous structure is usually assessed by means of several parameters and is defined as the *Amorphous Forming Ability* (AFA, for amorphous materials) or *Glass Forming Ability* (GFA, for metallic glasses), although this last one has been mostly used because most of the parameters include T_g.

2.2.2 Amorphous forming ability

There are some conditions for the formation of the amorphous structure and some alloys are more susceptible than others are to form this structure. There have been thousands of studies about how to predict AFA; most of them are based on the classical nucleation and growth theory. The homogeneous nucleation rate (I), and the growth rate (U) of a crystalline phase formed from a supercooled liquid can be expressed by [64]:

$$I = \frac{10^{30}}{\eta(T)} exp\left[\frac{-16\pi}{3}\frac{\alpha^3 \Delta S_f T^2}{R(T_l - T)^2}\right] \quad \text{2.2.2-1}$$

$$U = \frac{10^2 f}{\eta(T)}\left[1 - exp\left(-\frac{\Delta S_f (T_l - T)}{RT}\right)\right] \quad \text{2.2.2-2}$$

where η is the viscosity at the temperature T, f is the fraction of nucleation sites at the growth interface, α is a factor that depends on the atomic arrangement at the interface and has a value close to unity, ΔS_f is the change in entropy per mole due to melting, R corresponds to the universal gas constant and T_l is the liquidus temperature.

The target is to avoid crystal nucleation and growth; therefore, as is clearly shown in these equations, AFA can be analysed taking into account η, ΔS_f and $T/(T_l - T)$. For metallic alloys, ΔS_f does not change significantly; thus, only η and $T/(T_l - T)$ shall be considered [65]. η is a property difficult to measure in the liquid state; however it can be estimated from mathematical models [66]. There is a clear correlation between η and crystallisation; the increase in η provokes a delay in the crystallisation during solidification, which means that the TTT curve shifts to the right, increasing in this way R_C [59] and consequently, the formation of amorphous structure is favoured.

In the early years of research on non-crystalline materials, a large number of empirical criteria were proposed to assess the AFA and GFA of alloys. Turnbull demonstrated that when the reduced glass transition temperature (T_{rg}=T_g/T_l) is higher than 2/3, the homogenous crystal nucleation is slowed down and, hence, the crystallisation is essentially suppressed [67,68]. Donald & Davies [69] proposed a simple way to estimate the AFA of alloys with two or more elements by the rule of mixture liquidus temperature (ΔT^*). After these two criteria, several other parameters have been formulated including: ΔT_X, S, γ, δ, $\emptyset$, γ_m, ω, P', σ, λ, α, β, and new β. TABLE 2.2.2-I shows these parameters, as well as the references and equations to calculate them. All these parameters provide a good estimation of the GFA,

but some of them are not suitable for amorphous materials, where the T_g cannot be distinguished. To solve this, some researchers have proposed an approach to calculate T_g using T_m [70], but this kind of approximations do not consider many factors and can be considered just as a rough estimation. Despite all these parameters, the most direct and quantifiable indicator of the AFA or GFA is still R_C. Another slightly less direct but quantifiable parameter is the maximum section thickness (or diameter) of a sample (D_{max}) [64].

TABLE 2.2.2-I. Some quantitative criteria proposed by various authors to evaluate the GFA and AFA.

Parameter	Equation	Reference
Reduced glass transition temperature	$T_{rg} = T_g/T_l$	[67,68]
Rule of mixture liquidus temperature	$\Delta T^* = [T_l^{mix} - T_l]/T_l^{mix}$	[69]
Supercooled liquid region	$\Delta T_X = T_X - T_g$	[71]
S parameter	$S = [T_P - T_X]\cdot[T_P - T_g]/T_g$	[72]
γ parameter	$\gamma = T_X/[T_g+T_l]$	[73]
δ parameter	$\delta = T_X/[T_l - T_g]$	[64]
$\emptyset$ parameter	$\emptyset = T_{rg}\cdot[\Delta T_X/T_g]^{0.143}$	[66]
γ_m parameter	$\gamma_m = [2\cdot T_X - T_g]/T_l$	[74]
ω parameter	$\omega = T_g/T_X\text{-}2\cdot T_g/[T_g + T_l]$	[75]
P' parameter	$P' = C_B/[C_B+C_C]\cdot\lvert[v_B - v_A]/v_A\rvert + C_C/[C_B+C_C]\cdot\lvert[v_C - v_B]/v_A\rvert$	[76]
σ parameter	$\sigma = \Delta T^*\cdot P'$	[77]
λ parameter	$\sum_{(i=B)}^{Z} C_i\,\lvert[r_i/r_A]^3 - 1\rvert$	[78]
α parameter	$\alpha = T_X/T_l$	[79]
β parameter	$\beta = 1 + T_X/T_l = 1 + \alpha$	[79]
New β parameter	$\beta = [T_X\cdot T_g]/[T_l - T_X]^2$	[65]

Furthermore, based on extensive studies on amorphous materials and metallic glasses, Inoue has formulated three basic empirical rules for the formation of amorphous structure [59,80]:

i. The alloy must contain at least three components.

ii. A significant atomic size difference should exist among the constituent elements in the alloy (at least 12 % among the main constituent elements).

iii. There should be a negative heat of mixing among the major constituent elements in the alloy system.

Since the production of most amorphous materials involves a RSP, the production process must generate a high enough cooling rate to exceed R_c. The first amorphous material produced by Duwez et al. [56] was synthesised by the so-called gun technique [81], which achieves cooling rates approaching 10^6 K/s. In this process, a small quantity of molten metal is ejected using a shock wave onto a conducting substrate. The molten metal spreads in the form of a thin layer, typically of micrometres (20–50 μm). From this process, two basic requirement can be established to achieve high solidification rates: forming a thin layer of the molten metal and intimate thermal contact with a good heat-conducting substrate to rapidly extract the heat from the liquid metal. Obviously, the cooling rate required to form the amorphous structure will depend on AFA or GFA and can be either as high as 10^6 K/s or as low as 0.1 K/s [82]. The main problem of producing amorphous materials by the gun technique was that the material section was not homogenous and it was difficult to determine the physical and mechanical properties. To overcome this deficiency, a number of other techniques were developed, which allowed the materials to be synthesised as amorphous in different sizes and shapes (ribbons, wires, powders, etc.).

One of the most significant milestone in this field was the development of the chill block melt-spinning technique [83], which produces thin ribbons and can reach cooling rates as high as 10^6 K/s. This process has been also known as *Disk Cooling* technique [84] or more recently named as *Melt Spinning* process. There have been other processes that have achieved the synthesis of amorphous materials such as *Spark Erosion* [85] and *Atomisation* [86], however, they have not been successful due to the low production rates (as is the case of spark erosion) and lower cooling rates compared to melt spinning (as is the case of atomisation). Even though melt spinning is still the main fabrication process, the difficulties exhibited in using thin ribbons to manufacture components have led to seek new methods to synthesise amorphous materials. Despite that atomisation produces lower cooling rates than melt spinning, this process has become a promising alternative to produce amorphous materials due to the high production rates and versatility of powder (i.e., it allows manufacturing finished or semi-finished parts with various geometries and sizes). For that

reason, this process has been used in this work as RSP and its fundamental features will be described in detail in section 2.3.3.

As was previously mentioned, amorphous materials can be used in different applications due to their excellent soft magnetic properties. Some of the most studied amorphous compositions, in terms of soft magnetic properties, are those belongings to the ternary Fe-Si-B system. Various Fe-Si-B alloys have shown an extraordinary ability to be synthesised as amorphous and develop excellent soft magnetic properties (low coercivity, low magnetostriction, high saturation magnetisation, etc.) [87]. Owing to these characteristics, this ternary system has recently attracted the attention of researchers working on atomisation, and the main properties and advantages are discussed in the following section.

2.2.3 Nanocrystalline materials based on Fe-Si-B alloys

Nanocrystalline materials can be defined as materials that possess a crystalline structure with nanometric grain size. They are usually obtained under non-equilibrium conditions, where the diffusion of atoms is disrupted due to the fast drop of temperature. Many years ago, Yoshizawa et al. discovered that it was possible to reach the nanocrystallisation in amorphous Fe-Si-B alloys by doping the material with Cu and Nb, and subsequent heat treatments [24,25]. This milestone allowed several researchers to produce nanocrystalline materials from Fe-based amorphous structures, most of which were based on the ternary Fe-Si-B system.

Fe-Si-B system has been deeply studied due to its capacity to develop amorphous structure and excellent soft magnetic properties [88,89]. Numerous alloys of this system [88–90] have been produced since the 70s, when B was added to the binary alloy Fe-Si [84,85]. Since this first publication, many investigations can be found in the literature [91]; in fact, this composition was the basis of the commercial alloy known as METGLAS [22]. Initially, these compositions were produced by the well-known melt spinning process [92,93] and, after some attempts, it was possible to produce them as amorphous in powder form by mechanical alloying and/or gas/water atomisation below certain particle size [94–96]. As the fabrication of amorphous Fe-Si-B alloys involves rapid solidification, the formation of amorphous structure has been deeply studied. Thanks to many efforts of some researchers, it was possible to establish an amorphous forming region inside the ternary Fe-Si-B, which has facilitated the design of amorphous Fe-Si-B alloys [97–100].

After producing the amorphous structure, and in order to enhance the soft magnetic properties, heat treatments must be performed. The as-quenched structure possesses internal stresses and free volume, which cause an increase in H_C due to the presence of magnetoelastic anisotropy [101–103]. To achieve the structural relaxation of an as-quenched structure, the material has to be annealed at a temperature below T_g [59]. Annealing at higher temperatures will induce the precipitation of crystalline phases. Depending on the Fe/Si ratio, the first precipitation will correspond to the solid solutions α-Fe (A2), α-Fe(Si) (B2) or the ordered Fe_3Si (DO_3) [104]. Further increase of the annealing temperature will provoke the crystallisation of the metastable Fe_3B phase or stable Fe_2B phase [95,105,114–116,106–113]. These borides are undesirable because they deteriorate the soft magnetic properties, acting as pinning centres for the domain wall motion during the magnetisation process [117]. Several researchers have studied the soft magnetic properties of these alloys. They found that the best soft magnetic behaviour is attained with the Fe(Si) phase embedded in an amorphous structure [84,85].

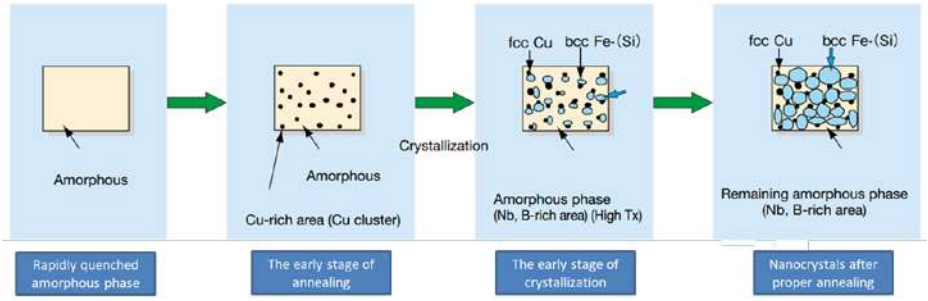

Figure 2.2.3-1. Nanocrystallisation process in amorphous materials (FINEMET-type) produced by proper annealing (modified figure from Ref. [118]).

The basis of the nanocrystallisation process can be well explained using as example the classical FINEMET-type alloys, which are based on Fe-Si-B doped with small amounts of Cu and Nb. First, the alloy must be produced as fully amorphous by a RSP, for example; the amorphous structure works as the starting matrix for the precipitation of nanocrystals. Then, the material has to be annealed in a range of temperatures within the first crystallisation peak obtained by *Differential Scanning Calorimetry* (DSC). In the early stage of annealing (usually slightly before the crystallisation temperature T_x) [119], Cu-rich clusters start to form in the amorphous matrix; this clusters work as nucleation sites for the formation of nanocrystals. In the early stage of crystallisation, the embryos form in the nucleation sites (Cu-rich clusters), which will grow if the activation energy is high enough. At this point, Nb plays an important role; the combination of the right amount of Nb and proper annealing make possible to control the

crystal growth. As a result, a nanocrystalline structure of the Fe(Si)-rich phase embedded in an amorphous matrix is produced. The amount of Cu is also crucial in the nanocrystallisation process; a higher Cu content decreases the AFA and, consequently, the production of the initial amorphous phase becomes more difficult. On the other hand, a higher Cu content helps to increase the nucleation sites and makes the distribution of nanocrystals more homogenous, which is favourable to attain excellent soft magnetic properties [105,120,121].

The main advantage of nanocrystalline materials in terms of their soft magnetic properties is the very low H_C because the local magnetocrystalline anisotropies of the crystals embedded in an amorphous structure are randomly averaged out when the ferromagnetic correlation exchange length (L_{ex} ~35 nm for α-Fe grains) is larger than D [30]. Beside the low H_C, this kind of alloys also exhibits high M_S, thanks to the two contributions arising from the amorphous and nanocrystalline phases [122], and low P_T, due to the high electrical resistivity. This high resistivity is achieved thanks to the complex electron scattering mechanism at the interface between the amorphous and nanocrystalline phase [123].

Nowadays, the main challenge is to find compositions with a good combination of high AFA, high M_S (and hence, high Fe or Co content), ultra-low H_C and reduced P_T. This has led to the development of new nanocrystalline alloys [33,124], including FeSiBP, FeSiBPNb, FeSiBPCu and FeSiBPNbCu, and various other Co-based alloys [125,126], which partially fulfil these requirements [127–131]. In addition, many efforts are focused on changing the fabrication process in order to overcome the barriers regarding the manufacturing of components and devices with complex geometries, being one of the possible solutions the use of *Powder Metallurgy* (PM) processes.

2.3 Powder Metallurgy

2.3.1 Basis of powder metallurgy

Powder metallurgy, known as PM, is a set of production methods for making finished or semi-finished precision components from powders. Some of these technologies are not new; older civilisations practised the art, as bear witness the iron pillar in Delhi, certain Egyptian implements and articles of precious metals made by the Incas [132]. Nevertheless, in the 1920s, it started to make an important contribution to materials production and processing, when people used PM technologies for producing tungsten

carbide and porous bronze bushes for bearings. Further developments have made possible the production of a great variety of ferrous and nonferrous materials. Nowadays, the advances in PM have led to the mass production of new types of powders with superior properties; non-equilibrium materials such as amorphous, microcrystalline or metastable alloys; fully dense materials by sintering process, etc. PM parts are used in vehicles, hardware, tools, cameras, farming and gardening equipment, office equipment, sporting goods, military products, and many more applications [133]. PM processing is many times more competitive than other methods (i.e., casting, stamping, machining, etc.). Some typical advantages are post-processing of components can be avoided, material losses due to the machining or post-processing can be considerably reduced, and the component weight can be reduced maintaining the same desired properties.

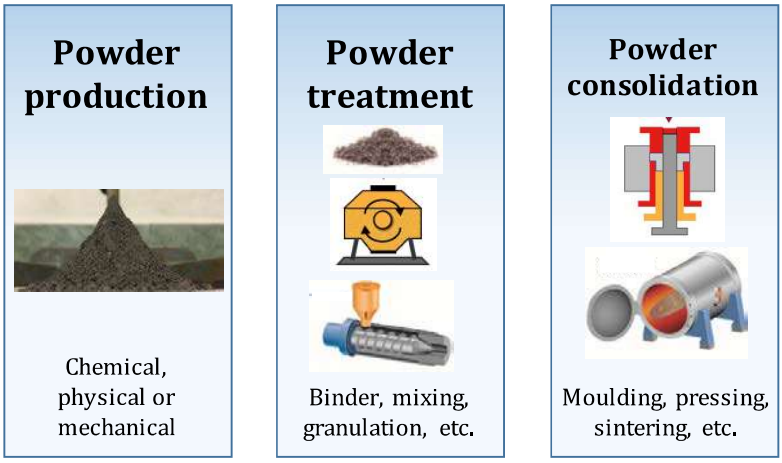

Figure 2.3.1-1. Sketch of the different steps in a powder metallurgy (PM) process.

PM process consists of mainly three different stages: powder production, conditioning and consolidation. Powder production methods may be classified as chemical, physical and mechanical. In this work, the physical method called atomisation was used to produce the powders and will be explained in the next sections. Powder conditioning consists of different treatments to improve or change the powder properties, i.e., annealing, powder mixing, particle size reduction, granulation and coating. During powder consolidation, the treated powder is shaped into a component and sintered using processes such as press and sintering, hot pressing, *Cold Isostatic Pressing* (CIP) and sintering, *Hot Isostatic Pressing* (HIP), powder extrusion, *Powder Injection Moulding* (PIM), plastic injection moulding, compression moulding, *Spark Plasma Sintering* (SPS) or some of the new additive manufacturing technologies. Occasionally, some secondary

operations are necessary to finish the component, such as coating, surface finish operations or heat treatments, among others (see Figure 2.3.1-1).

The quality and characteristics of the powders will have a great influence on the process and will determine the final properties of the products. For that reason, the choice of the right fabrication process should be done considering the available raw material and the end application. The powder characteristics will be considerably different depending on the production process. For instance, gas atomisation produces spherical powders, while hammer milling produces flakes; this difference will affect the properties of the powders (apparent density, tap density, flowability, etc.) and of the final product (i.e., density, mechanical properties, etc.) [134].

2.3.2 Powder properties

There are some powder properties that must be defined:

i. Apparent density: this property corresponds to the mass per unit of volume of loosed packed powder. To measure it, the powder is loaded into a funnel and permitted to flow through the discharge orifice into the centre of a density cap of 25 cm^3. When the powder fills and overflows the density cup, the funnel shall be rotated approximately 90° in a horizontal plane, so that the remaining powder falls away from the cup. Using a non-magnetic spatula, with the blade held perpendicular to the top of the cup, the powder must be levelled off flush with the top of the density cup. Then, the powder is transferred to a balance and weighed [135]. The apparent density (ρ_a) is calculated as:

$$\rho_a = \frac{m}{V_{dc}} \qquad 2.3.2\text{-}1$$

where m is the mass of the powder and V_{dc} is the volume of the density cup.

ii. Tap density: tap density is the maximum density reached by a metal powder when is vibrated or tapped under specific conditions. First, a mass of 50 – 100 g of metallic powder is poured into a clean and dry graduated cylinder. The filled cylinder is submitted to mechanical or hand tapping until no further decrease of the volume of the powder takes place. Then, the volume of powder into the cylinder is read and the tap density (ρ_t) is calculated as [136]:

$$\rho_t = \frac{m}{V_{tp}} \qquad 2.3.2\text{-}2$$

where m is the mass of the powder and V_{tp} is the volume of the tapped powder.

iii. Flowability: this property makes reference to the capability of a powder to free flow. The test consists of loading 50 g of dry and clean powder into a standardized funnel, while keeping the discharge orifice at the bottom of the funnel closed with a finger. A stopwatch will be started when finger is removed from the discharge orifice and stopped when the last particle leaves the funnel. The elapsed time recorded in seconds will be the flowability. This property is usually reported as second/50 g of powder [137].

iv. Particle size distribution: this property can be estimated by different techniques, i.e., sieving, microscopy, laser diffraction, etc. Sieve test is the most used, simplest and cheapest method, A representative sample of 100 g is placed on top of a series of sieves stacked from top to bottom in decreasing order of opening size. Then, the stack of sieves is located in a sieve shaker for 45 min. The particles will redistribute in the different sieves according to its size. Finally, each powder fraction is weighed and the particle size distribution is calculated from the mass fraction collected in each sieve [138]. This method is usually used for particles larger than 20 μm. Microscopy analysis is a complicated and time-consuming method; therefore, it is only used for qualitative comparison of different powders. However, laser diffraction is a very rapid and precise method, especially when the particles are very small. This method measures the angular variation in intensity of the light scattered as a laser beam passes through a dispersed particulate sample. The scattering angle is inversely proportional to the particle size, so the particle size distribution can be directly obtained from the intensity registered at each angle.

v. Morphology: the easiest and most popular method to assess particle shape qualitatively is the direct observation of a sample by optical or *Scanning Electron Microscopy* (SEM).

2.3.3 Gas atomisation process

Gas atomisation is one of the leading methods to manufacture the powders used in PM industry. The use of air, nitrogen, helium or argon as a gas for breaking up a molten stream is called gas atomisation and is a process that has been widely employed as an effective method to produce spherical metal powders. It is attractive because of the applicability to several materials with good process control.

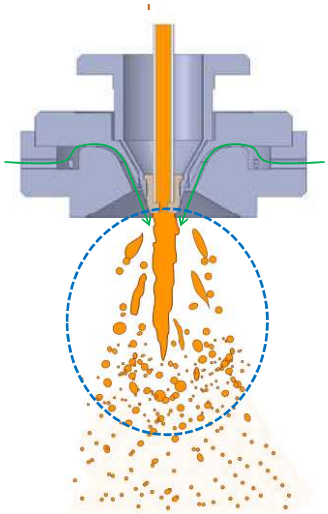

Figure 2.3.3-1. Schematic diagram of the break-up of a melt stream by the rapidly expanding gas.

The principle of gas atomisation is to transfer kinetic energy from a high-speed gas jet to a liquid metal stream, which becomes unstable. The gas expanding around the molten stream causes a dramatic depressurisation and disintegration of the liquid. On summary, it is possible to separate the gas atomisation in three stages. In the first stage (called primary atomisation), the liquid metal column is broken into large droplets or ligaments by the expanding gas. In the second stage (called secondary atomisation), the large droplets are again disintegrated forming smaller droplets, which solidify in fly during the third stage (an example of the process can be seen in Figure 2.3.3-1). Short distances between the gas exit and the melt stream favour the energy transfer, aiding the formation of smaller droplets [139].

The gas atomiser designs in industry are classified in close-coupled and free-fall types. The underlying difference between these two technologies is the location of gas-melt interaction zone. The gas exit is next

to the melt delivery tube exit in close-coupled atomisation, while in the free fall atomisation a distance varying from 10 to 30 cm is maintained between them. This distance allows the melt to flow downward under quiescent air before the high velocity gas interacts with the melt. Close-coupled atomisation is able to produce finer powders despite the drawbacks of backflow and freeze-up that normally do not occur during free-fall atomisation. The design of the gas nozzle is critical in order to achieve a gas velocity that is high enough to destabilize the melt. Up to now, two different gas nozzles are widely used for close-coupled atomisation, namely, the annular-slit and the discrete-jet nozzle. The annular-slit nozzle is an annular slot surrounding the melt feeding tube, while the discrete-jet nozzle is made of a number of discrete holes. The annular-slit nozzles are more widely used by industry due to their superior performance in comparison with the discrete-jet ones [139].

As is commonly reported in the literature, the influence of the processing variables is understood in terms of the energy delivery to the melt. The higher the energy of the pressurised gas, the lower the particle size. The resulting particle size also depends on several physicochemical properties of the gas and melt. Furthermore, the melt mass flow rate can be adjusted through the melt stream diameter and by pressurising the furnace chamber. A higher ratio of gas-metal mass flow rates ($GMR = m_g/m_m$, m_g is the mass flow rate of the gas and m_m is the mass flow rate of the melt) contributes to produce a finer powder. Another variable to control the particle size is the melt superheat (ΔT_m); as ΔT_m increases, the melt viscosity and surface tension decrease, resulting in smaller particles [140].

The cooling rates attained in gas atomisation have been reported to be between 10^4–10^5 K/s, depending on the particle size and atomising gas [139]. This cooling rate is very difficult to measure. Nevertheless, some methods to estimate it have been developed. One method that has been widely used consist of measuring the *Secondary Dendrite Arm Spacing* (SDAS) in the particles. This approach can be only applied to materials in which the dendrites can be observed [141], so it cannot be applied to amorphous powders. The cooling rate can also be estimated by using simplified models of heat transfer between one isolated melt droplet of a given diameter (d) and the surrounding gas [142,143].

Due to the high demand for new materials with better properties, and in order to reduce the material waste, gas atomisation is being used to produce amorphous and nanocrystalline materials. It has been recently demonstrated that Fe-, FeCo-based and other alloys can be produced as fully amorphous by this process [42,144,145], even though the cooling rates are

lower than in other RSP (for example, melt spinning). The ability to produce amorphous powders of different compositions at industrial scale has turned this process into an attractive alternative to fabricate soft magnetic materials for electrical and electronic devices [41].

Chapter 3

Appended Paper Details

This chapter has the aim of disclosing the main details of the appended papers, which include the results of this thesis. Since this thesis is presented in the paper format, a brief explanation of the work methodology will be presented first. Next, the journal details where each paper was published will be disclosed, including impact factor, publication category, journal quality, etc. As a third section, each paper will be introduced accompanied by a brief explanation of the previous planning, as well as how every paper is linked to each other by consecutives tasks. Finally, the last section is composed of a discussion of the entire work.

3.1 Work Methodology

The work methodology is mainly composed by three parts: material production, characterisation and consolidation. Even though the experimental procedures are well explained in the experimental procedure section of each paper, this section has the purpose of explaining how every

paper follows a sequence of tasks leading to the results. Figure 2.3.3-1shows a chart with the work methodology.

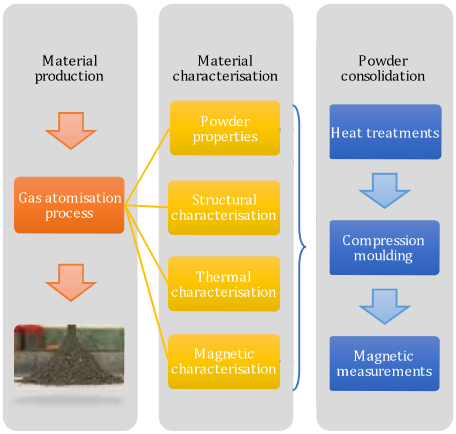

Figure 2.3.3-1. Work methodology chart.

3.1.1 Material production

All the compositions were produced by gas atomisation. The process involved melting and alloying the raw materials in an induction furnace under an argon atmosphere to avoid oxidation. First, the temperature was gradually increased up to 1700 °C in all the cases. Next, the stopper rod was lifted up, so that the melt flowed through the melt delivery pipe into the atomisation chamber. In the atomisation chamber, the melt stream was broken into droplets by a helium gas flow at 60 bar. After atomising the melt, and once the material was cooled down, the powder was collected from the hopper and was sieved with a mesh of 1000 µm to remove the splats and non-atomised material. The batch size was between 3.0 and 2.5 kg. The powder collected from the hopper (i.e., the yield of the atomisation) was between 94 and 99 % of the batch size. All the papers presented in this thesis include the explanation of the material production.

3.1.2 Material characterisation

Material characterisation is divided into four parts:

i. Powder characterisation: this part includes the experiments carried out in order to characterise the physical properties of the powders. The apparent and tap densities were measured according to standardised procedures (MPIF 04 [135] for apparent density and MPIF 46 [136] for tap density), whereas the true density of the

powders was measured using a He pycnometer. The particle size distribution was measured by laser diffraction and powder morphology was observed using SEM.

ii. Structural characterisation: structural properties comprise phase identification and microstructure. Phase identification was conducted using XRD and microstructure was observed using *Field Emission Gun Electron Scanning Microscopy* (FEGSEM). In some cases, to confirm the amorphous and/or nanocrystalline character, different TEM samples were prepared by *Focused Ion Beam* (FIB).

iii. Thermal characterisation: heat capacity changes, and exothermic (i.e., crystallisation of amorphous structure) and endothermic (i.e., ferro-paramagnetic transition and fusion) events were studied by DSC. These experiments helped to identify thermal parameters such as T_C, T_g, T_X, T_P, T_l and ΔH_C. These results were utilised to design the heat treatments and estimate GFA and AFA parameters.

iv. Magnetic characterisation: DC-properties of all compositions were characterised using a *Vibrating Sample Magnetometer* (VSM). The hysteresis loops, measured at room temperatures, and DC-magnetic properties, including H_C, M_S and H_K, were obtained from these measurements. AC-magnetic properties were measured on the consolidated samples; core loss (P_{CV}) and μ_r were obtained using a LCR meter and Ryowa permeameter, respectively.

In the experimental procedure section of all the papers, it will be found the description of characterisation techniques, as well as the characteristics of each instrument (supplier, instrument brand and model, software version, etc.).

3.1.3 Powder consolidation

This part consists of the consolidation of the powders and fabrication of powder cores as a final product. Firstly, the optimum compositions were selected and heat-treated. The main aim of the heat treatments was to achieve structural relaxation and/or nanocrystallisation, which were further confirmed by structural characterisations. Then, the annealed powders were mixed with an epoxy resin and SMCs were manufactured in a toroidal form by the compression moulding process. The cores were characterised by measuring P_{CV} and μ_r. This procedure will be only found in **Paper D**.

3.2 Journal Information

3.2.1 Journal of Alloys and Compounds

The Journal of Alloys and Compounds is an international peer-reviewed medium for the publication of work on materials comprising compounds as well as alloys. Its great strength lies in the diversity of disciplines which it encompasses, drawing together results from materials science, physical metallurgy, solid-state chemistry and physics. The interdisciplinary nature of the journal is evident in many subject areas.

Impact Factor 2018: 4.175

5-years Impact Factor: 3.624

Eigenfactor Score: 0.132

Article Influence Score: 0.601

Journal quartile: **Q1** (Material Science, Multidisciplinary).

TABLE 3.2.1-I. Journal Category and classification

Category of JCR	Classification in the category	Quartile in the category
Chemistry, Physical	47 of 148	Q2
Materials Science, Multidisciplinary	65 of 293	Q1
Metallurgy & Metallurgical Engineering	6 of 76	Q1

Papers A and **C** have been published in this Journal.

3.2.2 IEEE Transactions on Magnetics

IEEE Transactions on Magnetics is a peer-reviewed, archival journal in science and technology related to the basic physics and engineering of magnetism, magnetic materials, applied magnetics, magnetic devices, and magnetic data storage. The articles in this journal are peer reviewed in accordance with the requirements set forth in the IEEE PSPB Operations Manual (sections 8.2.1.C & 8.2.2.A). Each published article was reviewed by a minimum of two independent reviewers using a single-blind peer review

process, where the identities of the reviewers are not known to the authors, but the reviewers know the identities of the authors.

Impact Factor 2018: 1.651

5-years Impact Factor: 1.588

Eigenfactor Score: 0.03

Article Influence Score: 0.362

Journal quartile: **Q3** (Engineering, electrical & Electronic).

TABLE 3.2.2-I. Journal Category and classification

Category of JCR	Classification in the category	Quartile in the category
Engineering, electrical & Electronic	166 of 266	Q3
Physics, Applied	89 of 148	Q3

Paper B has been published in this Journal.

3.2.3 Journal of Magnetism and Magnetic Materials

The Journal of Magnetism and Magnetic Materials provides an important forum for the disclosure and discussion of original contributions covering the whole spectrum of topics, from basic magnetism to the technology and applications of magnetic materials. The journal encourages greater interaction between the basic and applied sub-disciplines of magnetism with comprehensive review articles, in addition to full-length contributions.

Impact Factor 2018: 2.683

5-years Impact Factor: 2.597

Eigenfactor Score: 0.03

Article Influence Score: 0.433

Journal quartile: **Q2** (Material Science, Multidisciplinary).

TABLE 3.2.3-I. Journal Category and classification

Category of JCR	Classification in the category	Quartile in the category
Materials Science, Multidisciplinary	121 of 293	Q2
Physics, Condensed Matter	29 of 68	Q2

Paper D has been published in this Journal

3.2.4 Nanomaterials

Nanomaterials is an international and interdisciplinary scholarly open access journal. It publishes reviews, regular research papers, communications, and short notes that are relevant to any field of study that involves nanomaterials, with respect to their science and application. Thus, theoretical and experimental articles will be accepted, along with articles that deal with the synthesis and use of nanomaterials. Articles that synthesize information from multiple fields, and which place discoveries within a broader context, will be preferred.

Impact Factor 2018: 4.034

5-years Impact Factor: 4.358

Eigenfactor Score: 0.008

Article Influence Score: 0.704

Journal quartile: **Q1** (Material Science, Multidisciplinary).

TABLE 3.2.4-I. Journal Category and classification

Category of JCR	Classification in the category	Quartile in the category
Materials Science, Multidisciplinary	71 of 293	Q1
Nanoscience & Nanotechnology	39 of 94	Q2

Paper E has been published in this Journal

3.3 Appended Papers

Paper A

K. L. Alvarez, J. M. Martín, M. Ipatov, and J. Gonzalez, Soft magnetic amorphous alloys (Fe-rich) obtained by gas atomisation technique, J. Alloys Compd. 735 (2018) 2646–2652.

The first stage of this thesis was dominated by the study of the state of art regarding soft magnetic materials, amorphous and nanocrystalline materials, and GFA. Based on the available information, it was necessary to design the first batch of atomisations, which was based on the ternary Fe-Si-B system. The initial target was to produce amorphous powders in this system with good soft magnetic properties by gas atomisation. As a result, five different compositions were chosen and gas-atomised varying the Fe content from 80 to 50 at. %. Once the powders were produced, they were characterised using the techniques described in section 3.1.2. This first publication comprises the main results of this work on powder production and characterisation.

As main results, fine powders were produced by gas atomisation, exhibiting a median particle size (D_{50}) below 18 μm. The powders are so fine because atomisation experiments were conducted under extreme conditions (i.e., the highest melt temperature, He as atomising gas because of its high thermal conductivity, and the highest possible gas pressure). The particle size varied depending on Si and B content due to the change in the surface tension and viscosity. One of the compositions ($Fe_{70}Si_{18}B_{12}$ at. %) exhibited a broad peak overlapped with the crystalline ones in the XRD pattern, which denoted the presence of amorphous particles. Since in gas atomisation the cooling rate is inversely proportional to the particle size, the smallest particles are cooled down at higher cooling rates, and therefore, it was expected that the smallest particles were amorphous. To confirm this, the particles smaller than 10 μm were separated by sieving and analysed. The particles below 10 μm did not exhibit Bragg's peaks in XRD, denoting its fully amorphous structure. Combining the information of the particle size distribution and the DSC traces, it was possible to obtain that the particles smaller than 16.7 μm exhibited fully amorphous structure. Consequently, the fraction of amorphous powder produced in this composition was nearly 55%. In addition, the soft magnetic properties of the as-atomised (the complete range of sizes) and amorphous (fraction below 10 μm) powders were analysed; the as-atomised powder exhibited a H_C = 12 Oe, whereas the fully amorphous particles exhibited a H_C = 7 Oe. These results denote that

gas atomisation process can be a promising alternative to synthesise amorphous Fe-Si-B particles below certain particle size.

Paper B

K. L. Alvarez, J. M. Martin, M. Ipatov, L. Dominguez, J. Gonzalez, "Magnetic properties of annealed amorphous $Fe_{72.5}Si_{12.5}B_{15}$ alloy obtained by gas atomization technique," IEEE Trans. Magn. 54 (2018) 2002405.

After producing the first batch of atomisations and according to the literature review, eight more compositions were selected from the ternary Fe-Si-B system. The compositions were carefully designed based on the amorphous forming region (inside the ternary Fe-Si-B diagram) reported by various authors; these previous investigations were based on the production of melt-spun ribbons and powder by spark erosion. The Fe content was varied from 80 to 70 at. %. The results showed that six of the eight atomised alloys exhibited different fractions of amorphous particles in the as-atomised state, denoted by the broad peak exhibited in the XRD patterns. One of these compositions ($Fe_{72.5}Si_{12.5}B_{15}$) exhibited the absence of Bragg's peaks in the XRD pattern, which denoted that this sample possesses the highest GFA within the studied alloys and was produced as fully amorphous, i.e., the entire range of particle sizes. This composition was chosen to study the soft magnetic behaviour at various structural relaxation levels and the results were published in this paper.

Since small particles showed better soft magnetic properties, amorphous particles below the 20 μm of the composition $Fe_{72.5}Si_{12.5}B_{15}$ were studied in more detail. The amorphous particles were annealed at three different temperatures below the crystallisation temperature, i.e., 250, 350 and 450 °C for 0 and 60 min. Annealing the powder below T_X produced only structural relaxation of the amorphous structure, without any sign of crystallisation. Furthermore, a substantial improvement in the soft magnetic properties was observed, reducing H_C from 3.26 Oe to 0.44 Oe in the annealed powder at 450 °C for 0 min (0 min means that the sample was heated up to the annealing temperature and immediately cooled down without any holding). In addition, an increase in T_C was also observed, which denoted that structural relaxation was also producing compositional changes of short-range order.

Paper C

Kenny L. Alvarez, J.M. Martín, N. Burgos, M. Ipatov, L. Domínguez, J. González, "Structural and magnetic properties of amorphous and

nanocrystalline Fe–Si–B–P–Nb–Cu alloys produced by gas atomization," J. Alloys Compd. 810 (2019) 151754.

After producing thirteen compositions in the ternary Fe-Si-B system by gas atomisation (five in the first batch [**Paper A**] and eight in the second batch [**Paper B**]), and thanks to the knowledge acquired during the first two years, thirteen more compositions were designed and a third batch of atomisations was conducted. The first objective of this thesis was to produce amorphous powders by gas atomisation, which was fulfilled with the results obtained and shown in **Paper B**, where a fully amorphous Fe-Si-B composition ($Fe_{72.5}Si_{12.5}B_{15}$) was produced. Therefore, in order to achieve the second objective of this thesis, i.e., to produce nanocrystalline powders, new alloys were designed based on the same ternary system doped with Cu, Nb and P. According to the literature, elements like Cu, Nb and P help to increase the nucleation sites and control the crystal growth, favouring the formation of nanocrystalline structures. For that reason, new compositions were designed and gas-atomised, within which three different groups can be identified:

i. FINEMET-type alloys: two samples were gas-atomised within this group, one was the classical FINEMET alloy and the second was based on our fully amorphous alloy reported in **Paper B** ($Fe_{72.5}Si_{12.5}B_{15}$), doped with of Cu and Nb.

ii. ($Fe_{72.5}Si_{12.5}B_{15}$)-based with P: this group is composed by six alloys based on our fully amorphous alloy reported in **Paper B** ($Fe_{72.5}Si_{12.5}B_{15}$), doped with of Cu, Nb and P. The amount of Cu and Nb was varied in order to study the influence of these elements on the GFA, nanocrystallisation and resulting soft magnetic properties.

iii. ($Fe_{76}Si_9B_{10}P_5$)-based: this group is based on a composition found in the literature. Other authors have been able to synthesise this alloy as amorphous; therefore, it was decided to study the influence of the addition of different amounts of Cu and Nb. Consequently, five different compositions were gas-atomised.

Seven of the thirteen compositions exhibited amorphous structure in the particles below 20 μm. Consequently, it was decided to focus the study only on these amorphous alloys. Thermal analysis showed that the addition of different amounts of Cu, Nb and P strongly affected the crystallisation behaviour; crystallisation took place in one, two or three events, and the crystallisation peaks were narrow or broad, depending on the amount of doping elements (Cu, Nb and P). All as-atomised amorphous powders

exhibited excellent soft magnetic properties, i.e., H_C <3.5 Oe and M_S >112 emu/g.

After structural and thermal characterisation of the as-atomised powders, the alloy with the best combination of soft magnetic properties and crystallisation behaviour (three peaks of crystallisation, broad first peak, high T_X, etc.) was selected in order to induce and study the nanocrystallisation ($[Fe_{0.76}Si_{0.09}B_{0.10}P_{0.05}]_{97.5}Nb_{2.0}Cu_{0.5}$). The analysis was again focused on the particles below 20 μm because they exhibited better soft magnetic properties. Several heat treatments were conducted on this alloy under different conditions (i.e., annealing temperatures and times), and the nanocrystallisation was analysed by XRD and TEM. The results showed that annealing the powder provokes structural relaxation and/or nanocrystallisation of the α-Fe phase, depending on the annealing conditions. XRD results were utilised to calculate the amount of nanocrystals and the average gran size by the well-known Rietveld method. Annealing the amorphous powder at 530 °C for 60 min produced the nanocrystallisation (47 wt. %) of phase α-Fe(Si), having an average grain size of 17 nm. Since the size of nanocrystals was smaller than 20 nm and they were homogeneously distributed in an amorphous matrix, H_C was reduced below 1 Oe and M_S increased ~5 %. These results are well explained by the RAM model and the Herzer's theory.

Paper D

Kenny L. Alvarez, H. A. Baghbaderani, J. M. Martín, N. Burgos, M. Ipatov, Z. Pavlovic, P. McCloskey, A. Masood and J. Gonzalez, Novel Fe-based amorphous and nanocrystalline powder cores for high-frequency power conversion, J. Magn. Magn. Mater 501 (2020) 166457.

The production of amorphous and nanocrystalline powders with excellent soft magnetic properties led to the consolidation and fabrication of soft magnetic components. FINEMET-type alloy with composition $(Fe_{0.725}Si_{0.125}B_{0.150})_{96.5}Nb_{3.0}Cu_{0.5}$ was selected to fabricate toroidal powder cores by the well-known compression moulding process. The particles smaller than 20 μm were separated and three different annealings were conducted according to the thermal behaviour obtained from DSC experiments. The heat treatments were carried out in the supercooled liquid region, at the temperature of the first crystallisation peak and at the end of the first crystallisation peak.

The annealed powders exhibited a nanocrystalline structure and excellent soft magnetic properties. The calculated grain size was smaller

than 20 nm in all the samples, demonstrating again that Cu and Nb work efficiently increasing the nucleation sites and controlling the grain growth, respectively. The best soft magnetic properties were observed in the powder annealed at 525 °C (H_C = 0.88 Oe and M_S = 134 emu/g). The as-atomised and annealed powders (<20 μm) were mixed with an epoxy resin (20 vol. %) and four toroidal cores were manufactured. Power loss measurements showed that the core loss of the as-atomised sample was significantly higher in the entire range of frequency (f = 50 kHz–1 MHz). On the other hand, due to the small particle size and good insulation film, the core loss increases only slightly as the frequency increases. Furthermore, the operating frequency was reported to be as high as 300 MHz, with a ferromagnetic resonance at f = 3 GHz. These results denoted that this material could be utilised in high-frequency applications such as voltage regulator (VR), resonant converter, etc.

Paper E

Kenny L. Alvarez, José Manuel Martín, Nerea Burgos, Mihail Ipatov, Lourdes Domínguez, Julián González, Coercivity and magnetic anisotropy of $(Fe_{0.76}Si_{0.09}B_{0.10}P_{0.05})_{97.5}Nb_{2.0}Cu_{0.5}$ amorphous and nanocrystalline alloy produced by gas atomization process, Nanomaterials 10(5) (2020) 884.

This paper comprises the analysis of the mechanisms of coercivity and magnetic anisotropy behaviours of the amorphous and nanocrystalline $(Fe_{0.76}Si_{0.09}B_{0.10}P_{0.05})_{97.5}Nb_{2.0}Cu_{0.5}$ alloy. The structural and magnetic properties of particles below 20 μm were analysed in detail in **Paper C**. However, the high H_C exhibited in this sample compared with similar compositions in the ribbon form (one order of magnitude higher) suggests that other source of anisotropy apart from the demagnetizing effect could be playing an important role in the magnetisation process of the powder. The relatively high value of H_C is likely due to the pinning of domain walls at the surface irregularities in gas-atomised powder. This pinning effect inhibits/thwarts the nucleation and propagation of domains walls during magnetisation reversal.

The average anisotropy field $\langle H_K \rangle$ was obtained from the anisotropy field distribution calculated from the hysteresis loop for non-annealed and annealed samples (480 °C for 30 min and 530 °C for 30 and 60 min). Surprisingly, $\langle H_K \rangle$ was lower in the non-annealed sample; therefore, the width of the anisotropy field distribution (FWHM) was smaller in the annealed ones, which is connected with the procedure of averaging out of the magnetocrystalline anisotropy of nanocrystals.

From a theoretical point of view, the expressions that explain anisotropy behaviour in nanocrystalline materials are based on the assumption that there exist exchange interaction between nanocrystals, being the exchange correlation length (around 35 nm) larger than the grain size ($\lesssim$20 nm). In this scenario, the so-called RAM, which was initially introduced to explain the soft magnetic character of amorphous alloys, was satisfactorily extended to nanocrystalline FINEMET-type melt-spun ribbon alloys. Nevertheless, nanocrystalline materials possess three structural components: i) single-domain crystallites, ii) thin surface layer surrounding the grains, which in this sample is enriched with Nb, B and P and iii) the amorphous matrix itself. This suggests some corrections of RAM for powder nanocrystalline alloys: it should consider the magnetostatic interaction, which seems to have a significant importance in a comprehensive model capable of describing magnetic properties of these nanocrystalline materials. Furthermore, the surface (grain and particle) heterogeneities are a relevant factor affecting H_C; the increase in $\langle H_K \rangle$ due to the appearance of nanocrystals in the annealed samples could be linked to a strong dipolar effect inside the particles and, consequently, to an enhanced demagnetising field. This demagnetising effect dominates over the random magnetocrystalline anisotropy and deteriorates exchange interactions between grains.

Paper F

Kenny L. Alvarez, H. Ahmadian Baghbaderani, J. M. Martín, N. Burgos, P. McCloskey, J. Gonzalez, A. Masood, Novel methodology to predict amorphisation capability of Fe-Si-B soft magnetic powders. In preparation.

The results coming from the gas-atomised Fe-Si-B powders were successfully used to analyse the amorphisation capability of compositions belonging to this ternary system. Amorphous forming ability (AFA) is a measure to evaluate the easiness of producing a given material with amorphous structure. This concept (instead of GFA) has been recently used in relation with some amorphous compositions, where the glass transition is not observed in the DSC traces, which is the case of most of the Fe-Si-B alloys reported in this thesis.

Eleven different compositions, belonging to the ternary Fe-Si-B system, were analysed. Structural and thermal properties were analysed by XRD and DSC, respectively, for both as-atomised and fully amorphous powders. The amorphous fraction (AF) was calculated from the crystallisation enthalpy (ΔH_C) of fully amorphous particles and the energy released upon heating by partially amorphous particles (ΔH). Next, the

maximum size of the amorphous particles was obtained from the particle size distribution. Finally, R_C was estimated for this maximum particle size using a simplified model of heat transfer between the particle and the atomising gas. In addition, the following AFA parameters were calculated: enthalpy of mixing (ΔH^{mix}), α, β and topological instability factor (λ).

The main results showed that no correlation can be established between AFA and ΔH^{mix}, α- or β-parameters. The alloy $Fe_{72.5}Si_{12.5}B_{15.0}$ exhibited 100 % of *AF*, which denotes that this alloy possesses the highest AFA within the studied alloys. The alloy $Fe_{80}Si_{12}B_8$ was produced fully crystalline, and the other nine compositions exhibited an *AF* between 27 – 82 %. Furthermore, thermodynamic modelling and λ-factor were combined into a single diagram and it was possible to establish a combination of requirements in order to identify Fe-Si-B alloys with high AFA:

i. The composition should be inside the region where the first solid phase that crystallises during solidification is Fe_2B. Compositions within this region have higher AFA than within the other regions.

ii. The relation solute/solvent concentration should be such that λ–factor takes values between 0.18 and 0.22. The maximum AFA was found between 0.20 and 0.21.

iii. Within these two limits, the alloys with lower liquidus temperature (i.e., closer to the eutectic composition) will have higher amorphisation capability.

These criteria will allow researchers to design compositions in the ternary Fe-Si-B system with the maximum AFA to be produced as amorphous for a given RSP. In this way, a given production process could be substituted by other RSPs with lower cooling rates but higher productivity (for example, gas atomisation for melt spinning), provided that the composition is tuned according to these criteria to increase AFA. This approach would help to reduce production costs.

Alternatively, the RSP in production may be substitute by another with higher cooling rate. In this case, the criteria may be used to design composition with lower AFA, but better performance (for example, soft magnetic alloys with higher Fe to increase the saturation magnetization).

3.4 Discussion

Twenty-six different alloys were produced by gas atomisation (Fe-Si-B-based), among which fourteen exhibited different fractions of amorphous particles in the as-atomised state (seven compositions of the ternary system Fe-Si-B, one Finemet-type alloy and six Fe-Si-B-P-Nb-Cu alloys). It was demonstrated that the cooling rate reached during gas atomisation strongly affects the formation of amorphous structure; higher cooling rates facilitate the formation of amorphous structures. The cooling rate in gas atomisation is inversely proportional to the particle size and, therefore, smaller particles are cooled down at higher cooling rate than coarser ones. Consequently, if the AFA of a material is not high enough to be produced fully amorphous by gas atomisation, the amorphous structure could be found in a fraction below certain particle size. In addition, particle size in Fe-Si-B alloys is mainly affected by the Si and B content, which strongly alters the viscosity and surface tension of the melt, favouring the breakup of the molten stream into droplets by the high velocity gas flow. Other atomisation parameters, such as GMR and ΔT_m, were also analysed and no correlation was found between theses parameters and the particle size.

Structural and thermal measurements were conducted in all the gas-atomised alloys. The amorphous structures were detected and the crystalline phases were identified by XRD. The use of this technique was key in quantifying the weight fraction of nanocrystalline phase and calculating its grain size by the well-known Rietveld method (for crystal size below 100 nm). On the other hand, thermal analysis by DSC experiments was another essential tool to identify magnetic and structural transitions and to calculate AFA parameters:

i. The ferro- to paramagnetic transition of the amorphous structures was successfully observed as a small endothermic peak in the DSC traces.

ii. The different crystallisation peaks observed in DSC traces permitted to identify the crystallisation characteristics of the amorphous structures (i.e., eutectic crystallisation, primary crystallisation and/or polymorphous crystallisation).

iii. Regarding the AFA, the amorphous fraction (AF) of the as-atomised powders was calculated as the ratio of the energy released upon heating of the as-atomised powders (ΔH) and fully amorphous particles (ΔH_C), which is presented as a parameter to quantify the AFA of the alloys.

iv. Thermal transition temperatures were also obtained from DSC experiments, including T_X, T_P, and T_l.

Several heat treatments were conducted in this work, which were designed based on thermal behaviour (i.e., crystallisation characteristics). The heat treatment results allowed us to conclude that annealing the amorphous structures leads to two main structural changes: structural relaxation and crystallisation. During rapid solidification, the atomic diffusion is strongly suppressed due to the lack of time to allow atoms to move. For that reason, amorphous structures possess internal stresses that must be removed to improve the soft magnetic performance. To activate the atoms movement, it is necessary to apply heat and let them enough time to rearrange and release the internal stresses. The main relief mechanism is by self-moving the atoms to the free-volume within the amorphous structure. The results pointed out that structural relaxation alters the soft magnetic properties; T_C rises while H_C and P_h decrease. This magnetic softening is well explained in the framework of the RAM and by the reduction (or the complete removal) of the magnetoelastic anisotropy.

Conversely, when the samples are annealed at temperatures higher than T_X, the energy applied is high enough to allow the structure to rearrange in its quasi-equilibrium state, leading to the crystallisation. This implies that the initial absence of long-range order is turned into an ordered crystalline structure. If the composition is such that the crystallisation takes place as primary crystallisation at a nanometric scale, the magnetic properties will be mainly controlled by the amount, type and grain size of the crystalline phase. The best soft magnetic properties are achieved in a nanocrystalline material embedded homogeneously in an amorphous matrix, being the grain size and amount of the magnetic phase <40 nm and ~70 wt. %, respectively.

After producing various types of fully amorphous Fe-based alloys by gas atomisation and optimising the annealing process, one composition (the Finemet-type alloy, $[Fe_{0.725}Si_{0.125}B_{0.150}]_{96.5}Nb_{3.0}Cu_{0.5}$) was selected to be used as raw material for the manufacturing of SMC cores, by mixing the amorphous or nanocrystalline powders with epoxy resin and consolidating them by compression moulding. The material selection was based on structural, thermal and magnetic properties. The SMC cores exhibited excellent core loss behaviour, i.e., the core loss was comparatively lower than other reported SMC cores. The annealed cores shown lower core loss than the as-atomised one, confirming the fact that proper annealing significantly contributes to magnetic softening. The novelty in this stage was the use of particle sizes below 20 μm, which according to our previous results, exhibit better soft magnetic properties (lower H_C than the coarser

ones). Furthermore, the use of smaller particle sizes along with a good insulation layer reduce both intra- and inter particle eddy currents, respectively. Consequently, the total power loss is considerably reduced. On the other hand, the production rate of this composition is reported as 1.03 kg/min, showing that besides its high GFA and excellent soft magnetic performance, this alloy can be mass produced.

Soft magnetic properties in amorphous and nanocrystalline ribbon alloys have been well explained in terms of RAM, which considers as the main feature the averaging out of anisotropies. Nevertheless, in the case of powder alloys, it is necessary to extend this model assuming additional mechanisms to the exchange interactions between nanograins in order to explain both, H_C and anisotropy field behaviour. In this context, dipolar effects are clearly pointed out on the surface of particles and nanocrystals, which affect the effective magnetic anisotropy. Furthermore, these surfaces are acting as pinning centres for the domain wall motion, increasing H_C (where the demagnetising field is absent) and deteriorating exchange, so that its effect dominates over the random magnetocrystalline anisotropy.

Regarding the amorphisation analysis, the formation of the amorphous structure is a complex phenomenon that is altered by several parameters. It has been widely reported that GFA is strongly dependent on T_l and T_g, and eutectic compositions have shown higher GFA. For that reason, many GFA parameters are based on these two variables. Nevertheless, in most of the compositions with low GFA, T_g cannot be easily observed and, other parameters must be used. This thesis demonstrates that the combined use of T_l, the first phase formed from the liquid under equilibrium conditions and λ-factor as amorphisation criteria allows predicting the AFA. This approach provides a methodology to design compositions that can be obtained with amorphous structure by processes that produce relatively low cooling rates (as is the case of gas atomisation).

Despite that melt spinning has been (and is still) the main fabrication process of most amorphous and glassy materials, this thesis demonstrates that gas atomisation is an excellent alternative and can be considered as a mass production process for the fabrication of amorphous soft magnetic materials.

Chapter 4

Conclusions and Future Work

Fe-based powders were successfully produced as amorphous by gas atomisation. The amorphous powders exhibit excellent soft magnetic properties, which are improved by proper heat treatments, thus resulting in a nanocrystalline structure of the Fe(Si) phase embedded in a residual amorphous matrix and in which the grain size is below 20 nm. The amorphous and nanocrystalline powders were used to fabricate soft magnetic cores, which exhibit exceptionally low loss in the radio-frequency range. The main conclusions are as follows:

i. Amorphous forming ability (AFA or GFA) is key in producing amorphous powders by gas atomisation. For that reason, before producing a material via this process, it is necessary to carefully design the composition, taking into account their AFA and the expected properties.

ii. Amorphous Fe-based powders exhibit good soft magnetic properties, which can be improved by proper heat treatments

designed from DSC curves. This enhancement of soft magnetic properties can be explained by the reduction of magnetoelastic and magnetocrystalline anisotropies due to the structural relaxation and crystallisation of the Fe(Si) phases (a requirement being a grain size $\lesssim$20 nm). Moreover, RAM is not completely suitable for explaining the softening in powders because it does not consider dipolar and pinning effect arising from the surface region of the nanocrystals and particles.

iii. The addition of Cu, Nb and P to alloys based on Fe-Si-B alters significantly the AFA, and therefore, the right amount of these elements is a crucial aspect to produce alloys by gas atomisation. Furthermore, the addition of these elements changes the crystallisation mode from eutectic to primary crystallisation, which favours the nanocrystallisation of the Fe(Si) phase, delaying the precipitation of iron borides/phosphides.

iv. The use of finer amorphous and nanocrystalline particles with an optimised insulation layer significantly improve the AC-magnetic properties; the core loss and permeability under an alternating current are such that the material can reaches an operating frequency above hundreds of MHz.

v. Gas atomisation is presented as an excellent alternative for producing amorphous powders, even for compositions where the AFA is not very high. The production rate can reach nearly 1-2 kg/min, making this process suitable for mass production of raw materials for soft magnetic and high-frequency applications.

This thesis has increased our knowledge on amorphous and nanocrystalline powders, opening new research lines and directions. In terms of powder production, future developments in technology will allow gas atomisation to produce a wider range of different compositions as fully amorphous. To achieve this, it will be necessary to study the AFA of more systems using the tools developed in this thesis.

Research on the surface of particles under a magnetic field, such as magneto-optical Kerr effect, should be conducted to elucidate the contribution of the surface to the overall soft magnetic response. This study is relevant to explain the abnormally high coercivity of powders compared with ribbons. The domain wall, typically of around 100 nm, is smaller than the particle size of around 10 μm. Apparently, the surface produces a pinning effect on the domain wall movement, resulting in an increase in H_C., but the details of this effect are unknown.

Further studies are needed in order to increase the permeability of soft magnetic composites (SMCs). This low permeability is due to the high demagnetising effect; this one arises from the low relative density of SMCs and the use of spherical particles. It has been reported in the literature that it is possible to reduce this effect by modifying particle shape, but the reduction is still small and it is necessary to study this point more closely. Furthermore, the resin-particle ratio must be optimised in order to reach the desired response in working conditions. For that reason, one novel research line is the study how to increase the volume fraction of magnetic powder in the core (e.g., using of a thinner insulation layer on the particle surface). As a result, permeability and magnetic flux density would be increased considerably.

On the other hand, the fabrication of components is still a concern in many sectors. The fabrication of components is tending even more towards miniaturisation, which complicates the mass production and manufacturing of complex geometries. This is leading to a search for new material processing routes. One promising process is the well-known spark plasma sintering (SPS), which can consolidate powders by simultaneously applying pressure and heat (at very high heating rates, ~500 °C/min). The advantage of this process is that higher consolidation temperatures can be reached while preserving the amorphous or nanocrystalline structure due to the high heating rates achieved in the process, and component density can consequently be significantly improved. Additionally, as the heating rate is extremely high, the increase in the consolidation temperature will not result in the crystallisation of the undesired phases. Another family of processing technologies that may be suitable for these materials are additive manufacturing technologies based on melting the powders with a laser or electron beam, such as selective laser melting (SLM), laser metal deposition (LMD) or electron beam melting (EBM). One common characteristic of these processes is the high solidification rate of the material after deposition, comparable to the rates achieved in gas atomisation. Consequently, materials with a high AFA may be built fully amorphous and subsequently annealed for structural relaxation or nanocrystallization in order to attain optimum soft magnetic properties.

Finally, one of the near-future challenges will be to increase the yield of smaller particles (≤10 μm) in the atomisation process. This could be possible by introducing changes either in the process or in the compositions. If the compositions are modified to reduce the particle size, there is a risk of decreasing also the AFA. Additionally, heat-treating and consolidating powders that are so fine make more difficult these steps also. Consequently, the whole problem could be the topic of a new thesis. Using an extremely

small particle size together with an optimised insulation film will considerably reduce eddy current losses, resulting in an excellent high-frequency performance, even in the GHz range.

Chapter 5

References

5.1 Reference Statistics

5.1.1 Most cited Journals

Rank	Journal Name	Time cited
1	Journal of Magnetism and Magnetic Materials	18
2	IEEE Transactions on Magnetics	11
3	Journal of Non-Crystalline Solids	10
4	Journal of Applied Physics	9
5	Materials Science and Engineering: A	8
6	Journal of Alloys and Compounds	7
7	Journal of Materials Science	6
8	Materials Transaction	4

5.1.2 Most cited Authors

Rank	Author Name	Times cited
1	Akihisa Inoue	14
2	Akihiro Makino	10
3	Chuntao Chang	7
4	Tsuyoshi Masumoto	5
5	Xin-Min Wang	5
6	Yaqiang Dong	4

5.1.3 Number of references for range of years

Range of years	Number of references
Present-2015	22
2014-2010	25
2009-2005	26
2004-2000	12
1999-1995	9
1994-1990	18
1989-1980	19
Before 1980	14

5.2 Reference List

[1] B.D. Cullity, C.D. Graham, Introduction to magnetic materials, 2nd ed., IEEE Press, US, 2009.

[2] J.M. Coey, Magnetism and magnetic materials, Cambridge University Press, Cambridge, UK, 2010.

[3] D.C. Mattis, The theory of magnetism - vol I, Springer, Berlin, Germany, 1981.

[4] W.D. Callister, D.G. Rethwisch, Materials science and engineering, 9th Intern, John Wiley & Sons, Inc., Asia, 2014.

[5] R.C. O'Handley, Modern Magnetic Materials, Principles and applications, 1st ed., John Wiley & Sons, Inc., Totonto, Canada, 1999.

[6] J. Perez A., Moldeo por comprensión de polvo base NdFeB producido mediante atomización con gas, University of Navarra, 2017.

[7] G. Sarriegui, J.M. Martín, M. Ipatov, A.P. Zhukov, J. Gonzalez, Magnetic properties of

NdFeB alloys obtained by gas atomization technique, IEEE Trans. Magn. 54 (2018) 2103105.

[8] F. Fiorillo, C. Appino, M. Pasquale, Soft Magnetic Materials, Wiley Encycl. Electr. Electron. Eng. (2016) 1–42.

[9] R.S. De Biasi, T.C. Devezas, Anisotropy field of small magnetic particles as measured by resonance, J. Appl. Phys. 49 (1978) 2466–2469.

[10] J. Kyung Sung, Y. Mo Koo, Magnetic properties of Fe and Fe-Si alloys with {100}0vw texture, J. Appl. Phys. 113 (2013) 1–4.

[11] J. De La Torre Medina, M. Darques, L. Piraux, A. Encinas, Application of the anisotropy field distribution method to arrays of magnetic nanowires, J. Appl. Phys. 105 (2009) 1–9.

[12] J.M. Barandiarán, M. Vazquez, A. Hernando, J. Gonzalez, G. Rivero, Distribution of the magnetic anisotropy in amorphous alloys ribbons, IEEE Trans. Magn. 25 (1989) 3330–3332.

[13] P. Kollár, Z. Bircáková, J. Füzer, R. Bures, M. Fáberová, Power loss separation in Fe-based composite materials, J. Magn. Magn. Mater. 327 (2013) 146–150.

[14] O. De La Barrière, C. Appino, F. Fiorillo, C. Ragusa, H. Ben Ahmed, M. Gabsi, F. Mazaleyrat, M. Lobue, Loss separation in soft magnetic composites, J. Appl. Phys. 109 (2011) 1–4.

[15] M. De Wulf, L. Anestiev, L. Dupré, L. Froyen, J. Melkebeek, Magnetic properties and loss separation in iron powder soft magnetic composite materials, J. Appl. Phys. 91 (2002) 7845–7847.

[16] G. Ouyang, X. Chen, Y. Liang, C. Macziewski, J. Cui, Review of Fe-6.5 wt%Si high silicon steel—A promising soft magnetic material for sub-kHz application, J. Magn. Magn. Mater. 481 (2019) 234–250.

[17] W.F. Barrett, W. Brown, R.A. Hadfield, Electrical conductivity and magnetic permeability of various alloys of Iron, Sci. Trans. Roy. Soc. Dublin. 7 (1900) 67–126.

[18] A. Campbell, On the magnetic properties of silicon iron (stalloy) in alternating magnetic fields of low value, in: Proc. Phys. Soc. London, 1919: pp. 232–243.

[19] E. Gumlich, D.I.P. Goerens, Magnetic properties of iron-carbon and iron-silicon alloys, Trans. Faraday Soc. 8 (1912) 98–114.

[20] J.M. Silveyra, E. Ferrara, D.L. Huber, T.C. Monson, Soft magnetic materials for a sustainable and electrified world, Science (80-.). 362 (2018) eaao0195.

[21] F. Fiorillo, Chapter 10 - Uncertainty and Confidence in Measurements, in: F. Fiorillo (Ed.), Charact. Meas. Magn. Mater., Academic Press, 2004: pp. 581–611.

[22] Y. Ogawa, M. Naoe, Y. Yoshizawa, R. Hasegawa, Magnetic properties of high B_s Fe-

based amorphous material, J. Magn. Magn. Mater. 304 (2006) 675–677.

[23] A. Kojima, H. Horikiri, Y. Kawamura, A. Makino, A. Inoue, T. Masumoto, Production of nanocrystalline b.c.c. FeNbB bulk alloys by warm extrusion and their magnetic properties, Mater. Sci. Eng. A. 179–180 (1994) 511–515.

[24] Y. Yoshizawa, K. Yamauachi, Fe-based soft magnetic alloys composed of ultrafine grain structure, Mater. Trans. JIM. 31 (1990) 307–314.

[25] Y. Yoshizawa, S. Oguma, K. Yamauchi, New Fe-based soft magnetic alloys composed of ultrafine grain structure, J. Appl. Phys. 64 (1988) 6044–6046.

[26] Amorphous Metals VITROVAC Catalogue, 7th ed., Vacuumschmelze GmbH, Hanau, Germany, 1989.

[27] J. Petzold, Advantages of softmagnetic nanocrystalline materials for modern electronic applications, J. Magn. Magn. Mater. 242–245 (2002) 84–89.

[28] M.A. Willard, D.E. Laughlin, M.E. McHenry, D. Thoma, K. Sickafus, J.O. Cross, V.G. Harris, Structure and magnetic properties of $(Fe_{0.5}Co_{0.5})_{88}Zr_7B_4Cu_1$ nanocrystalline alloys, J. Appl. Phys. 84 (1998) 6773–6777.

[29] A. Makino, Nanocrystalline soft magnetic Fe-Si-B-P-Cu alloys with high *B* of 1.8-1.9 T contributable to energy saving, IEEE Trans. Magn. 48 (2012) 1331–1335.

[30] G. Herzer, Modern soft magnets: Amorphous and nanocrystalline materials, Acta Mater. 61 (2013) 718–734.

[31] R.B. Schwarz, T.D. Shen, U. Harms, T. Lillo, Soft ferromagnetism in amorphous and nanocrystalline alloys, J. Magn. Magn. Mater. 283 (2004) 223–230.

[32] M.E. McHenry, M.A. Willard, D.E. Laughlin, Amorphous and nanocrystalline materials for applications as soft magnets, Prog. Mater. Sci. 44 (1999) 291–433.

[33] A. Wang, C. Zhao, A. He, H. Men, C. Chang, X. Wang, Composition design of high B_s Fe-based amorphous alloys with good amorphous-forming ability, J. Alloys Compd. 656 (2016) 729–734.

[34] G. Herzer, Grain size dependence of coercivity and permeability in nanocrystalline ferromagnets, IEEE Trans. Magn. 26 (1990) 1397–1402.

[35] G. Herzer, Grain structure and magnetism of nanocrystalline ferromagnets, IEEE Trans. Magn. 25 (1989) 3327–3329.

[36] R. Alben, J.J. Becker, M.C. Chi, Random anisotropy in amorphous ferromagnets, J. Appl. Phys. 49 (1978) 1653–1658.

[37] T. Bitoh, A. Makino, A. Inoue, Quasi-Dislocation Dipole-Type Defects and Low Coercivity af Fe-Based Soft Magnetic Glassy Alloys, J. Metaestable Nanocrystalline Mater. 24–25 (2005) 427–430.

[38] T. Bitoh, A. Makino, A. Inoue, Origin of low coercivity of Fe-(Al, Ga)-(P, C, B, Si, Ge) bulk glassy alloys, Mater. Trans. 44 (2003) 2020–2024.

[39] T. Ueno, H. Tsuruta, T. Saito, A. Watanabe, T. Ishimine, K. Yamada, Practical and potential applications of soft magnetic powder cores with superior magnetic properties, SEI Tech. Rev. (2016) 9–15.

[40] H. Shokrollahi, K. Janghorban, Soft magnetic composite materials (SMCs), J. Mater. Process. Technol. 189 (2007) 1–12.

[41] K.J. Sunday, M.L. Taheri, Soft magnetic composites: recent advancements in the technology, Met. Powder Rep. 72 (2017) 425–429.

[42] Y.B. Kim, D.H. Jang, H.K. Seok, K.Y. Kim, Fabrication of Fe–Si–B based amorphous powder cores by cold pressing and their magnetic properties, Mater. Sci. Eng. A Struct. Mater. Prop. Microstruct. Process. 449–451 (2007) 389–393.

[43] B. V. Neamţu, T.F. Marinca, I. Chicinaş, F. Popa, O. Isnard, Preparation and characterization of amorphous soft magnetic FeSiB powders and spark plasma sintered compacts, Solid State Phenom. 216 (2014) 163–168.

[44] B. V. Neamţu, T.F. Marinca, I. Chicinaş, O. Isnard, F. Popa, P. Păşcuţă, Preparation and soft magnetic properties of spark plasma sintered compacts based on Fe-Si-B glassy powder, J. Alloys Compd. 600 (2014) 1–7.

[45] M. Anhalt, Systematic investigation of particle size dependence of magnetic properties in soft magnetic composites, J. Magn. Magn. Mater. 320 (2008) 366–369.

[46] G.Q. Lin, Z.W. Li, L. Chen, Y.P. Wu, C.K. Ong, Influence of demagnetizing field on the permeability of soft magnetic composites, J. Magn. Magn. Mater. 305 (2006) 291–295.

[47] Y.Y. Zheng, Y.G. Wang, G.T. Xia, Amorphous soft magnetic composite-cores with various orientations of the powder-flakes, J. Magn. Magn. Mater. 396 (2015) 97–101.

[48] B.K. Pugh, D.P. Kramer, C.H. Chen, Demagnetizing factors for various geometries precisely determined using 3-D electromagnetic field simulation, IEEE Trans. Magn. 47 (2011) 4100–4103.

[49] Y. Liu, Y. Yi, W. Shao, Y. Shao, Microstructure and magnetic properties of soft magnetic powder cores of amorphous and nanocrystalline alloys, J. Magn. Magn. Mater. 330 (2013) 119–133.

[50] C. Chang, Y. Dong, M. Liu, H. Guo, Q. Xiao, Y. Zhang, Low core loss combined with high permeability for Fe-based amorphous powder cores produced by gas atomization powders, J. Alloys Compd. 766 (2018) 959–963.

[51] K. Yoshida, M. Bito, J. Kageyama, Y. Shimizu, M. Abe, A. Makino, Unusual high B_s for Fe-based amorphous powders produced by a gas-atomization technique, AIP Adv. 6 (2016) 1–8.

[52] Y. Zhang, P. Sharma, A. Makino, Fe-Rich Fe-Si-B-P-Cu Powder Cores for High-

Frequency Power Electronic Applications, IEEE Trans. Magn. 50 (2014) 2006804.

[53] J. Füzerová, J. Füzer, P. Kollár, R. Bureš, M. Fáberová, Complex permeability and core loss of soft magnetic Fe-based nanocrystalline powder cores, J. Magn. Magn. Mater. 345 (2013) 77–81.

[54] Y. Dong, Z. Li, M. Liu, C. Chang, F. Li, X.M. Wang, The effects of field annealing on the magnetic properties of FeSiB amorphous powder cores, Mater. Res. Bull. 96 (2017) 160–163.

[55] Z. Li, Y. Dong, S. Pauly, C. Chang, R. Wei, F. Li, X.M. Wang, Enhanced soft magnetic properties of Fe-based amorphous powder cores by longitude magnetic field annealing, J. Alloys Compd. 706 (2017) 1–6.

[56] W. Klement, R.H. Willens, P. Duwez, Non-crystalline structure in solidified Gold–Silicon alloys, Nature. 187 (1960) 869–870.

[57] D.R. Askeland, P.P. Fulay, W.J. Wright, The Science and Engineering of Materials, Sixth, Cengage Learning, Stamford, USA, 2011.

[58] F.C. Li, T. Liu, J.Y. Zhang, S. Shuang, Q. Wang, A.D. Wang, J.G. Wang, Y. Yang, Amorphous–nanocrystalline alloys: fabrication, properties, and applications, Mater. Today Adv. 4 (2019).

[59] C. Suryanarayana, A. Inoue, Bulk Metallic Glasses, CRC/Taylor & Francis, US, 2011.

[60] C.A. Queiroz, J. Šesták, Aspects of the non-crystalline state, Phys. Chem. Glas. Eur. J. Glas. Sci. Technol. Part B. 51 (2010) 165–172.

[61] P.K. Gupta, Non-crystalline solids: glasses and amorphous solids, J. Non. Cryst. Solids. 195 (1996) 158–164.

[62] Burton, Amorphous metallic alloys, 1st ed., Butterworths, UK, 1983.

[63] T. Egami, Magnetic amorphous alloys: physics and technological applications, Rep. Prog. Phys. 47 (1984) 1601–1725.

[64] Q. Chen, J. Shen, D. Zhang, H. Fan, J. Sun, D.G. McCartney, A new criterion for evaluating the glass-forming ability of bulk metallic glasses, Mater. Sci. Eng. A. 433 (2006) 155–160.

[65] Z.Z. Yuan, S.L. Bao, Y. Lu, D.P. Zhang, L. Yao, A new criterion for evaluating the glass-forming ability of bulk glass forming alloys, J. Alloys Compd. 459 (2008) 251–260.

[66] G.J. Fan, H. Choo, P.K. Liaw, A new criterion for the glass-forming ability of liquids, J. Non. Cryst. Solids. 353 (2007) 102–107.

[67] D. Turnbull, Under What Conditions Can A Glass Be Formed?, Contemp. Phys. 10 (1969) 473–488.

[68] Z.P. Lu, Y. Li, S.C. Ng, Reduced glass transition temperature and glass forming ability

of bulk glass forming alloys, J. Non. Cryst. Solids. 270 (2000) 103–114.

[69] I.W. Donald, H.A. Davies, Prediction of glass-forming ability for metallic systems, J. Non. Cryst. Solids. 30 (1978) 77–85.

[70] H.G. Jiang, J. Baram, Estimation of the glass transition temperature in metallic glasses, Mater. Sci. Eng. A. 208 (1996) 232–238.

[71] A. Inoue, T. Zhang, T. Masumoto, Glass-forming ability of alloys, J. Non. Cryst. Solids. 156–158 (1993) 473–480.

[72] M. Saad, M. Poulain, Glass forming ability criterion, Mater. Sci. Forum. 19–20 (1987) 11–18.

[73] Z.P. Lu, C.T. Liu, A new glass-forming ability criterion for bulk metallic glasses, Acta Mater. 50 (2002) 3501–3512.

[74] X.H. Du, J.C. Huang, C.T. Liu, Z.P. Lu, New criterion of glass forming ability for bulk metallic glasses, J. Appl. Phys. 101 (2007) 23–25.

[75] Z. Long, H. Wei, Y. Ding, P. Zhang, G. Xie, A. Inoue, A new criterion for predicting the glass-forming ability of bulk metallic glasses, J. Alloys Compd. 475 (2009) 207–219.

[76] E.S. Park, W.T. Kim, D.H. Kim, A simple model for determining alloy composition with large glass forming ability in ternary alloys, Metall. Mater. Trans. A Phys. Metall. Mater. Sci. 32 (2001) 200–202.

[77] E.S. Park, D.H. Kim, W.T. Kim, Parameter for glass forming ability of ternary alloy systems, Appl. Phys. Lett. 86 (2005) 061907.

[78] T. Egami, Y. Waseda, Atomic size effect on the glass forming ability of metallic alloys, J. Non. Cryst. Solids. 64 (1984) 113–134.

[79] K. Mondal, B.S. Murty, On the parameters to assess the glass forming ability of liquids, J. Non. Cryst. Solids. 351 (2005) 1366–1371.

[80] A. Takeuchi, A. Inoue, Classification of bulk metallic glasses by atomic size difference, heat of mixing and period of constituent elements and its application to characterization of the main alloying element, Mater. Trans. 46 (2005) 2817–2829.

[81] P. Duwez, Metastable phases obtained by rapid quenching fromt he liquid state, Prog. Solid State Chem. 3 (1967) 377–400.

[82] I.-R. Lu, G. Wilde, G.P. Görler, R. Willnecker, Thermodynamic properties of Pd-based glass-forming alloys, J. Non. Cryst. Solids. 250–252 (1999) 577–581.

[83] L.A. Jacobson, J. McKittrick, Rapid solidification processing, Mater. Sci. Eng. R. R11 (1994) 355–408.

[84] K. Narita, J. Yamasaki, H. Fukunaga, Dependence on metalloid content for magnetic properties of Fe-Si-B metallic glasses, IEEE Trans. Magn. 13 (1977) 1544–1546.

[85] T. Yamaguchi, K. Narita, Magnetothermal charateristics of amorphous Fe-Si-B powder produced by spark erosion, IEEE Trans. Magn. MAG-13 (1977) 1621–1623.

[86] T. Yamaguchi, K. Narita, Preparation of amorphous magnetic powder by atomization technique, Appl. Phys. Lett. 33 (1978) 468–470.

[87] M. Hagiwara, A. Inoue, T. Masumoto, Mechanical properties of Fe-Si-B amorphous wires produced by in-rotating-water spinning method, Metall. Trans. A. 13 (1982) 373–382.

[88] M.G. Poletti, L. Battezzati, Assessment of the ternary Fe-Si-B phase diagram, Calphad Comput. Coupling Phase Diagrams Thermochem. 43 (2013) 40–47.

[89] A.I. Zaitsev, N.E. Zaitseva, A.A. Kodentsov, A thermodynamic study of liquid Fe-Si-B alloys; an influence of ternary associates on a liquid → glass transition, Metall. Mater. Trans. B. 34 (2003) 887–898.

[90] X. Li, L.B. Liu, Y. Jiang, G.X. Huang, X. Wang, Y.R. Jiang, J.S. Liang, L.G. Zhang, X. Shi, Thermodynamic evaluation of the phase equilibria and glass-forming ability of the Al–Co–Gd system, Calphad. 52 (2016) 57–65.

[91] M. Kopcewicz, W. Dmowski, B. Ratkiewicz, Magnetic and structural properties of amorphous Fe-Si-B alloys, J. Magn. Magn. Mater. 51 (1985) 218–224.

[92] Y.R. Zhang, R. V. Ramanujan, Microstructural observations of the crystallization of amorphous Fe–Si–B based magnetic alloys, Thin Solid Films. 505 (2006) 97–102.

[93] M.A. Gibson, G.W. Delamore, Nucleation and growth kinetics of stable and metastable eutectics in FeSiB metallic glasses, Acta Metall. Mater. 38 (1990) 2621–2629.

[94] A.E. Berkowitz, J.C. Grande, S.A. Miller, R.J. Murphy, J.L. Walter, Structures and Properties of Powders of $Fe_{75}Si_{15}B_{10}$ Produced by Gas-Water Atomization, Mater. Sci. Eng. 62 (1984) 217–230.

[95] J.L. Walter, A.E. Berkowitz, E.F. Koch, Crystallization of amorphous $Fe_{75}Si_{15}B_{10}$ ribbon and powder, Mater. Sci. Eng. 60 (1983) 31–44.

[96] H. Shokrollahi, The magnetic and structural properties of the most important alloys of iron produced by mechanical alloying, Mater. Des. 30 (2009) 3374–3387.

[97] T. Sato, Study on powder properties of Fe-P-C and Fe-B-Si alloy powders prepared by water atomization, J. Mater. Sci. 26 (1991) 2329–2336.

[98] F.E. Luborsky, J.J. Becker, J.L. Walter, H.H. Liebermann, Formation and magnetic properties of Fe-B-Si amorphous alloys, IEEE Trans. Magn. 15 (1979) 1146–1149.

[99] T. Sato, Effect of composition on glass-forming regions of iron-base alloy powders prepared by water atomization, J. Mater. Sci. Lett. 6 (1987) 844–846.

[100] N. Decristofaro, A. Freilich, G. Fish, Formation and magnetic properties of Fe-B-Si metallic glasses, J. Mater. Sci. 17 (1982) 2365–2370.

[101] C. Antonione, M. Baricco, G. Riontino, Structural relaxation kinetics in FeSiB amorphous alloys, J. Mater. Sci. 23 (1988) 2225–2229.

[102] T. Egami, Structural relaxation in amorphous alloys - compositional short range ordering, Mater. Res. Bull. 13 (1978) 557–562.

[103] L. Zhu, Y.G. Wang, S. Lan, X.L. Wang, C.Y. Lu, X.B. Zhai, Y. Meng, Structural relaxation in a Fe-based metallic glass: Changes in local structure and role of heterogeneity, Intermetallics. 103 (2018) 72–77.

[104] I. Ohnuma, S. Abe, S. Shimenouchi, T. Omori, R. Kainuma, K. Ishida, Experimental and thermodynamic studies of the Fe-Si binary system, ISIJ Int. 52 (2012) 540–548.

[105] F. Zhou, K. He, M. Sui, Nucleation and growth characteristics of amorphous Fe-Si-B-(Cu)-(Nb) alloys during isothermal crystallization process, Mater. Sci. Eng. A Struct. Mater. Prop. Microstruct. Process. 181–182 (1994) 1419–1422.

[106] I. Mat'ko, E. Illeková, P. Švec, P. Duhaj, Crystallization characterisics in the Fe-Si-B glassy ribbon system, Mater. Sci. Eng. A Struct. Mater. Prop. Microstruct. Process. 225 (1997) 145–152.

[107] D.S. dos Santos, D.R. dos Santos, Crystallization kinetics in Fe-B-Si metallic glasses, J. Non. Cryst. Solids. 304 (2002) 56–63.

[108] M.P. Trujillo, A. Orozco, M. Casas-Ruiz, R.A. Ligero, R. Jimenez-Garay, Crystallization kinetics study of Fe-B-Si metallic glasses in the theoretical frame of the JMA model, Mater. Lett. 24 (1995) 287–290.

[109] R. Singhal, A.K. Majumdar, Crystallization of glassy $Fe_{80}B_{20-x}Si_x$($0<x<12$) alloys, J. Magn. Magn. Mater. 115 (1992) 245–249.

[110] E. Jakubczyk, L. Krajczyk, P. Siemion, M. Jakubczyk, Crystallization kinetics of $Fe_{78}Si_9B_{13}$ metallic glass, Opt. Appl. XXXVII (2007) 359–370.

[111] S.U. Jen, Isothermal crystallization of amorphous $Fe_{78}B_{13}Si_9$, Mater. Sci. Eng. A Struct. Mater. Prop. Microstruct. Process. 133 (1991) 479–481.

[112] A.P. Shpak, A.G. Il'inskii, A. V. Marunyak, O.I. Slukhovskyy, Y. V. Lepeeva, A. Dekhtyar, I. Kaban, N. Mattern, J. Eckert, Crystallization of $Fe_{82}Si_2B_{16}$ and $Fe_{82}Si_4B_{14}$ metallic glasses upon isothermal and non-isothermal annealing, EPJ Web Conf. 15 (2011) 01008.

[113] K. Chrissafis, M.I. Maragakis, K.G. Efthimiadis, E.K. Polychroniadis, Detailed study of the crystallization behaviour of the metallic glass $Fe_{75}Si_9B_{16}$, J. Alloys Compd. 386 (2005) 165–173.

[114] M.A. Gibson, G.W. Delamore, Crystallization of stable and metastable eutectics in FeSiB metallic glasses, J. Mater. Sci. 25 (1990) 93–97.

[115] A. Załuska, H. Matyja, Crystallization characteristics of amorphous Fe-Si-B alloys, J. Mater. Sci. 18 (1983) 2163–2172.

[116] A. Inoue, M. Komuro, T. Masumoto, Fe-Si-B amorphous alloys with high silicon concentration, J. Mater. Sci. 19 (1984) 4125–4132.

[117] T. Gheiratmand, H.R.M. Hosseini, Finemet nanocrystalline soft magnetic alloy: Investigation of glass forming ability, crystallization mechanism, production techniques, magnetic softness and the effect of replacing the main constituents by other elements, J. Magn. Magn. Mater. 408 (2016) 177–192.

[118] HITACHI, Nanocrystalline soft magnetic material FINEMET®, (2010).

[119] A. Makino, K. Suzuki, A. Inoue, Y. Hirotsu, T. Masumoto, Magnetic properties and microstructure of nanocrystalline bcc Fe-M-B (M = Zr, Hf, Nb) alloys, J. Magn. Magn. Mater. 133 (1994) 329–333.

[120] W.T. Kim, P.W. Jang, S.C. Yu, B.S. Chun, Heat treatment of melt-spun amorphous Fe-Si-B-Cu-Nb alloy, Mater. Sci. Eng. A Struct. Mater. Prop. Microstruct. Process. 179–180 (1994) 309–315.

[121] J.D. Ayers, V.G. Harris, J.A. Sprague, W.T. Elam, H.N. Jones, A model for nucleation of nanocrystals in the soft magnetic alloy $Fe_{73.5}Nb_3Cu_lSi_{13.5}B_9$, NanoStructured Mater. 9 (1997) 391–396.

[122] J. González, Magnetic properties arising from two additive contributions in soft magnetic nanocrystalline alloys, Appl. Phys. Lett. 85 (2004) 5944–5946.

[123] V. DeGeoge, S. Shen, P.R. Ohodnicki, M. Andio, M.E. McHenry, Multiphase resistivity model for magnetic nanocomposites developed for high frequency high power transformation, J. Electron. Mater. 43 (2014) 96–108.

[124] R. Hasegawa, Advances in amorphous and nanocrystalline magnetic materials, J. Magn. Magn. Mater. 304 (2006) 187–191.

[125] A. Masood, H.A. Baghbaderani, V. Ström, P. Stamenov, P. McCloskey, C. Mathúna, S. Kulkarni, Fabrication and soft magnetic properties of rapidly quenched Co-Fe-B-Si-Nb ultra-thin amorphous ribbons, J. Magn. Magn. Mater. 483 (2019) 54–58.

[126] A. Inoue, B. Shen, Formation and Soft Magnetic Properties of Co-Fe-Si-B-Nb Bulk Glassy Alloys, Mater. Trans. 43 (2005) 1230–1234.

[127] A.D. Wang, H. Men, B.L. Shen, G.Q. Xie, A. Makino, A. Inoue, Effect of P on crystallization behavior and soft-magnetic properties of $Fe_{83.3}Si_4Cu_{0.7}B_{12-X}P_X$ nanocrystalline soft-magnetic alloys, Thin Solid Films. 519 (2011) 8283–8286.

[128] Z. Li, A. Wang, C. Chang, Y. Wang, B. Dong, S. Zhou, FeSiBPNbCu alloys with high glass-forming ability and good soft magnetic properties, Intermetallics. 54 (2014) 225–231.

[129] A. Makino, T. Kubota, M. Makabe, C.T. Chang, A. Inoue, FeSiBP metallic glasses with high glass-forming ability and excellent magnetic properties, Mater. Sci. Eng. B Solid-State Mater. Adv. Technol. 148 (2008) 166–170.

[130] J. Guo, Y. Dong, Q. Man, Q. Li, C. Chang, X.M. Wang, R.W. Li, Fabrication of FeSiBPNb amorphous powder cores with high DC-bias and excellent soft magnetic properties, J. Magn. Magn. Mater. 401 (2016) 432–435.

[131] T. Suzuki, P. Sharma, L. Jiang, Y. Zhang, A. Makino, Fabrication and Properties of Under 10 μm Sized Amorphous Powders of High B_s Soft Magnetic Alloy for High-Frequency Applications, IEEE Trans. Magn. 54 (2018) 2801705.

[132] G.S. Upadhyaya, Powder Metallurgy Technology, Cambridge International Science Publishing, Cambridge, UK, 2002.

[133] R.M. German, Powder Metallurgy & Particulate Materials Processing, Metal Powder Industries Federation (MPIF), Princeton, NJ, USA, 2005.

[134] H. Masuda, K. Higashitani, H. Yoshida, Powder Technology: Fundamentals of Particles, Powder Beds, and Particle Generation, 4th ed., Boca Raton, FL, USA, 2007.

[135] MPIF Standard 04: Determination of apparent density of free-flowing metal powders using the hall apparatus, (1992).

[136] MPIF Standard 46: Determination of tap density of metal powders, (1992).

[137] MPIF Standard 03: Determination of flow rate of free-flowing metal powders using the hall apparatus, (1985).

[138] MPIF Standard 05: Determination of Sieve Analysis of Metal Powders, (1992).

[139] A.J. Yule, J.J. Dunkley, Atomization of Melts for Powder Production and Spray Deposition, Oxford University Press, UK Oxford, 1994.

[140] E. Urionabarrenetxea, Estudio experimental y simulación del proceso de producción de polvos metálicos mediante atomización con gas., University of Navarra, 2015.

[141] A.M. Mullis, L. Farrell, R.F. Cochrane, N.J. Adkins, Estimation of cooling rates during close-coupled gas atomization using secondary dendrite arm spacing measurement, Metall. Mater. Trans. B Process Metall. Mater. Process. Sci. 44 (2013) 992–999.

[142] H. Shiwen, L. Yong, G. Sheng, Cooling rate calculation of non-equilibrium aluminum alloy powders prepared by gas atomization, Rare Met. Mater. Eng. 38 (2009) 353–356.

[143] A. Inoue, Light-metal based amorphous alloys, in: Curr. Top. Amorph. Mater., Elsevier B.V., 1993: pp. 159–166.

[144] N. Ciftci, N. Ellendt, R. Von Bargen, H. Henein, L. Mädler, V. Uhlenwinkel, Atomization and characterization of a glass forming alloy $\{(Fe_{0.6}Co_{0.4})_{0.75}B_{0.2}Si_{0.05}\}_{96}Nb_4$, J. Non. Cryst. Solids. 394–395 (2014) 36–42.

[145] N. Ciftci, N. Ellendt, E. Soares Barreto, L. Mädler, V. Uhlenwinkel, Increasing the amorphous yield of $\{(Fe_{0.6}Co_{0.4})_{0.75}B_{0.2}Si_{0.05}\}_{96}Nb_4$ powders by hot gas atomization, Adv. Powder Technol. 29 (2017) 380–385.

Appendix I

Appended Papers

Journal of Alloys and Compounds 735 (2018) 2646-2652

Contents lists available at ScienceDirect

Journal of Alloys and Compounds

journal homepage: http://www.elsevier.com/locate/jalcom

Soft magnetic amorphous alloys (Fe-rich) obtained by gas atomisation technique

Kenny L. Alvarez [a, b, *], José Manuel Martín [a], Mihail Ipatov [c], Julian Gonzalez [d]

[a] *CEIT-IK4 and Tecnun (University of Navarra), P° Manuel de Lardizábal 15, 20018, San Sebastián, Spain*

[b] *Escuela de Ingeniería Mecánica, Pontificia Universidad Católica de Valparaíso, Av. Brasil 2950, Valparaíso, Chile*

[c] *SGIker (Magnetic Measurements), University of the Basque Country, Av. Tolosa 72, 20018, San Sebastián, Spain*

[d] *Department Materials Physics, Faculty of Chemistry, University of the Basque Country, P° Manuel de Lardizábal 3, 20018, San Sebastián, Spain*

Abstract

We report a research describing a new route for the production of Fe-Si-B powders, which is the so-called gas atomisation technology, being one of the challenges to study the conditions under which the glass structure is achieved. There have been produced powders of five different compositions in the Fe-Si-B ternary system. The particles with a diameter below 10 μm of the alloy $Fe_{70}Si_{18}B_{12}$ (at%) were completely amorphous, exhibiting an excellent soft magnetic behaviour (coercivity of around 7 Oe), which is, without any doubt, of significant scientific merit and supports the use of this new route to produce soft amorphous magnetic materials.

Keywords: Metallic glasses, rapid-solidification, calorimetry, magnetic measurements, metallography, X-ray diffraction.

1. Introduction

It is now nearly 60 years since the first metallic glass was produced by rapid quenching from the liquid state by P. Duwez *et al.* [1,2]. This proved to be a crucial point in opening new fields of research in material science, magnetism and technology, such as metastable crystalline phases and structures; extended solid solubilities of solutes with associated

* Corresponding author Tel.: + 34 943 212 800
Email address: kalvarez@ceit.es/kenny.alvarez@pucv.cl (K. L. Alvarez).
https://doi.org/10.1016/j.jallcom.2017.11.272

improvements of mechanical and physical properties; and nanocrystalline, nanocomposite and amorphous materials which, in some cases, have unique combinations of properties (magnetic, mechanical, corrosion, etc.). Technological development of the fabrication technique and studies of the structure, glass forming ability (GFA), and thermodynamics and magnetism of amorphous alloys were intensively performed in the sixties and seventies. It is important to remark that the specific properties are obtained after rapid-solidification and subsequent heat treatments, achieving amorphous and nanocrystalline structures. The amorphous structure requires high cooling rates, so the conventional production process is melt-spinning. Main attention was paid to amorphous ribbons. These aspects have been extensively analysed in some review papers and books [3–6]. Their excellent magnetic softness and high wear and corrosion resistance made them very attractive in recording head and microtransformer industries.

One of the most studied alloy systems is Fe-Si-B due to the excellent combination of high glass forming ability and good soft magnetic properties (low coercivity, high magnetic susceptibility, low energy losses, etc.). The first works began in the 70s, when several researchers added Si to Fe-B binaries alloys. This allowed improving the soft magnetic properties while keeping the glass forming ability [7,8]. Subsequent studies focused on microstructural characterization and magnetic behaviour [9–13], providing important scientific information for the development of new materials [14,15].

Concerning amorphous ferromagnetic alloys, the usual approach to the atomic structure of a magnetic order connected to a lattice periodicity is not applicable. In fact, these materials can be defined as solids in which the orientation of local symmetry axes fluctuates with a typical correlation length of 10 Å. The local structure can be characterized by a few local configurations. As a consequence of such structural disorder, the amorphous metallic alloys exhibit physical properties that, in some cases, are very attractive for technical applications (e.g. they have larger electrical resistivity than the same crystalline alloy, leading to low energy losses [16]).

There are several techniques of materials production involving rapid-solidification. The best known is melt-spinning, but others can be mentioned (as for example, spark erosion, planar flow casting, etc.) that involve cooling rates of the order of 10^6 K/s. Another technique of rapid-solidification is gas atomisation, which is used to produce metal powders. This technique consists on breaking a liquid metal stream into droplets by

means of a high velocity flow. These droplets become powder particles after solidification. The small size of the droplets, typically in the microns range, and the high velocity of the gas enable a fast heat transfer between both and, in this way, it is possible to achieve very high cooling rates [17]. Gas atomisation typically produces spherical powders.

Some of the last advances in magnetic materials are based on exploring new routes to produce them. In this paper, we report on microstructural and magnetic characterization of Fe-Si-B amorphous alloys obtained in powder form by gas atomisation. This process is presented as an alternative technology of rapid quenching to produce amorphous metallic alloys. Since the product is a spherical powder, it is subjected to fewer restrictions than the ribbon obtained by the conventional melt-spinning technique in terms of shaping the material into a component with any desired geometry [18].

2. Material and methods

The gas atomisation experiments were carried out using a convergent-divergent, close-coupled atomiser in an atomisation unit PSI model Hermiga 75/3VI. The amount of powder produced per batch was nearly 2.5 kg. Iron (supplied by Allied Metal Corp.), silicon (supplied by Cometal S.A.) and boron (supplied by H.C. Starck) of commercial purity were melted in an induction furnace under a high purity Ar atmosphere. In addition, the atomisation chamber was evacuated and purged with He to minimize oxidation. The atomising gas was He at a pressure of 60 bar. The melt temperature in the furnace was 1973 K in all the cases. The atomised compositions correspond to the empirical formula $Fe_x(Si_{15}B_{10})_{1-x}$ with x=80, 75, 70, 60 and 50 (at%).

The particle size distribution of the powders was measured by laser diffraction in an equipment Sympatec Helos (H0852). The true density was measured in a He pycnometer Micrometrics Accupyc 1330. Useful information on magnetic and structural transitions was obtained by differential scanning calorimetry (DSC) in an equipment TA Instrument DSC 2920. DSC experiments were performed using a sample of about 50 mg, at a heating rate of 10 K/min and under Ar atmosphere.

Phase identification was carried out by X-ray diffraction (XRD) in a Philips 1PW1825 diffractometer, using the characteristic wavelength of K_α line for Cu (wavelength of 1.542 Å). Electrons were generated in a W filament applying a current of 40 mA and accelerated toward the Cu anode

under a potential of 40 kV. The diffraction angle (2θ) was varied between 25 ° and 90 ° at a scanning rate of 0.005 °/s (in steps of 0.02 ° with a holding time of 4 seconds at each angle).

Particle shape and microstructure were studied using conventional (Philips XL30CP) and field emission gun (JEOL JSM-7100F) scanning electron microscopy (SEM). For microstructural observation, the powder was mounted in an epoxy resin. Next, the sample was grinded with SiC paper and polished with several diamond suspensions, being the abrasive particle size progressively reduced. The last polishing step was carried out with a suspension of SiO_2 (abrasive particle size of 0.04 μm). Finally, the sample was etched with Nital (2 % of nitric acid in ethanol) for approximately 10 s.

Thin foils were prepared using a FEI Quanta 3D FEG focused ion beam (FIB) milling instrument by the lift out technique from the sample. First, a Pt line is deposited and two stair-step FIB trenches are cut at both sides of the area of interest. Next, the specimen is further thinned to less than 1 μm in thickness and a slice of the specimen is cut free. The obtained lamella is removed using a micromanipulator and welded to a Cu grid suitable for transmission electron microscopy (TEM) analysis. Final milling down to less than 100 nm is carried out by employing successively lower voltages up to 2 kV. The obtained specimen was examined by conventional bright-field imaging in a JEOL JEM-2100F (S)TEM microscope operated at 200 kV with a LaB_6 filament.

Magnetic properties at room temperature of the powders were evaluated from the hysteresis loop obtained in an equipment Quantum Design PPMS-9T system with vibrating sample magnetometer (VSM) option Model P525.

3. Results and discussion

3.1 Powder properties

Several atomisation parameters and powder properties for the five compositions are reported in Table 1. It is interesting to remark that there is not an evident correlation between the powder particle size and the atomisation parameters, i.e. gas-metal mass flow rate ratio (GMR) or melt superheat (ΔT_m). In contrast, the particle size decreases as the amount of Fe is reduced, showing that this trend is mostly related with the composition of the alloy. Such a tendency is expected when the surface tension and/or viscosity of the alloy decrease with in increasing content of Si and/or B.

Experimental results in the ternary Fe-Si-B system indicate that rising Si causes a strong reduction of surface tension, whereas the effect of B is just moderate [19]. In the binary Fe-B system, surface tension goes down with B additions until a relative minimum is reached at 17 at% B (i.e. the eutectic composition); next, it goes up until a relative maximum at 24 at% B; and it decreases again for higher B contents [20]. Regarding viscosity, the partial substitution of B for Si in the ternary system Fe-Si-B increases the viscosity (alloys with 70 to 80 at% Fe) [21] or leaves it unchanged (alloys with 90 at% Fe) [22]. In the binary system Fe-Si, viscosity decreases until a relative minimum at 5 at% Si; next, it goes up until a relative maximum at 25 at% Si; and finally it goes down again for higher concentrations of Si [21]. Viscosity declines in the binary system Fe-B until a minimum is reached for 17 at% B and it goes up for higher concentrations [20]. Consequently, it seems that the main reason for the observed particle size reduction is the strong drop of surface tension when the Si content is raised.

Table 1. Atomisation parameters and powder properties of the as-atomised powders. [a]

Experiment	Composition	m_m (g/s)	m_g (g/s)	GMR	T_l (K)	ΔT_m (K)	Particle size distribution			Apparent density (%) [b]	Tap density (%) [b]	True density (g/cm³)
							D_{10} (µm)	D_{50} (µm)	D_{90} (µm)			
AG16-71	$Fe_{80}Si_{12}B_8$	21.28	17.8	0.83	1432	541	4.1	17.5	75.5	38.9	64.5	7.26
AG16-75	$Fe_{75}Si_{15}B_{10}$	14.69	14.2	0.97	1423	550	4.2	17.2	70.9	40.4	69.7	7.04
AG16-76	$Fe_{70}Si_{18}B_{12}$	14.1	14.2	1.01	1412	561	4.1	14	48.2	37.1	64.3	6.84
AG16-77	$Fe_{60}Si_{24}B_{16}$	11.8	14.2	1.2	1459	514	3.7	12.8	44.6	38.4	63.9	6.63
AG16-78	$Fe_{50}Si_{30}B_{20}$	13.61	14.2	1.04	1593	380	2.6	10.1	40.2	37.1	64.6	6.33

[a] m_m: mass flow rate of melt; m_g: mass flow rate of gas; $GMR=m_g/m_m$: gas-metal mass flow rate ratio; T_l: liquidus temperature, measured by DSC; ΔT_m: melt superheat; D_{10}: 10th percentile of the particle size distribution; D_{50}: Median particle size; D_{90}: 90th percentile of the particle size distribution.
[b] Apparent and tap densities are reported as percentage of the true density.

Since the amount of internal porosity is small, the He pycnometer density is very close to the true density of the powders. This density decreases when the iron content is reduced, which agrees with previous observations [19]; this trend is mostly due to the substitution of the heavy atoms of Fe by low atomic weight atoms of Si and B. Apparent and tap densities in Table 1 are reported as percentage of the true density. Apparent density values are very low indicating a high interparticle friction due to the fine particle size. In contrast, tap densities are high, showing that vibration is very efficient to improve the packing of the particles. Fractional densities after tapping are similar to the values measured in random packing beds of spherical powders [23]. It will be shown in section 3.2 that the particle shape is actually spherical.

3.2 DSC and microstructural characterization

Figure 1 shows the DSC trace corresponding to the powder fraction <10 μm of composition $Fe_{70}Si_{18}B_{12}$. It is the typical, widely reported curve for this kind of amorphous alloys [24]. Firstly, it exhibits an endothermic peak around 694.4 K corresponding to the Curie temperature (T_C). Next, it is observed a change in the slope of the baseline at 728.5 K, linked to the glass transition temperature (T_g). Finally, the two exothermic peaks are associated with crystallization, being the onset temperature for this process (T_X) equals to 820.0 K. It is noteworthy to remark that the values of T_C , T_g and T_X are in good agreement with those reported in the literature [7]. One of the parameters that have been proposed to evaluate the GFA of a given composition is the reduced glass temperature (T_{rg}), defined as $T_{rg}=T_g/T_l$ [5,25]. The GFA increases with T_{rg}. It is considered that an alloy can be obtained in glass form when T_{rg} is at least 0.4. In the present case, since T_l=1412 K and T_g=728.5 K, it is obtained that T_{rg}=0.52, indicating a high enough GFA for composition $Fe_{70}Si_{18}B_{12}$.

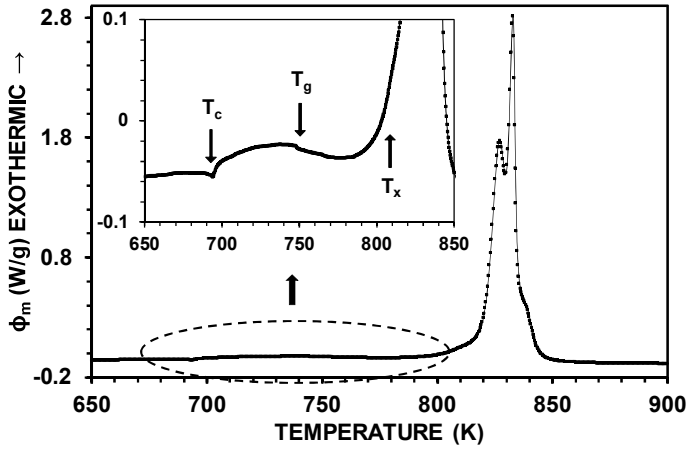

Figure 1. DSC trace corresponding to the powder fraction <10 μm of composition $Fe_{70}Si_{18}B_{12}$, demonstrating the glassy structure of fine particles. The temperatures of Curie (T_C), glass transition (T_g) and crystallization (T_X) are 694.4 K, 728.5 K and 820.0 K, respectively.

Interesting information can be drawn from the analysis of the X-ray diffraction traces of the five atomised alloys depicted in Figure 2. It can be seen that the major phase in the alloy with the highest Fe content ($Fe_{80}Si_{12}B_8$) is α-Fe(Si), which also contains Fe_2B as a minor constituent. It is thought that the next two alloys in decreasing order of Fe amount ($Fe_{75}Si_{15}B_{10}$ and $Fe_{70}Si_{18}B_{12}$) present as main phase the ordered compound Fe_3Si.

Nevertheless, the presence of α-Fe(Si) cannot be ruled out because its diffraction peaks are very close to those of Fe_3Si. In composition $Fe_{75}Si_{15}B_{10}$, there is also a residual amount of Fe_2B phase. The compositions with lower amount of Fe ($Fe_{60}Si_{24}B_{16}$ and $Fe_{50}Si_{30}B_{20}$) show patterns that are more complex. Thus, in the case of alloy $Fe_{60}Si_{24}B_{16}$, the peaks observed between the angles 25 ° and 55 ° correspond to the compound $Fe_{4.9}Si_2B$, in good agreement with those reported in reference [11] for similar compositions. The peaks observed at larger angles could not be identified, but they may correspond to the same $Fe_{4.9}Si_2B$ phase, according to the ternary phase diagram Fe-Si-B [26]. Finally, it is worthy to mention that two other phases, identified as FeB and FeSi, were observed in the alloy with the lowest Fe content ($Fe_{50}Si_{30}B_{20}$).

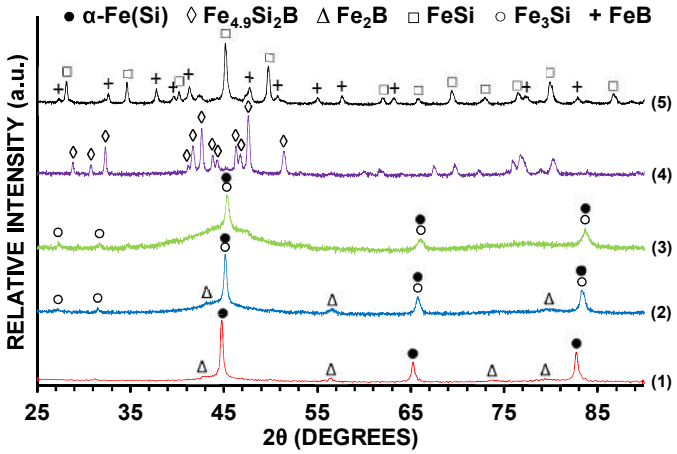

Figure 2. XRD pattern of the investigated alloys: (1) $Fe_{80}Si_{12}B_8$, (2) $Fe_{75}Si_{15}B_{10}$, (3) $Fe_{70}Si_{18}B_{12}$, (4) $Fe_{60}Si_{24}B_{16}$ and (5) $Fe_{50}Si_{30}B_{20}$.

The XRD pattern of composition $Fe_{70}Si_{18}B_{12}$ displays a broad peak between 35 ° and 55 °, indicating the coexistence of particles with amorphous and crystalline character. Figure 3 shows the diffraction pattern of this alloy for the powder fraction with a particle size <10 μm. It is noticeable the absence of peaks, demonstrating that these particles are completely amorphous, in agreement with the DSC trace shown in Figure 1.

The SEM image in Figure 4 illustrates the typical morphology of the He atomised powders. All the alloys exhibit similar features concerning the particle shape. As it is expected for powders atomised with an inert gas, the particles are spherical, with some satellites attached on the surface. As

remarked in section 3.1, this particle shape explains the high tap density of the powders.

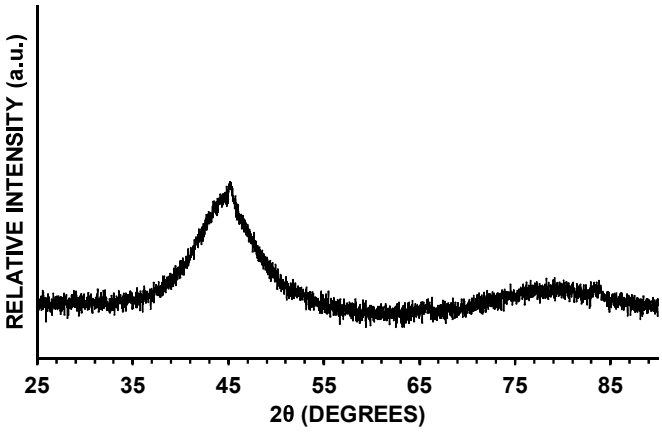

Figure 3. XRD pattern of the powder fraction <10 μm of alloy $Fe_{70}Si_{18}B_{12}$.

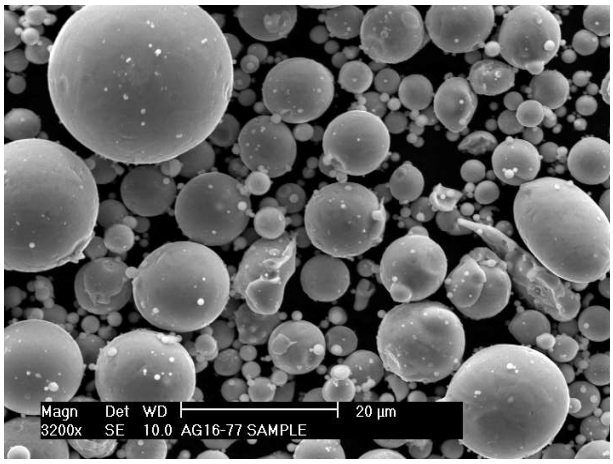

Figure 4. Representative particle shape of as-atomised powders (alloy $Fe_{60}Si_{24}B_{16}$).

Microstructural characterization focused on composition $Fe_{70}Si_{18}B_{12}$, which is formed by a mix of crystalline and amorphous particles. Figure 5 depicts the microstructure of this alloy. Figure 5 (a) shows the microstructure of crystalline particles at low magnification. There are two microstructures with different characteristics and refinement degree. One of them is formed by equiaxial colonies, with a very fine lamellar inner structure, being the lamella thickness in the scale of the nanometres. This is the predominant microstructure. The other one is coarser and dendritic.

Obviously, both microstructures are linked to different solidification rates in distinct regions of the same particles, that is, nucleation and growth of the crystallites occurred under different conditions. Figure 5 (b) shows at higher magnification that there are two phases in both microstructures. It is though that the different contrast could be due to microsegregation, caused by a diffusion-controlled modulation of the interface during solidification, with the formation of iron-rich and silicon-rich zones growing at different rates, as reported for the binary Fe-12 at% Si alloy [27]. Thus, the alloy may actually contains only Fe_3Si, with two different compositions, or two crystallographic phases, Fe_3Si and α-Fe(Si). In the finest particles, it cannot be detected any microstructural detail by high resolution SEM, suggesting that they may be non-crystalline. To confirm this observation, a TEM foil was prepared by FIB from a particle with less than 10 μm in diameter. The bright field image and the diffraction figure insert in Figure 5 (c) prove that such a particle is amorphous, in agreement with DSC and XRD results.

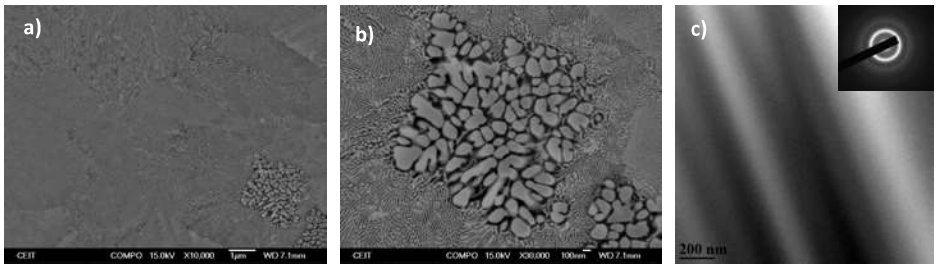

Figure 5. Microstructure of $Fe_{70}Si_{18}B_{12}$ alloy: a) Backscattered electrons image of crystalline particles at low magnification, b) Backscattered electrons image of crystalline particles at high magnification and c) Bright field image and diffraction figure of an amorphous particle.

The cooling rate of gas atomised particles is higher when the particle size is smaller. As a result, small particles are rapidly cooled below the glass transition temperature (T_g), avoiding the crystallization of metastable or of equilibrium phases. Thus, it is obtained a structure with absence of atomic order, that is, amorphous [13]. One interesting question is to determine the critical cooling rate (R_c) and associated critical particle size (d_c) to obtain the glassy structure in the case of alloy $Fe_{70}Si_{18}B_{12}$.

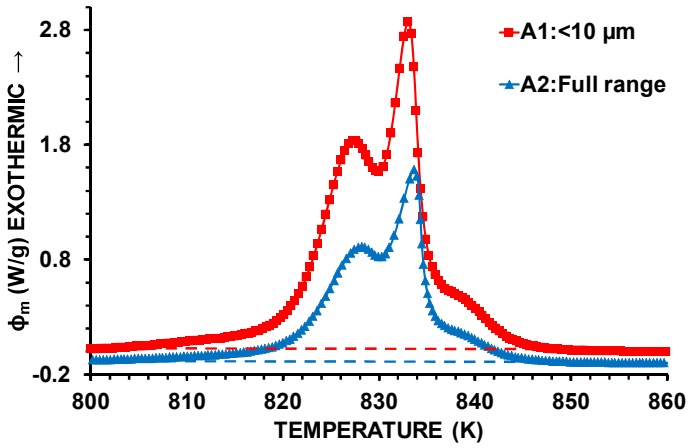

Figure 6. DSC traces showing the relative size of the crystallization peaks for the powder fraction <10 μm (*A1*) and the full range of particle sizes (*A2*) of composition $Fe_{70}Si_{18}B_{12}$.

Figure 6 compares the DSC crystallization peaks for the powder fraction <10 μm and for the complete particle size distribution of alloy $Fe_{70}Si_{18}B_{12}$. It has been proved that particles below 10 μm are fully amorphous. Consequently, the area below the crystallization peaks per unit of mass (*A1*) is the crystallization enthalpy of the alloy. Since the as-atomised powder (i.e. including all the particle sizes) contains a mix of crystalline and non-crystalline particles, the equivalent area (*A2*) is lower. The weight (or volume) fraction of non-crystalline particles (X_{nc}) in the as-atomised powder can be calculated as the ratio $X_{nc}=A2/A1$ [28]. In the present case $A1$=166 J/g and $A2$=91 J/g, so X_{nc}=0.55, i.e. 55 % of $Fe_{70}Si_{18}B_{12}$ powder is amorphous. Additionally, Figure 7 shows the cumulative particle size distribution of as-atomised $Fe_{70}Si_{18}B_{12}$ alloy determined by laser diffraction. As indicated in the graph, a cumulative weight fraction of 55 % corresponds to a critical particle size of d_c=16.7 μm, i.e. particles below this diameter are going to be mostly non-crystalline.

The average cooling rate of non-crystalline alloy particles during gas atomisation can be estimated using the following simplified equation [29]:

$$\frac{dT}{dt} \approx \frac{12k_g\left(T_f - T_o\right)}{\rho_m C_{pm} d^2} \qquad (1)$$

where T is temperature, t_i is time, T_f is the temperature of the melt droplet immediately after its formation, T_o is the temperature of the atomising gas,

ρ_m is the average density, C_{pm} is the average specific heat at constant pressure, d is the particle diameter and k_g is the average thermal conductivity of the atomising gas. This equation yields actually a lower limit of the true average cooling rate, since it neglects the enhanced convention heat transfer due to the relative velocity between the particle and the atomisation gas, and the minor effect of heat loss by radiation. Figure 8 shows the average cooling rate estimated with equation (1) as a function of the particle size (d). In order to perform this calculation, the following numerical values have been used: T_f≈1973 K, T_o≈300 K, ρ_m≈6.84 g/cm^3, C_{pm}≈770 J/(kg·K) [30], and k_g≈0.150 W/(m·K) for He, 0.0178 W/(m·K) for Ar and 0.0259 W/(m·K) for N_2 [17]. For the critical particle size d_c=16.7 μm, the estimated critical cooling rate of composition $Fe_{70}Si_{18}B_{12}$ is R_c≈2.11x10^6 K/s. The values of R_c reported in the literature for similar compositions are of the same order of magnitude [31].

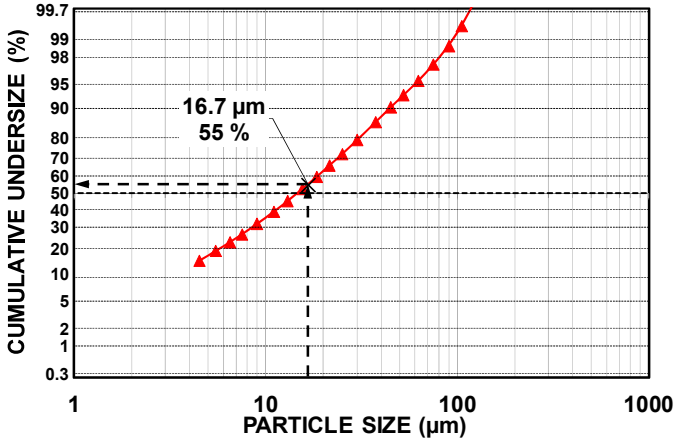

Figure 7. Cumulative particle size distribution of composition $Fe_{70}Si_{18}B_{12}$ measured by laser diffraction. The critical particle size below which the powder exhibits a non-crystalline structure is indicated.

This cooling rate is higher than the typical values reported for gas atomisation. The generally acknowledged cooling rates are between 10^2 and 10^5 K/s, depending on processing conditions, atomising gas and particle size [17,32]. Here, it is important to highlight that, since the particle size distribution is quite broad, particle size can vary from one to three orders of magnitude within the same powder batch. As the cooling rate is inversely proportional to the square of the particle size, it changes between two and nine orders of magnitude. This fact is often overlooked in gas atomisation, since authors are mostly concerned with the cooling rate of the particles with a diameter close to D_{50}. Usually, the atomising gases are nitrogen, air or

argon because of economic reasons. However, the use of helium, whose thermal conductivity is an order of magnitude higher and produces finer powders under the same operating conditions [17], increases the cooling rate by a factor of 10. Figure 8 demonstrates that, for the same critical cooling rate, the critical particle size is only 5.7 μm when atomising with Ar and 6.8 μm with N_2, reducing drastically the fraction of powder with an amorphous structure. As explained before, the use of He increases this fraction until 55 %, which corresponds to an output of 7.76 g/s (0.47 kg/min) of non-crystalline material in the present case. This yield is high enough to consider He gas atomisation a promising process for the future industrial production of the amorphous alloy, specially taking into account the spherical morphology of the product.

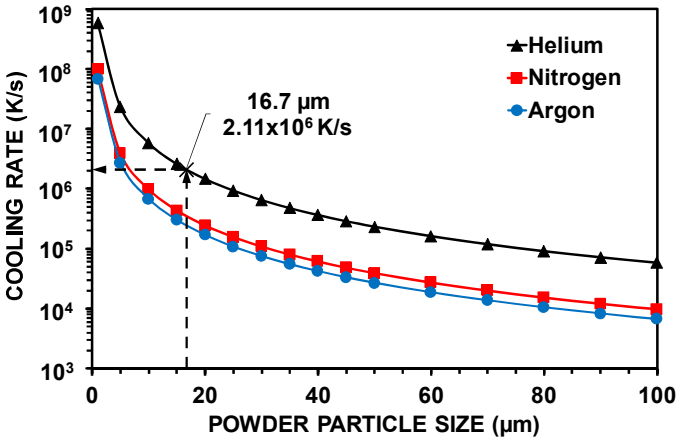

Figure 8. Cooling rate curve of gas atomised particles as a function of their size for different atomisation gases.

3.3 *Magnetic characterization*

Hysteresis loops of the studied samples are shown in Figure 9. The relevant magnetic properties are summarized in Table 2. As expected, the saturation magnetization (M_S) decreases when Fe content is reduced, which is due to the associated drop of the effective magnetic moment. The hysteresis loops of the samples with high Fe content (x=80, 75 and 70) denote the soft magnetic character associated with very low values of coercive field (H_{ci}) and magnetic energy loss. The main phases in these compositions, i.e. α-Fe(Si), Fe_3Si and amorphous phase, exhibit soft magnetic character. In addition, the hysteresis loops of the three alloys with the largest Fe content show an inclined linear region from the beginning (i.e. when the

magnetic field is zero) until the point where they become curved due to the proximity of magnetic saturation. Such a linear zone of the hysteresis loop can be associated with the presence of uniaxial magnetic anisotropy transversely to the direction of the applied magnetic field. Therefore, the magnetization process of the material in this range of the applied magnetic field takes place by coherent rotation of the magnetization that is laying transversally to the direction of the applied magnetic field. The magnetic field in the zone of the curvature previous to magnetic saturation is related with the distribution of the anisotropy field of Gaussian-type (see reference [33]), being the average value ($<H_K>$) of around 3000 Oe. Considering that the value of M_S in these amorphous alloys is 1.5-1.6 T (169-181 emu/g) [8], this anisotropy field leads to values of anisotropy energy of around 1.5×10^5 J/m^3. This value of the anisotropy energy is one order of magnitude larger than the magnetoelastic energy of Fe-rich amorphous alloys, which should be attributed to a strong demagnetizing effect.

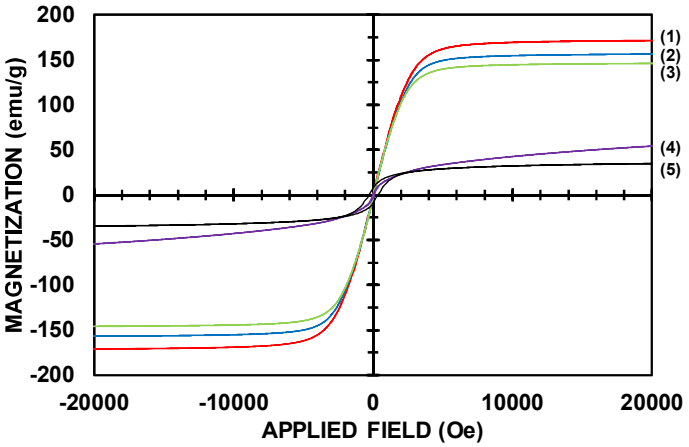

Figure 9. Hysteresis loops at room temperature of the alloys: (1) $Fe_{80}Si_{12}B_8$, (2) $Fe_{75}Si_{15}B_{10}$, (3) $Fe_{70}Si_{18}B_{12}$, (4) $Fe_{60}Si_{24}B_{16}$ and (5) $Fe_{50}Si_{30}B_{20}$.

The hysteresis loop corresponding to the sample x=60 also shows a low value of coercivity, maintaining a soft magnetic behaviour, although as it is expected, the saturation magnetization is lower due to the reduction of Fe content. It is noteworthy to point out that this composition does present neither Fe_3Si nor α-Fe(Si) phases. Nevertheless, the absence of an initial linear zone, together with the presence of a strong and wide curvature when approaching magnetic saturation, leads to think on a magnetization mechanism that is different of the explained one for the previous compositions, that is, incoherent rotation of the magnetization inside the

magnetic domains. This sample does not reach saturation even at a high magnetic field of 20000 Oe. The alloy seems to contain only $Fe_{4.9}Si_2B$ grains, which is a phase no found in the other compositions and whose magnetic properties have not been reported previously. The measurements suggest that it shows a harder magnetic character and, consequently, it is more difficult to achieve the magnetic saturation.

Table 2. Magnetic properties of the investigated alloys.

Experiment	Composition (at%)	H_{ci} (Oe)	M_s (emu/g)	$\langle H_k \rangle$ (Oe)
AG16-71	$Fe_{80}Si_{12}B_8$	23	173	3219
AG16-75	$Fe_{75}Si_{15}B_{10}$	22	158	2985
AG16-76 full range	$Fe_{70}Si_{18}B_{12}$	12	147	2799
AG16-76 <10 μm	$Fe_{70}Si_{18}B_{12}$	7	149	2956
AG16-77	$Fe_{60}Si_{24}B_{16}$	51	81	3049
AG16-78	$Fe_{50}Si_{30}B_{20}$	189	39	1999

The quite large value of coercivity showed by the alloy x=50 suggests an intergranular decoupling due to prevalence of the dipolar interaction over the exchange interaction. This should be attributed to the presence of crystalline phases, especially iron boride, as it was detected by XRD measurements. It is well known that this kind of compounds leads to a significant magnetic hardening.

Finally, it is interesting to remark that the powder fraction <10 μm of composition $Fe_{70}Si_{18}B_{12}$, which is completely amorphous, presents a coercive field of 7 Oe (see Table 2), lower than the coercivity measured for the full range of particle sizes of the same alloy.

4. Conclusions

This paper demonstrates the production of a soft magnetic amorphous Fe-Si-B alloy by He gas atomisation. Applied to this family of materials, this is a novel technology and a good alternative to the conventional melt-spinning technique. By the appropriate selection of the composition and atomisation conditions, a significant fraction of powder (55 %) that is fine enough (<16.7 μm) to exhibit a non-crystalline structure could be produced. Another relevant characteristic of the product is the spherical shape of the particles, which opens new processing possibilities to manufacture complex geometries. Gas atomisation is a mass production technology (about 0.47 kg/min for the present alloy) that may enlarge the

technological applications of amorphous Fe-Si-B materials, especially considering the excellent soft magnetic properties obtained in this work, with a coercivity of 7 Oe. New studies to increase the atomisation yield and improve the magnetic behaviour by annealing treatments are underway.

Acknowledgements

The authors thank SGIker of UPV/EHU for technical and human support. This work was supported by the European Commission (ERDF and ESF programs). Authors Mihail Ipatov and Julian Gonzalez acknowledge the University of the Basque Country for the support under the scheme "Ayudas a Grupos Consolidados" (Ref. PPG17/35).

References

[1] P. Duwez, R.H. Willens, W. Klement, Continuous series of metastable solid solutions in silver-copper alloys, J. Appl. Phys. 31 (1960) 1136–1137, https://doi.org/10.1063/1.1735777.

[2] W. Klement, R.H. Willens, P. Duwez, Non-crystalline structure in solidified gold–silicon alloys, Nature. 187 (1960) 869–870, https://doi.org/10.1038/187869b0.

[3] P. Duwez, Metastable phases obtained by rapid quenching from the liquid state, Prog. Solid State Chem. 3 (1967) 377–406, https://doi.org/10.1016/0079-6786(67)90038-6.

[4] H. Jones, Splat cooling and metastable phases, Rep. Prog. Phys. 36 (1973) 1425–1497, https://doi.org/10.1088/0034-4885/36/11/002.

[5] F.E. Luborsky, Amorphous Metallic Alloys, Butterworths, http://www.sciencedirect.com/science/book/9780408110303, 1983. (Accessed 14 July 2017).

[6] A. Zhukov, J. Gonzalez, Amorphous and nanocrystalline soft magnetic materials: tailoring of magnetic properties, magnetoelastic and transport properties, in: Handb. Adv. Magn. Mater., 2006: pp. 1091–1157, https://doi.org/10.1007/1-4020-7984-2_27.

[7] K. Narita, J. Yamasaki, H. Fukunaga, Dependence on metalloid content for magnetic properties of Fe-Si-B metallic glasses, IEEE Trans. Magn. 13 (1977) 1544–1546, https://doi.org/10.1109/TMAG.1977.1059638.

[8] F. Luborsky, J. Becker, J. Walter, H. Liebermann, Formation and magnetic properties of Fe-B-Si amorphous alloys, IEEE Trans. Magn. 15 (1979) 1146–1149, https://doi.org/10.1109/TMAG.1979.1145870.

[9] N. Decristofaro, A. Freilich, G. Fish, Formation and magnetic properties of Fe-B-Si metallic glasses, J. Mater. Sci. 17 (1982) 2365–2370, https://doi.org/10.1007/BF00543746.

[10] M. Hagiwara, A. Inoue, T. Masumoto, Mechanical properties of Fe-Si-B amorphous wires produced by in-rotating-water spinning method, Metall. Trans. A. 13 (1982) 373–382, https://doi.org/10.1007/BF02643346.

[11] A. Inoue, M. Komuro, T. Masumoto, Fe-Si-B amorphous alloys with high silicon concentration, J. Mater. Sci. 19 (1984) 4125–4132, https://doi.org/10.1007/BF00980780.

[12] T. Sato, Effect of composition on glass-forming regions of iron-base alloy powders prepared by water atomization, J. Mater. Sci. Lett. 6 (1987) 844–846, https://doi.org/10.1007/BF01729033.

[13] T. Sato, Study on powder properties of Fe-P-C and Fe-B-Si alloy powders prepared by water atomization, J. Mater. Sci. 26 (1991) 2329–2336, https://doi.org/10.1007/BF01130177.

[14] Y. Yoshizawa, S. Oguma, K. Yamauchi, New Fe-based soft magnetic alloys composed of ultrafine grain structure, J. Appl. Phys. 64 (1988) 6044–6046, https://doi.org/10.1063/1.342149.

[15] Y. Yoshizawa, K. Yamauchi, Fe-based soft magnetic alloys composed of ultrafine grain structure, Mater. Trans. JIM. 31 (1990) 307–314.

[16] R. Hasegawa, Present status of amorphous soft magnetic alloys, J. Magn. Magn. Mater. 215–216 (2000) 240–245, https://doi.org/10.1016/S0304-8853(00)00126-8.

[17] A.J. Yule and J.J. Dunkley, Atomization of Melts for Powder Production and Spray Deposition, Oxford University Press,UK, Oxford, 1994.

[18] R.M. German, Powder Metallurgy and Particulate Materials Processing, Metal Powder Industries Federation (MPIF), Princeton, NJ, USA, 2005.

[19] S.V. Lukin, V.I. Zhuchkov, N.A. Vatolin, The surface tension, density and oxidation kinetics of Fe-Si-B alloys, J. Less Common Met. 67 (1979) 399–405, https://doi.org/10.1016/0022-5088(79)90018-3.

[20] M. Tomut, H. Chiriac, M. Marinescu, F. Necula, Viscosity and surface tension measurements on Fe-rich FeB liquid alloys, J. Non-Cryst. Solids. 250–252 (1999) 655–659, https://doi.org/10.1016/S0022-3093(99)00153-2.

[21] A.L. Bel'tyukov, V.I. Lad'yanov, A.I. Shishmarin, S.G. Menshikova, Viscosity of liquid amorphizing alloys of iron with boron and silicon, J. Non-Cryst. Solids. 401 (2014) 245–249, https://doi.org/10.1016/j.jnoncrysol.2014.01.048.

[22] A.L. Bel'tyukov, A.I. Shishmarin, V.I. Lad'yanov, Viscosity of $Fe_{90}B_XSi_{(10-X)}$ melts, High Temp. 53 (2015) 302–304, https://doi.org/10.1134/S0018151X15020066.

[23] R.M. German, Particle Packing Characteristics, Metal Powder Industries Federation (MPIF), Princeton, NJ, USA, 1989.

[24] B.V. Neamţu, T.F. Marinca, I. Chicinaş, O. Isnard, F. Popa, P. Păşcuţă, Preparation and soft magnetic properties of spark plasma sintered compacts based on Fe–Si–B glassy powder, J. Alloys Compd. 600 (2014) 1–7, https://doi.org/10.1016/j.jallcom.2014.02.115.

[25] C. Suryanarayana, A. Inoue, Bulk Metallic Glasses, CRC Press, Boca Raton, Florida, USA, 2011.

[26] M.G. Poletti, L. Battezzati, Assessment of the ternary Fe–Si–B phase diagram, Calphad. 43 (2013) 40–47, https://doi.org/10.1016/j.calphad.2013.08.001.

[27] H. Monstadt, E. Hornbogen, Microstructure of melt-spun $Fe_{1-x}Si_x$ alloys ($0 \leq \times \leq 0.5$), Mater. Sci. Eng. A 133 (1991) 836–841, https://doi.org/10.1016/0921-5093(91)90197-U.

[28] M.E. Brown, Introduction to Thermal Analysis: Techniques and Applications, second ed., Kluwer Academic Publishers, 2004. https://rd.springer.com/book/10.1007%2F0-306-48404-8.

[29] A. Inoue, Light-metal based amorphous alloys, Curr. Top. Amorph. Mater., (1993) 159–166, https://doi.org/10.1016/B978-0-444-81576-7.50023-X.

[30] J. Zhang, H. Fujimori, A. Inoue, T. Masumoto, Specific heat behaviour on soft magnetic thick amorphous ribbons of an Fe-B-Si alloy, Mater. Sci. Eng. 99 (1988) 35–38, https://doi.org/10.1016/0025-5416(88)90286-8.

[31] T. Tokunaga, H. Ohtani, M. Hasebe, Thermodynamic evaluation of the phase equilibria and glass-forming ability of the Fe–Si–B system, Calphad. 28 (2004) 354–362, https://doi.org/10.1016/j.calphad.2004.11.004.

[32] A.E. Berkowitz, J.C. Grande, S.A. Miller, R.J. Murphy, J.L. Walter, Structures and properties of powders of $Fe_{75}Si_{15}B_{10}$ produced by gas-water atomization, Mater. Sci. Eng. 62 (1984) 217–230, https://doi.org/10.1016/0025-5416(84)90225-8.

[33] J.M. Barandiaran, M. Vazquez, A. Hernando, J. Gonzalez, G. Rivero, Distribution of the magnetic anisotropy in amorphous alloys ribbons, IEEE Trans. Magn. 25 (1989) 3330–3332, https://doi.org/10.1109/20.42293.

IEEE Transactions on Magnetics 54 (2018) 2002405

Magnetic Properties of Annealed Amorphous $Fe_{72.5}Si_{12.5}B_{15}$ Alloy obtained by Gas Atomization Technique

Kenny L. Alvarez [1, 2, *], José Manuel Martín [1], Mihail Ipatov [3], Lourdes Domínguez [4], and Julian Gonzalez [5]

[1] *CEIT-IK4 and Tecnun (University of Navarra), P° Manuel de Lardizábal 15, 20018, San Sebastián, Spain*
[2] *Escuela de Ingeniería Mecánica, Pontificia Universidad Católica de Valparaíso, Av. Brasil 2950, Valparaíso, Chile*
[3] *SGIker (Magnetic Measurements), University of the Basque Country, Av. Tolosa 72, 20018, San Sebastián, Spain*
[4] *Department of Applied Physics I, Engineering School, University of the Basque Country, Plaza Europa s/n, 20018 San Sebastián, Spain*
[5] *Department Materials Physics, Faculty of Chemistry, University of the Basque Country, P° Manuel de Lardizábal 3, 20018, San Sebastián, Spain*

Abstract

In this work, we report the effect of thermal treatment at different temperatures (523, 623, and 723 K) on the magnetic properties of an amorphous powder with composition $Fe_{72.5}Si_{12.5}B_{15}$ obtained by gas atomization. Differential scanning calorimetry curves indicate that a significant structural rearrangement takes place during annealing before crystallization. As expected, the intrinsic coercivity decreases with the annealing temperature, being the most significant drop from 3.26 Oe to 0.44 Oe for the powder with a particle size <20 μm, non-annealed and annealed at 723 K, respectively. An analysis of the effect of annealing on the anisotropy field distribution obtained directly from the magnetization curve is presented for both the non-annealed and the annealed sample with the lowest value of coercive field. The probability density function of the anisotropy field exhibits a lower applied field value at the maximum and is better fitted by a Gaussian distribution after the heat treatment, which is a sign of better amorphicity after structural relaxation.

Keywords: Amorphous materials, heat treatment, magnetic variable measurement, soft magnetic materials.

* Corresponding author Tel.: + 34 943 212 800
Email address: kalvarez@ceit.es/kenny.alvarez@pucv.cl (K. L. Alvarez).
https://doi.org/10.1109/TMAG.2018.2839258

1. Introduction

Fe-Si-B (Fe-rich) soft magnetic amorphous alloys have strongly attracted the interest because they are widely used in high frequency transformers, inductors, and sensors [1], [2]. These materials are typically produced by the well-known melt-spinning technique, involving the rapid solidification of the molten alloy. It is important to remark that amorphous ribbons obtained by melt-spinning have shown vastly superior properties as soft magnetic materials than the equivalent microcrystalline alloys. In this way, important advances have been achieved in this research field, concerning the exploration of new routes to fabricate soft magnetic materials. Thus, one alternative technique of rapid solidification that we have successfully used [3] is inert gas atomization. This technology produces spherical metal powders, being possible to achieve cooling rates >10^6 K/s in the finest powder fraction. The soft magnetic character of Fe-Si-B amorphous alloys obtained by gas atomization, with a low coercive field of around 7 Oe, was reported in [3].

The soft magnetic behavior of amorphous alloys is mainly due to the small value of the magnetic anisotropy of magnetoelastic character. Such magnetic anisotropy associated to the amorphous compounds shows a Gaussian distribution [4], [5]. In this case, it was obtained in reference [6] an expression for the distribution of magnetic anisotropy field, because the knowledge of the exact distribution of the anisotropy is also of interest to understand such soft magnetic character.

It is well known that a thermal treatment below the glass transition temperature (T_g) relaxes the structure, maintaining its amorphous character, and results in moderate magnetic softening due to the relief of intrinsic quenched-in stresses [7]. Many authors have discussed the influence of thermal treatment on the structure and magnetic properties of this type of amorphous alloy (see, for example, the review in reference [8]). In fact, the structural relaxation produced by thermal treatment involves two kinds of processes. The first one is related to changes in chemical composition at atomic length scale and the second corresponds to the annihilation of the free-volume [9], [10]. These two phenomena cause a decrease in the magnetoelastic anisotropy. In addition, coercivity is directly related with the magnetic anisotropy and, therefore, structural relaxation in amorphous alloys improves the soft magnetic character. In this work, we analyze the effect of thermal treatment temperature (523, 623, and 723 K) on the magnetic behavior (intrinsic coercivity and distribution of the

anisotropy field) of an amorphous powder of $Fe_{72.5}Si_{12.5}B_{15}$ alloy produced by gas atomization.

2. Experimental Procedure

Fe-Si-B amorphous alloy, with the nominal composition of $Fe_{72.5}Si_{12.5}B_{15}$ (at. %), was produced by gas atomization in an atomization unit PSI model Hermiga 75/3VI, using a convergent-divergent close-coupled atomizer. The amount of produced powder was nearly 2.5 kg. Iron (supplied by Allied Metal Corp.), silicon (supplied by Cometal S.A.), and boron (supplied by H.C. Starck) of commercial purity were melted in an induction furnace under a high purity Ar atmosphere. In addition, the atomization chamber was evacuated and purged with He to minimize oxidation. The atomizing gas was He at a pressure of 60 bar. The melt temperature in the furnace was 1973 K.

The particle size distribution of the powders was measured by laser diffraction in an equipment Sympatec Helos (H0852). The true density was measured in a He pycnometer Micromeritics Accupyc 1330. Particle shape was studied using conventional (Philips XL30CP) scanning electron microscopy (SEM).

The amorphous character of the alloy was checked by X-ray diffraction (XRD) in a Philips PW1825 diffractometer, using the characteristic wavelength of K_α line for Cu (wavelength of 1.542 Å). Electrons were generated in a W filament applying a current of 40 mA and accelerated toward the Cu anode under a potential of 40 kV. The scanning rate was 0.005 °/s (in steps of 0.02 ° with a holding time of 4 seconds at each angle). Useful information on magnetic and structural transitions was obtained by differential scanning calorimetry (DSC), in an equipment TA Instrument DSC 2920. DSC experiments were performed using a sample of about 10 mg, at a heating rate of 10 K/min, and under Ar atmosphere.

The powder was sieved to separate the fraction with a particle size <20 μm. This fraction was subjected to heat treatments at different temperatures (523, 623, and 723 K) for two different times (0 and 60 min) under Ar atmosphere. The annealing time of 0 min means that the sample was heated up to the annealing temperature and immediately cooled down without any holding.

Thin foils were prepared using a FEI Quanta 3D FEG focused ion beam (FIB) milling instrument by the lift out technique from the sample.

First, a Pt line is deposited and two stair-step FIB trenches are cut at both sides of the area of interest. Next, the specimen is further thinned to less than 1 μm in thickness and a slice of the specimen is cut free. The obtained lamella is removed using a micromanipulator and welded to a Cu grid suitable for transmission electron microscopy (TEM) analysis. Final milling down to less than 100 nm is carried out by employing successively lower voltages up to 2 kV. The obtained specimen was examined by conventional bright-field imaging in a JEOL JEM-2100F (S)TEM microscope operated at 200 kV with a LaB_6 filament.

Magnetic properties at room temperature of the powders were evaluated from the hysteresis loop obtained in an equipment Quantum Design PPMS-9T system with vibrating sample magnetometer (VSM) option Model P252. The step of magnetic field change near the coercive field was 5 Oe. Before the measurement of the samples, the equipment was calibrated with a paramagnetic Dy_2O_3 standard sample. The correction parameters to compensate the magnet remanence were determined. The measurement of the paramagnetic standard demonstrates the reliability of the measurements up to units of Oe.

3. Experimental Results and discussion

3.1 As-atomized Powder Characterization

TABLE I
Atomization Parameters and Properties of As-atomized Powders.

Property		Value
Mass flow rate of melt (g/s)		12.18
Mass flow rate of gas (g/s)		14.19
Gas-metal mass flow rate ratio *(GMR)*		1.17
Liquidus temperature (K)		1417
Melt superheat (K)		556
Particle size distribution (μm)[a]	D_{10}	4.5
	D_{50}	14.9
	D_{90}	48.7
Apparent density (% of true density)		34.2
Tap density (% of true density)		64.7
True density (g/cm³)		6.96

[a]D_{10}: 10th percent percentile; D_{50}: median particle size; D_{90}: 90th percent percentile.

TABLE I summarizes the physical properties of as-atomized powder and the relevant atomization variables. As reported for other compositions [3], apparent density is very low due to the fine particle size, whereas tap density is high because the powder is spherical [11]. The spherical particle shape can be seen in Fig. 1. A broad peak in the X-ray diffraction pattern between 35° and 55° (Fig. 2) demonstrates that the as-atomized powder is mostly amorphous. Nevertheless, a small sharp peak at $2\theta = 45°$ reveals the presence of some crystallites in the largest particles. Crystallization takes place in large particles because the cooling rate during gas atomization is inversely proportional to the square of the particle size [3].

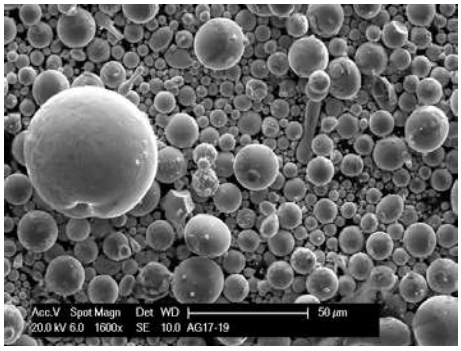

Fig. 1. SEM image of as-atomized powder.

3.2 *Structural Relaxation*

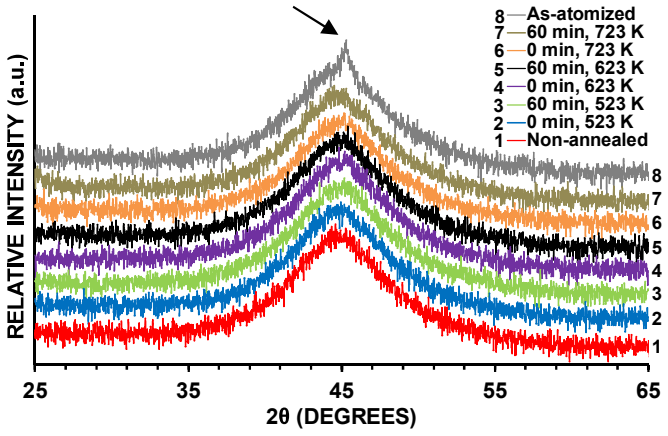

Fig. 2. XRD pattern of the as-atomized, annealed (particle size <20 µm), and non-annealed (particle size <20 µm) samples. The arrowed sharp peak in trace number 8 indicates the presence of some crystalline phase in the as-atomized sample.

After heat-treating the powder fraction with a particle size <20 μm, the amorphous character of the annealed samples was checked by X-ray diffraction technique. Fig. 2 confirms that the material is fully amorphous. Such spectra can be fitted to a Gaussian curve with a full width at half maximum of 6°.

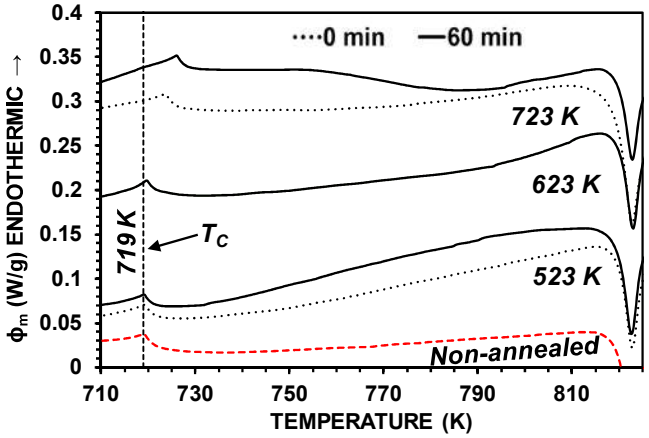

Fig. 3. DSC traces corresponding to the non-annealed sample and to samples annealed at 523, 623, and 723 K for 0 min (····) and 60 min (—).

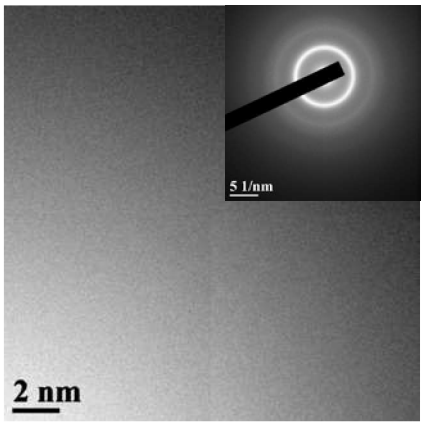

Fig. 4. Bright field image and selected area diffraction pattern of a thin foil taken from the specimen annealed at 723 K for 60 min.

Fig. 3 shows the DSC traces of the annealed and non-annealed samples. These traces display a higher slope between the Curie (T_C) and the crystallization (T_X) temperatures in the case of the annealed samples, which proves that the powder relaxes its amorphous structure. In addition, the amount of enthalpy recovery increases with the holding time and decreases

with the annealing temperature. This tendency is in agreement with the literature [12], [13]. It is interesting to remark that the trace of the specimen annealed at 723 K for 60 min is significantly different to other curves and that the corresponding enthalpy recovery turns out to be negative. This behavior can be linked to a substantial structural rearrangement leading to atoms clustering and the formation of embryos before crystallization is detected [14]. In fact, the TEM image and the corresponding selected area diffraction pattern shown in Fig. 4 do not show any sign of crystallization.

3.3 *Magnetic Behavior*

It has been reported [15], [16] that the structural relaxation can modify T_C in Fe-Ni-based amorphous alloys annealed at 473-573 K for 1-3 h, but such change is less than 10 K. In the present case, the Curie temperature of the non-annealed sample is 719 K. This temperature does not change when the material is annealed at 523 K or 623 K (Fig. 3). However, it increases to 724-726 K in the specimen annealed at 723 K. We consider that this change of T_C is associated to the formation of clusters that are richer in Si than the surrounding matrix. As a result, the chemical composition of the surrounding amorphous phase is modified as well as its T_C [17]. DSC traces exhibit three exothermic peaks associated with crystallization of Fe_3Si and iron borides, which is accompanied of magnetic hardening, being the onset temperature (T_X) for this process equals to 820 K. It is noteworthy to remark that the measured values of T_C and T_X are in good agreement with those reported in the literature [18], [19].

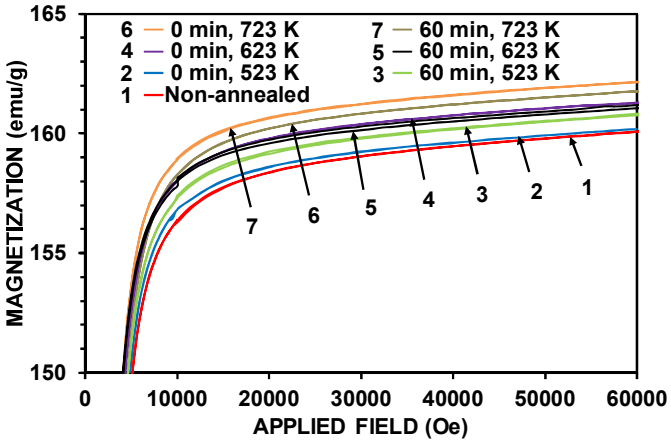

Fig. 5. Hysteresis loops detail showing the saturation magnetization (M_S).

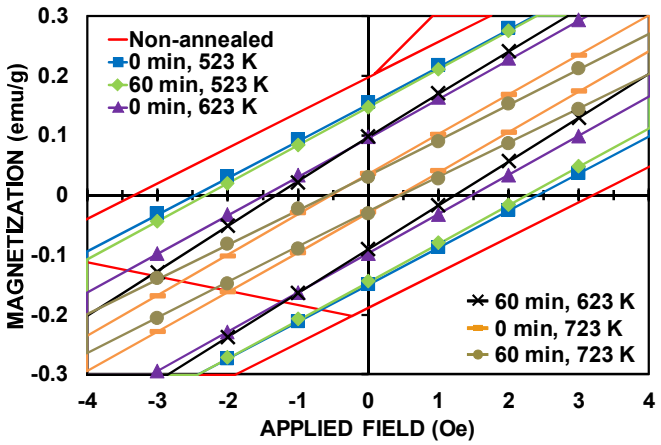

Fig. 6. Hysteresis loops magnified at the origin of coordinates to show the intrinsic coercivity (H_{Ci}).

Fig. 5, Fig. 6 and TABLE II show the magnetic properties obtained from the measured hysteresis loops. The very low value of coercive field denotes the soft magnetic character of the material. The hysteresis loops of the annealed samples could be connected probably with a domain structure stabilization linked to a structural relaxation mechanism. As it is well known, the soft magnetic character is attributed mainly to the absence of magnetocrystalline anisotropy, playing an important role the magnetoelastic anisotropy arising from the residual internal stresses. In addition, the rapid solidification processes (RSP) suppress atomic diffusion and, therefore, cause excess of free volume [9] and, consequently, internal stresses. Thus, optimization of the magnetic properties requires stress relief treatments at temperatures below T_g.

TABLE II

Magnetic Properties of As-atomized Powder and of the Sieved Fraction <20 μm Before and After Annealing.

Magnetic properties[a]	As-atomized	<20 μm						
		Non-annealed	Annealed (0 min)			Annealed (60 min)		
			523 K	623 K	723 K	523 K	623 K	723 K
H_{Ci} (Oe)	8.92	3.26	2.46	1.5	0.44	2.28	1.23	0.57
M_S (emu/g)	160	161	161	162	163	161	162	162
$\langle H_K \rangle$ (Oe)	2950	3140	2940	2830	2770	2890	2540	3110

[a] H_{Ci}: intrinsic coercivity; M_S: saturation magnetization; $\langle H_K \rangle$: average anisotropy field, calculated as the H field of the maximum value of $P(H_K)$ in Fig.8.

In fact, the coercive field decreases significantly (see Fig. 7) from 3.26 Oe (non-annealed) to 0.44 Oe (annealed) in the specimens annealed at 723 K for 0 min. There is an influence of the time on this drop, since intrinsic coercivity values are lower in the samples heat-treated for 60 min than in the specimens annealed for 0 min at 523 K or 623 K. The above mentioned behavior of the intrinsic coercivity should be ascribed to the structural relaxation associated with the thermal annealing, which reduces the internal stresses and leads to a significant drop of the magnetoelastic anisotropy. In contrast, the powders heat-treated at 723 K exhibit a slight increment of intrinsic coercivity with the time linked to atoms clustering and embryos formation, as explained before. The associated magnetoelastic anisotropies, of course, limit the achievable soft magnetic properties. Since our samples are highly magnetostrictive Fe-base alloys (with a saturation magnetostriction of around 30 ppm), the magnetic properties are determined by uniaxial anisotropies induced during heat treatment either by a magnetic field or by mechanical creep.

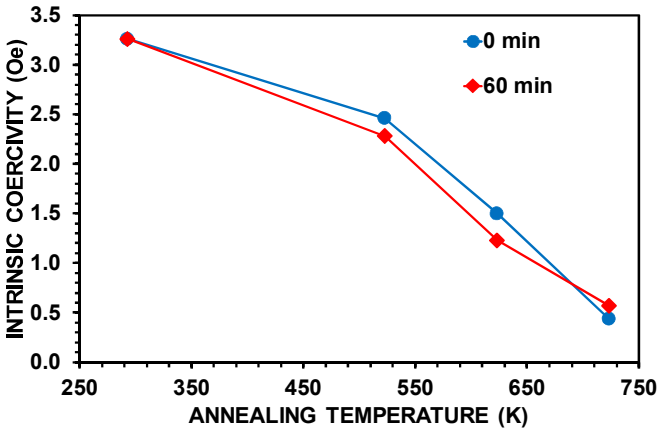

Fig. 7. Influence of the annealing temperature on the intrinsic coercivity at different times.

On the other hand, considering only perpendicular anisotropies, which is reasonable according to the magnetization curves of Fig. 5, the following expression was deduced for the distribution of anisotropy field [6]:

$$P(H_K) = -H[d^2m/dH^2] \quad (1)$$

where $P(H_K)$ represents the probability of the anisotropy field function (H_K) to take the value H of magnetic field and $m = M/M_S$ is the magnetization (M) normalized by saturation magnetization (M_S). Then, we shall suppose that no parallel anisotropy is present or, if present, the remanence has been subtracted from the magnetization curve. $P(H_K)$ is depicted as a function of the applied magnetic field (H) in Fig. 8 for the non-annealed and annealed (annealed at 723 K for 0 min) specimens. It is interesting to note that the H value at the maximum $P(H_K)$ decreases significantly in the heat-treated sample, which is a strong indication of the softer magnetic character of the annealed sample. Moreover, the $P(H_K)$ curve can be fitted better by a Gaussian function in the case of the annealed material, which is a sign of better amorphicity after structural relaxation.

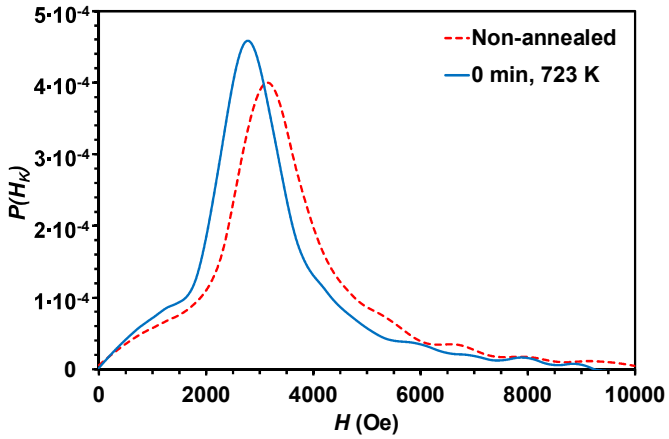

Fig. 8. Distribution of the anisotropy field, $P(H_K)$, as a function of the applied field (H) of the samples non-annealed and annealed at 723 K for 0 min.

The average anisotropy field $\langle H_K \rangle$ of the samples has values between 2500 to 3100 Oe, approximately. Considering that the value of M_S in these amorphous samples is 1.40-1.43 T (160-163 emu/g), this anisotropy field leads to values of anisotropy energy of around 1.6×10^5 J/m^3 [20]. This value of the anisotropy energy is one order of magnitude larger than the magnetoelastic energy of Fe-rich amorphous alloys, which should be attributed to a strong demagnetizing effect due to the holder dimension that contains the powder sample. Since the holder was the same for all samples, the reported differences in $\langle H_K \rangle$ and in the anisotropy field distributions (Fig. 8) can only be attributed to the degree of structural relaxation.

4. Conclusion

Gas atomization was successfully used to produce amorphous powder of $Fe_{72.5}Si_{12.5}B_{15}$ alloy with a high yield, proving the feasibility of this technology for the industrial production of this kind of soft magnetic materials. The obtained powder is spherical and fine, with a median particle size of 14.9 μm. The as-atomized powder has soft magnetic character (high saturation magnetization and low intrinsic coercivity). The size fraction below 20 μm was annealed to achieve structural relaxation and improve the soft magnetic properties. The results show an important drop of the intrinsic coercivity from 3.26 Oe (non-annealed) to 0.44 Oe (annealed at 723 K during 0 min). The anisotropy field also decreases from 3140 to 2770 Oe in the same samples. XRD and TEM observations indicate that crystallization does not occur after annealing for 60 min at 723 K. However, an increase of the Curie temperature (from 719 to 726 K), of the intrinsic coercivity (from 0.44 Oe to 0.57 Oe), of the anisotropy field (from 2770 to 3100 Oe), and changes in the DSC trace suggest that atoms clustering is producing composition changes of short range order.

Acknowledgements

Author Kenny L. Alvarez thanks to Becas Chile (CONICYT) for the financial support. The authors thank SGIker of UPV/EHU for technical and human support. This work was supported by the European Commission (ERDF and ESF programs). Authors M. Ipatov, L. Domínguez and J. Gonzalez acknowledge the University of the Basque Country for the support under the scheme “Ayudas a Grupos Consolidados” (Ref. PPG17/35).

References

[1] F. E. Luborsky, *Amorphous Metallic Alloys*. London, U.K.: Butterworths, 1983.

[2] A. Zhukov and J. Gonzalez, “Amorphous and Nanocrystalline Soft Magnetic Materials : Tailoring of Magnetic Properties, Magnetoelastic and Transport Properties,” in *Handbook of Advanced Magnetic Materials, vol. 3*, Y. Liu, D. J. Sellmyer, and D. Shido, Eds. New York, USA: Springer, 2006, pp. 115–181.

[3] K. L. Alvarez, J. M. Martín, M. Ipatov, and J. Gonzalez, “Soft magnetic amorphous alloys (Fe-rich) obtained by gas atomisation technique,” *J. Alloys Compd.*, vol. 735, pp. 2646–2652, Feb. 2018.

[4] M. Vázquez, W. Fernengel, and H. Kronmüller, “The Effect of tensile stresses on the magnetic properties of $Co_{58}Fe_5Ni_{10}Si_{11}B_{16}$ amorphous alloys,” *Phys. Status Solidi* A, vol. 80, no. 1, pp. 195–204, 1983.

[5] J. González, M. Vázquez, and J. M. Barandiarán, "On the dependence of the magnetization curve on applied tensile stress in amorphous alloys with positive magnetostriction," *Phys. Status Solidi A*, vol. 93, no. 2, pp. K165–K170, 1986.

[6] J. M. Barandiarán, M. Vazquez, A. Hernando, J. Gonzalez, and G. Rivero, "Distribution of the magnetic anisotropy in amorphous alloys ribbons," *IEEE Trans. Magn.*, vol. 25, no. 5, pp. 3330–3332, Sep. 1989.

[7] F. Luborsky, J. Becker, and R. McCary, "Magnetic annealing of amorphous alloys," *IEEE Trans. Magn.*, vol. TMAG-11, no. 6, pp. 1644–1649, Nov. 1975.

[8] T. Egami, "Magnetic amorphous alloys: physics and technological applications," *Rep. Prog. Phys.*, vol. 47, no. 12, pp. 1601–1725, 1984.

[9] C. Suryanarayana and A. Inoue, *Bulk Metallic Glasses*. Boca Raton, FL, USA: CRC Press, 2011.

[10] T. Egami, "Structural relaxation in amorphous $Fe_{40}Ni_{40}P_{14}B_6$ studied by energy dispersive X-ray diffraction," *J. Mater. Sci.*, vol. 13, pp. 2587–2599, Dec. 1978.

[11] R. M. German, *Particle Packing Characteristics*. Princeton, NJ, USA: Metal Powder Industries Federation, 1989.

[12] A. Slipenyuk and J. Eckert, "Correlation between enthalpy change and free volume reduction during structural relaxation of $Zr_{55}Cu_{30}Al_{10}Ni_5$ metallic glass," *Scripta Mater.*, vol. 50, no. 1, pp. 39–44, 2004.

[13] M. E. Launey, J. J. Kruzic, C. Li, and R. Busch, "Quantification of free volume differences in a $Zr_{44}Ti_{11}Ni_{10}Cu_{10}Be_{25}$ bulk amorphous alloy," *Appl. Phys. Lett.*, vol. 91, no. 5, pp. 26–28, 2007.

[14] M. Vázquez, P. Marin, H. A. Davies, and A. O. Olofinjana, "Magnetic hardening of FeSiBCuNb ribbons and wires during the first stage of crystallization to a nanophase structure," *Appl. Phys. Lett.*, vol. 64, no. 23, pp. 3184–3186, 1994.

[15] Y.-N. Chen and T. Egami, "Effect of annealing on the Curie temperature of amorphous alloys," *J. Appl. Phys.*, vol. 50, no. B11, pp. 7615–7617, 1979.

[16] J. S. Blázquez, S. Lozano-Pérez, and A. Conde, "Enthalpy and Curie temperature relaxation effects in FeSiB–CuNb alloys prepared at different quenching rates," *Mater. Lett.*, vol. 45, no. 5, pp. 246–250, 2000.

[17] T. Egami, "Structural relaxation in amorphous alloys-compositional short range ordering," *Mater. Res. Bull.*, vol. 13, no. 6, pp. 557–562, 1978.

[18] K. Narita, J. Yamasaki, and H. Fukunaga, "Dependence on metalloid content for magnetic properties of Fe-Si-B metallic glasses," *IEEE Trans. Magn.*, vol. TMAG-13, no. 5, pp. 1544–1546, Sep. 1977.

[19] U. Carow-Watamura, D. V. Louzguine, and A. Takeuchi, "B-Fe-Si (144)," in *Physical Properties of Ternary Amorphous Alloys. Part 2: Systems from B-Be-Fe to Co-W-Zr. Landolt-Börnstein-Group III Condensed Matter* (Numerical Data and Functional Relationships in Science and Technology), vol. 37B2, Y. Kawazoe, U. Carow-Watamura, and J. Z. Yu, Eds. Berlin, Germany: Springer, 2011, pp. 200–253.

[20] G. Herzer, "Grain size dependence of coercivity and permeability in nanocrystalline ferromagnets," *IEEE Trans. Magn.*, vol. 26, no. 5, pp. 1397–1402, Sep. 1990.

Journal of Alloys and Compounds 810 (2019) 151754

Contents lists available at ScienceDirect

Journal of Alloys and Compounds

journal homepage: http://www.elsevier.com/locate/jalcom

Structural and magnetic properties of amorphous and nanocrystalline Fe-Si-B-P-Nb-Cu alloys produced by gas atomization

Kenny L. Alvarez [a, b, *], José Manuel Martín [a], Nerea Burgos [a], Mihail Ipatov [c], Lourdes Domínguez [d], Julian Gonzalez [e]

[a] *CEIT-IK4 and Tecnun (University of Navarra), P° Manuel de Lardizábal 15, 20018, San Sebastián, Spain*

[b] *Escuela de Ingeniería Mecánica, Pontificia Universidad Católica de Valparaíso, Av. Brasil 2950, Valparaíso, Chile*

[c] *SGIker (Magnetic Measurements), University of the Basque Country, Av. Tolosa 72, 20018, San Sebastián, Spain*

[d] *Department of Applied Physics I, Engineering School, University of the Basque Country, Plaza Europa s/n, 20018 San Sebastián, Spain*

[e] *Department Materials Physics, Faculty of Chemistry, University of the Basque Country, P° Manuel de Lardizábal 3, 20018, San Sebastián, Spain*

Abstract

Fe-Si-B-Nb-Cu alloy powders, with and without P additions, were produced by gas atomization. The particles smaller than 20 μm are fully amorphous, exhibiting good soft magnetic properties. The crystallization process was studied by differential scanning calorimetry, demonstrating that its kinetics changes dramatically with small variations in the composition. The $(Fe_{0.76}Si_{0.09}B_{0.10}P_{0.05})_{97.5}Nb_{2.0}Cu_{0.5}$ (at. %) alloy was annealed in the supercooled liquid region (480 °C) and at the first crystallization peak (530 °C). The structural characterization by means of differential scanning calorimetry, X-ray diffraction, and transmission electron microscopy provided information that explained the excellent soft magnetic properties. Annealing at 480 °C produced an amorphous relaxed structure with improved soft magnetic properties. At 530 °C, a two-phase material formed by nanocrystals with an average grain size of 16-17 nm embedded in an amorphous matrix was developed. Partial nanocrystallization increased the saturation magnetization from 139 to 144 emu/g and reduced the coercivity from 2.24 to 0.69 Oe. These results can be understood in terms of the algebraic contribution of both phases to the magnetization and the application of the random anisotropy model to nanocrystalline soft magnetic materials.

* Corresponding author Tel.: + 34 943 212 800
Email address: kalvarez@ceit.es/kenny.alvarez@pucv.cl (K. L. Alvarez).
https://doi.org/10.1016/j.jallcom.2019.151754

Keywords: Amorphous materials, gas atomization, magnetic measurements, nanocrystallization, soft magnetic materials.

1. Introduction

There is a strong demand for new magnetic materials for use in electrical and electronic devices that aim to minimize energy consumption and reduce greenhouse gas emissions, which has led to the exploration of alternative routes of production. There is currently a large worldwide research effort to develop such new fabrication methods. One technology that has been recently used to produce soft and hard magnetic materials is gas atomization [1–6] because it is suitable for the mass production of powders. Initially, soft magnetic Fe-based alloys produced by gas atomization were crystalline with relatively large values of coercivity of about tens of Oe at room temperature (see reference [3] and others therein).

We have recently reported [2] on the microstructure and magnetic properties of gas atomized Fe-Si-B powders. There is a strong dependence of the cooling rate with the particle size in gas atomization [2,7]. It was determined that the smallest particles were amorphous and, consequently, exhibited very interesting soft magnetic properties (a low coercive field of approximately 7 Oe). This feature is ascribed to a higher cooling rate when the particle size is decreased, so that the cooling rate occurring in particles below 20 μm was sufficient to avoid crystallization. The particle size is also very important in suppressing eddy current loss at high frequencies [5,8].

In this context, the production of new soft magnetic materials using gas atomization seems quite attractive in order to minimize the magnetic energy loss. This implies decreasing the coercivity (with an increase in the magnetic susceptibility). In particular, the well-known nanocrystalline FINEMET (Fe-Si-B-Cu-Nb) alloy obtained by rapid quenching (ribbon shape) [9] has attracted significant attention because it exhibits extremely soft magnetic behavior after annealing the precursor amorphous structure (typically at 500-550 °C for 30-60 min). The debate concerning the dominant microscopic mechanisms of this soft magnetic behavior in various materials still persists. However, compared with their amorphous counterparts, the low saturation magnetostriction (λ_s), high effective permeability (μ_e), and saturation magnetic flux density (B_S) of the nanocrystalline soft magnetic alloys are currently being utilized in different applications and are being considered in an equally diverse range of future ones [10,11].

Therefore, the possibility of producing soft nanocrystalline alloys by annealing amorphous gas atomized powders is a topic of interest, following the successful production of soft magnetic amorphous Fe-Si-B alloys [2]. The addition of small amounts of Nb, Cu, and P plays a crucial role in the nanocrystallization process. Cu and Nb are critical for developing the nanocrystalline structure, with approximately 70-80 volume % of α-Fe(Si) nanograins approximately 10-15 nm in size embedded in the residual amorphous matrix [12]. Thus, due to Cu doping, a uniform nanocrystalline microstructure and excellent soft magnetic properties can be obtained after annealing. The introduction of Cu prompts the nucleation of α-Fe(Si) nanoclusters of a few nanometers in the amorphous matrix. This element controls the primary crystal density, greatly affecting the grain size of the annealed nanocrystalline alloys. More Cu should be added when a higher density of homogeneously distributed nucleation sites is required [9]. The growth of such nanoclusters is hindered by the addition of Nb, resulting in the aforementioned nanocrystalline structure.

The objective of this paper is to report the production of novel amorphous Fe-based alloys via gas atomization, as well as the doping effect of Cu, Nb, and P upon their properties. The paper is structured into two broad sections. First we have studied the performance of several amorphous powders as soft magnetic materials. In the second section, we have performed heat treatments to induce the nanocrystallization of a selected composition from its amorphous precursor. There are only a few reports on the fabrication and properties of this family of magnetic alloys by gas atomization, in contrast with the vast literature dealing with melt spun ribbons. New publications about alternative compositions are necessary to delimit the boundaries within which Fe-rich amorphous and nanocrystalline powders with good magnetic properties can be produced by gas atomization.

2. Material and methods

The nominal compositions of the alloys studied in this work are: (1) $(Fe_{0.725}Si_{0.125}B_{0.150})_{96.5}Nb_{3.0}Cu_{0.5}$, (2) $([Fe_{0.725}Si_{0.125}B_{0.150}]_{0.95}P_{0.05})_{98.5}Nb_{1.0}Cu_{0.5}$, (3) $([Fe_{0.725}Si_{0.125}B_{0.150}]_{0.95}P_{0.05})_{98.25}Nb_{1.00}Cu_{0.75}$, (4) $([Fe_{0.725}Si_{0.125}B_{0.150}]_{0.95}P_{0.05})_{97.5}Nb_{2.0}Cu_{0.5}$, (5) $(Fe_{0.76}Si_{0.09}B_{0.10}P_{0.05})_{98.75}Nb_{1.00}Cu_{0.25}$, (6) $(Fe_{0.76}Si_{0.09}B_{0.10}P_{0.05})_{97.5}Nb_{2.0}Cu_{0.5}$, and (7) $(Fe_{0.76}Si_{0.09}B_{0.10}P_{0.05})_{96.5}Nb_{3.0}Cu_{0.5}$. The compositions of (1), (2), (3), and (4) are based on a ternary alloy $Fe_{0.725}Si_{0.125}B_{0.150}$ obtained with an amorphous structure via gas atomization in a previous work of the authors

[13]. Cu and Nb were added to this base composition in order to obtain a FINEMET-type alloy (sample (1)). P was also added to evaluate the influence of this element on the magnetic and thermal properties (samples (2), (3), and (4)) [14]. Compositions (5), (6), and (7) were chosen because they have a high glass forming ability (GFA) and good magnetic properties [15]. The powders of these alloys were produced via He gas atomization. The as-atomized powders were sieved to separate the particles with a size <20 μm, which is the size fraction of interest. The experimental details about the process can be found in reference [2].

Isothermal heat treatments were conducted in a conventional laboratory furnace (CARBOLITE model RHF 14/35, United Kingdom). Approximately 15 g of powder were placed in a high purity alumina tray. Before heating up the sample, the furnace chamber was purged with high purity Ar (H_2O ≤ 3 ppm, O_2 ≤ 3 ppm C_nH_m ≤ 3 ppm), which constituted the annealing atmosphere. The temperature was controlled with a thermocouple placed inside the chamber as close as possible to the powder sample. The holding time was measured from the time at which the sample reached the annealing temperature.

Differential scanning calorimetry (DSC) was used to obtain information about the enthalpy changes that the material underwent when the temperature was raised (i.e., glass transition, structural relaxation, ferro to paramagnetic transition, and crystallization). The DSC experiments were conducted in an equipment TA Instruments DSC 2920 (United States) at a heating rate of 10 K/min under an Ar atmosphere, using a powder sample of approximately 10 mg inside the copper pans.

The constituent phases were identified via X-ray diffraction (XRD). The experiments were conducted in a diffractometer Philips X´pert MRD (The Netherlands), using the characteristic wavelength of the K_α line for Cu (wavelength of 1.542 Å). The diffraction angle (2θ) varied from 25 ° to 90 ° at a scanning rate of 0.005 °/s, in steps of 0.02 ° with a holding time of 4 s at each diffraction angle. Subsequently, a higher quality XRD pattern was obtained in a diffractometer Bruker D8 Advance A25 (United States), using the same radiation and diffraction angle range, a step size of 0.02 ° in 2θ and a scan speed of 2 s/step. This higher quality pattern was used for phase quantification, applying the internal standard method, and the crystallite size was determined by performing a Rietveld analysis/refinement with the software package TOPAS V6.0.

The Rietveld method [16] allows for quantitatively determining the amount of each crystalline phase in a sample. If the sample contains an amorphous phase it cannot be quantified directly, since it does not contribute to the diffraction peaks. To quantify the weight fraction of each crystalline phase in a sample with some amorphous content, it is necessary to mix the sample with a known weight amount of a 100 % crystalline standard substance (i.e., an internal standard). In such a case, the weight percent of each phase can be calculated using the following expression:

$$X_j = \frac{X_s S_j (ZmV)_j}{S_s (ZmV)_s} \quad (1)$$

where X is the weight fraction of a given phase, S is the scale factor (as derived in a multicomponent Rietveld analysis of the powder diffraction pattern), m is the mass of the unit cell, V is the volume of the unit cell, and Z is the number of chemical formula units per unit cell. The subscript j refers to each crystalline phase in the sample and the subscript s to the internal standard. Finally, the weight fraction of the amorphous phase ($X_{amorphous}$) is calculated as:

$$X_{amorphous} = 1 - X_s - \sum_j X_j \quad (2)$$

The peak profile is a convolution of the profiles from any contribution, such as the instrument peak profile, crystallite size, microstrain (nonuniform lattice distortions, faulting, dislocations, antiphase domain boundaries, and grain surface relaxation), solid solution inhomogeneity, and temperature factors. The crystallite size calculation performed by TOPAS takes the instrumental factor into account and uses the Double-Voigt approach to estimate both the crystallite size and the microstrain from the peak broadening. This approach consists of fitting the Lorentzian and Gaussian components to the peak broadening, depending on which phenomena produces the broadening.

Thin foils were prepared using an FEI Quanta 3D FEG focused ion beam (FIB) microscope (United States) by the lift-out technique. First, a particle of approximately 20 μm was selected and a Pt line was deposited on the surface. Two stair-step FIB trenches were cut on both sides of the Pt line. Next, the specimen was further thinned to less than 1 μm in thickness and a slice of the specimen was cut free. The obtained lamella was removed using

a micromanipulator and welded with Pt to a Cu grid that was suitable for transmission electron microscopy (TEM) analysis. A final milling down to less than 100 nm was conducted by employing successively lower voltages of up to 2 kV. The obtained specimen was examined by a conventional bright-field imaging in a JEOL JEM-2100F (S)TEM microscope (Japan), operated at 200 kV with an LaB_6 filament.

The magnetic properties of the powders at room temperature were evaluated from the hysteresis loop obtained in a Quantum Design PPMS-9T (United States), system with a vibrating sample magnetometer (VSM) option Model P525. The step of the magnetic field change near the coercive field was 5 Oe. Before measuring the samples, the equipment was calibrated with a paramagnetic Dy_2O_3 standard. The correction parameters to compensate for the magnet remanence were then determined. The measurement of the paramagnetic standard demonstrates the reliability of the quantities up to units of Oe.

3. Results and discussion

3.1 *As-atomized alloys*

In this section, the microstructural and magnetic characterizations of the gas atomized alloys with particle size below 20 μm are presented. Fig. 1 shows the X-ray diffraction (XRD) patterns for this size fraction. The single, broad diffraction peak at approximately 45 ° demonstrates that the alloys are structurally amorphous. As was explained in reference [2], the cooling rate is inversely proportional to the particle size. Therefore, the production of fine powders is important for achieving a high yield of amorphous phase in gas atomization. The XRD patterns demonstrate that, for particles sizes of these compositions below 20 μm, the actual cooling rate is higher than the critical one in order to avoid nucleation of the crystalline phases.

Fig. 2 shows the DSC traces of the as-atomized alloys. Depending on the composition, between one and three main crystallization stages are observed. The beginning (T_{X1}, T_{X2}, and T_{X3}) and the maximum (T_{P1}, T_{P2}, and T_{P3}) of each crystallization peak are reported in Table 1. Fig. 2 (1) corresponds to a powder with a FINEMET-like composition, i.e., without P. As in classical alloys [17,18], it is possible to observe two separated crystallization peaks, the first one with a maximum at 574.7 °C and the second one with a maximum at 669.2 °C. It is well-known that the first one

is caused by the nanocrystallization of the α-Fe(Si) phase, whereas the second one is due to the precipitation of the Fe_2B and/or Fe_3B borides.

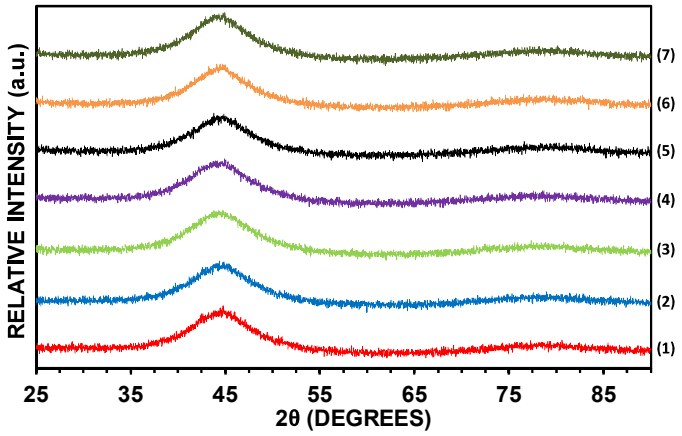

Fig. 1. X-ray diffraction patterns of gas atomized powders with particle size < 20 μm: (1) $(Fe_{0.725}Si_{0.125}B_{0.150})_{96.5}Nb_{3.0}Cu_{0.5}$, (2) $([Fe_{0.725}Si_{0.125}B_{0.150}]_{0.95}P_{0.05})_{98.5}Nb_{1.0}Cu_{0.5}$, (3) $([Fe_{0.725}Si_{0.125}B_{0.150}]_{0.95}P_{0.05})_{98.25}Nb_{1.00}Cu_{0.75}$, (4) $([Fe_{0.725}Si_{0.125}B_{0.150}]_{0.95}P_{0.05})_{97.5}Nb_{2.0}Cu_{0.5}$, (5) $(Fe_{0.76}Si_{0.09}B_{0.10}P_{0.05})_{98.75}Nb_{1.00}Cu_{0.25}$, (6) $(Fe_{0.76}Si_{0.09}B_{0.10}P_{0.05})_{97.5}Nb_{2.0}Cu_{0.5}$, and (7) $(Fe_{0.76}Si_{0.09}B_{0.10}P_{0.05})_{96.5}Nb_{3.0}Cu_{0.5}$.

Fig. 2 (2), (3), and (4) display the DSC plots for three modifications of the same $Fe_{0.725}Si_{0.125}B_{0.150}$ base alloy, with a small addition of P and a lower Nb. The main effect of these composition changes is narrowing the temperature range for crystallization. In the case of alloys with 1 at. % of Nb (Fig. 2 [2] and [3]), crystallization occurs in one stage with a peak temperature (T_{P1}) of approximately 575 °C, which indicates that a eutectic reaction is taking place [19]. The sharp peak indicates the compositional homogeneity of the crystallites precipitated during the heat treatment. When Nb is increased to 2 at. % (Fig. 2 [4]), this sharp peak is shifted to 596.8 °C (i.e., Nb delays the eutectic crystallization).

The other three alloys are chemical variations of the base composition $Fe_{0.76}Si_{0.09}B_{0.10}P_{0.05}$. These alloys exhibit two or three crystallization stages that are revealed by the DSC traces as exothermic reactions (Fig. 2 [5], [6] and [7]), suggesting a change in the crystallization kinetics. The temperature interval ΔT_P between T_{P1} and T_{P2} ($\Delta T_P = T_{P2} - T_{P1}$) is reported in Table 1. An increase in ΔT_P is favorable for promoting α-Fe(Si) precipitation as well as achieving excellent soft magnetic properties by annealing glassy precursors [9,20,21].

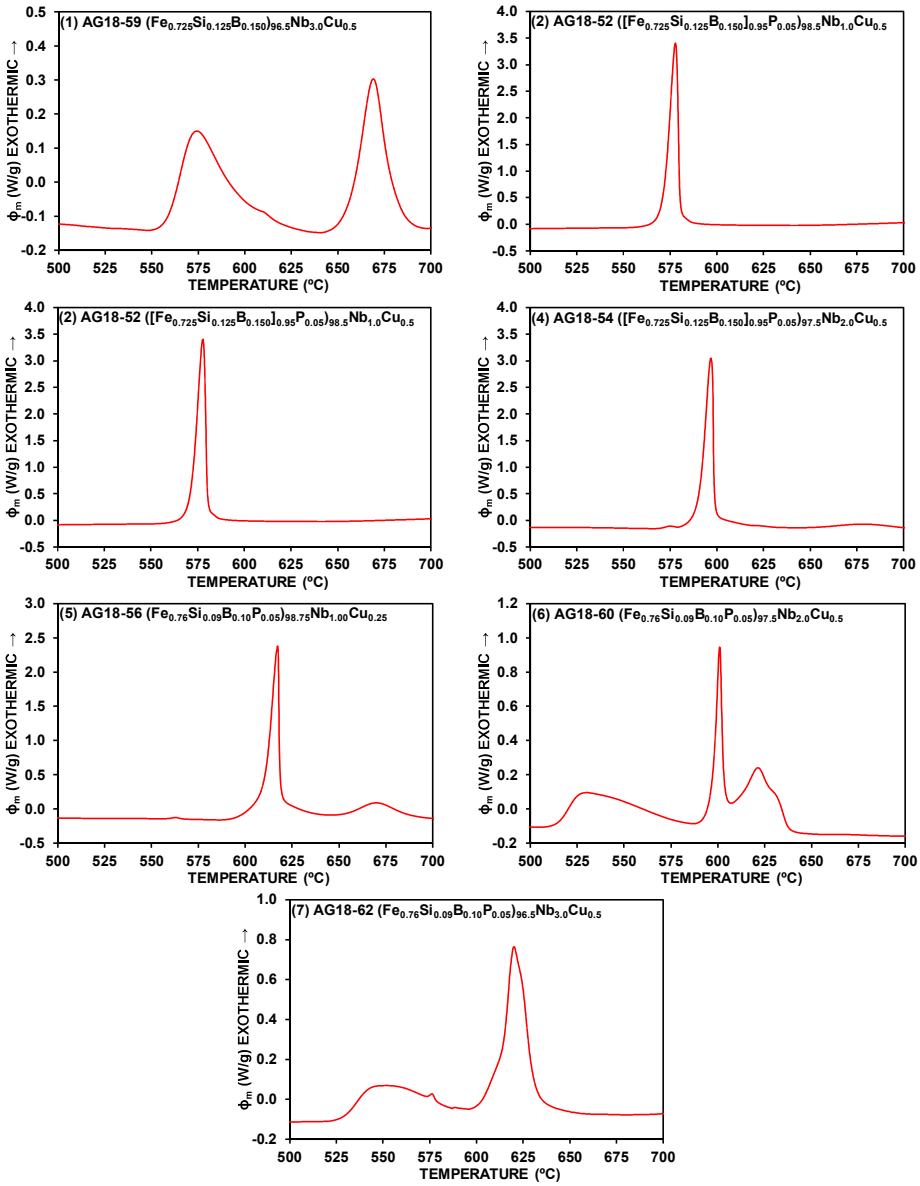

Fig. 2. DSC traces of the gas atomized powders (< 20 μm): (1) $(Fe_{0.725}Si_{0.125}B_{0.150})_{96.5}Nb_{3.0}Cu_{0.5}$, (2) $([Fe_{0.725}Si_{0.125}B_{0.150}]_{0.95}P_{0.05})_{98.5}Nb_{1.0}Cu_{0.5}$, (3) $([Fe_{0.725}Si_{0.125}B_{0.150}]_{0.95}P_{0.05})_{98.25}Nb_{1.00}Cu_{0.75}$, (4) $([Fe_{0.725}Si_{0.125}B_{0.150}]_{0.95}P_{0.05})_{97.5}Nb_{2.0}Cu_{0.5}$, (5) $(Fe_{0.76}Si_{0.09}B_{0.10}P_{0.05})_{98.75}Nb_{1.00}Cu_{0.25}$, (6) $(Fe_{0.76}Si_{0.09}B_{0.10}P_{0.05})_{97.5}Nb_{2.0}Cu_{0.5}$, and (7) $(Fe_{0.76}Si_{0.09}B_{0.10}P_{0.05})_{96.5}Nb_{3.0}Cu_{0.5}$.

Although the DSC trace of sample (5) (Fig. 2 [5], with the lowest Nb and Cu content) shows two peaks, it is surprising that the first one at 617.1 °C is sharp, whereas the second one at 669.9 °C is broad. The first one, which is similar to the peak in samples (2), (3), and (4), seems to be associated with the simultaneous precipitation of the α-Fe(Si) and $Fe_3(B,P)$ phases. The second broad peak at 669.9 °C is ascribed to the precipitation of the Fe_2B phase.

As for the compositions with higher Nb and Cu (see Fig. 2 [6] and Fig. 2 [7]), T_{P1} is approximately 30-45 °C lower and T_{P2} is approximately 50-70 °C lower than those in the FINEMET-type alloy (without P, Fig. 2 [1]). Despite the fact that the temperature interval ΔT_P is reduced from 95 to 70 °C, the gap is still large enough to only allow for precipitation of the α-Fe(Si) nanocrystals (i.e., without borides). The second peak in sample (7) could correspond to the precipitation of the Fe_2B hard magnetic phase, as in the case of sample (1). Sample (6) exhibits three crystallization peaks, which is in agreement with the data on this alloy obtained by rapid solidification [15]; the second and third peaks in this composition correspond to the crystallization of the $Fe_3(B,P)$ and Fe_2B phases, respectively [15].

There is a dependence of the crystallization behavior on the P content. The presence of P atoms could decrease the activation energy of crystallization, that is, the thermal barrier to reconstruct the atomic configuration of the atoms in the α-Fe(Si) phase. Moreover, it improves the thermal stability of the residual amorphous phase during the crystallization process, since a longer range rearrangement of the atoms is required to form the structures of phases Fe_2B and $Fe_3(B,P)$ [22]. It is noteworthy to mention that the presence of both Fe_2B and Fe_3B reveals that the crystallization of Fe_2B occurs with the formation of Fe_3B as an intermediate phase. At higher temperatures (e.g., samples heat treated at 700 °C), Fe_3B is transformed into the more stable Fe_2B phase, since this is the only stable boride in the Fe-B phase diagram [23–25].

Table 1 presents the magnetic parameters obtained from the hysteresis loop at room temperature (Fig. 3) the coercive field (H_C) and saturation magnetization (M_S) of the amorphous as-atomized alloys with particle size < 20 μm. A clear dependency with the Fe content is not observed because the presence of additional elements (P, Nb, and Cu) modifies the distance between the Fe atoms in different ways. As is well known, the characteristics of the magnetization curve in the soft magnetic amorphous alloys are predominantly governed by structural defects (see for example

reference [26]). In particular, the values of H_C are very sensitive to magnetoelastic anisotropy, which depends on the internal stresses as well as of the saturation magnetostriction coefficient (λ_s). Since λ_s increases with the Fe content (up to approximately 3 x 10^{-5}), a higher value of H_C with the Fe concentration is expected. Moreover, the lowest value of H_C in the FINEMET-type amorphous alloy, sample (1), could be related to the lower value of $\lambda_s \approx$ 1.2-1.8 x 10^{-5} reported for this alloy [27,28]. It must be noted that the values of H_C in these gas atomized alloys are larger than those reported in the same alloys obtained in the ribbon shape via melt-spinning (values of H_C approximately 0.1-0.3 Oe in the case of ribbons produced by the classical rapid solidification method). Of course, H_C is not affected by demagnetizing effects (magnetization at the applied magnetic field of H_C is zero); therefore, larger values of H_C in gas atomized alloys should be mainly attributed to a particle surface effect. The main source of low coercivity in the case of ribbons is the magnetoelastic anisotropy via coupling with the internal stresses, which can be negligible against the mentioned surface effect.

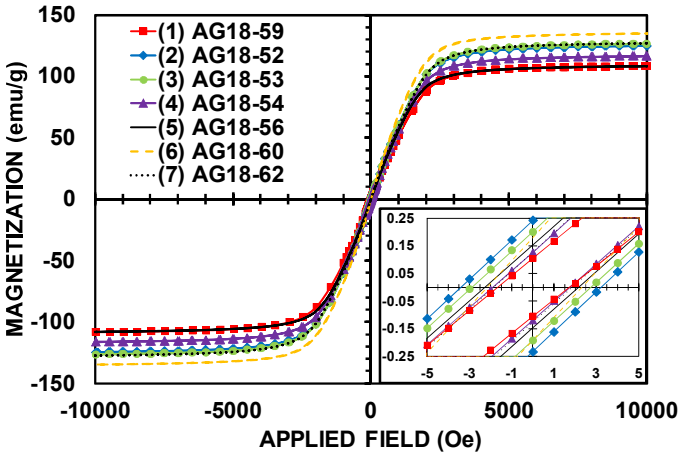

Fig. 3. Hysteresis loop measured at room temperature of gas atomized powders with particle size < 20 μm: (1) $(Fe_{0.725}Si_{0.125}B_{0.150})_{96.5}Nb_{3.0}Cu_{0.5}$, (2) $([Fe_{0.725}Si_{0.125}B_{0.150}]_{0.95}P_{0.05})_{98.5}Nb_{1.0}Cu_{0.5}$, (3) $([Fe_{0.725}Si_{0.125}B_{0.150}]_{0.95}P_{0.05})_{98.25}Nb_{1.00}Cu_{0.75}$, (4) $([Fe_{0.725}Si_{0.125}B_{0.150}]_{0.95}P_{0.05})_{97.5}Nb_{2.0}Cu_{0.5}$, (5) $(Fe_{0.76}Si_{0.09}B_{0.10}P_{0.05})_{98.75}Nb_{1.00}Cu_{0.25}$, (6) $(Fe_{0.76}Si_{0.09}B_{0.10}P_{0.05})_{97.5}Nb_{2.0}Cu_{0.5}$, and (7) $(Fe_{0.76}Si_{0.09}B_{0.10}P_{0.05})_{96.5}Nb_{3.0}Cu_{0.5}$. The insert shows the hysteresis loop magnified at the origin of coordinates.

Table 1. Thermal and magnetic parameters of gas atomized alloys with particle size < 20 μm.

N°	Experiment	Composition	T_C (°C)	First peak		Second peak		ΔT_P (°C)	Third peak		H_C (Oe)	M_S (emu/g)
				T_{X1} (°C)	T_{P1} (°C)	T_{X2} (°C)	T_{P2} (°C)		T_{X3} (°C)	T_{P3} (°C)		
1	AG18-59	$(Fe_{0.725}Si_{0.125}B_{0.150})_{96.5}Nb_3Cu_{0.5}$	334.6	558.3	574.7	655.7	669.2	94.5	---	---	1.71	112
2	AG18-52	$([Fe_{0.725}Si_{0.125}B_{0.150}]_{0.95}P_{0.05})_{98.5}Nb_{1.0}Cu_{0.5}$	336.6	571.2	577.7	---	---	---	---	---	3.32	128
3	AG18-53	$([Fe_{0.725}Si_{0.125}B_{0.150}]_{0.95}P_{0.05})_{98.25}Nb_{1.0}Cu_{0.75}$	343.9	569.3	575.3	---	---	---	---	---	2.83	130
4	AG18-54	$([Fe_{0.725}Si_{0.125}B_{0.150}]_{0.95}P_{0.05})_{97.5}Nb_2Cu_{0.5}$	304.3	590.3	596.8	---	---	---	---	---	1.84	121
5	AG18-56	$(Fe_{0.76}Si_{0.09}B_{0.10}P_{0.05})_{98.75}Nb_{1.00}Cu_{0.25}$	267.9	609.8	617.1	653.1	669.9	52.8	---	---	2.22	113
6	AG18-60	$(Fe_{0.76}Si_{0.09}B_{0.10}P_{0.05})_{97.5}Nb_2Cu_{0.5}$	336.1	514.6	529.5	596.6	600.9	71.4	603.2	621.3	2.24	139
7	AG18-62	$(Fe_{0.76}Si_{0.09}B_{0.10}P_{0.05})_{96.5}Nb_3Cu_{0.5}$	293.9	529.2	547.7	611.9	620.2	72.6	---	---	1.86	132

3.2 *Nanocrystalline alloys*

Sample (6) with a composition of $(Fe_{0.76}Si_{0.09}B_{0.10}P_{0.05})_{97.5}Nb_{2.0}Cu_{0.5}$ has been selected to develop a nanocrystalline alloy for two reasons. First, it exhibits the highest value of M_S. Second, its first peak of crystallization is clearly separated from the second one, which makes possible to develop a fine nanocrystalline structure by heat treating that is comparable to the structure widely reported in the classical FINEMET and similar compositions [9,20]. Annealing of the alloy was conducted in the supercooled liquid region, between the glass transition temperature (T_g = 469.4 °C) and the crystallization temperature (T_{X1}), and at the first peak temperature (T_{P1}) for 30 and 60 min. Fig. 4 shows the DSC curves of the non-annealed sample and the annealed ones under different conditions. It is observed that the first peak disappears in the samples that are heat treated at 530 °C. In contrast, the heat treatment in the supercooled liquid region does not change the first peak, which indicates that the heat treatment mainly produces structural relaxation or the nucleation of nanograins with a very small size (a few nanometers). Additionally, the other two peaks are approximately maintained with the same shape, size, and position as those in the non-annealed sample, independent of the annealing temperature and time, showing that the borides do not precipitate.

The Curie temperature (T_C) obtained from the DSC traces is listed in Table 2. T_C is ascribed to the magnetic transition (ferro to paramagnetic) of the amorphous matrix. An increase in T_C is observed with the heat treatment at 480 °C (from 336.1 °C in the non-annealed sample to 352.1 °C in the annealed one), which can be associated with a decrease in the Fe-Fe atomic distances due to the structural relaxation [29,30]. Structural relaxation occurs when annealing below or slightly above the glass transition

temperature (T_g), which dramatically affects the physical properties of the precursor amorphous alloy. This annealing causes a release of the internal stresses, a reduction of the free volume, and changes in the interatomic distances. Therefore, small clusters are formed in a solute enriched amorphous phase [13,31,32]. As is well known, this process is inevitably related to the topological and chemical variation of the local structure of cluster units proposed for metallic glasses [33–35].

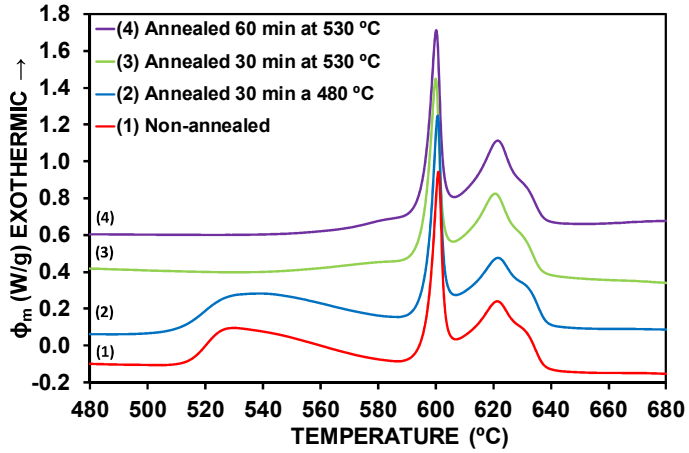

Fig. 4. DSC traces of the $(Fe_{0.76}Si_{0.09}B_{0.10}P_{0.05})_{97.5}Nb_{2.0}Cu_{0.5}$ powder in different conditions: (1) non-annealed, (2) annealed at 480 °C (supercooled liquid region) for 30 min, (3) annealed at 530 °C (peak temperature) for 30 min, and (4) annealed at 530 °C (peak temperature) for 60 min.

Table 2. Thermal, microstructural, and magnetic properties of non-annealed and annealed $(Fe_{0.76}Si_{0.09}B_{0.10}P_{0.05})_{97.5}Nb_{2.0}Cu_{0.5}$ powders with particle size <20 μm.

N°	Annealing		T_C (°C)	First peak		Second peak		Third peak		X_D (%)	D (nm)	H_C (Oe)	M_S (emu/g)
	Temperature (°C)	Time (min)		T_{X1} (°C)	T_{P1} (°C)	T_{X2} (°C)	T_{P2} (°C)	T_{X3} (°C)	T_{P3} (°C)				
1	Non-annealed		336.1	514.6	529.5	596.6	600.9	603.2	621.3			2.24	139
2	480	30	352.1	512.0	534.6	596.3	600.8	604.9	621.5			0.94	146
3	530	30	---	595.4	600.0	605.6	620.8	---	---	23	16	0.69	144
4	530	60	---	595.4	600.2	606.8	621.6	---	---	46	17	0.81	145

X_D: Weight percent of the crystalline phase; D: Average size of the nanocrystals; H_C: Coercivity; M_S: Saturation magnetization.

The XRD patterns of the as-atomized and annealed $(Fe_{0.76}Si_{0.09}B_{0.10}P_{0.05})_{97.5}Nb_{2.0}Cu_{0.5}$ samples are plotted in Fig. 5. It is evident that all the samples exhibit a broad peak at approximately $2\theta = 45°$ due to the presence of an amorphous phase. The non-annealed sample and the

sample annealed at 480 °C (numbers 1 and 2 in Fig. 5) only display this typical halo, proving that they are amorphous except for perhaps a negligible nanocrystallization in the annealed sample. In contrast, the samples that were annealed at 530 °C (number 3 and 4 in Fig. 5) exhibit clear crystalline peaks, confirming that the first crystallization stage of this composition (Fig. 4) belongs to the α-Fe(Si) phase. The Rietveld method, which was applied to the entire diffraction pattern, gave an average grain size of approximately 17 nm and approximately 46 wt. % of the crystalline phase in the sample that was annealed for 60 min (see Table 2). It has been widely reported that these microstructural parameters are a prerequisite for developing the soft magnetic behavior in the partial nanocrystalline alloys.

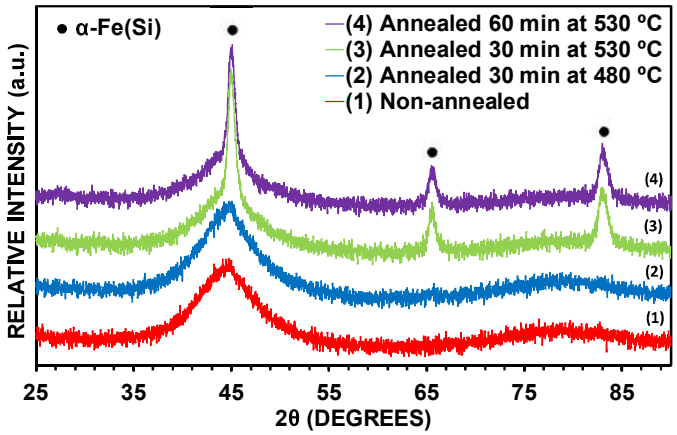

Fig. 5. X-ray diffraction patterns of the as-atomized and annealed $(Fe_{0.76}Si_{0.09}B_{0.10}P_{0.05})_{97.5}Nb_{2.0}Cu_{0.5}$ powders. (1) non-annealed, (2) annealed at 480 °C (supercooled liquid region) for 30 min, (3) annealed at 530 °C (peak temperature) for 30 min, and (4) annealed at 530 °C (peak temperature) for 60 min.

The amorphous structure of the non-annealed sample and the nanocrystalline structure of the samples annealed at 530 °C are further confirmed by TEM observations. Fig. 6 shows the bright field TEM images of the composition $(Fe_{0.76}Si_{0.09}B_{0.10}P_{0.05})_{97.5}Nb_2Cu_{0.5}$ when it is both non-annealed and annealed at 530 °C for 30 and 60 min. The selected-area diffraction patterns, included as inserted images, display the continuous rings produced by the amorphous structure in the non-annealed sample (Fig. 6 [1]). In the annealed samples (Fig. 6 [2] and [3]), the continuous rings produced by the amorphous matrix are displayed, along with some spots coming from the randomly oriented α-Fe(Si) nanocrystals. The alloy exhibits a very homogeneous microstructure with a narrow crystallite size distribution. Most of the crystallites have a size below 20 nm, which is

compatible with the XRD measurements. This kind of structure is typical of nanocrystalline alloys obtained by homogeneous nucleation from an amorphous precursor upon annealing, as in FINEMET-type alloys [24,36].

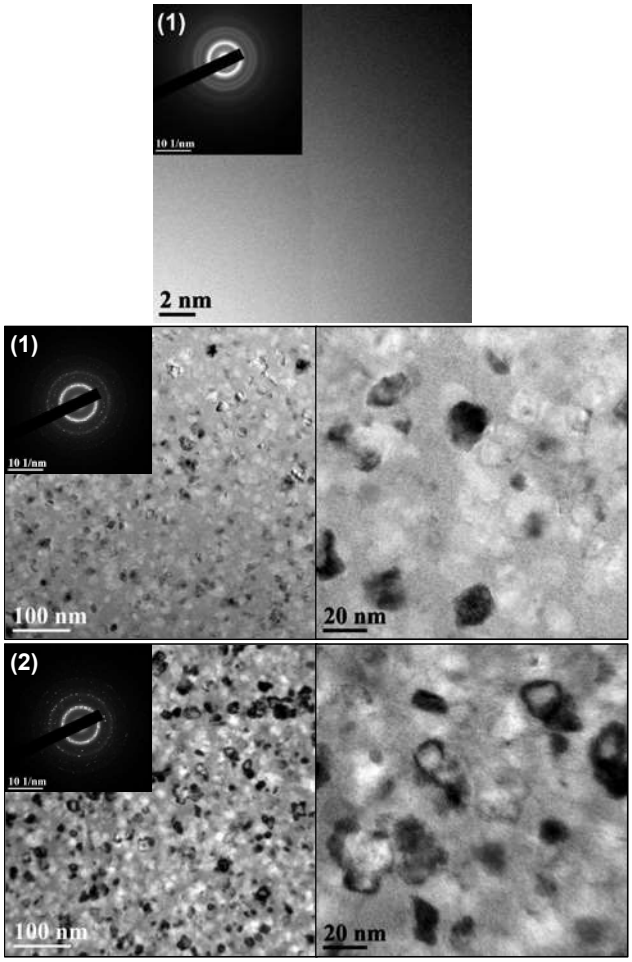

Fig. 6. Bright field TEM images of $(Fe_{0.76}Si_{0.09}B_{0.10}P_{0.05})_{97.5}Nb_{2.0}Cu_{0.5}$ alloy: (1) non-annealed sample, (2) annealed sample at 530 °C (peak temperature) for 30 min, and (3) annealed sample at 530 °C (peak temperature) for 60 min.

The magnetic properties of the non-annealed and annealed samples, as obtained from the hysteresis loops at room temperature, are presented in Table 2. Annealing the sample in the supercooled liquid region produced a significant reduction in H_C due to the relaxation of internal stresses [37]. Surprisingly, the saturation magnetization increased, which could be due to

the change in the average interatomic distance between the Fe atoms arising from vacancies elimination and the formation of Fe-Si rich clusters [10].

Variations in the saturation magnetization, M_S, and coercive field, H_C, when annealing at 530 °C can be understood in terms of the magnetic properties of biphasic nanocrystalline alloys [21,38]. The changes in M_S were successfully explained in reference [38] as the addition of two contributions arising from the relative volume fractions of the crystalline phase ($M_S{}^{\alpha-\mathrm{Fe(Si)}}$) and the residual amorphous matrix ($M_S{}^{am}$), which allows for:

$$M_S = v_D\, M_S{}^{\alpha-Fe(Si)} + (1 - v_D)\, M_S{}^{am} \quad (3)$$

where v_D is the volume fraction of the nanograins. It is important to note that M_S, at room temperature, is rather similar for the amorphous relaxed sample (annealed at 480 °C) and for the nanocrystalline alloys (annealed at 530 °C), indicating that $M_S{}^{\alpha-\mathrm{Fe(Si)}} \approx M_S{}^{am}$ (relaxed). The situation is very different in other alloys; for example, in Fe-Zr-B-Cu alloys, the contribution of the α–Fe(Si) nanograins is much larger than the contribution of the amorphous phase, for which $T_C \approx 80$ °C and M_S is low [39].

H_C is significantly lower in the nanocrystalline samples than in the non-annealed one (see Table 2). This extreme magnetic softening is a consequence of the size and volume fraction of the nanocrystallites. The exchange coupling of crystallites occurs because Nb is preventing classical grain coarsening. Moreover, it is worthy to mention that the nanocrystalline samples are softer than the amorphous alloy relaxed at 480 °C. The decrease in H_C with the nanocrystallization depends on the effective magnetic anisotropy [40] through the expression:

$$H_C = P_c\, \frac{\langle K \rangle}{J_s} \approx P_c\, \frac{K_1^4\, D^6}{J_s\, A^3} \quad (4)$$

where P_c is a dimensionless factor, $\langle K \rangle$ is the average magnetic anisotropy, J_s is the saturation polarization, $K_1 \approx 8$ kJ/m^3 is the magnetocrystalline anisotropy of the nanograins, $A_C \approx 10^{-11}$ J/m is the exchange constant of Fe, and D is the nanograins diameter. Local anisotropies, mainly coming from the nanograins (K_1), are randomly averaged within the ferromagnetic correlation exchange length (L_{ex}) for the small nanocrystals embedded homogeneously in the amorphous matrix. This averaging process of magnetocrystalline anisotropy involves a number of exchange coupled

grains within the volume L_{ex}^3 [40]. As a result, in the framework of the random anisotropy model initially proposed for amorphous alloys [41] and extended later to nanocrystalline alloys [40], the anisotropy of the nanograins is averaged out. This makes the effective anisotropy very low, leading to a decrease of H_C. This situation is favorable for achieving good soft magnetic properties in the case of nanocrystalline materials [12].

Compared to their amorphous counterparts, the corresponding nanocrystallized alloys typically exhibit a lower λ_s, a higher effective permeability (μ_e), and a higher B_s [15]. The magnetic properties (saturation magnetization and magnetostriction) of FINEMET nanocrystalline alloys have been modeled as the algebraic sum of the contributions arising from both constituent phases [38], although some discrepancies suggest the relevance of another contribution from the surface region of the nanograins [42,43]. A precise evaluation of this effect is complex due to the compositional gradient at the interphase.

4. Conclusions

a) The production of new compositions of Fe-Si-B-P-Nb-Cu powders by gas atomization with amorphous structure when the particle size is below 20 μm is demonstrated.

b) Depending on the composition of the alloy, crystallization took place in one, two or three stages. The $(Fe_{0.76}Si_{0.09}B_{0.10}P_{0.05})_{97.5}Nb_{2.0}Cu_{0.5}$ composition showed a temperature gap between the first and the second stages of approximately 70 °C, which is wide enough to allow for only α-Fe(Si) nanocrystals to precipitate (i.e., without borides).

c) Annealing this alloy in the supercooled liquid region (at 480 °C) mainly produced structural relaxation, yielding a significant reduction of the coercive field (from 2.24 to 0.94 Oe) and an increment of the saturation magnetization (from 139 to 146 emu/g).

d) Annealing at the first peak temperature (at 530 °C), produced a microstructure formed by α-Fe(Si) nanocrystals of approximately 16-17 nm in diameter, embedded homogeneously in an amorphous matrix. This material exhibited better soft magnetic properties than the amorphous precursor (saturation magnetization of 144 emu/g and a coercive field of 0.69 Oe in the sample annealed for 30 min, and 145 emu/g and 0.81 Oe in the sample annealed for 60 min).

e) The saturation magnetization at room temperature is rather similar for the amorphous relaxed sample (annealed at 480 °C) and for the nanocrystalline alloys (annealed at 530 °C), indicating that both the crystalline and the relaxed amorphous phases have similar saturation magnetization.

f) The very low coercivity of the nanocrystalline alloy is explained by the random averaging of the magnetocrystalline anisotropy of the α-Fe(Si) nanocrystals within a larger ferromagnetic correlation exchange volume.

Acknowledgements

Author Kenny L. Alvarez thanks to Becas Chile (CONICYT) for the financial support. The authors thank SGIker of UPV/EHU for technical and human support. This work was supported by the European Commission (ERDF and ESF programs). Authors M. Ipatov, L. Domínguez, and J. Gonzalez acknowledge the University of the Basque Country for the support under the scheme "Ayudas a Grupos Consolidados" (Ref. PPG17/35).

References

[1] X. Li, A. Makino, H. Kato, A. Inoue, T. Kubota, $Fe_{76}Si_{9.6}B_{8.4}P_6$ glassy powder soft-magnetic cores with low core loss prepared by spark-plasma sintering, Mater. Sci. Eng. B 176 (2011) 1247–1250, https://doi.org/10.1016/j.mseb.2011.06.017.

[2] K.L. Alvarez, J.M. Martín, M. Ipatov, J. Gonzalez, Soft magnetic amorphous alloys (Fe-rich) obtained by gas atomisation technique, J. Alloys Compd. 735 (2018) 2646–2652, https://doi.org/10.1016/j.jallcom.2017.11.272.

[3] A. García-Escorial, M. Lieblich, A. Hernando, A. Aragón, P. Marín, Temperature dependence of the coercive field of gas atomized $Fe_{73.5}Si_{13.5}B_9Nb_3Cu_1$, J. Alloys Compd. 536 (2012) S300–S303, https://doi.org/10.1016/j.jallcom.2011.11.015.

[4] T. Suzuki, P. Sharma, L. Jiang, Y. Zhang, A. Makino, Fabrication and properties of under 10 μm sized amorphous powders of high B_s soft magnetic alloy for high-frequency applications, IEEE Trans. Magn. 54 (2018) 2801705, https://doi.org/10.1109/TMAG.2018.2833138.

[5] L. Chang, L. Xie, M. Liu, Q. Li, Y. Dong, C. Chang, X.M. Wang, A. Inoue, Novel Fe-based nanocrystalline powder cores with excellent magnetic properties produced using gas-atomized powder, J. Magn. Magn. Mater. 452 (2018) 442–446, https://doi.org/10.1016/j.jmmm.2017.12.049.

[6] G. Sarriegui, J.M. Martín, M. Ipatov, A.P. Zhukov, J. Gonzalez, Magnetic properties of NdFeB alloys obtained by gas atomization technique, IEEE Trans. Magn. 54 (2018) 2103105, https://doi.org/10.1109/TMAG.2018.2839906.

[7] A.J. Yule, J.J. Dunkley, Atomization of Melts for Powder Production and Spray

Deposition, Oxford University Press, Oxford, UK, 1994.

[8] Y. Zhang, P. Sharma, A. Makino, Fe-Rich Fe-Si-B-P-Cu powder cores for high-frequency power electronic applications, IEEE Trans. Magn. 50 (2014) 2006804, https://doi.org/10.1371/journal.pcbi.1000729.

[9] Y. Yoshizawa, S. Oguma, K. Yamauchi, New Fe-based soft magnetic alloys composed of ultrafine grain structure, J. Appl. Phys. 64 (1988) 6044–6046, https://doi.org/10.1063/1.342149.

[10] M. Ohta, Y. Yoshizawa, Magnetic properties of nanocrystalline $Fe_{82.65}Cu_{1.35}Si_xB_{16-x}$ alloys (x=0-7), Appl. Phys. Lett. 91 (2007) 7–10, https://doi.org/10.1063/1.2769956.

[11] Y.Y. Sun, M. Song, X.Z. Liao, Y.H. He, Mechanical properties of a FeCuSiB alloy with amorphous and/or crystalline structures, J. Alloys Compd. 509 (2011) 6603–6608, https://doi.org/10.1016/j.jallcom.2011.03.103.

[12] G. Herzer, Modern soft magnets: Amorphous and nanocrystalline materials, Acta Mater. 61 (2013) 718–734, https://doi.org/10.1016/j.actamat.2012.10.040.

[13] K.L. Alvarez, J.M. Martin, M. Ipatov, L. Dominguez, J. Gonzalez, Magnetic properties of annealed amorphous $Fe_{72.5}Si_{12.5}B_{15}$ alloy obtained by gas atomization technique, IEEE Trans. Magn. 54 (2018) 2002405, https://doi.org/10.1109/TMAG.2018.2839258.

[14] A.D. Wang, H. Men, B.L. Shen, G.Q. Xie, A. Makino, A. Inoue, Effect of P on crystallization behavior and soft-magnetic properties of $Fe_{83.3}Si_4Cu_{0.7}B_{12-X}P_X$ nanocrystalline soft-magnetic alloys, Thin Solid Films 519 (2011) 8283–8286, https://doi.org/10.1016/j.tsf.2011.03.110.

[15] Z. Li, A. Wang, C. Chang, Y. Wang, B. Dong, S. Zhou, FeSiBPNbCu alloys with high glass-forming ability and good soft magnetic properties, Intermetallics 54 (2014) 225–231, https://doi.org/10.1016/j.intermet.2014.06.010.

[16] G. Will, Powder Diffraction: the Rietveld Method and the Two Stage Method to Determine and Refine Crystal Structures from Powder Diffraction Data, Springer, Berlin, Heidelberg, Germany, 2016.

[17] L.K. Varga, É. Bakos, É. Kisdi-Koszó, É. Zsoldos, L.F. Kiss, Time and temperature dependence of nanocrystalline structure formation in a Finemet-type amorphous alloy, J. Magn. Magn. Mater. 133 (1994) 280–282, https://doi.org/10.1016/0304-8853(94)90546-0.

[18] A. Serebryakov, A. Gurov, N. Novokhatskaya, Crystal nucleation in FINEMET-type alloys as evidenced by calorimetric measurements, Mater. Sci. Eng. A 203 (1995) L10–L12, https://doi.org/10.1016/0921-5093(95)09985-9.

[19] C. Suryanarayana, A. Inoue, Bulk Metallic Glasses, CRC/Taylor & Francis, US, 2011.

[20] A. Makino, A. Inoue, T. Masumoto, Nanocrystalline soft magnetic Fe-M-B (M=Zr, Hf, Nb) alloys produced by crystallization of amorphous phase, Mater. Trans. JIM 36 (1995) 924–938, https://doi.org/10.2320/matertrans1989.36.924.

[21] G. Herzer, Grain structure and magnetism of nanocrystalline ferromagnets, IEEE Trans. Magn. 25 (1989) 3327–3329, https://doi.org/10.1109/20.42292.

[22] A. Wang, C. Zhao, H. Men, A. He, C. Chang, X. Wang, R.W. Li, Fe-based amorphous alloys for wide ribbon production with high B_s and outstanding amorphous forming ability, J. Alloys Compd. 630 (2015) 209–213, https://doi.org/10.1016/j.jallcom.2015.01.056.

[23] V.A. Blagojević, M. Vasić, B. David, D.M. Minić, N. Pizúrová, T. Žák, D.M. Minić, Microstructure and functional properties of $Fe_{73.5}Cu_1Nb_3Si_{15.5}B_7$ amorphous alloy, Mater. Chem. Phys. 145 (2014) 12–17, https://doi.org/10.1016/j.matchemphys.2013.10.040.

[24] L. Cui, H. Men, A. Makino, T. Kubota, K. Yubuta, M. Qi, A. Inoue, Effect of Cu and P on the crystallization behavior of Fe-Rich hetero-amorphous FeSiB alloy, Mater. Trans. 50 (2009) 2515–2520, https://doi.org/10.2320/matertrans.M2009206.

[25] M.G. Poletti, L. Battezzati, Assessment of the ternary Fe-Si-B phase diagram, Calphad 43 (2013) 40–47, https://doi.org/10.1016/j.calphad.2013.08.001.

[26] H. Kronmüller, Micromagnetism and microstructure of amorphous alloys (invited), J. Appl. Phys. 52 (1981) 1859–1864, https://doi.org/10.1063/1.329552.

[27] Y. Yoshizawa, Y. Bizen, S. Arakawa, Magnetic properties of Fe-Cu-Nb-Si-B nanocrystalline alloys with low magnetostriction, Mater. Sci. Eng. A 181–182 (1994) 871–875, https://doi.org/10.1016/0921-5093(94)90759-5.

[28] Y. Yoshizawa, K. Yamauchi, Fe-based soft magnetic alloys composed of ultrafine grain structure, Mater. Trans. JIM 31 (1990) 307–314.

[29] J.S. Blázquez, S. Lozano-Pérez, A. Conde, Enthalpy and Curie temperature relaxation effects in FeSiB–CuNb alloys prepared at different quenching rates, Mater. Lett. 45 (2000) 246–250, https://doi.org/10.1016/S0167-577X(00)00113-0.

[30] Y.-N. Chen, T. Egami, Effect of annealing on the Curie temperature of amorphous alloys, J. Appl. Phys. 50 (1979) 7615–7617, https://doi.org/10.1063/1.326862.

[31] E. V. Kaevitser, S.D. Kaloshkin, B. V. Jalnin, V. V. Tcherdyntsev, Y. V. Baldokhin, The study of structural relaxation kinetics in amorphous alloy $Fe_{73.5}Nb_3Cu_1Si_{13.5}B_9$ using Curie temperature measurements, Mater. Sci. Eng. A 375–377 (2004) 683–687, https://doi.org/10.1016/j.msea.2003.10.084.

[32] D. Srolovitz, T. Egami, V. Vitek, Radial distribution function and structural relaxation in amorphous solids, Phys. Rev. B. 24 (1981) 6936–6944, https://doi.org/10.1103/PhysRevB.24.6936.

[33] J. Dai, Y.G. Wang, X.F. Miao, L. Yang, G.Q. Guo, G.T. Xia, Atomic-scale mechanisms of annealing-induced coercivity modification in metallic glass, J. Mater. Sci. 51 (2016) 8655–8662, https://doi.org/10.1007/s10853-016-0125-z.

[34] L. Zhu, Y.G. Wang, S. Lan, X.L. Wang, C.Y. Lu, X.B. Zhai, Y. Meng, Structural relaxation in a Fe-based metallic glass: changes in local structure and role of heterogeneity, Intermetallics 103 (2018) 72–77, https://doi.org/10.1016/j.intermet.2018.10.007.

[35] T. Egami, Structural relaxation in amorphous alloys - compositional short range ordering, Mater. Res. Bull. 13 (1978) 557–562, https://doi.org/10.1016/0025-5408(78)90178-2.

[36] Y.R. Zhang, R. V. Ramanujan, Microstructural observations of the crystallization of amorphous Fe–Si–B based magnetic alloys, Thin Solid Films 505 (2006) 97–102, https://doi.org/10.1016/j.tsf.2005.10.016.

[37] N. He, L. Song, W. Xu, J. Huo, J.Q. Wang, R.W. Li, The evolution of relaxation modes during isothermal annealing and its influence on properties of Fe-based metallic glass, J. Non-Cryst. Solids 509 (2019) 95–98, https://doi.org/10.1016/j.jnoncrysol.2018.12.035.

[38] J. González, Magnetic properties arising from two additive contributions in soft magnetic nanocrystalline alloys, Appl. Phys. Lett. 85 (2004) 5944–5946, https://doi.org/10.1063/1.1833583.

[39] K. Suzuki, A. Makino, A. Inoue, T. Masumoto, Soft magnetic properties of nanocrystalline bcc Fe-Zr-B and Fe-M-B-Cu (M=transition metal) alloys with high saturation magnetization (invited), J. Appl. Phys. 70 (1991) 6232–6237, https://doi.org/10.1063/1.350006.

[40] G. Herzer, Grain size dependence of coercivity and permeability in nanocrystalline ferromagnets, IEEE Trans. Magn. 26 (1990) 1397–1402, https://doi.org/10.1109/20.104389.

[41] R. Alben, J.J. Becker, M.C. Chi, Random anisotropy in amorphous ferromagnets, J. Appl. Phys. 49 (1978) 1653–1658, https://doi.org/10.1063/1.324881.

[42] A. Ślawska-Waniewska, M. Pont, F.J. Lázaro, J.L. García, P. Nowicki, J.S. Munoz, AC susceptibility in amorphous and nanocrystalline FeZrB alloys, J. Magn. Magn. Mater. 140–144 (1995) 453–454, https://doi.org/10.1016/0304-8853(94)01235-0.

[43] T. Szumiata, R. Zuberek, J. Gonzalez, A. Ślawska-Waniewska, H. Szymczak, Model of surface magnetostriction in nanostructured materials, J. Magn. Magn. Mater. 203 (1999) 262–264, https://doi.org/10.1016/S0304-8853(99)00270-X.

Journal of Magnetism and Magnetic Materials 501 (2020) 166457

Contents lists available at ScienceDirect

Journal of Magnetism and Magnetic Materials

journal homepage: www.elsevier.com/locate/jmmm

Novel Fe-based amorphous and nanocrystalline powder cores for high-frequency power conversion

Kenny L. Alvarez [a, b, *], H. A. Baghbaderani [c], José Manuel Martín [a], Nerea Burgos [a], Mihail Ipatov [d], Zoran Pavlovic [c], Paul McCloskey [c], Ansar Masood [c], Julian Gonzalez [e]

[a] *CEIT-IK4 and Tecnun (University of Navarra), P° Manuel de Lardizábal 15, 20018, San Sebastián, Spain*

[b] *Escuela de Ingeniería Mecánica, Pontificia Universidad Católica de Valparaíso, Av. Brasil 2950, Valparaíso, Chile*

[c] *Tyndall National Institute, University College Cork, Lee Maltings Complex, Dyke Parade, T12R5CP, Cork, Ireland*

[d] *SGIker (Magnetic Measurements), University of the Basque Country, Av. Tolosa 72, 20018, San Sebastián, Spain*

[e] *Department Materials Physics, Faculty of Chemistry, University of the Basque Country, P° Manuel de Lardizábal 3, 20018, San Sebastián, Spain*

Abstract

The present work demonstrates the high-frequency core loss performance of Fe-based amorphous and nanocrystalline powder cores, initially produced by gas atomised powder, consolidated using sieved particles ≤ 20 μm, and isolated by a precise insulating layer of polymer to limit the inter- and intra-particle eddy currents to attain enhanced performance. The large glass forming ability (GFA) of the gas atomised powder, reflected by different glass forming instruments, such as the supercooled region (ΔT_X = 54 °C) and the reduced glass transition temperature (T_{rg} = 0.56), is consistent with the substantial amorphisation capability of the alloy. To the best of our knowledge, this is the first-ever report to reveal a large ΔT_X in the Finemet-type alloy powders, an essential parameter to gas-atomise the amorphous powders with significantly lower cooling rates compared to the melt-spun ribbons. Further, subsequent annealing of the amorphous powders, between the exothermic events guided by differential scanning calorimetry (DSC), lead to the growth of a fine nanocrystalline structure of grains ≤ 15 nm, thanks to the positive enthalpy of mixing of Cu with the constituents to act as a nucleation agent, to retain the excellent soft magnetic properties. The DC soft magnetic properties of the powders were

* Corresponding author Tel.: + 34 943 212 800
Email address: kalvarez@ceit.es/kenny.alvarez@pucv.cl (K. L. Alvarez).
https://doi.org/10.1016/j.jmmm.2020.166457

significantly improved on thermal annealing, confirmed by hysteretic loops, quantified by reduced coercivity H_C < 1 Oe of annealed powder at < 575 °C, and attributed to the reduced magnetoelastic contribution due to zero/near-zero magnetostriction anisotropy, attained due to the homogenous nanocrystalline structure. The amorphous and nanocrystalline powder cores, consolidated by compression moulding, show ultra-high loss performance, due to the ultra-low coercivity attained on nanocrystallisation, and negligible eddy currents loss, owning to efficient insulation of small particles, for high-frequency power conversion applications, such as voltage regulator (VR), and resonant converters, in automotive industry and data storage centres.

Keywords: Gas atomization, amorphous and nanocrystalline powders, powder cores, core loss, high-frequency.

1. Introduction

The high-saturation flux density (B_s > 1.5 T), ultra-low coercivity (H_c < 1 A/m) and high-permeability ($\mu_r > 10^5$) of amorphous and nanocrystalline materials, as compared to soft-ferrites (B_s < 0.5 T), makes them a potential candidate for device miniaturisation in high-frequency power converters, such as voltage regulator (VR) and resonant converters, for applications in automotive industry and data storage centres [1,2]. Amorphous and nanocrystalline alloys are generally produced in melt-spun ribbon form, well investigated for their soft magnetic properties, and commercially available for low-frequency power conversion. However, as the device operating frequency (f) approaches MHz range, the eddy current loss (P_{ec} α f^2) abruptly increases, as compared to the hysteresis loss (P_h α f), and consequently, the total core loss (P_{CV}) is dominated by P_{ec} at f > 100 kHz [3]. The large P_{ec} significantly deteriorates the soft magnetic properties, resulting in a substantial amount of joule heating, that restricts the device design freedom, and hence, limits the high flux concentration advantage of amorphous and nanocrystalline materials for high-frequency power applications [4]. To overcome the challenge of eddy current loss at MHz switching frequencies, magnetic cores made by insulated amorphous and nanocrystalline powders are one of the possible solutions, where inter-particle eddy currents can be limited using insulated particles. The efficiency of magnetic cores can be further enhanced if ultra-small powder particles (≤ 20 μm) are used to avoid the eddy currents inside insulated particles [5–7].

Soft magnetic amorphous powders are generally produced by gas atomisation which emerged as a novel route for bulk scale amorphous powder production to form complex geometries using different consolidation techniques and hence, provides a unique solution to overcome the intrinsic problem of low glass forming ability (GFA) of amorphous metals

to produce in bulk dimensions [8–10]. The gas atomisation consists of breaking a metal stream into droplets using a high-velocity gas flow and is a well industrialised mass production method [11]. The high velocity of the gas and the small diameter of the droplets (microns range) allow rapid solidification of the melt with reasonably high cooling rates to produce amorphous powders [12,13]. However, if GFA of the alloys, which is a measure of critical cooling rates to produce alloys into amorphous form, is not large enough, it is challenging to produce amorphous powders [14]. The production of amorphous metal powders by gas atomisation, while retaining their excellent soft magnetic properties, is rather a new area of the research and hence, provides a potential route to utilise this novel class of materials for a broader range of applications, including high-frequency power conversion [15].

The purpose of the present work is manyfold; it demonstrates the production of amorphous powders by gas atomisation, reveals the high amorphisation capability of the alloy powders, shows the grain growth mechanisms of nanocrystallisation, and correlates the structural and soft magnetic properties. Finally, it demonstrates the high-frequency core loss mechanisms of amorphous and nanocrystalline powder cores, consolidated by compression moulding, using precisely isolated ultra-small (≤ 20 μm) powders to overcome the inter- and intra-particle eddy currents at various excitation fields.

2. Material and methods

Amorphous $(Fe_{0.725}Si_{0.125}B_{0.150})_{96.5}Nb_{3.0}Cu_{0.5}$ (atomic %) composition is based on the ternary Fe-Si-B alloy obtained in previous work [13]. The powder was produced via gas atomisation using a convergent-divergent, close-coupled atomiser in an atomisation unit PSI model Hermiga 75/3VI. The amount of powder produced was nearly 2.5 kg. Fe (Allied Metal Corp.), Si (Cometal S.A.), B (H.C. Starck), Nb and Cu (AMPERE alloys S.A.) of commercial purity were melted in an induction furnace under a high purity argon atmosphere. The atomisation chamber was evacuated and purged with helium to minimise oxidation. The melt pouring temperature was 1700 °C. The atomising gas was helium at a pressure of 60 bar. The particle size distribution of the powders was measured by Sympatec Helos (H 0852) laser diffractometer. The true density was measured in a He pycnometer Micromeritics AccuPyc 1330.

Isothermal heat treatment of powder was carried out in a conventional laboratory furnace (CARBOLITE, RHF 14/35). The powder was

sieved ≤ 20 μm, and 15 g sample was used for annealing in an alumina crucible. Before annealing, the chamber was purged with high purity argon (H_2O ≤ 3 ppm, O_2 ≤ 3 ppm C_nH_m ≤ 3 ppm). The temperature was precisely controlled, using a thermocouple, to anneal samples at three different temperatures (525 °C, 575 °C, 625 °C) for 30 minutes dwell time.

The isothermally annealed powder of ≤ 20 μm was uniformly mixed with 20 vol.% of Araldite AT 1-1 epoxy resin. Toroidal powder cores (~ Ø 22 × ~ Ø 10 × ~t 6.5 mm) were prepared by compression moulding. The samples were pressed uniaxially in a Tinius-Olsen 30T press at 200 MPa using a floating die. Then, the temperature was raised to 120 °C for 10 min. Finally, the sample was cooled down to room temperature, the pressure was released, and the compact was ejected from the die by pushing with the upper punch. After shaping the toroidal cores, the organic binder was completely cured for 24 hours at 120 °C under an ambient atmosphere. The homogeneous distribution of particles and binder was analysed on a fracture surface using field emission gun scanning electron microscopy (FEI Quanta 3D FEG). The geometric density of the compacts was calculated from their weight and dimensions.

Differential scanning calorimetry (DSC) was used to identify the thermal transitions of the powders. The DSC experiments were conducted in a TA Instruments DSC 2920, at a heating rate of 10 °C/min under an argon atmosphere, using a powder of ~ 10 mg on a copper pan, covered with copper lid. Particle shape was studied using scanning electron microscopy (SEM, Philips XL30CP). The constituent phases were identified via X-ray diffraction (XRD, Philips X´pert MRD, Cu-K_α, λ = 1.542 Å). The diffraction angle (2θ) varied from 25 ° to 90 ° (scanning rate of 0.005 °/s, step size = 0.02°, holding time = 4 sec). Furthermore, the Rietveld refinement method was performed, using another refined XRD pattern obtained from Bruker D8 Advance A25 diffractometer, to estimate the size and the volume fraction of crystalline phases, the detailed procedure is published elsewhere [16]. Thin foils from powders were prepared using focused ion beam (FIB, FEI Quanta 3D FEG) milling instrument by lift-out technique. In the first step, a particle of ~ 20 μm was selected, and a Pt line was deposited on the surface. Two stair-step FIB trenches were cut on both sides of the Pt line. In the second step, the specimen was further thinned to less than 1 μm, and a slice of the specimen was cut free. The obtained lamella was removed using a micromanipulator and welded with Pt to a Cu grid that was suitable for transmission electron microscopy (TEM) analysis. Final milling < 100 nm was conducted by employing successively lower voltages of up to 2 kV. The

obtained specimen was examined by a conventional bright-field imaging TEM microscope (JEOL JEM-2100F), operated at 200 kV with LaB_6 filament.

The DC magnetic properties of the powders were evaluated using a vibrating sample magnetometer (VSM, Quantum Design PPMS-9T, Model P525), calibrated with a paramagnetic Dy_2O_3 standard. The step size at the low magnetic field was calibrated as 5 Oe. The temperature dependence of magnetisation *M(T),* was measured using the magneto-thermo-gravimetric (MTG) technique, and the Curie temperature (T_c) was calculated using the steepest temperature derivative, *dM(T)/dT*, the detailed procedure is published elsewhere [17]. The P_{CV} and μ_r were calculated based on resistance and inductance measurements, respectively, of an inductor prototype using LCR meter (Agilent E4980A). The prototype windings consist of 30 uniformly distributed copper turns. The measurements were conducted at frequencies from 50 kHz to 1 MHz and at four different current levels (25, 50, 75, and 100 mA). The power loss and permeability of the hollow toroidal plastic core, with the same dimensions as air-core, was also measured in order to subtract the copper winding loss. Additionally, the high-frequency permeameter (PMM 9G, Ryowa Electronics) was used to measure the μ_r spectrum in the 10-9000 MHz frequency range, using a square sample (4 mm × 4 mm × 0.5 mm) diced from a consolidated specimen (80 vol. % of powder mixed with 20 vol. % of epoxy resin).

3. Results and discussion

3.1 Thermal and structural characterisation of the powder

The gas-atomisation parameters and physical properties of the as-atomised powders (i.e., as received after atomisation, before sieving or annealing) are summarised in Table 1. A broad distribution of particle size was obtained with a 10th percent percentile D_{10} = 5.1 μm and a 90th percent percentile D_{90} = 60.0 μm. The powder particle was obtained with a median size (D_{50}) of 17.5 μm. The apparent density (defined as the mass per unit of volume of loose packed powders) was measured as 35.3 % of the true density. The tap density, i.e., the powder's packing ability without applying any pressure, was 68.5 % of the true density.

The fine particle size of atomised powder could be attributed to the high gas pressure during the atomisation and use of helium gas (for example, helium velocity is about three times higher than argon velocity for the same atomisation pressure) [11]. The high thermal conductivity of helium as compared to argon enhances the cooling rate by one order of magnitude,

helping to obtain the amorphous structure of the powders [12]. The low apparent density of powder could be attributed to the ultra-fine nature of the particles due to high inter-particle friction. The high relative tap density (i.e., the tap density expressed as a percentage of the true density) demonstrates that vibratying the powder was significantly effective in improving powder packing, which, in other words, indicates the spherical nature of the powder produced during the present study.

Table1. Atomisation parameters and thermal and physical properties of the as-atomised powder.

Property		Value
Mass flow rate of melt (g/s)		17.24
Mass flow rate of gas (g/s)		12.63
Gas-metal mass flow rate ratio *(GMR)*		0.73
Liquidus temperature (°C)		1124
Melt superheat (°C)		576
Particle size distribution of as-atomised powder (μm)	D_{10}	5.1
	D_{50}	17.5
	D_{90}	60.0
Particle size distribution of the fraction ≤ 20 μm (μm)	D_{10}	4.3
	D_{50}	9.2
	D_{90}	19.6
Apparent density (% of true density)		35.3
Tap density (% of true density)		68.5
True density (g/cm^3)		7.02

D_{10}: 10th percent percentile; D_{50}: median particle size; D_{90}: 90th percent percentile.

Fig. 1 presents the XRD pattern of the as-atomised powder. A typical broad halo pattern in the range 2θ = 35 - 55°, with no distinguishable narrow diffraction peaks, which confirms the amorphous nature of the powder. Fig. 1 (inset) shows a secondary electrons image of the as-atomised powder. The particles were spherical, which is a typical characteristic of the powders produced via inert gas atomisation. In addition, the SEM revealed the broad size distribution range of the particles. It is worth mentioning that Cu, in the present alloy, has a positive enthalpy of mixing with the constituent elements and has a high tendency to start nucleation of crystallites if cooling rates are insufficient during atomisation process [18]. The XRD and SEM confirm that Fe-Si-B-Nb-Cu alloy preserves a tremendous capacity to be produced in amorphous spherical particles with a broad particle size (5 - 60 μm) distribution via helium gas atomisation with high productivity (1 kg/min) and yield (100 %).

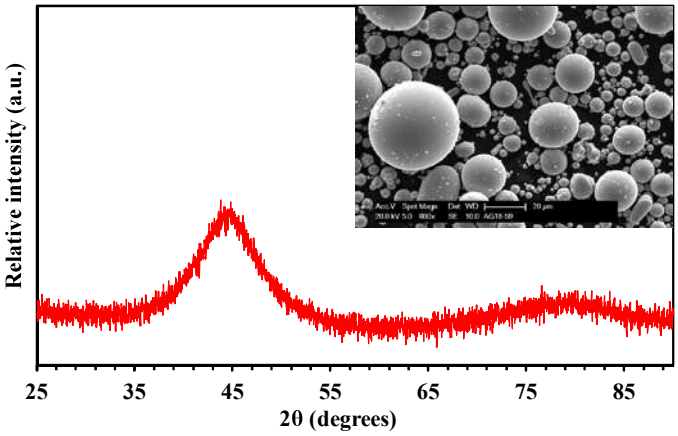

Fig. 1. X-ray diffraction pattern (XRD) of the as-atomised $(Fe_{0.725}Si_{0.125}B_{0.150})_{96.5}Nb_{3.0}Cu_{0.5}$ powder. The inset shows the SEM image of the as-atomised powder.

Fig. 2 shows the DSC trace of the as-atomised powder. The small endothermic peak observed at 335 °C corresponds to the T_C of the alloy. The change observed in the heat capacity at the glass transition temperature T_g = 504 °C is due to the glass transition. Two different exothermic events were distinguished in DSC, where the first peak corresponds to the crystallisation of Fe_3Si at T_{X1} = 558 °C, and the second peak can be ascribed to the precipitation of Fe_2B at T_{X2} = 656 °C [19]. In order to evaluate the GFA of the powders, two different parameters, such as supercooled liquid region ΔT_X (= T_{X1} - T_g) and the reduced glass transition temperature T_{rg} (= T_g/T_1, T_1 = liquidus temperature), were calculated from the DSC [20]. The large ΔT_X = 54 °C and high T_{rg} = 0.56 confirms the high GFA of the alloy, which is essentially required to quench the amorphous alloys at low cooling rates [21,22]. In addition, the amorphous structure of the large particles (60 μm) further justifies the substantial amorphisation capability of the alloy. The large ΔT_X (i.e., 54 °C) of Fe-Si-B-Nb-Cu shows high thermal stability against crystallisation, which is of significant importance to retain the amorphous atomic structure at under robust working conditions. To the best of our knowledge, this is the first-ever report to reveal a large ΔT_X in a Finemet-type powder alloy.

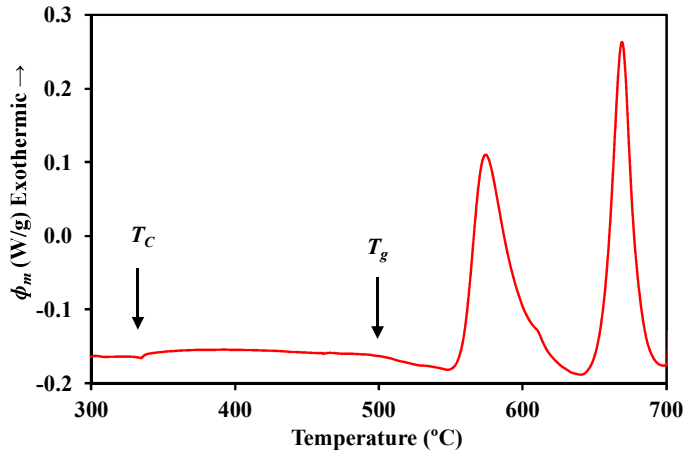

Fig. 2. Differential scanning calorimetry (DSC) trace of as-atomised sieved $(Fe_{0.725}Si_{0.125}B_{0.150})_{96.5}Nb_{3.0}Cu_{0.5}$ powder (≤ 20 μm).

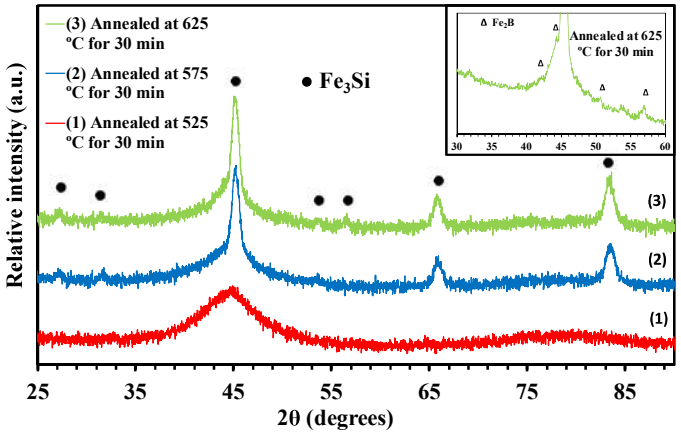

Fig. 3. X-ray diffraction pattern (XRD) of ≤ 20 μm powders annealed at 525 °C, 575 °C, and 625 °C temperatures for 30 min. Inset shows XRD pattern of high quality of the sample annealed at 625 °C.

In order to investigate the effect of structural relaxation and nanocrystallisation on the soft magnetic properties, the sieved powders ≤ 20 μm were annealed at three different temperatures, based on DSC, such as; (a) 525 °C (below the onset of first crystallisation peak,), (b) 575 °C (at the peak of first exothermic event) and (c) 625 °C (between first and second exothermic event). Fig. 3 shows the XRD patterns of the annealed powders. The XRD analysis of the powders annealed at 525 °C (i.e., the supercooled liquid region) did not show any sign of crystallisation; rather, it showed a broad maximum of amorphous structure. The powders annealed at 575 °C

and 625 °C revealed sharp Bragg's peaks, corresponding to the crystalline phase Fe_3Si (DO_3). The precipitation of Fe_3Si phase has been observed in similar alloys and reported elsewhere [23]. The size of nanocrystalline grains D, as well as the weight fraction X_D of Fe_3Si phases, were calculated by the Rietveld refinement method and summarised in Table 3. Annealing at 575 °C produced crystallisation of 23 wt. % of the as-atomised amorphous structure, where the precipitated phase was confirmed as Fe_3Si with a crystal size of 11.7 nm. Increasing the annealing temperature to 625 °C lead to a slight increment of the crystal size (up to 13.4 nm), while the amount of Fe_3Si phase increased to ~ 47 wt. %.

Fig. 4 shows the bright field TEM image of 525 °C, 575 °C, and 625 °C annealed powders, whereas the inset presents the selected area electron diffraction (SAED) patterns. The TEM of the 525 °C annealed sample revealed a minimal volume fraction of nanocrystals of size ≤ 10 nm. The anomalous precipitation of the nanocrystalline phase below T_X (i.e., 558 °C) was surprising, as a highly dense amorphous atomic structure was anticipated upon structural relaxation. Furthermore, no signs of crystallisation were visible for the 525 °C annealed powders by the XRD and SAED patterns, see Fig. 3 and inset Fig. 4 (a). The 575 and 625 °C annealed samples revealed the nanocrystallisation of the Fe_3Si phase, and SAED patterns showed diffused rings of the amorphous structure along with small diffraction patterns coming from the randomly oriented Fe_3Si nanocrystals. Since the alloy contains Cu and Nb, this nanocrystallisation was expected after annealing the powder at the first crystallisation peak. Cu helps to increase the nucleation sites because Cu-rich clusters are formed during the sample heating, and, as a result, a homogeneous crystallisation randomly distributed in the amorphous matrix, takes place in Cu depleted zones. On the other hand, Nb hinders nanocrystals growth [24] and is so effective that crystal size barely grows even if the annealing temperature is increased 50 °C above the crystallisation peak temperature (from 575 to 625 °C). The size of the nanocrystals and volume fraction measured by TEM was in good agreement with the XRD analysis of the powders shown in Table 3.

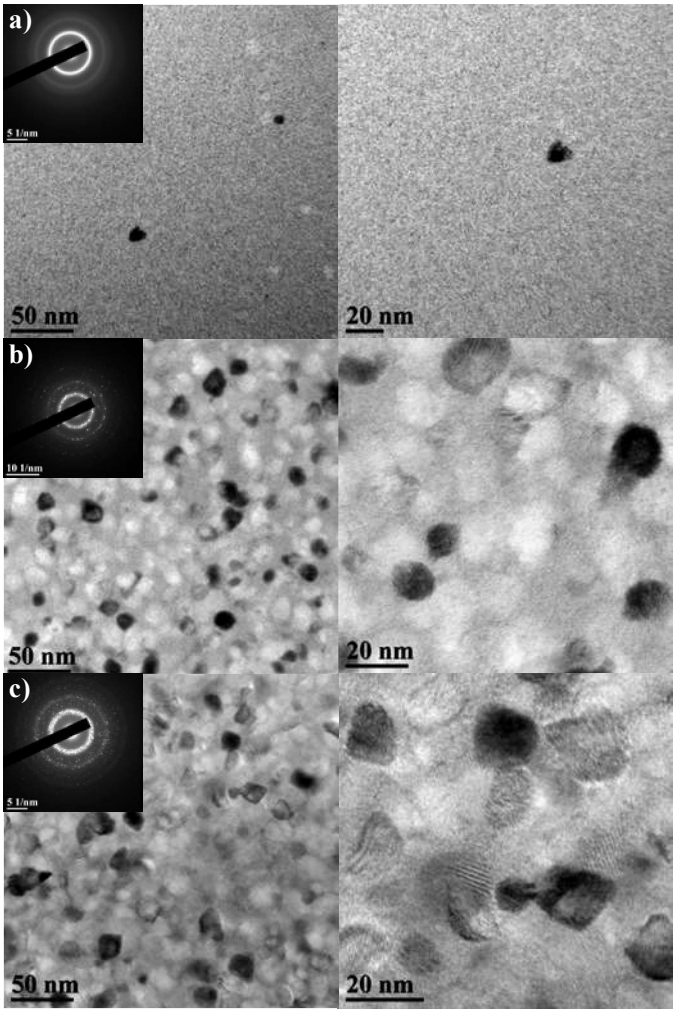

Fig. 4. Bright-field TEM images of the samples annealed at a) 525 °C, b) 575 °C and c) 625 °C. Insets show the selected area electron diffraction (SAED).

The Curie temperature (T_C) intrinsically depends on the atomic structure of the magnetic material and is a useful instrument to investigate any small structural changes appearing during the annealing process of the amorphous alloys. Fig. 5 shows the *M(T)* of the as-atomised and annealed powders. The magnetisation of the as-atomised powders approached zero at T_C = 335 °C. The single-phase monolithic behaviour of *M(T),* without showing any "kink" before the evolution of 2nd magnetic phase on crystallisation, confirms the amorphous nature of the as-atomised powders [3,17]. The *M(T)* of the 525 °C annealed powders exhibited T_C = 369 °C,

higher than the T_C of as-atomised powder. The higher T_C of annealed powder could be attributed to the enhanced exchange interaction between Fe-Fe atoms, due to the highly-dense atomic packing achieved on the structural relaxation of the amorphous phase [13,17,25]. More interestingly, the magnetisation of 525 °C annealed powder never reached zero at T_C = 369 °C; rather it approached the temperature where a new magnetic phase precipitated after the 2nd exothermic event (see Fig. 2). This behaviour of *M(T)* is well-known for two-phase magnetic materials, where the area under the curve can be utilised to quantify the volume fraction of the precipitated phases [17]. The anomalous precipitation of the nanocrystalline phase at 525 °C was not expected since it is well below the crystallisation temperature (T_X = 558 °C, see Fig. 2) of the powders. The existence of small crystallites observed by the *M(T)* of 525 °C annealed powder is in good agreement with the high-resolution TEM imaging (see Fig. 4), thanks to the ultra-high sensitivity of the MTG technique to detect the minimal volume fraction of nanocrystals, which otherwise is not obvious from conventional diffraction techniques (i.e., XRD, SAED).

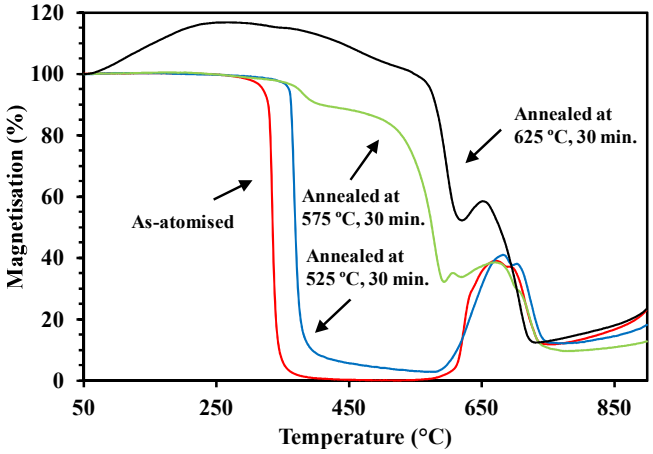

Fig. 5. Temperature dependence of magnetisation behaviour *M(T)* of powders annealed at 525 °C, 575 °C, and 625 °C for 30 min. The *M(T)* of the as-atomised powder was presented for comparison.

Moreover, the *M(T)* of the 575 °C annealed powder showed two-phase magnetic behaviour by revealing the significant volume fraction of the nanocrystalline phase in the amorphous matrix. The T_C = 380 °C of the remaining amorphous matrix was slightly higher than that of the 525 °C annealed powders. The T_C of the nanocrystalline phase in 575 °C annealed powders was measured 567 °C. The direct measurement of T_C = 567 °C from the *M(T)* further confirms the presence of the Fe_3Si phase, which was initially

observed by structural investigations (see Figs. 3 and 4) and agrees with theoretically estimated values for the Fe_3Si phase [26]. Furthermore, a small peak in the *M(T)* of 575 °C annealed powders was observed after the T_C of Fe_3Si phase, which is the same temperature (~ 610 °C) at which small overlapped peak was emerged in DSC curve (see Fig. 2). The contribution of the new phase precipitated at 610 °C is distinct from *M(T)* of 625 °C annealed powders, suggesting a new magnetic phase as compared to 525 °C and 575 °C annealed powders.

3.2 *DC soft magnetic properties of amorphous and nanocrystalline powders*

Fig. 6 shows the hysteresis loop of as-atomised and annealed powders measured at room temperature. The soft magnetic behaviour of as-atomised and annealed powders was confirmed by the small H_C (see inset in Fig. 6). The magnetic properties obtained from the hysteresis loops are summarised in Table 2. The H_C of the as-quenched amorphous powder was measured as 1.71 Oe, which reduced to 0.88 Oe on annealing at 525 °C (i.e., the temperature in the supercooled liquid region). The H_C of powders slightly increased to 0.91 Oe after annealing at 575 °C (i.e., the first crystallisation peak temperature). However, an abrupt increase in the H_C = 14.42 Oe was observed after annealing at 625 °C. Despite low H_C of powders annealed below 525 °C, the coercivity is still higher as compared to melt-spun amorphous ribbons. The higher H_C of powders could be ascribed to a magnetic surface effect due to the large specific surface of gas-atomised powders.

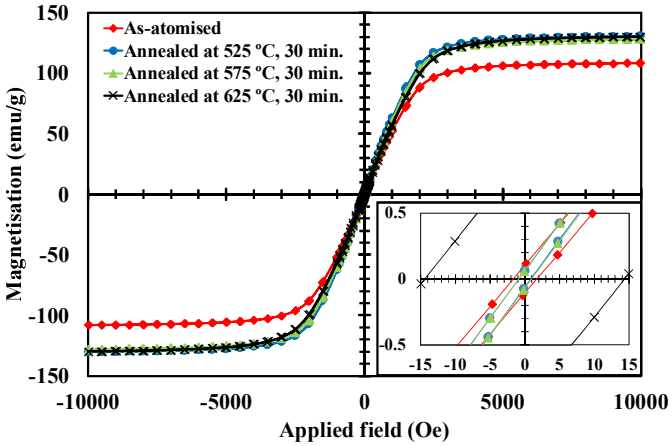

Fig. 6. Hysteresis loop measured at room temperature of the as-atomised and annealed powders ≤ 20 μm. Inset shows the magnification at the origin of coordinates.

The H_C of amorphous and nanocrystalline materials depends on the effective magnetic anisotropy [27]. The high H_C (1.71 Oe) of the as-atomised powders could be attributed to the large residual stress induced due to the nature of the production process. In addition, the large magnetostriction constant (λ_S) of Fe-based amorphous alloys play a vital role in defining the high H_C. The soft magnetic properties of amorphous materials can be significantly improved by thermal treatment of the alloys. The annealing can either relax the amorphous atomic structure by releasing the residual stress or grow a nanocrystalline structure inside the amorphous matrix. The reduced H_C of 525 °C and 575 °C annealed powders can be explained by the reduction of magnetoelastic anisotropy energy, due to structural relaxation of the amorphous phase or precipitation of significant volume fraction of nanocrystalline phase, which consequently makes the $\lambda \approx 0$, as confimed by XRD, TEM, and *M(T)* analysis (see Figs. 3-5). In the case of the nanocrystalline materials, the magnetic softening depends on the size, volume fraction, and homogenous distribution of the nanocrystals. In the present alloy system, Cu works as a nucleation agent, due to the positive enthalpy of mixing with constituent elements, while the Nb works as an inhibitor, due to its large atomic size, to controll the grain growth process. The nucleation and grain growth process in gas-atomised powders resulted in precisely cotrolled crystallites of ≤ 20 nm grains homogenously distributed in the amorphous matrix, which is of significant importance to attain excellent soft magnetic properties and is well explained by Herzer's random anisotropy model (RAM). According to the RAM model, the local magnetic anisotropies (mainly of magnetocrystalline nature) of nanocrystalline grains are randomly averaged out since the ferromagnetic correlation exchange length ($L_{ex} \sim 35$ nm for α-Fe grains) is larger than the size of nanocrystals (D) embedded homogeneously in the amorphous matrix. The RAM model was initially proposed for amorphous materials [28], and later extended to nanocrystalline alloys under the assumption that $L_{ex} > D$ [27]. Further, deterioration in soft magnetic properties of the powders annealed at 625 °C (i.e., H_C = 14.42 Oe) could be ascribed to the precipitation of borides. The DSC trace in Fig. 2 shows a small overlapped peak at ~ 610 °C that could be due to the precipitation of the metastable phase Fe_3B or the stable phase Fe_2B [29]. The precipitation of borides in powders annealed at 625 °C was also observed in *M(T)* curves (see Fig. 5). Furthermore, a high-resolution XRD was performed on the 625 °C annealed powders, where the formation of a stable Fe_2B phase was confirmed (see inset in Fig. 3) [30]. It was believed that the high H_C of the 625 °C annealed powders is due to the Fe_2B phase, which contains significantly high magnetocrystalline anisotropy and cannot be averaged out even though the

grain size of Fe_3Si remains 13.4 nm and hence, does not follow the RAM model [31].

Table 2. Magnetic properties of as-atomised and annealed powers.

Property	As-atomised	Annealed 30 min		
		525 °C	575 °C	625 °C
H_C (Oe)	1.71	0.88	0.91	14.42
M_S (emu/g)	112	134	132	133
$<H_K>$ (Oe)	2070	2020	2040	2150
FWHM	1185	955	992	1242

H_C: coercivity obtained from the hysteresis loop; M_S: saturation magnetisation; $<H_K>$: average anisotropy field, calculated as the H field of the maximum value of the anisotropy field distribution $P(H_K)$ [32]; *FWHM*: full width at half maximum of the anisotropy field distribution.

Moreover, the distribution of anisotropy field was analysed to confirm the magnetic softening of amorphous and annealed powders [32]. The average anisotropy field, $<H_K>$, of as-atomised powders reduced from 2070 Oe to 2020 Oe after annealing at 525 °C and then increased to 2040 Oe for 575 °C annealed powders (see Table 2). The full width at half maximum (*FWHM*) of distribution anisotropy field of amorphous and annealed powders are summarised in Table 2. The smaller *FWHM* of 525 °C and 575 °C annealed powders, as compared to as-atomised, confirmed the magnetic softening achieved after annealing. However, large $<H_K>$ and *FWHM* of 625 °C annealed powders could be associated with the deteriorated soft magnetic properties due to the precipitation of borides during the annealing.

The hysteresis loops presented in Fig. 6 were used to measure the saturation magnetisation M_S of the powders. The M_S = 112 emu/g of the as-atomised powder increased to 132 - 134 emu/g after annealing. The increase in M_S values can be understood in terms of the two different contributions coming from the relative volume fractions of the crystalline phase Fe_3Si and the remaining amorphous phase [33]. The three annealed powders have a close value of M_S, despite that the weight fraction of Fe_3Si ranges between 0 and 47 wt. %, which shows that M_S is somewhat similar to the amorphous relaxed phase and Fe_3Si.

3.3 Core fabrication and high-frequency soft magnetic properties

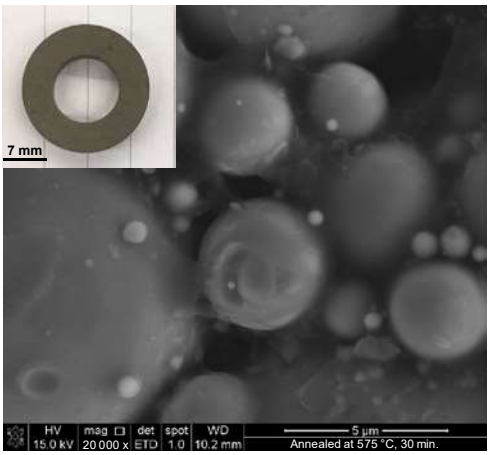

Fig. 7. Representative SEM image of magnetic core annealed at 575 °C for 30 min. The inset shows an optical image of the core.

The magnetic cores were fabricated by mixing the as-atomised or annealed powder (≤ 20 μm) with 20 vol. % of the resin, the detailed procedure is explained in section 2. Fig. 7 shows a typical SEM image of the fractured surface of the core, while the inset illustrates an optical image of the core. The SEM analysis confirmed the homogeneous distribution of organic binder and powder particles. In fact, a thin layer of epoxy worked as an insulating coating around particles. The presence of an organic insulating film at the contact area between magnetic particles, compressed at high pressure (200 MPa) and temperature (120 °C), cannot be directly observed with SEM technique. However, its presence with a thickness of < 100 Å has been demonstrated by X-ray photoelectron spectroscopy during the uniaxial pressing of iron compacts at 600 MPa [34]. Consequently, it appears that such an insulating film subsists in the present case. The insulating layer helps to reduce the inter-particle eddy current and, consequently, the associated core loss.

From true density of the magnetic powder (7.02 g/cm^3) and epoxy resin (1.25 g/cm^3), the theoretical density of the mix with 20 vol. % of the organic binder was calculated to be 5.87 g/cm^3. The geometric density of the cores (ρ_{core}, in g/cm^3 and as % of the theoretical density of the mix), as well as the volume fraction of magnetic powder ($X_{v\text{-}powder}$), resin ($X_{v\text{-}epoxy}$) and porosity ($X_{v\text{-}porosity}$), are summarised in Table 3. The volume fraction of magnetic powder was higher than the relative tap density due to the applied

pressure during moulding. The brittle nature of the amorphous powders does not allow particles to flow plastically, and consequently, only a marginal increment of the volume fraction of magnetic powder above the relative tap density was observed.

Table 3. The structural and AC magnetic properties of different magnetic cores.

Property	As-atomised	Annealed 30 min		
		525 °C	575 °C	625 °C
ρ_{core} (g/cm³)	5.19	5.11	5.06	5.09
ρ_{core} (% of theor. dens.)	88.54	87.15	86.26	86.83
$X_{v\text{-}powder}$ (%)	70.83	69.72	69.01	69.47
$X_{v\text{-}epoxy}$ (%)	17.71	17.43	17.25	17.37
$X_{v\text{-}porosity}$ (%)	11.46	12.85	13.74	13.16
X_D (wt. %)	-	-	23	47
D (nm)	-	-	11.7	13.4
Core loss (mW/cm³)	1.41	0.64	0.62	0.58
μ_r (-)	16.09	15.85	15.30	13.97

ρ_{core}: core density; $X_{v\text{-}powder}$: volume fraction of magnetic powder; $X_{v\text{-}epoxy}$: volume fraction of epoxy resin; $X_{v\text{-}porosity}$: volume fraction of porosity; X_D: weight percentage of Fe_3Si phase; D: Fe_3Si crystallite size; Core loss (P_{CV}) at 1 MHz for B_m = 1 mT; μ_r: relative permeability.

Fig. 8 shows the materials loss performance at different frequencies and excitation fields of cores made by as-atomised and annealed powders. The materials loss can be broadly divided into three categories, such as hysteresis loss (P_h), eddy current loss (P_e), and anomalous loss (P_{an}) [5]. The total P_{CV} can be written as:

$$P_{CV} = P_h + P_{ec} + P_{an} \quad (1)$$

The P_h in powder cores is generally dominant at low frequencies, whereas the P_{ec} and P_{an} become significant at higher frequencies [35]. Fig. 8 (a) shows the core loss performance of the as-atomised and annealed cores as a function of frequency at different excitations (B_m = 0.5 - 1 mT). The core loss of as-atomised powder cores was significantly higher in the entire frequency spectrum (50 kHz - 1000 kHz). The high core loss of the as-atomised powder core can be associated with the dominant P_h due to the substantial magnetoelastic contributions, intrinsically associated with the high saturation magnetostriction ($\lambda = 10 - 30 \times 10^{-6}$) of Fe-based amorphous alloys [36]. In addition, a marginal increment in the frequency-dependent slope of core loss suggests the dominant loss appears from the hysteresis

contributions at low frequencies and remained significant up to the MHz range. The core loss performance significantly improved after annealing at 525 °C, 575 °C, and 625 °C. The improved loss performance of annealed cores can be associated with the reduced magnetoelastic contributions, due to zero/near-zero λ, achieved on the growth of homogeneously dispersed nanocrystalline structure [31,37]. The slope of the core loss behaviour of annealed cores became steeper as compared to as-atomised cores, suggesting the frequency dependent dynamic mode of aforementioned loss components.

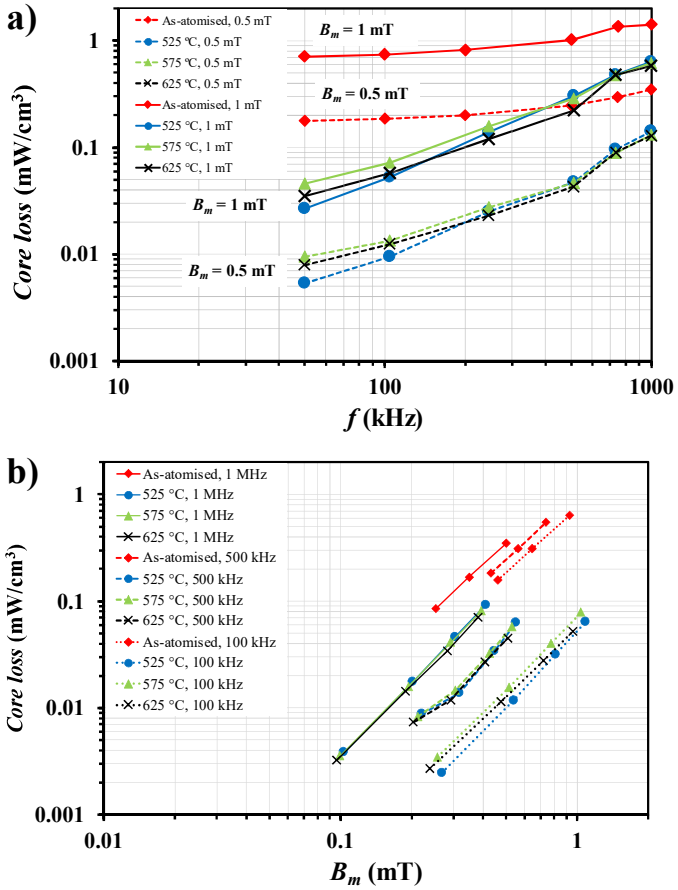

Fig. 8. Core loss (P_{cv}) of the samples as-atomised and annealed at 525, 575, and 625 °C for 30 min. a) Core loss for different frequencies (f) at two magnetic flux densities (B_m = 1 and 0.5 mT); b) Core loss for different magnetic flux densities at three different frequencies (f = 100 kHz, 500 kHz and 1 MHz).

The dynamic mode of loss components in powder cores is evident from the crossover and immediate increase in the slope of core loss when frequency approaches MHz range. For example, 525 °C annealed cores exhibit the best loss performance, as compared to the other nanocrystalline cores, at f = 50 - 200 kHz (B_m = 0.5 mT), could be associated with the ultra-low P_h due to small H_C = 0.88 Oe (see Table 2 and Fig. 6). However, when f approaches ≥ 200 kHz, the loss of the 525 °C core increased and became higher than the loss of 625 °C annealed cores (see Fig. 8). The higher core loss of 525 °C annealed cores, as compared to 625 °C, at f ≥ 200 kHz could be attributed to the transition in dominant loss mechanisms as a function of frequency. It is believed that the intra-particle P_{ec} in 525 °C annealed cores was higher as compared to 625 °C annealed cores at f ≥ 200 kHz, and hence, the overall loss of 525 °C cores increased. The eddy current loss depends on the resistivity and size of the powder particles. While having a similar size of powder for both core, it seems that the resistivity of the nanocrystalline powder was higher than 525 °C annealed powders. The high resistivity of two phase nanocrystalline materials, as compared to amorphous metals, is expected due to the complex electron scattering mechanism at the interface of grain boundaries between amorphous and nanocrystalline phases. A similar crossover was observed in the loss performance of the 525 °C, and 625 °C annealed cores at B_m = 0.1 mT, but at a comparatively lower frequency (f = 110 kHz). Furthermore, an abrupt change in the slope of the core loss performance of all cores was observed at 500 kHz. The change in slope might be due to a capacitive coupling effect that promotes displacement currents between the particles through the resin so that the overall material loss is abruptly increased. It is suggested that the inter-particle displacement current, which emerged due to capacitive coupling, can be reduced by the coating of individual powder particles or by increasing the volume fraction of the resin [38].

Fig. 9 shows the high-frequency permeability spectrum of 525 °C annealed powders. Remarkably, 525 °C annealed powders revealed a very stable permeability behaviour with a ferromagnetic resonance at f = 3 GHz, which suggests that the operational frequency range of these cores can reach up to several hundreds of MHz.

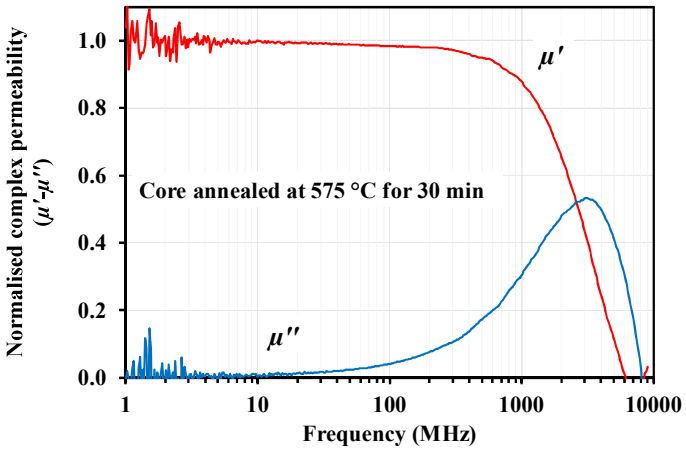

Fig. 9. Normalised complex permeability (μ'-μ'') at high frequencies of the core annealed at 575 °C for 30 min.

4. Conclusions

Amorphous powders of $(Fe_{0.725}Si_{0.125}B_{0.150})_{96.5}Nb_{3.0}Cu_{0.5}$ alloy were successfully produced via helium gas atomisation, and subsequently annealed to grow nanocrystalline structures to attain excellent core loss performance. The thermal analysis of the amorphous powders showed high GFA, as confirmed by different glass forming parameters such as supercooled region (ΔT_X = 54 °C) and reduced glass transition temperature (T_{rg} = 0.56). The high amorphisation capability of the alloy was further justified by the amorphous nature of the broad size distribution (5 - 60 μm) of the powder. Two exothermic events in the DSC were used as a guide for the selection of the annealing temperatures to grow the soft magnetic nanocrystalline structure. The annealing at 525 °C (i.e., < T_{X1}) resulted in the anomalous crystallisation, which was unexpected due to the large ΔT_X of the alloy, and experimentally confirmed by *M(T)* experiments, thanks to its ultra-high sensitivity, which otherwise is challenging by conventional diffraction techniques (i.e., XRD, SAED). Further annealing of powders at 575 °C (i.e., > T_{X1}) precipitated the nanocrystalline Fe_3Si phase of 23 wt.%, being the average crystallite size of 11.7 nm. The homogeneous distribution of nanocrystalline grains in the amorphous matrix, confirmed by XRD and TEM, revealed the effective role of Cu, as a nucleation agent, and Nb, as an inhibitor, to control the nucleation and grain growth crystallisation dynamic in the powders.

The DC soft magnetic properties of the powders were significantly improved on thermal annealing, confirmed by hysteretic loops, quantified by reduced H_C < 1 Oe of powders annealed at ≤ 575 °C, and hence, attributed to the reduced magnetoelastic contribution due to zero/near-zero magnetostriction anisotropy attained due to the homogenous nanocrystalline structure. A degradation in H_C = 14.42 Oe after annealing at 625 °C, despite having ultra-fine nanocrystalline grains (< 15 nm) to follow the Herzer's RAM model, shows the non-vanishing effective magnetocrystalline anisotropy of minimal boride phases. Last but not least, high-frequency core loss performance of the nanocrystalline cores significantly improved, as compared to as-atomised powder cores, and ascribed to the significant reduction of the hysteresis loss contribution due to aforementioned vanishing magnetoelastic anisotropy energies. The dynamic mode of loss components in nanocrystalline powder cores revealed the change of dominant loss mechanism as a function of frequency, and hence, displacement currents, due to capacitive coupling, abruptly increase the loss when frequency approaches MHz range. The ease of powder atomisation, high GFA of the alloy composition, and controlled nanocrystallisation capability to retain excellent core loss performance makes the materials ideal candidate for high frequency power conversions, such as voltage regulators and resonant converters, for automotive industry and data centres.

CRediT authorship contribution statement

Kenny L. Alvarez: Conceptualization, Methodology, Formal analysis, Investigation, Writing - original draft. **H.A. Baghbaderani:** Methodology, Formal analysis, Investigation, Writing - review & editing. **J.M. Martín:** Conceptualization, Methodology, Validation, Resources, Writing - review & editing, Supervision, Project administration. **N. Burgos:** Formal analysis, Investigation. **M. Ipatov:** Formal analysis, Investigation. **Z. Pavlovic:** Formal analysis, Investigation. **P. McCloskey:** Resources, Writing - review & editing, Supervision, Project administration. **A. Masood:** Conceptualization, Methodology, Validation, Investigation, Writing - original draft. **J. Gonzalez:** Conceptualization, Resources, Supervision.

Declaration of Competing Interest

The authors declare that they have no known competing financial interests or personal relationships that could have appeared to influence the work reported in this paper.

Acknowledgements

Author Kenny L. Alvarez thanks to Becas Chile (CONICYT) for the financial support. The authors thank for technical and human support provided by SGIker Medidas Magneticas Gipuzkoa (UPV/EHU/ERDF, EU), and for the MTG experimental support by the Professor Dr. Valter Ström and Ms. Esmat Dastanpoor from The Royal Institute of Technology - KTH.

References

[1] Y. Zhang, P. Sharma, A. Makino, Fe-Rich Fe-Si-B-P-Cu Powder Cores for High-Frequency Power Electronic Applications, IEEE Trans. Magn. 50 (2014) 2006804, https://doi.org/10.1371/journal.pcbi.1000729.

[2] R. Hasegawa, Applications of amorphous magnetic alloys in electronic devices, J. Non Cryst. Solids. 287 (2001) 405–412, https://doi.org/10.1016/S0022-3093(01)00633-0.

[3] A. Masood, H.A. Baghbaderani, V. Ström, P. Stamenov, P. McCloskey, C. Mathúna, S. Kulkarni, Fabrication and soft magnetic properties of rapidly quenched Co-Fe-B-Si-Nb ultra-thin amorphous ribbons, J. Magn. Magn. Mater. 483 (2019) 54–58, https://doi.org/10.1016/j.jmmm.2019.03.079.

[4] K.J. Sunday, M.L. Taheri, Soft magnetic composites: recent advancements in the technology, Met. Powder Rep. 72 (2017) 425–429, https://doi.org/10.1016/j.mprp.2016.08.003.

[5] P. Kollár, Z. Bircáková, J. Füzer, R. Bures, M. Fáberová, Power loss separation in Fe-based composite materials, J. Magn. Magn. Mater. 327 (2013) 146–150, https://doi.org/10.1016/j.jmmm.2012.09.055.

[6] H. Shokrollahi, K. Janghorban, Soft magnetic composite materials (SMCs), J. Mater. Process. Technol. 189 (2007) 1–12, https://doi.org/10.1016/j.jmatprotec.2007.02.034.

[7] M. De Wulf, L. Anestiev, L. Dupré, L. Froyen, J. Melkebeek, Magnetic properties and loss separation in iron powder soft magnetic composite materials, J. Appl. Phys. 91 (2002) 7845–7847, https://doi.org/10.1063/1.1446115.

[8] T. Suzuki, P. Sharma, L. Jiang, Y. Zhang, A. Makino, Fabrication and properties of under 10 μm sized amorphous powders of high B_s soft magnetic alloy for high-frequency applications, IEEE Trans. Magn. 54 (2018) 2801705, https://doi.org/10.1109/TMAG.2018.2833138.

[9] L. Chang, L. Xie, M. Liu, Q. Li, Y. Dong, C. Chang, X.M. Wang, A. Inoue, Novel Fe-based nanocrystalline powder cores with excellent magnetic properties produced using gas-atomized powder, J. Magn. Magn. Mater. 452 (2018) 442–446, https://doi.org/10.1016/j.jmmm.2017.12.049.

[10] Y.B. Kim, D.H. Jang, H.K. Seok, K.Y. Kim, Fabrication of Fe–Si–B based amorphous powder cores by cold pressing and their magnetic properties, Mater. Sci. Eng. A

Struct. Mater. Prop. Microstruct. Process. 449–451 (2007) 389–393, https://doi.org/10.1016/j.msea.2006.02.394.

[11] A.J. Yule, J.J. Dunkley, Atomization of Melts for Powder Production and Spray Deposition, Oxford University Press, UK Oxford, 1994.

[12] K.L. Alvarez, J.M. Martín, M. Ipatov, J. Gonzalez, Soft magnetic amorphous alloys (Fe-rich) obtained by gas atomisation technique, J. Alloys Compd. 735 (2018) 2646–2652, https://doi.org/10.1016/j.jallcom.2017.11.272.

[13] K.L. Alvarez, J.M. Martin, M. Ipatov, L. Dominguez, J. Gonzalez, Magnetic properties of annealed amorphous $Fe_{72.5}Si_{12.5}B_{15}$ alloy obtained by gas atomization technique, IEEE Trans. Magn. 54 (2018) 2002405, https://doi.org/10.1109/TMAG.2018.2839258.

[14] A. García-Escorial, M. Lieblich, A. Hernando, A. Aragón, P. Marín, Temperature dependence of the coercive field of gas atomized $Fe_{73.5}Si_{13.5}B_9Nb_3Cu_1$, J. Alloys Compd. 536 (2012) S300–S303, https://doi.org/10.1016/j.jallcom.2011.11.015.

[15] A.M. Leary, P.R. Ohodnicki, M.E. Mchenry, Soft magnetic materials in high-frequency, high-power conversion applications, Jom. 64 (2012) 772–781, https://doi.org/10.1007/s11837-012-0350-0.

[16] K.L. Alvarez, J.M. Martín, N. Burgos, M. Ipatov, L. Dominguez, J. Gonzalez, Structural and magnetic properties of amorphous and nanocrystalline Fe–Si–B–P–Nb–Cu alloys produced by gas atomization, J. Alloys Compd. 810 (2019) 151754, https://doi.org/10.1016/j.jallcom.2019.151754.

[17] S. Lee, A. Masood, T. Tamaki, S. Valter, K. V. Rao, A. Makino, A. Inoue, Magneto-thermo-gravimetric technique to investigate the structural and magnetic properties of Fe-B-Nb-Y Bulk Metallic Glass, J. Phys. Conf. Ser. 144 (2009) 8–12, https://doi.org/10.1088/1742-6596/144/1/012074.

[18] A. Takeuchi, A. Inoue, Classification of bulk metallic glasses by atomic size difference, heat of mixing and period of constituent elements and its application to characterization of the main alloying element, Mater. Trans. 46 (2005) 2817–2829, https://doi.org/10.2320/matertrans.46.2817.

[19] P. Duhaj, I. Maťko, P. Švec, D. Janičkovič, Structural characterization of the finemet type alloys, J. Non. Cryst. Solids. 192–193 (1995) 561–564, https://doi.org/10.1016/0022-3093(95)00407-6.

[20] C. Suryanarayana, A. Inoue, Bulk Metallic Glasses, CRC/Taylor & Francis, US, 2011.

[21] A. Masood, A. Biswas, V. Ström, L. Belova, J. Ågren, K. V. Rao, The effect of Ni-substitution on physical properties of $Fe_{72-x}B_{24}Nb_4Ni_x$ bulk metallic glassy alloys, Mater. Res. Soc. Symp. Proc. 1300 (2011) 52–57, https://doi.org/10.1557/opl.2011.304.

[22] A. Masood, V. Ström, L. Belova, K. V. Rao, J. Ågren, Effect of Ni-substitution on glass forming ability, mechanical, and magnetic properties of FeBNbY bulk metallic glasses, J. Appl. Phys. 113 (2013) 013505, https://doi.org/10.1063/1.4772753.

[23] N. Mattern, Structure of nanocrystalline soft-magnetic materials, Mater. Sci. Forum. 79–82 (1991) 607–612, https://doi.org/10.4028/www.scientific.net/MSF.79-

82.607.

[24] Y. Yoshizawa, K. Yamauachi, Fe-based soft magnetic alloys composed of ultrafine grain structure, Mater. Trans. JIM. 31 (1990) 307–314, https://doi.org/10.2320/matertrans1989.31.307.

[25] S. Kaloshkin, M. Churyukanova, V. Zadorozhnyi, I. Shchetinin, R.K. Roy, Curie temperature behaviour at relaxation and nanocrystallization of Finemet alloys, J. Alloys Compd. 509 (2011) S400–S403, https://doi.org/10.1016/j.jallcom.2011.01.090.

[26] I. Ohnuma, S. Abe, S. Shimenouchi, T. Omori, R. Kainuma, K. Ishida, Experimental and thermodynamic studies of the Fe-Si binary system, ISIJ Int. 52 (2012) 540–548, https://doi.org/10.2355/isijinternational.52.540.

[27] G. Herzer, Grain size dependence of coercivity and permeability in nanocrystalline ferromagnets, IEEE Trans. Magn. 26 (1990) 1397–1402, https://doi.org/10.1109/20.104389.

[28] R. Alben, J.J. Becker, M.C. Chi, Random anisotropy in amorphous ferromagnets, J. Appl. Phys. 49 (1978) 1653–1658, https://doi.org/10.1063/1.324881.

[29] C. Yang, F. Liu, S. Ren, G. Yang, Microstructure and magnetic properties of a two-phase alloy of α-Fe and metastable Fe_3B, J. Magn. Magn. Mater. 321 (2009) 91–94, https://doi.org/10.1016/j.jmmm.2008.08.041.

[30] X. Luo, Y. Wu, M. Han, L. Deng, High frequency permeability of Fe-Cu-Nb-Si-B nanocrystalline flakes with the distribution of shape anisotropy fields, J. Magn. Magn. Mater. 451 (2018) 5–10, https://doi.org/10.1016/j.jmmm.2017.10.113.

[31] G. Herzer, Modern soft magnets: Amorphous and nanocrystalline materials, Acta Mater. 61 (2013) 718–734, https://doi.org/10.1016/j.actamat.2012.10.040.

[32] J.M. Barandiarán, M. Vazquez, A. Hernando, J. Gonzalez, G. Rivero, Distribution of the magnetic anisotropy in amorphous alloys ribbons, IEEE Trans. Magn. 25 (1989) 3330–3332, https://doi.org/10.1109/20.42293.

[33] J. González, Magnetic properties arising from two additive contributions in soft magnetic nanocrystalline alloys, Appl. Phys. Lett. 85 (2004) 5944–5946, https://doi.org/10.1063/1.1833583.

[34] E. Hjortsberg, L. Nyborg, H. Vidarsson, Microscopic characterisation of topography and lubricant distribution on surface of powder compacts, Powder Metall. 48 (2005) 345–353, https://doi.org/10.1179/174329005X73711.

[35] Y. Liu, Y. Yi, W. Shao, Y. Shao, Microstructure and magnetic properties of soft magnetic powder cores of amorphous and nanocrystalline alloys, J. Magn. Magn. Mater. 330 (2013) 119–133, https://doi.org/10.1016/j.jmmm.2012.10.043.

[36] S. Ito, K. Aso, Y. Makino, S. Uedaira, Magnetostriction and magnetization of iron-based amorphous alloys, Appl. Phys. Lett. 37 (1980) 665–666, https://doi.org/10.1063/1.92029.

[37] A. Ślawska-Waniewska, H.K. Lachowicz, Magnetostriction in soft magnetic nanocrystalline materials, Scr. Mater. 48 (2003) 889–894,

https://doi.org/10.1016/s1359-6462(02)00623-1.

[38] T. Suzuki, P. Sharma, A. Makino, Extending the operational frequency range of high B_s – FeSiBP amorphous alloy to GHz by coating the powder surface with silicon oxide, J. Magn. Magn. Mater. 491 (2019) 165641, https://doi.org/10.1016/j.jmmm.2019.165641.

nanomaterials

MDPI

Article

Coercivity and magnetic anisotropy of $(Fe_{0.76}Si_{0.09}B_{0.10}P_{0.05})_{97.5}Nb_{2.0}Cu_{0.5}$ amorphous and nanocrystalline alloy produced by gas atomization process

Kenny L. Alvarez[1,2], José Manuel Martín[1], Nerea Burgos[1], Mihail Ipatov[3], Lourdes Domínguez[4] and Julián González[5,*]

[1] CEIT-IK4 and Tecnun (University of Navarra), P° de Manuel Lardizábal 15, 20018, San Sebastián, Spain; kalvarez@ceit.es (K.L.A.); jmmartin@ceit.es (J.M.M.) nburgos@ceit.es (N.B.)
[2] Escuela de Ingeniería Mecánica, Pontificia Universidad Católica de Valparaíso, Av. Brasil 2950, Valparaíso, Chile
[3] SGIker (Magnetic Measurements), University of the Basque Country, Av. Tolosa 72, 20018, San Sebastián, Spain; mihail.ipatov@ehu.es
[4] Department of Applied Physics I, Engineering School, University of the Basque Country, Plaza Europa s/n, 20018 San Sebastián, Spain; marialourdes.dominguez@ehu.es
[5] Department of Materials Physics, Faculty of Chemistry, University of the Basque Country, P° de Manuel Lardizabal 3, 20018, San Sebastián, Spain; julianmaria.gonzalez@ehu.es

* Correspondence: julianmaria.gonzalez@ehu.es

Received: 19 March 2020; Accepted: 29 April 2020; Published: 4 May 2020

Abstract: We present the evolution of the magnetic anisotropy obtained from the magnetization curve of $(Fe_{0.76}Si_{0.09}B_{0.10}P_{0.05})_{97.5}Nb_{2.0}Cu_{0.5}$ amorphous and nanocrystalline alloy produced by gas atomization process. The material obtained by this process is powder exhibiting amorphous character in the as-atomized state. Heat treatment at 480 °C provokes structural relaxation, while annealing the powder at 530 °C during 30 and 60 minutes develops a fine nanocrystalline structure. Magnetic anisotropy distribution is explained by considering dipolar effects and the modified random anisotropy model.

Keywords: gas atomization; amorphous and nanocrystalline materials; magnetic characterization; anisotropy field; soft magnetic materials.

1. Introduction

FeSiBPNbCu amorphous alloys have recently attracted the attention owing the possibility to be used as inductors and other reactors in electromagnetic devices, etc. [1–4]. In fact, in the last ten years, the amount of investigations has exponentially increased due to the industrial interest and the high demand of soft magnetic powders to be used in soft magnetic composites (SMCs) [5,6]. Due to their excellent soft magnetic properties, they are being considered for many audio-frequency applications (<100 kHz), such as transformers and inductors [7,8]. Furthermore, it has been recently demonstrated that SMCs, fabricated from nanocrystalline well-insulated particles with particle size below 20 μm, exhibit an exceptional power loss behavior at high-frequency (>1 MHz) [9,10].

These alloys can exhibit excellent soft magnetic character in the nanocrystalline state, which is developed by submitting the amorphous precursor to careful thermal treatments (typically around 550 °C between 30 and 60 minutes). As a result of such annealing, a bi-phase material is obtained with α-Fe(Si) nanograins (10-20 nm) embedded in the residual amorphous matrix. It is noteworthy that the presence of Cu is favorable for the massive precipitation of nanocrystals, whereas the presence of Nb-rich phase induces an enhancement of the effective magnetic anisotropy constant of the grain [11] and is very efficient in hindering the crystal growth to attain a nanocrystalline structure [12].

The soft magnetic behavior of Fe-based nanocrystalline alloys has been successfully explained within the framework of the random anisotropy model (RAM) proposed for amorphous alloys [13], where the anisotropy of the nanograins is averaged out and the effective anisotropy has a very low value. This situation is be favorable for achieving good soft magnetic properties in the case of nanocrystalline materials [14].

The gas atomization process has recently been used to produce Fe-rich amorphous alloys [15,16]. Such amorphous character was observed in the smallest particles (normally particles <20 μm) exhibiting low coercive field value. The addition of P, Nb and Cu elements is favorable for developing nanocrystalline structure by careful thermal treatment (at the first peak of the crystallization process) [17]. In this work the magnetic anisotropy of the $(Fe_{0.76}Si_{0.09}B_{0.10}P_{0.05})_{97.5}Nb_{2.0}Cu_{0.5}$ amorphous and nanocrystalline alloy produced by the gas atomization process is analyzed in depth.

2. Experimental details

The nominal composition $(Fe_{0.76}Si_{0.09}B_{0.10}P_{0.05})_{97.5}Nb_{2.0}Cu_{0.5}$ was produced by gas atomization. The atomization process was carried out in a convergent-divergent, close-coupled atomizer, in an atomization unit PSI model Hermiga 75/3VI (Hailsham, East Sussex, Uk). The process consisted of melting all the elements in an induction furnace under a high-purity argon atmosphere. The atomization chamber was evacuated and purged with helium to minimize oxidation. The raw material used in the process was Fe (Allied Metal Corp., Auburn Hills, MI, USA), Si (Cometal S.A., Victoria-Gasteiz, Álava, Spain), B (H.C. Starck, Müchen, Germany), Nb, Cu and Fe_3P (AMPERE alloys S.A., Sant Just Desvern, Barcelona, Spain) of commercial purity. The amount of powder atomized was approximately 2.5 kg. The process was conducted with helium at a pressure of 60 bar, and the melt temperature of 1700 °C.

Structural characterization was conducted by means of X-ray diffraction (XRD) experiments in a Philips X'pert MRD diffractometer (Malvern, UK), using the characteristic wavelength of the K_α line for Cu (λ = 1.542 Å). The diffraction angle (2ϑ) varied from 25° to 90°, at a scanning rate of 0.005°/s, in steps of 0.02° with a holding time of 4 s at each diffraction angle. The phase quantification and nanocrystal size analysis were conducted applying the internal standard method, and were determined by performing a Rietveld analysis/refinement with the software package TOPAS V6.0 (Coelho et al., Brisbane, Australia, 2016). More details about the refinement method and the procedure can be found elsewhere [17].

Isothermal heat treatments of powder were carried out in a conventional laboratory furnace CARBOLITE, RHF 14/35 (Hope Valley, UK). Samples of ~15 gr of sieved powder (<20 μm) were used for annealing in an alumina crucible. Before annealing, the chamber was purged with high purity argon (H2O $\leqslant$ 3 ppm, O2 $\leqslant$ 3 ppm CnHm $\leqslant$ 3 ppm), which constituted the annealing atmosphere. The heat treatments were conducted at three different temperatures, which were precisely controlled using a thermocouple positioned as close as possible to the powder sample: 480 and 530 °C for 30 min, and 530 °C for 60 min.

For microstructural observation, thin foil was prepared using a FEI Quanta 3D FEG (Hillsboro, OR, USA) focused ion beam (FIB) milling instrument by the lift out technique from the annealed powder sample. First, a Pt line was deposited and two stair-step FIB trenches were cut at both sides

of the area of interest. Next, the specimen was further thinned to less than 1 μm in thickness and a slice of the specimen was cut free. The obtained lamella was removed using a micromanipulator and welded to a Cu grid suitable for transmission electron microscopy (TEM) analysis. Final milling down to less than 100 nm was carried out by employing successively lower voltages up to 2 kV. The obtained specimen was examined by conventional bright-field imaging in a JEOL JEM-2100F (S) TEM microscope (Akishima, Tokio, Japan) operated at 200 kV with a LaB_6 filament.

Magnetization curves at room temperature of the non-annealed and annealed (480 and 530 °C during 30 and 60 minutes) powders were obtained using a Quantum Design PPMS-9T (San Diego, CA, USA) system with vibrating sample magnetometer (VSM) option Model P525. The step of magnetic field change near the coercive field was 5 Oe. Before the measurement of the samples, the equipment was calibrated with a paramagnetic Dy_2O_3 standard sample. The correction parameters to compensate for the magnet remanence were determined. The measurement of the paramagnetic standard demonstrates the reliability of the measurements up to units of Oe.

3. Experimental results

The most relevant structural features of the amorphous and nanocrystalline samples of this alloy were widely reported in Ref. [17] (i.e., thermal, magnetic and structural properties). Thus, the heat treatments resulted in structural relaxation and nanocrystalline structure which consists of α-Fe(Si) nanograins embedded in an amorphous residual matrix. Annealing the powder at 480 °C for 30 min resulted in structural relaxation (see Figure 1(b)), whereas annealing the powder at 530 °C provokes a massive nanocrystallization of the phase α-Fe(Si) (see Figure 1(c,d)). Increasing the annealing time from 30 min to 60 min, causes a slight increase in the nanocrystal size (from 16 to 17 nm) and a considerable increase in the crystallized fraction (from 23% to 46%) [17]. Figure 2 shows the magnetization curves of the non-annealed and annealed alloys. Table 1 summarizes several magnetic parameters that can be deduced from the hysteresis loop of the non-annealed and annealed samples. Thermal treatment at 530 °C led to the development of a fine nanocrystalline structure of α-Fe(Si) nanograins embedded in a residual amorphous matrix and as result this annealed alloy exhibited soft magnetic character (coercive field clearly lower than 1 Oe as can be seen in Table 1).

The good soft magnetic properties of gas-atomized powders allows us to assume that magnetoelastic contribution to magnetic properties can be considered negligible. The large value of H_C of these amorphous powders comparing with the same amorphous ribbons can largely be explained by the contribution of surface heterogeneities produced during the gas atomization process. The relatively high value of H_C is likely due to the pinning of the domain walls at the large surface irregularities expected in gas-atomized amorphous powders. Consequently, the magnetization reversal process is dominated by the pinning of domain walls due to the roughness of the surface of the particle.

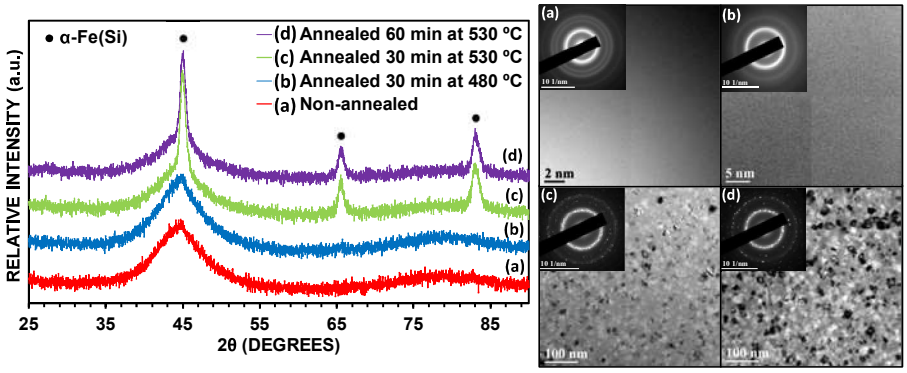

Figure 1. XRD patterns (left) and TEM images (right) of non-annealed and annealed $(Fe_{0.76}Si_{0.09}B_{0.10}P_{0.05})_{97.5}Nb_{2.0}Cu_{0.5}$ alloy. (a) Non-annealed powder; (b) Annealed powder at 480 °C for 30 min; (c) Annealed powder at 530 °C for 30 min; (d) Annealed powder at 530 °C for 60 min. Figure modified from Ref. [17].

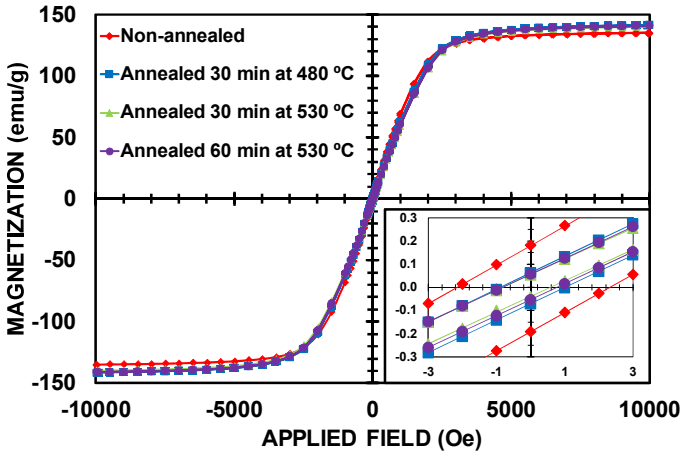

Figure 2. Hysteresis loop measured at room temperature, of the non-annealed and annealed $(Fe_{0.76}Si_{0.09}B_{0.10}P_{0.05})_{97.5}Nb_{2.0}Cu_{0.5}$ alloy with particle size <20 μm. The inset shows the hysteresis loop magnified at the origin of coordinates.

Conversely, in a multi-domain regime, the magnetization reversal process is due to the domain wall motion [18], and the domain wall propagates in an energy landscape influenced by some of the factors, such as grain boundaries, surface roughness, and defects. Therefore, the potential barriers and potential minima, the so-called pinning sites, inhibit the nucleation and propagation of the domain walls. Thus, in thinner ribbons surface irregularities act as local barriers, which may inhibit the nucleation and motion of the domain wall, during the magnetization reversal. In addition to the surface heterogeneities, the partial instability of free volume below melting point in the disorder atomic structure, known as voids, are the source of pinning sites for the domain wall motion [19,20]. The voids in amorphous metals are similar to the defects in crystalline materials and work as stress sources [21]. The fluctuation of internal stress or the number of voids can be reduced by annealing the amorphous alloys in the supercooled regime before crystallization [22]. Amorphous powders (<20 μm) were annealed in the temperature range 480-530 °C, and characterized for their soft magnetic properties. The improved soft magnetic properties could be attributed to the highly dense disorder atomic structure, and a reduced number of voids attained during the annealing process [22].

Table 1. Magnetic parameters of the non-annealed and annealed $(Fe_{0.76}Si_{0.09}B_{0.10}P_{0.05})_{97.5}Nb_{2.0}Cu_{0.5}$ alloy with particle size <20 μm.

N°	Annealing		H_C (Oe)	M_S (emu/g)	$\langle H_K \rangle$ (Oe)	FWHM (Oe)
	Temperature (°C)	Time (min)				
1	Non-annealed		2.24	139	2030	1438
2	480	30	0.94	146	2230	1241
3	530	30	0.69	144	2410	1185
4	530	60	0.81	145	2380	1200

Focusing attention on the magnetization curves of amorphous and nanocrystalline alloys, linear behavior from zero applied magnetic field near the magnetic saturation can be observed. The linear character and low coercivity indicates the presence of a strong dipolar magnetic anisotropy, while the applied magnetic field of the curvature region of the approach magnetic saturation could be assigned to the anisotropy field.

Consequently, the derivative of the magnetization with respect to the applied magnetic field allows to obtain the distribution of anisotropy field [21]:

$$P(H_K) = -H\left(\frac{d^2m}{dH^2}\right) \quad (1)$$

where $P(H_K)$ represents the probability of the anisotropy field function taking the value H of magnetic field, m is the magnetization normalized to saturation magnetization, M_S, ($m = M/ M_S$). Then, we shall suppose that no parallel anisotropy is present or, if present, the remanence has been subtracted from the magnetization curve. Figure 3 shows the anisotropy field distribution of the non-annealed and annealed samples. From the observation of the hysteresis loops, a perpendicular anisotropy is evident.

The distribution is quite sharp and asymmetric. It can be seen, the Gaussian shaped distributions are found in the non-annealed and annealed samples. The value of the applied magnetic field corresponding to the maximum of the curve is denoted as $<H_K>$ (anisotropy field). The distribution surprisingly shifts to higher $<H_K>$ increasing in the annealed samples with respect to the non-annealed sample. Nevertheless, the width of the distribution decreases in the annealed samples, which could be connected with the procedure of averaging out of the magnetocrystalline anisotropy of the nanograins. It seems that when annealing the powder, the anisotropy is better defined and the width of its distribution is smaller with respect to the non-annealed sample.

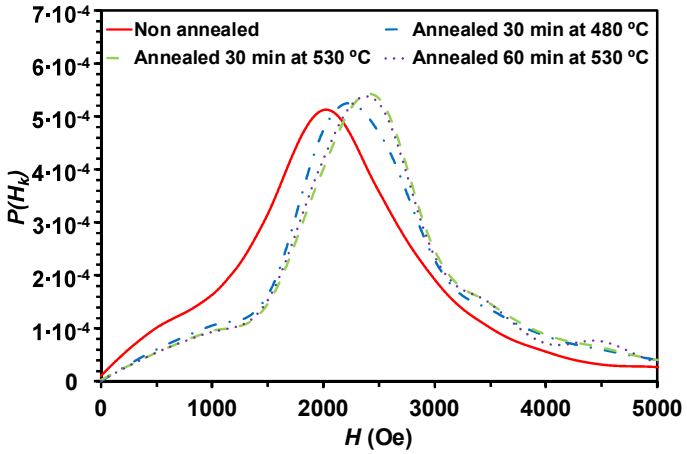

Figure3. Anisotropy field distribution of the non-annealed and annealed $(Fe_{0,76}Si_{0,09}B_{0,10}P_{0,05})_{97,5}Nb_{2,0}Cu_{0,5}$ alloy with particle size <20 μm, calculated from the approximation to the saturation in the hysteresis loops of the Figure 2.

4. Discussion

The discussion of structural and magnetic properties of soft type nanocrystalline media leads us naturally to a problem of formulation of adequate theoretical model capable of describing the behaviour of this type of media.

From purely structural point of view, one can consider nanocrystalline media as a collection of single-domain crystalline nanograins surrounded by amorphous ferromagnetic matrix having different magnetic characteristics. As it was previously suggested in [2,23], the existence of thin surface layers around the nanograins, with the different composition both from nanograins and amorphous matrix, play a relevant role. Though there is little information about the structure, composition and thickness of these hypothetical surface layers, their properties may have influence on the strength of the effective exchange interaction between single-domain crystalline nanograins and amorphous matrix. Therefore, a comprehensive model capable of describing the magnetic properties of nanocrystalline media probably has to take into account the following basic structural components: i) single-domain crystalline nanograins having randomly distributed directions of easy anisotropy axes, ii) thin surface layers surrounding the nanograins and iii) the amorphous matrix itself. The nanograins are coupled to the amorphous matrix by strong exchange interaction. There are magnetostatic interactions between nanograins, as well as between nanograins and amorphous matrix. This question is far from being solved at present.

Probably, single-domain nanograins are the only well defined structural elements of typical nanogranular media. Actually, because the grains are crystalline, they can be completely characterized by a set of phenomenological magnetic parameters, such as saturation magnetization, anisotropy constant, directions of the easy anisotropy axes, components of a tensor of magnetostriction coefficients, etc. Note that a proper description of the magnetic properties of the amorphous matrix surrounding the crystalline nanograins is a more difficult problem.

The interesting soft magnetic behaviour of Fe-based nanocrystalline alloys has been interpreted in the frame of the so-called random anisotropy model (RAM). The random anisotropy model was introduced by Harris et al. [24] to describe magnetic properties of amorphous ferromagnets and successfully applied to amorphous alloys by Alben et al. [13] and by Herzer

[25] for Fe-based nanocrystalline materials. The main statement of this model is based on the random walk considerations used earlier to explain the properties of amorphous magnetic material [26]. Namely, it is suggested that one can introduce an average anisotropy constant (Equation (2)):

$$\langle K_1 \rangle = \frac{K_1}{\sqrt{N}} \tag{2}$$

which governs the magnetization process in a nanocrystalline sample. In this expression, K_1 is the magnetocrystalline anisotropy constant of the nanocrystalline material, N is the effective number of exchanged coupled grains in the nanocrystalline sample. It is supposed that for a bulk system this quantity can be estimated as follows (Equation (3)):

$$N = \left(\frac{L_{ex}}{D_g}\right)^3 \tag{3}$$

where D_g is the average nanograin diameter and L_{ex} is the so-called 'exchange correlation length' of a nanocrystalline material. By analogy with the crystalline magnetic material, it is assumed that the exchange correlation length can be defined self–consistently taking into account the competition between the exchange energy density and the average anisotropy energy density, so that (Equation (4)):

$$L_{ex} = \eta \sqrt{\frac{A}{\langle K_1 \rangle}} \tag{4}$$

where A is the exchange constant and η is a numerical coefficient of the order of unity.

The approach based on Equations (2)-(4) seems physically very attractive. These Equations can be combined and it is easy to get the relation (Equation (5)):

$$\langle K_1 \rangle = \frac{1}{\eta^6} K_1 \left(\frac{K_1}{A}\right)^3 D_g^6 \sim K_1 \left(\frac{D_g}{\lambda}\right)^6 \tag{5}$$

where $\lambda = \sqrt{A/K_1}$ has the meaning of the domain wall width in nanocrystalline material. As we have mentioned above, according to Herzer [25], the strong dependence of the magnetic properties of nanocrystalline materials on the grain size D_g suggested by the Equation (5) is in reasonable agreement with experimental data for many nanocrystalline compositions.

From theoretical point of view, the present status of RAM does not free from certain criticism. Firstly, RAM completely ignores the existence of amorphous ferromagnetic matrix surrounding the crystalline nanograins, whereas the volume fraction of amorphous matrix in optimally annealed nanograins media is of the order of 30–40%. Next, it is implicitly assumed that in the Equation (4) the exchange constant A corresponds to the nanocrystalline material. However, the exchange interaction energy of nanograins is mainly determined by the value of the exchange interaction links existing between closest nanograins. The later may have different origin, especially if one takes into account the existence of thin layers at the surface of nanograins enriched with Nb, B and other nonmagnetic elements. Therefore, it seems incorrect to use the exchange constant A of a nanocrystalline material in the Equation (4). It worth noting also that Equation (4) is mostly written based on dimensions consideration. Moreover, in soft magnetic media there is another important correlation length, $L_0 \sim \sqrt{A}/M_S$. Probably, this characteristic length has also to be taken into account in a more general approach including the existence of magnetostatic interactions between nanograins, as well as between the nanograins and amorphous matrix.

Conversely, another important characteristic of the nanocrystalline magnetic materials should be the characteristic value of the exchange interaction links existing between the isolated nanograins and amorphous ferromagnetic matrix. It seems reasonable to introduce two kinds of exchange interaction links, $J_{1,ij}$ and $J_{2,ij}$. The first coefficients are necessary to describe the exchange interaction between nanograins and auxiliary amorphous elements, whereas the second coefficients have to describe the exchange interaction between the amorphous elements themselves to take into account the continuous character of the intergranular amorphous material. From a theoretical point of view, one can consider the coefficients $J_{1,ij}$ and $J_{2,ij}$ as the phenomenological parameters of the model. Even in this case, one can obtain interesting results to explain the behaviour of a nanograins media, at least on a qualitative level. However, to understand the properties of a nanograins media with well defined composition and

microstructure, a proper estimation of these phenomenological parameters is highly desirable.

Finally, we suggest the consideration of the presence of long-range uniaxial anisotropy associated with demagnetizing effects, K_d, which influences the exchange correlation length value and yields an anisotropy average given by [27] (Equation (6)):

$$\langle K \rangle = K_d + \frac{1}{2}\left\{\frac{\left[\left(K_d^{1/2}\right)K_1^2\right]}{A^{3/2}}\right\} \quad (6)$$

From the slope of the linear region of Figure 2, the demagnetizing factor and $\mu_0 M_S$ = 1.2 T, K_d = 10^5 J/m^3 can be roughly estimated. Taking K_1 = 8 x 10^3 J/m^3 and A = 10^{-12} J/m, the second contribution of the right term of Equation (6) is one order of magnitude lower than K_d. This second term could be assigned to $\langle K_1 \rangle$ and the high value should be linked to the influence of the strong dipolar effects inside the particle. Note that the second term of the amorphous alloy (non-annealed) should be negligible as comparing with the annealed samples, which explain the lowest $\langle H_K \rangle$ value of the non-annealed sample. When this first contribution of the right term of Equation (6) is larger than the second one, the coherent uniaxial anisotropies due mainly to demagnetizing effects and deteriorated exchange intergrain interactions dominate over the random magnetocrystalline anisotropy.

5. Conclusions

Analysis of the Gaussian anisotropy field distribution of amorphous and nanocrystalline $(Fe_{0.76}Si_{0.09}B_{0.10}P_{0.05})_{97.5}Nb_{2.0}Cu_{0.5}$ alloy obtained by gas atomization process is reported. Magnetic anisotropy could be reasonably explained in the framework of RAM, but further extension of RAM dealing with the influence of magnetostatic interactions should be of great interest to obtain more detailed information on such distribution. A description of the properties of nanocrystalline ferromagnetic materials is a very complicated theoretical problem connected to the strong dipolar interactions in this type of soft magnetic alloy prepared by gas atomization process. A further theoretical study of the dependence of the coercive field on the grain size and the temperature according to these considerations is currently in progress.

Author Contributions: Experimental data: K.L.A., N.B. and M.I.; methodology, J.M.M. and L.D.; software, M.I.; formal analysis, J.M.M., M.I. and J.G.; writing—original draft preparation, J.G.; writing—review and editing, K.L.A. and J.G. All authors have read and agreed to the published version of the manuscript.

Funding: This research received no external funding.

Acknowledgement: Author Kenny L. Alvarez thanks to Becas Chile (CONICYT) for the financial support. The authors thank SGIker of UPV/EHU for technical and human support. This work was supported by the European Commission (ERDF and ESF programs). Authors M. Ipatov, L. Domínguez and J. Gonzalez acknowledge the University of the Basque Country for the support under the scheme "Ayudas a Grupos Consolidados" (Ref. PPG17/35).

Conflicts of Interest: The authors declare no conflicts of interest.

References

1. Li, X.; Makino, A.; Kato, H.; Inoue, A.; Kubota, T. $Fe_{76}Si_{9.6}B_{8.4}P_6$ glassy powder soft-magnetic cores with low core loss prepared by spark-plasma sintering. Mater. Sci. Eng. B Solid-State Mater. *Adv. Technol.* **2011**, *176*, 1247–1250.
2. Wang, A.D.; Men, H.; Shen, B.L.; Xie, G.Q.; Makino, A.; Inoue, A. Effect of P on crystallization behavior and soft-magnetic properties of $Fe_{83.3}Si_4Cu_{0.7}B_{12-x}P_x$ nanocrystalline soft-magnetic alloys. *Thin Solid Films* **2011**, *519*, 8283–8286.
3. García-Escorial, A.; Lieblich, M.; Hernando, A.; Aragón, A.; Marín, P. Temperature dependence of the coercive field of gas atomized $Fe_{73.5}Si_{13.5}B_9Nb_3Cu_1$. *J. Alloys Compd.* **2012**, *536*, S300–S303.
4. Suzuki, T.; Sharma, P.; Jiang, L.; Zhang, Y.; Makino, A. Fabrication and Properties of Under 10 μm Sized Amorphous Powders of High B_s Soft Magnetic Alloy for High-Frequency Applications. *IEEE Trans. Magn.* **2018**, *54*, 2801705.
5. Sunday, K.J.; Taheri, M.L. Soft magnetic composites: recent advancements in the technology. *Met. Powder Rep.* **2017**, *72*, 425–429.
6. Shokrollahi, H.; Janghorban, K. Soft magnetic composite materials (SMCs). *J. Mater. Process. Technol.* **2007**, *189*, 1–12.
7. Zhang, Y.; Sharma, P.; Makino, A. Fe-Rich Fe-Si-B-P-Cu Powder Cores for High-Frequency Power Electronic Applications. *IEEE Trans. Magn.* **2014**, *50*, 2006804.
8. Chang, L.; Xie, L.; Liu, M.; Li, Q.; Dong, Y.; Chang, C.; Wang, X.M.; Inoue, A. Novel Fe-based nanocrystalline powder cores with excellent magnetic properties produced using gas-atomized powder. *J. Magn. Magn. Mater.* **2018**, *452*, 442–446.

9. Silveyra, J.M.; Ferrara, E.; Huber, D.L.; Monson, T.C. Soft magnetic materials for a sustainable and electrified world. *Science.* **2018**, *362*, eaao0195.

10. Alvarez, K.L.; Baghbaderani, H.A.; Martín, J.M.; Burgos, N.; Ipatov, M.; Pavlovic, Z.; Mccloskey, P.; Masood, A.; Gonzalez, J. Novel Fe-based amorphous and nanocrystalline powder cores for high-frequency power conversion. *J. Magn. Magn. Mater.* **2020**, *501*, 166457.

11. García-Escorial, A.; Lieblich, M.; López, M.; Marín, P. Microstrucural characterization of gas atomized $Fe_{73,5}Si_{13,5}B_9Nb_3Cu_1$ and $Fe_{97}Si_3$ alloys. *J. Alloys Compd.* **2011**, *509*, 239–242.

12. Gheiratmand, T.; Hosseini, H.R.M. Finemet nanocrystalline soft magnetic alloy: Investigation of glass forming ability, crystallization mechanism, production techniques, magnetic softness and the effect of replacing the main constituents by other elements. *J. Magn. Magn. Mater.* **2016**, *408*, 177–192.

13. Alben, R.; Becker, J.J.; Chi, M.C. Random anisotropy in amorphous ferromagnets. *J. Appl. Phys.* **1978**, *49*, 1653–1658.

14. Herzer, G. Modern soft magnets: Amorphous and nanocrystalline materials. *Acta Mater.* **2013**, *61*, 718–734.

15. Alvarez, K.L.; Martín, J.M.; Ipatov, M.; Gonzalez, J. Soft magnetic amorphous alloys (Fe-rich) obtained by gas atomisation technique. *J. Alloys Compd.* **2018**, *735*, 2646–2652.

16. Alvarez, K.L.; Martin, J.M.; Ipatov, M.; Dominguez, L.; Gonzalez, J. Magnetic Properties of Annealed Amorphous $Fe_{72,5}Si_{12,5}B_{15}$ Alloy Obtained by Gas Atomization Technique. *IEEE Trans. Magn.* **2018**, *54*, 2002405.

17. Alvarez, K.L.; Martín, J.M.; Burgos, N.; Ipatov, M.; Dominguez, L.; Gonzalez, J. Structural and magnetic properties of amorphous and nanocrystalline Fe–Si–B–P–Nb–Cu alloys produced by gas atomization. *J. Alloys Compd.* **2019**, *810*, 151754.

18. Ahmadian, H.; Masood, A.; Pavlovic, Z.; Alvarez, K.L.; Ómathúna, C.; Mccloskey, P.; Stamenov, P. On the mechanisms limiting power loss in amorphous CoFeB-based melt- spun ribbons. *J. Magn. Magn. Mater.* **2020**, *502*, 166535.

19. Bitoh, T.; Makino, A.; Inoue, A. Origin of low coercivity of Fe-(Al, Ga)-(P, C, B, Si, Ge) bulk glassy alloys. *Mater. Trans.* **2003**, *44*, 2020–2024.

20. Bitoh, T.; Makino, A.; Inoue, A. Quasi-Dislocation Dipole-Type Defects and Low Coercivity af Fe-Based Soft Magnetic Glassy Alloys. *J. Metaestable Nanocrystalline Mater.* **2005**, *24–25*, 427–430.

21. Barandiarán, J.M.; Vazquez, M.; Hernando, A.; Gonzalez, J.; Rivero, G. Distribution of the magnetic anisotropy in amorphous alloys ribbons. *IEEE Trans. Magn.* **1989**, *25*, 3330–3332.

22. Masood, A.; Ström, V.; Belova, L.; Rao, K. V.; Ågren, J. Effect of Ni-substitution on glass forming ability, mechanical, and magnetic properties of FeBNbY bulk metallic glasses. *J. Appl. Phys.* **2013**, *113*, 013505.

23. Szumiata, T.; Zuberek, R.; Gonzalez, J.; Ślawska-Waniewska, A.; Szymczak, H. Model of surface magnetostriction in nanostructured materials. *J. Magn. Magn. Mater.* **1999**, *203*, 262–264.

24. Harris, R.; Plischke, M.; Zuckermann, M.J. New model for amorphous magnetism. *Phys. Rev. Lett.* **1978**, *31*, 160–162.

25. Herzer, G. Grain size dependence of coercivity and permeability in nanocrystalline ferromagnets. *IEEE Trans. Magn.* **1990**, *26*, 1397–1402.

26. Herzer, G. Soft magnetic nanocrystalline materials. *Scr. Metall. Mater.* **1995**, *33*, 1741–1756.

27. Suzuki, K.; Herzer, G.; Cadogan, J.M. The effect of coherent uniaxial anisotropies on the grain-size dependence of coercivity in nanocrystalline soft magnetic alloys. *J. Magn. Magn. Mater.* **1998**, *177–181*, 949–950.

Paper in preparation

Novel methodology to predict amorphisation capability of Fe-Si-B soft magnetic powders

Kenny L. Alvarez[a, b*], H. A. Baghbaderani[c, d], J. M. Martín[a, b], N. Burgos[a, b], P. McCloskey[c], Julian Gonzalez[e], A. Masood[c]

[a] *CEIT-Basque Research and Technology Alliance (BRTA), Manuel de Lardizabal 15, 20018, San Sebastián, Spain*
[b] *Universidad de Navarra, Tecnun, Manuel de Lardizabal 15, 20018, San Sebastián, Spain*
[c] *Tyndall National Institute, University College Cork, Lee Maltings Complex, Dyke Parade, T12R5CP, Cork, Ireland*
[d] *School of Physics and CRANN, Trinity College, Dublin 2, Ireland*
[e] *Department Materials Physics, Faculty of Chemistry, University of the Basque Country, P° Manuel de Lardizábal 3, 20018, San Sebastián, Spain*

Abstract

The present work is focused on developing accurate amorphisation capability criteria of Fe-Si-B powders, which can be used to design soft magnetic material alloy compositions. The amorphous forming ability (AFA) of Fe-Si-B powders was initially evaluated by conventional empirical glass forming parameters and later extended to the CALPHAD methodology combined with the topological instability factor (λ). This was achieved by gas-atomising the powders, performing the structural characterisation, investigating the thermal properties and calculating the amorphous fraction, *AF* (%), of the powders. In the first step, the AFA of Fe-Si-B alloys was evaluated using the conventional empirical glass forming parameters (ΔH^{mix}, α- and β-parameters), which, unfortunately, did not accurately predict the amorphisation capability of the powders. As a second step, the critical cooling rate (R_C), critical particle size (d_C), and λ-factor were calculated using mathematical models. These were superimposed to the ternary Fe-Si-B phase diagram, calculated using CALPHAD methodology, to find the region of best AFA. The alloy with the highest amorphisation capability (*AF* = 100%) in Fe-Si-B system was only realised when optimum atomic size mismatch remained in the vicinity of λ = 0.204. Not all regions in the phase diagrams were promising to design an alloy with high *AFA*, except where Fe_2B phase precipitates after equilibrium solidification. Within these two limits, the alloys with lower liquidus temperatures (T_l), i.e., closer to the eutectic point, successfully maintained higher amorphisation capability. The proposed evaluation criteria of Fe-Si-B alloys can be used as a tool to design future amorphous or glassy alloys with high amorphisation capability suitable for fabrication using different methods.

* Corresponding author Tel.: + 34 943 212 800
Email address: kalvarez@ceit.es/kenny.alvarez@pucv.cl (K. L. Alvarez).
https://doi.org/XXXX

Keywords: Amorphous forming ability, glass forming ability, amorphous materials, gas atomization, soft magnetic powders.

1. Introduction

Since the discovery of disordered alloys by P. Duwez et al. [1] in the 1960s, amorphous metals have been extensively investigated for fundamental as well as technological applications, including structural, biomedical, aerospace, and energy conversion [2]. Amorphous metals are metastable materials, conventionally solidified in ~20–30 μm ribbons at ultra-high cooling rates (~10^6 K/s), and maintain an atomic structure exhibiting only short-range order. If the short-range atomic order of amorphous alloys is similar to the precursor melt and concurrently reveal a distinct glass transition temperature (T_g) well below the crystallisation temperature (T_X), the alloys are known as "metallic glasses (MGs)" [3,4]. Contrary to amorphous metals, MGs can be solidified at phenomenally low cooling rates (as low as natural cooling) [5]. The functionality of MGs can be remarkably augmented if the glass forming ability (GFA), i.e., ease of glass formation, which determines the critical cooling rate, can be substantially increased. Glass formation involves the thermal stability of the liquid phase and the crystallisation dynamics upon the cooling of melts [6]. To synthesise MGs at modest cooling rates, the kinetics of phase transformation and the mechanism of glass formation has emerged as an intriguing subject [7]. However, why only specific alloys retain significant amorphisation capability, while others show a high degree of crystallisation during solidification, remains an open question to the material science community [7,8].

A large number of empirical glass forming parameters have been proposed to predict the GFA of alloys, though the origin of all the criteria relies on the classical nucleation and growth theory [6]. For example, Turnbull demonstrated that when the reduced glass transition temperature (T_{rg} = T_g/T_l, being T_l the liquidus temperature) is higher than 2/3, the homogenous crystal nucleation rate decreases, as a result the crystallisation kinetic becomes more sluggish [9,10]. Similarly, Donald & Davies [11] proposed a simple way to estimate the GFA of alloys with two or more elements using the rule of mixture liquidus temperature (ΔT^*). Furthermore, Inoue formulated three empirical rules to predict the GFA, stating as; (i) alloy must contain at least three elements, (ii) constituents should include a significant atomic size difference (≥12 %) and (iii) a negative heat of mixing among the major constituents is preferable [12,13]. Several other GFA

parameters have been discovered, including ΔT_X [14], S [15], γ [16], δ [17], $\emptyset$ [18], γ_m [19], ω [20], and new β [21]. All these parameters use T_g to estimate the GFA. Despite all these parameters have demonstrated to be sufficiently accurate to measure the GFA of alloys, the critical cooling rate, R_c and critical diameter, D_{max} are still the most direct and quantifiable parameters. Since R_c and D_{max} are challenging to be measured, other criteria like P' [22], σ [23], λ [24], α (= T_X/T_l) and β (= 1 + α) [25] have been developed, even for conventional amorphous alloys where T_g is not obvious. However, none of criterion is valid for a broad range of MGs. Conventionally, the field of amorphous metals is based on empirical rules that is a trial-and-error approach; it is time-consuming and costly, hence designing alloys with high amorphous forming ability (AFA) using thermodynamic modelling would be a step forward.

Among the broad range of amorphous metals, Fe-based alloys are of significant importance for their high demand in power conversion applications [26,27]. One of the most investigated systems is Fe-Si-B, thanks to its unique capability to retain exceptional soft magnetic properties, high corrosion resistance and excellent mechanical properties [28]. Fe-Si-B alloys are generally melt-spun into ~20 μm amorphous ribbons at ultra-high cooling rates [29]. One of the fundamental drawbacks of melt-spun ribbons is their shape, which restricts them to ring shape wound core deployment, and hence limits the high-flux concentration advantage for a broad range of applications. Contrary to that, amorphous powders provide the flexibility to make complex shaped cores, hence is considered as a superior material for technological applications [30,31]. Amorphous powders are usually produced by gas-atomisation, which is a well-industrialised mass production technique to produce micron size powders. This process consists of breaking the liquid melt stream into droplets by using a supersonic gas flow. However, one of the fundamental limits of gas-atomisation is the low cooling rate (~10^4–10^5 K/s) as compared to melt-spinning [32]. If GFA of the alloys is not sufficiently high, the powders could exhibit a crystalline structure, deteriorating the soft magnetic performance and making them unsuitable for power conversion applications. Therefore, designing Fe-based alloys with high AFA that can be atomised as amorphous powders is essential to fully take advantage of the high-flux concentration capabilities of these novel materials.

The present work is focused on establishing amorphisation capability criteria for Fe-Si-B powders by combining the CALPHAD (CALculation of PHAse Diagram) methodology with topological instability

factor (λ). This was achieved by selecting Fe-Si-B alloys within the high GFA region of the ternary phase diagram (Fe-rich). These alloys were gas-atomised into powders and in the first step, the amorphisation capability of the alloys was evaluated using conventional empirical parameters, such as enthalpy of mixing, ΔH^{mix}, α-, and β-parameters. Finally, the CALPHAD methodology was combined with λ to obtain the highest amorphisation capability region inside the ternary Fe-Si-B system.

2. Materials and methods

The compositions of Fe-Si-B alloys were selected within the glass-forming region of the ternary phase diagram, as reported in the bibliography [33–35]. The gas atomisation experiments were carried out using a convergent-divergent, close-coupled atomiser in an atomisation unit PSI model Hermiga 75/3VI. Eleven different compositions of the ternary Fe-Si-B system were atomised (see compositions in Table I). Regarding the raw materials, iron (supplied by Allied Metal Corp.), silicon (supplied by Cometal S.A.) and boron (supplied by H.C. Starck) of commercial purity were melted in an induction furnace. First, the chamber was purged with helium in order to evacuate the oxygen and avoid oxidation. Then, the temperature was increased by induction heating up to the melt temperature. The amount of powder produced per batch was nearly 2.5 kg. Helium at a pressure of 60 bar was used as atomising gas. The melt temperature in the furnace was 1700 °C for all the compositions.

Thermal transitions were analysed by Differential Scanning Calorimetry (DSC). The powders were analysed using a TA Instrument DSC 2920. The experiments were performed using a sample of about 10 mg on a copper pan with a lid, at a heating rate of 10 °C/min up to 700 °C and under an argon atmosphere. The crystallisation temperatures (T_X), crystallisation enthalpies (ΔH_C) and energy released by partially amorphous powders (as-atomised, ΔH) were obtained from these experiments.

Structural characterisation of the powders was carried out via X-ray diffraction (XRD), using a diffractometer (Philips PW1825) and the characteristic wavelength of K_α line for Cu (λ = 1.542 Å). The diffraction angle (2θ) varied from 25 ° to 90 ° at a scanning rate of 0.005 °/s, in steps of 0.02 ° with a holding time of 4 s at each diffraction angle.

Thermodynamic calculations and modelling have been carried out using PANDAT™ version 2019, using the thermodynamic database for multi-component Fe-rich alloys PanIron. PANDAT™ is an integrated

computational tool developed based on CALPHAD (CALculation of PHAse Diagram) approach for multi-component phase diagram calculation and materials property simulation. The liquidus temperatures (T_l) reported in this paper were calculated using this software.

The particle size distribution of the powders was measured by laser diffraction in an instrument Sympatec Helos (H0852). The true density was measured in a He pycnometer Micrometrics Accupyc 1330.

3. Results and discussion

3.1 Structural analysis of the powders

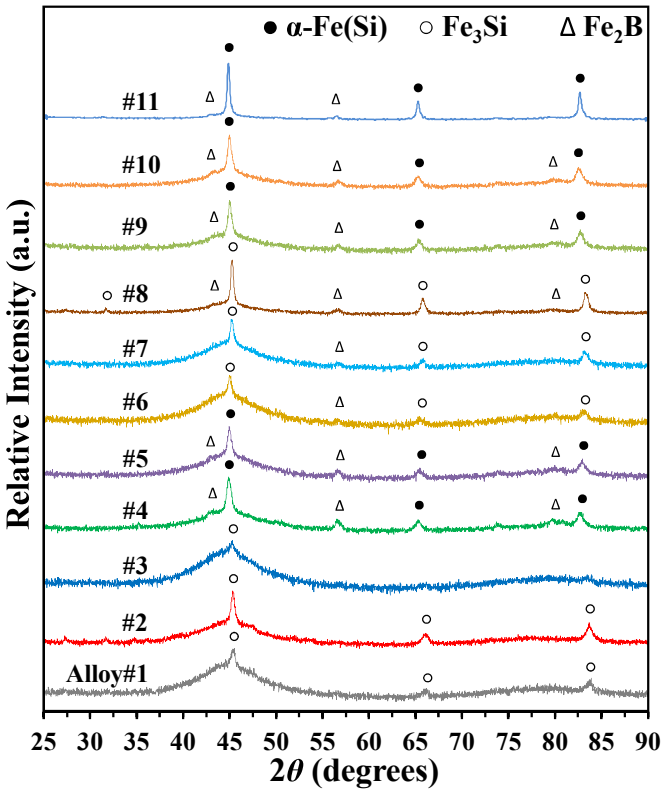

Fig. 1. XRD patterns of the as-atomised powders of alloy#1–11.

XRD patterns of the as-atomised powders, presented in Fig.1, shows the precipitation of different crystalline phases during the solidification process, which were identified as α-Fe(Si), Fe_2B and Fe_3Si. Broads peaks

between 2θ = 35 and 55° along with sharp Bragg's peaks indicate the simultaneous formation of amorphous and crystalline phases on gas-atomisation of alloy#1-10. Nevertheless, alloy#11 shows only sharp Bragg's peak at 2θ = 45° without a broad halo, showing the full crystalline state of the powder. Interestingly, the peak broadening in each alloy is different, indicating the varying weight fraction of amorphous and crystalline structures in each composition. For instance, alloy#3 shows a single broad peak at 45 ° (2θ) with a little shoulder kink, demonstrating the highest weight fraction of the amorphous phase in the investigated alloys. The small peak in alloy#3 is due to surface crystallisation of the largest particles (i.e., >100 μm) due to the nature of the production process [36,37].

The cooling rate in gas atomisation is inversely proportional to the particle size (see Appendix A) [32], suggesting that the amorphisation is more likely in the smaller particle size fraction in each alloy. Accordingly, the as-atomised powders were sieved to separate the fraction <20 μn. The XRD patterns of the sieved powders (<20 μm), presented in Fig. 2(a), show only a broad halo between 35 and 55° (2θ) to confirm the amorphous nature of alloy#1, #3, #6 and #7. Contrary to that, the other alloys (alloy#2, #4, #5, #8, #9, and #10) reveal Bragg's peaks of the crystalline phases, identified as α-Fe(Si), Fe_2B and Fe_3Si. Interestingly, the relative intensity of the crystalline peaks of sieved powders (<20 μm) was significantly smaller than the as-atomised powders (see Fig 1), confirming the higher weight fraction of amorphous particles in the fraction <20 μm as compared to as-atomised. The higher amorphous fraction of sieved powders can be utilised as an "amorphisation capability indicator" for the alloys. On the other hand, the absence of broadening between 35 and 55° (2θ) in the fraction <10 μm of alloy#11 confirms the fully crystalline character.

Furthermore, in order to find the particle size below which fully amorphous structure can be found, the partially crystalline powders in the fraction <20 μm (Fig. 2(a)) were further sieved to separate the fraction <10 μm. As can be seen in the XRD patterns shown in Fig. 2(b), the absence of Bragg's peaks in the fraction <10 μm of alloy#2, #4, #5 and #9 confirms the amorphous nature of particles below the 10 μm. Conversely, the alloy#8 and #10 exhibit crystalline structure even in the particles <10 μm, which indicates the low amorphisation capability of these alloys.

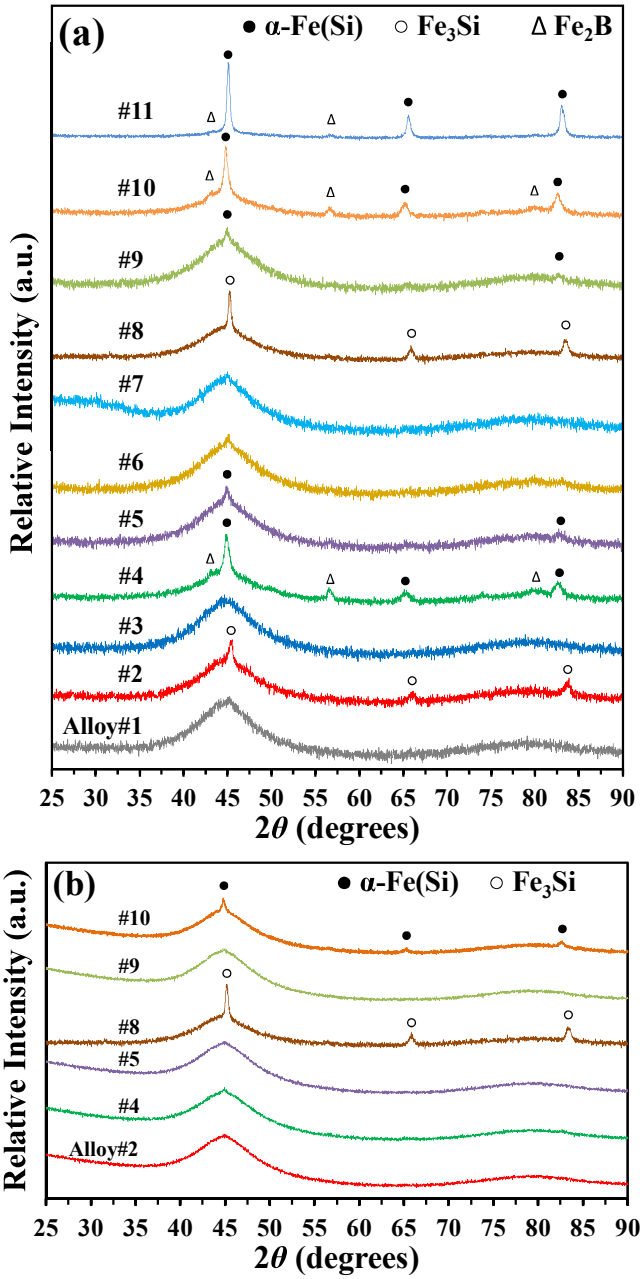

Fig. 2. a) XRD patterns of the sieved powders (<20 μm) of alloy#1–11 and (b) XRD patterns of the sieved powders (<10 μm) of alloy# 2, #4, #5 and #8–10.

Fig. 3 presents the nature of crystalline phases formed as a function of Si and B content. Other authors have reported regions where the different phases can be formed according to the Si and B content in ternary Fe-Si-B alloys [38] (Fe-rich). These regions are represented in Fig. 3 and can be identified as follow: below the dotted line (region-I), between dotted and dashed line (region-II) and above the dashed line (region-III). It is evident that the crystallisation of α-Fe(Si) (B2) phase takes place in region-I and the ordered Fe_3Si (DO_3) phase crystallises in region-II, which agrees with the reported elsewhere [38]. On the other hand, an unknown phase is formed in region-III that cannot be confirmed by this work due to no composition was produce within this region. Nevertheless, it has been demostrated that when the Si and B content exceeds 30 at.%, the phase $Fe_{4.9}Si_2B$ precipitates [38,39]. Consequently, it can establish an upper and lower limit for the formation of α-Fe(Si) and Fe_3Si considering the amount of Si and B content. In addition, Fe_2B phase precipitates in some as-atomised alloys (see Fig. 1), though no correlation between the Fe_2B and Si and B content can be established.

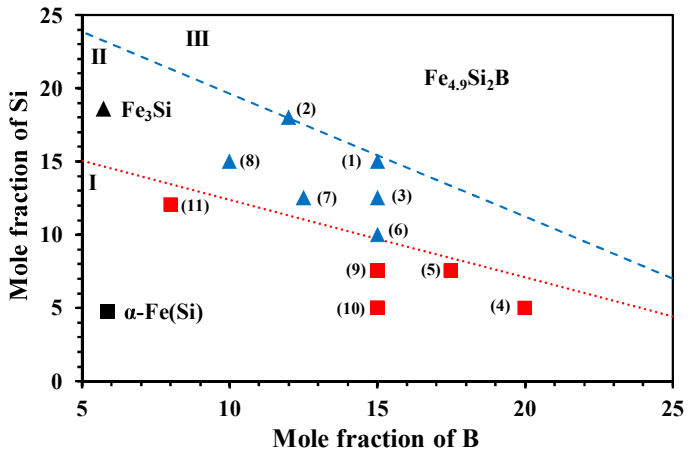

Fig. 3. Mole fraction of Si versus mole fraction of B showing the limit for the formation of the phases α-Fe(Si) (■) and Fe_3Si (▲), according to the XRD results shown in Fig. 1 of the as-atomised alloys (alloy#1–11).

3.2 Amorphous fraction (AF) of as-atomised powders

The thermal transitions of the as-atomised powders were analysed using DSC, as presented in Fig. 4. The crystallisation starts in a broad temperature range, i.e., T_X is comprised between 489 and 553 °C, as summarised in Table I. The powders reveal one, two or three exothermic events, depending on the crystallisation mode of the alloys (i.e., polymorphous, primary or eutectic crystallisation [13]). Alloy#1 exhibits

only one crystallisation peak that corresponds to the simultaneous crystallisation of Fe_3Si and Fe_2B phases, i.e., eutectic crystallisation mode. In the alloys possessing two crystallisation peaks (alloy#2, #4, #5, #6, #8, #9 and #10), the first peak is linked to the crystallisation of α-Fe(Si) or Fe_3Si, and the second one corresponds to the precipitation of Fe_2B. On the other hand, alloy#3 and #7 exhibit more than two peaks: the first peak is linked to the crystallisation of α-Fe(Si) or Fe_3Si, the second one corresponds to the precipitation of the metastable Fe_3B phase and the third peak is due to phase transformation from Fe_3B to stable Fe_2B [40,41].

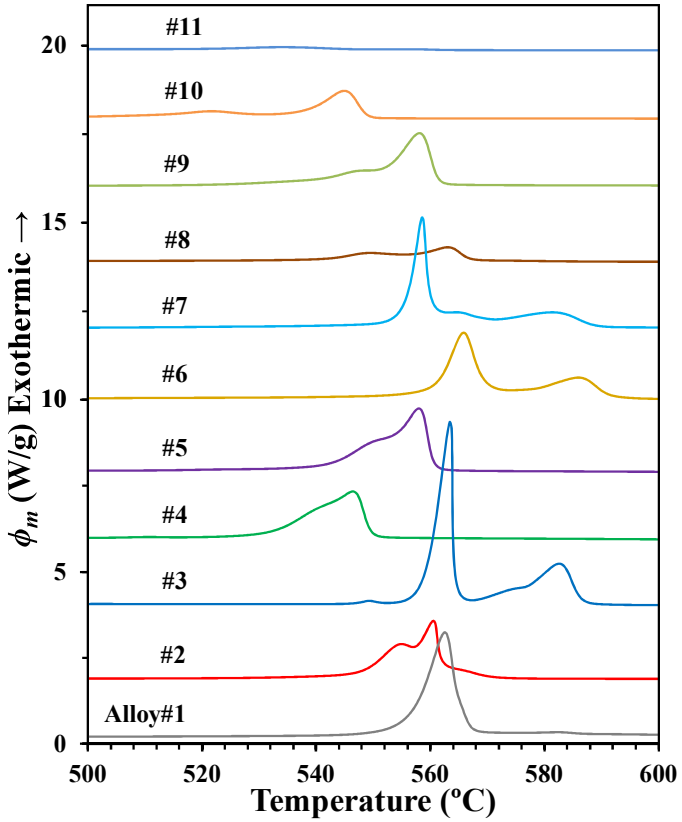

Fig. 4. DSC traces of the as-atomised powders of alloy#1–11.

The multi-crystallisation peak characteristic observed in alloy#2–10 is attributed to the primary crystallisation mode, in which the Si-rich phase precipitates in the remaining amorphous, which at the same time is enriched with B atoms [38,42,43]. Moreover, overlapped exothermic peaks in some alloys show that the crystallisation of the second and/or third phase starts

even before the completion of the previous phase. The sharp peak characteristic observed in some alloys (alloy#1, #3 and #7) indicates the compositional homogeneity of the crystallites precipitated during heating.

Table I. DSC results of the as-atomised and sieved powders[1].

Alloy#	Composition (at.%)	T_X (°C)	ΔH_C (J/g)	ΔH (J/g) (as-atomised powder)	AF (%)
1	$Fe_{70}Si_{15}B_{15}$	557	161.0	132.0	82
2	$Fe_{70}Si_{18}B_{12}$	547	166.0	91.0	55
3	$Fe_{72.5}Si_{12.5}B_{15}$	547	170.0	170.0	100
4	$Fe_{75}Si_5B_{20}$	530	178.8	95.5	54
5	$Fe_{75}Si_{7.5}B_{17.5}$	542	178.0	113.0	63
6	$Fe_{75}Si_{10}B_{15}$	553	179.0	146.0	82
7	$Fe_{75}Si_{12.5}B_{12.5}$	547	164.0	134.0	82
8	$Fe_{75}Si_{15}B_{10}$	528	184[2]	49.4	27
9	$Fe_{77.50}Si_{7.5}B_{15}$	525	173.0	111.0	64
10	$Fe_{80}Si_5B_{15}$	489	---	70.6	<27
11	$Fe_{80}Si_{12}B_8$	---	---	---	0

[1] T_X: crystallisation temperature; ΔH_C: crystallisation enthalpy; ΔH: area of exothermic peak of partially amorphous powders (as-atomised); AF: amorphous fraction calculated with Eq. (A.5) shown in Appendix A.
[2] Value obtained from Ref [45,46].

The crystallisation enthalpy (ΔH_C) i.e., the area under the crystallisation peak of a fully amorphous alloy, of the powders was used to calculate the amorphous fraction of the powders in the as-atomised state [44]. A partially amorphous structure results in the reduction of the energy released during crystallisation, and consequently, the area of the exothermic peak is reduced. This reduction is proportional to the crystalline phase existing in the sample and can be used as an instrument to measure the weight fraction (%) of the amorphous phase. The ΔH_C of the amorphous powders of each alloy, obtained after sieving process and later confirmed by XRD (see Fig. 2), was measured and compared with the area of the exothermic peaks of partially amorphous powders (as-atomised, ΔH) using Eq. A.5 (see Appendix A). Due to alloy#8 and #10 exhibited Bragg's peak even in the fraction <10 μm (see Fig. 2(b)), ΔH_C of the amorphous structures could not be estimated. The ΔH_C of alloy#8 was obtained from the literature [45,46], while for alloy#10, ΔH_C was considered as the area of the exothermic peak of partially amorphous particles of the fraction <10 μm; consequently, AF of alloy#10 is presented as a range. The amorphous fraction (AF) of the as-atomised powders is summarised in Table I. Alloy#3 reveals 100% of

amorphous fraction in the series of investigated alloys, which is in good agreement with XRD results (see Fig. 1). Furthermore, alloy#1, #6, and #7 revealed AF = 82%, which is the second-highest AF among the investigated alloys. The AF of alloy#2, #4, #5 and #9 remained in the range of 54–64%. On the other hand, the AF of alloy#8 and #10 were estimated as 27% and <27%, respectively, denoting the low amorphisation capability of these alloys. However, the AF of alloy#11 was found zero; the negligible exothermic peak in the range of 500–550 °C of alloy#11 (see Fig. 4) shows the presence of a minor amount of amorphous phase related to the very small amorphous particles (≲1 μm) that may have produced during atomisation.

3.3 Evaluation of amorphisation capability of the alloys

The AF is a good measure of the amorphisation capability of alloys and other parameters can be derived further using AF, such as the critical particle size, d_C, and critical cooling rate, R_C (see Appendix A for the calculation procedure). The AF, d_C, and R_C can be used to show how conventional empirical criteria are useful in predicting the amorphisation capability of the gas-atomised powders. Different conventional amorphisation capability parameters of the investigated alloys were calculated and are summarised in Table II. Since the alloys were amorphous and did not show any glass transition (or supercooled liquid region) in the DSC traces (see Fig. 4), only parameters that do not use T_g were analysed to estimate the AFA. Alloy#3 ($Fe_{72.5}Si_{12.5}B_{15}$) was atomised into 100% AF (along with largest d_C ~96 μm and lowest R_C ~6.3 × 10^4 K/s among others), suggesting that it has the highest amorphisation capability within the series of investigated alloys.

According to Inoue's empirical rules [12], the enthalpy of mixing, ΔH^{mix}, significantly favours the formation of amorphous structure and is a good measure of the AFA. The more negative the ΔH^{mix}, the higher the AFA of an alloy. The enthalpy of mixing of the alloys is summarised in Table II; the detailed calculation procedure is reported elsewhere [47]. Interestingly, ΔH^{mix} does not correlate with the AF; the most negative ΔH^{mix} was observed for alloy#2, which was produced partially amorphous (AF = 55%). The most negative ΔH^{mix} coincides with the alloys showing lowest T_l, and consequently, closest to the deepest eutectic point (see Table II). Similarly, no correlation was established for α- and β-parameters with the highest AF of the alloys [25], being the largest values of α ~0.480 and β ~1.480 for the

alloy#2 that was only produced with AF = 55 % (with small d_C ~16.7 μm and high R_C ~2.1× 10^6 K/s).

Table II. Amorphisation capability parameters*.

Alloy#	Composition (at.%)	AF (%)	ΔH^{mix} (kJ/mol)	α (= T_X/T_l)	β (= 1 + α)	d_C (μm)	R_C (K/s)	T_l (°C)	λ-factor
1	$Fe_{70}Si_{15}B_{15}$	82	-268800	0.469	1.469	43.6	3.0E+05	1188	0.220
2	$Fe_{70}Si_{18}B_{12}$	55	-275856	0.480	1.480	16.7	2.1E+06	1139	0.214
3	$Fe_{72.5}Si_{12.5}B_{15}$	100	-250475	0.452	1.452	96.1	6.3E+04	1210	0.204
4	$Fe_{75}Si_5B_{20}$	54	-214100	0.411	1.411	21.5	1.2E+06	1290	0.197
5	$Fe_{75}Si_{7.5}B_{17.5}$	63	-222600	0.431	1.431	30.9	6.0E+05	1257	0.193
6	$Fe_{75}Si_{10}B_{15}$	82	-230400	0.453	1.453	43.3	3.1E+05	1220	0.188
7	$Fe_{75}Si_{12.5}B_{12.5}$	82	-237500	0.465	1.465	55.4	1.9E+05	1177	0.183
8	$Fe_{75}Si_{15}B_{10}$	27[2)]	-243900	0.447	1.447	8.8[2)]	7.6E+06[2)]	1180	0.179
9	$Fe_{77.50}Si_{7.5}B_{15}$	64	-208575	0.431	1.431	31.8	5.8E+05	1217	0.172
10	$Fe_{80}Si_5B_{15}$	<27	-185000	0.407	1.407	<10.0	>5.8E+06	1202	0.156
11	$Fe_{80}Si_{12}B_8$	0	-206336	---	---	---	---	1261	0.143

[1)] AF: amorphous fraction calculated with Eq. A.5 shown in Appendix A; ΔH^{mix}: enthalpy of mixing calculated by the procedure shown in Ref. [47]; α and β: GFA parameters [25]; d_C: critical particle size calculated following the procedure shown in Appendix A; R_C: critical cooling rate estimated with Eq. A.6 shown in Appendix A; T_l: liquidus temperature calculated by PANDAT™; λ-factor: calculated by E1. (1).
[2)] Values calculated based on the crystallisation enthalpy obtained from amorphous wires from Ref [45,46] (see also Table I).

3.4 Establishing the amorphisation criteria for the alloys

The *AFA* was evaluated by combining thermodynamic modelling and topological instability factor (λ) of the Fe-Si-B alloys. The liquidus surface projection (blue lines) of the Fe-Si-B phase diagram in the vicinity of Fe-rich zone is presented in Fig. 5(a). Isothermal lines (solid green) are drawn to show how T_l decreases towards the eutectic point E1. In addition, it displays the primary stable phases just below liquidus temperature in the equilibrium condition as well as all Fe-Si-B alloys investigated in the present study (see numbered black spots in Fig. 5(a)).

The λ-factor of the Fe-Si-B alloys was calculated using Eq. (1), which only considers topological aspects and was initially proposed for binary alloys [24] and later extended to multi-component systems by Yan *et al.* [48]. This parameter describes the minimum solute concentration needed for producing a material as amorphous, and is defined as:

$$\lambda = \sum_{i=B}^{Z} C_i |(r_i/r_A)^3 - 1| \quad (1)$$

where C_i is the solute atomic concentration (mole), r_i is the solute atomic radius (nm), and r_A is the solvent atomic radius (nm). Assuming the fact that amorphous metals comprise of several icosahedra clusters, it has been proven that the optimal glass formation for numerous multi-component alloys is acquired when $\lambda = 0.18$ [48]. Recently, λ-factor, along with CALPHAD methodology, was reported to predict the glass forming ability for ternary Zr-Fe-Al [49] and Fe-Nb-B [50] bulk metallic glasses produced by Cu-mould casting, showing that the optimal λ-factor can change from 0.14 to 0.22 depending on the composition. Consequently, in order to obtain the optimal λ-factor for a given ternary system, λ-factor should be evaluated experimentally.

Table II shows λ-factor calculated for all the investigated alloys, showing the variation in the range of 0.143–0.220. On the other hand, Fig. 5(b)–(d) displays three amplified regions of Fig. 5(a), where λ-factor lines are superimposed on the liquidus surface projection in a range of 0.14–0.23 as well as isothermal lines showing how T_l decreases towards the deepest eutectic composition E1. In this figure it is possible to identified: i) *AF* estimated for all the investigated alloys and represented as percentages (see Fig. 5(b)), ii) estimated R_C for all the investigated alloys (see Fig. 5(c)), and iii) estimated locus of constant R_C for 1.0×10^5 K/s (red dashed line), 5.0×10^5 K/s (red dash-dotted line) and 1.0×10^6 K/s (red two-dashed line) (see Fig. 5(d)).

All these parameters make possible to analyse the AFA of Fe-Si-B alloys classifying the compositions into three groups, depending on the first solid phase formed upon equilibrium solidification (i.e., BCC, Fe_5SiB_2 and Fe_2B), their T_l and the λ-parameter, as listed in Table II.

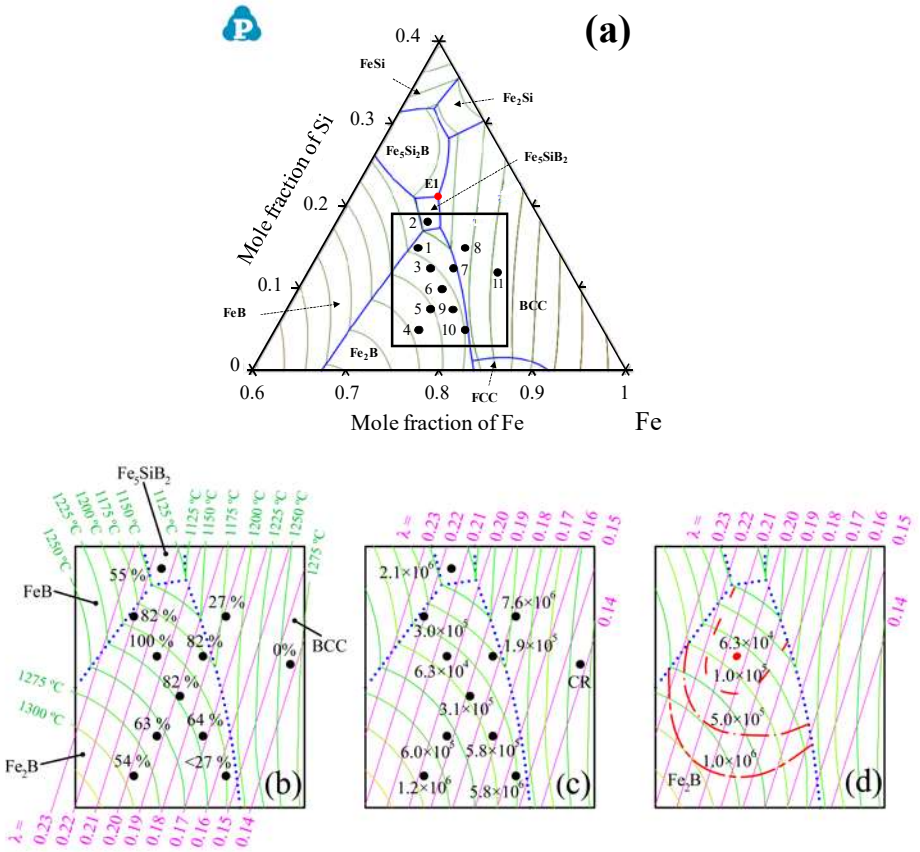

Fig. 5. a) Liquidus surface projection (solid blue line) of the ternary Fe-Si-B diagram in the Fe-rich zone showing the investigated alloys, eutectic point E1 and first equilibrium solid phase formed upon solidification; b) Amplified region showing λ-factor lines (solid magenta lines), *AF* of all the investigated alloys and isotherms every 25 °C; c) R_C of all the investigated alloys; d) Estimated locus of constant R_C for 1.0×10^5 K/s (red dashed line), 5.0×10^5 K/s (red dash-dotted line) and 1.0×10^6 K/s (red two-dashed line).

i. **BCC**: two alloys were atomised within this region, being one fully crystalline (alloy#11) and the other with *AF* = 27% (alloy#8). Lowering the T_l plays a significant role in the amorphisation capability of alloys in this region; reducing T_l from 1261 °C (alloy#11) to 1180 °C (alloy#8), the *AF* increases from 0 to ~27 % (see Table II). Interestingly, it is possible to obtain melt-spun amorphous ribbons of compositions belongings to this region, as reported elsewhere [33–35]. The lower cooling rates in gas atomisation as compared to melt-spinning, however, do not allow producing a high fraction of amorphous powders. The low AFA of the

alloy#11 could be attributed to the lower λ = 0.143 as compared to the optimal value (i.e., λ = 0.18) of glass formation. On the contrary, alloy#8 with a good combination of λ = 0.179 and low T_l = 1180 ^{o}C was expected to reveal high *AF*. Nevertheless, the low *AF* (= 27%) of alloy#8 suggests that the region where compositions are selected has a significant influence on the AFA. This can be easily pointed out by comparing alloy#8 with alloy#7; alloy#7 has similar λ (= 0.183) and T_l (= 1177 ^{o}C), but *AF* of this alloy is 82 %, i.e., three times higher than alloy alloy#8.

ii. **Fe_5SiB_2**: only one composition (alloy#2, $Fe_{70}Si_{18}B_{12}$) was produced within this region, corresponding to the lowest T_l = 1139 °C (see Table II). According to the bibliography, AFA significantly improves when T_l is lower or closer to the eutectic composition [13]. However, alloy#2 was only partially amorphous (*AF* = 55 %), and R_C was as high as ~2.1 × 10^6 K/s, suggesting that a low T_l is not enough to produce the high AFA. The λ-factor of this alloy was calculated as 0.214, which is significantly higher than the optimal value (i.e., λ = 0.18) reported elsewhere [48].

iii. **Fe_2B**: most of the compositions were produced within this region (8 samples), varying *AF* from 54 to 100%. The results showed before suggested that this region is highly favourable for the amorphous formation of Fe-Si-B alloys. The best combination of T_l and λ-factor was found for alloy#7 (i.e., lowest T_l = 1177 ^{o}C in the region with λ=0.183 close to the optimal value). However, alloy#7 only retained *AF* = 82%. Interestingly, alloy#3 revealed 100 % of amorphous structure (as confirmed by XRD and Eq. A.5), suggesting that the optimal value of λ-factor for Fe-Si-B alloys is 0.204. It seems that amorphous fraction of Fe-Si-B compositions systematically converge to 100% when approaching to the composition of alloy#3 (see Fig 5 (b)). For instance, alloy#3 is encircled by alloy#1 (λ = 0.220), #6 (λ = 0.188), and #7 (λ = 0.183), which revealed *AF* = 82%. More interestingly, alloy#9 (T_l = 1217 °C) and alloy#6 (T_l = 1220) possess similar T_l values in Fe_2B region, while *AF* increased from 64% to 82 %, respectively. This significant increase in *AF*, while having the similar T_l, can be attributed to the increase in λ-factor from 0.172 (alloy#9) to 0.188 (alloy#6), suggesting that λ-factor is the most critical parameter for the amorphisation capability criteria of the Fe-Si-B alloys.

These results can be used as an instrument to carefully select compositions of the ternary Fe-Si-B system with high AFA. Furthermore, this methodology to establish the optimum AFA region could be extended and experimentally proven in other ternary system, where amorphous formation is challenging.

4. Conclusion

Amorphisation crieteria for Fe-Si-B alloys were establish in order to find the optimum region in the ternary Fe-Si-B system with high amorphisation capability. In the first step, the amorphous forming ability (AFA) of Fe-Si-B alloys was evaluated using the conventional empirical glass forming parameters (ΔH^{mix}, α- and β-parameters), which, unfortunately, were not predictive enough for the amorphisation capability of the alloys. As a second step, the critical cooling rate, R_C, critical particle size, d_C, and topological instability factor, λ, were calculated and superimposed to the ternary Fe-Si-B phase diagram, calculated using CALPHAD methodology. The alloys with high amorphisation capability in Fe-Si-B system can be designed by using the follwing rules:

i. Not all regions of the liquidus surface projection of phase diagrams are suitable for high AFA. For Fe-Si-B system, the composition should be inside the region where Fe_2B phase precipitates after equilibrium solidification. Compositions within this region have higher AFA as compared to the others.

ii. The relative solute/solvent concentration should be such that λ-factor values vary in the range of 0.18–0.22. However, the highest AFA can be only achieved at the optimum atomic size mismatch of alloys when λ remains in the vicinity of 0.204.

iii. Within these two limits, the alloys with lower liquidus temperatures will have higher amorphisation capability, i.e., closer to the eutectic composition.

The above-mentioned criteria can be used to design alloys of the ternary Fe-Si-B system with high AFA to be produced by processes where cooling rates are not as high as the conventional methods.

Appendix A

A.1 Amorphisation analysis theory

A.1.1 Cooling rate in gas atomisation

The cooling rate during gas atomisation can be estimated using thermodynamic and heat transfer parameters of the alloy melt and atomising gas, as given by the following equation [51,52]:

$$-V \cdot \rho \cdot C_p \cdot \frac{\mathrm{d}T_d}{\mathrm{d}t} = h \cdot A \cdot (T_d - T_f) \tag{A.1}$$

where V, ρ, C_p, h, A, t, T_d, and T_f are the droplet volume, density of molten droplet, specific heat of the melt, heat transfer coefficient between droplet and gas, surface area of droplet, time, droplet temperature and atomising gas temperature, respectively. Since the gas-atomised powder is mostly spherical, Eq. (A.1) can be further simplified:

$$\frac{\mathrm{d}T_d}{\mathrm{d}t} = -\frac{h \cdot A}{V \cdot \rho \cdot C_p} \cdot \left(T_d - T_f\right) = -\frac{6h}{d \cdot \rho \cdot C_p} \cdot \left(T_d - T_f\right) \tag{A.2}$$

where d is the particle diameter. The heat transfer coefficient (h) between the inert gas and molten droplets can be calculated by:

The heat transfer coefficient (h) between the inert gas and molten droplets can be calculated by:

$$h = \frac{k_g}{d}\left(2.0 + 0.6\sqrt{R_e} \cdot \sqrt[3]{P_r}\right) \tag{A.3}$$

where k_g is the gas thermal conductivity, P_r is the gas Prandlt number given by $C_g\mu_g/k_g$ (where C_g and μ_g are the specific heat and kinetic viscosity of the gas, respectively) and R_e corresponds to the Reynolds number defined by $\rho_g d\left[v_d - v_g\right]/\mu_g$ (where ρ_g, v_d and v_g are the density of gas, velocity the of the molten droplets and velocity of the gas, respectively). In gas atomisation, the smaller droplets are accelerated very quickly, reaching the gas velocity

promptly. In the case of larger particles, they separate from the gas [51]. Considering these two aspects and that, the investigated alloys are mostly fine with D_{50} ≤20 µm (see Table A.I), the relative velocity ($v_d - v_g$) between the droplets and gas can be assumed zero, and the equation can be further simplified as:

$$\left|\frac{\mathrm{d}T_d}{\mathrm{d}t}\right| = \left|\frac{12}{\rho \cdot C_p} \cdot \left(T_d - T_f\right)\frac{k_g}{d^2}\right| \tag{A.4}$$

As can be seen in Eq. (A.4), the cooling rate in gas atomisation is directly proportional to k_g, suggesting that the highest cooling rate can be achieved using helium as atomising gas (i.e., helium has higher k_g than argon or nitrogen). This simplified equation can be used to estimate the minimum cooling rate at which one particle of a given diameter was cooled down. Indeed, if every parameter (Reynold and Prandtl number) is considered, the cooling rate will be higher than estimated.

A.1.2 Amorphous fraction (AF)

The large surface area of small particles during gas atomisation allows experiencing high cooling rates, which consequently increases the fraction of the amorphous phase. Based on this fact, the fully amorphous particles were separated from as-atomised powders using sieves with different opening meshes in order to find the particle size fraction below fully amorphous particles are found; their amorphous atomic structure was confirmed using XRD. Then, the energy released upon heating by fully amorphous particles (i.e., crystallisation enthalpy, ΔH_C) and as-atomised powders (i.e., ΔH) was calculated using DSC. Finally, the amorphous fraction was calculated using the following equation [39,44,53]:

$$AF = \frac{A_2}{A_1} \tag{A.5}$$

where AF is the amorphous fraction, A_2 is the energy released by partially amorphous particles (as-atomised) equivalent to ΔH, and A_1 is the crystallisation enthalpy (ΔH_C), of the fully amorphous particles.

A.1.3 Critical cooling rate (R_C)

Since the cooling rate in gas atomisation is inversely proportional to the particle size [32], the possibility of amorphisation is higher in the smallest particles. However, it is difficult to affirm that every particle containing amorphous phase is fully amorphous [53]. Some particles may possess a mixture of the amorphous structure together with dendrites and/or crystallites. In the case of Fe-Si-B powders, the amount of crystallites in the particles with amorphous phase is minimal [37]; therefore, it can be neglected. Thus, the fraction of amorphous phase calculated from Eq. (A.5) can be considered as the fraction of amorphous particles. This leads to an equation to estimate R_C, using the particle size distribution and particle cooling rate as follows [39]:

$$R_C = \left|\frac{\mathrm{d}T_d}{\mathrm{d}t}\right| = \left|\frac{12}{\rho \cdot C_p} \cdot \left(T_d - T_f\right)\frac{k_g}{d_c^2}\right| \tag{A.6}$$

where d_c is the critical particle diameter below the amorphous fraction was found according to the particle size distribution (see Table A.1), and it is equivalent to the parameter D_{max} [17].

A.1.4 Calculation data

In order to carry out the calculation of R_C, the following numerical values were used: ρ of all the investigated alloys are listed in Table A.I, C_p = 35 J/(mol·K) [54], T_d = 1973 K, T_f = 300 K, k_g = 0.150 W/(m·K) for He [52] and d_C was obtained from the particle size distribution (see Table A.1), considering the amorphous fraction calculated by Eq. (A.5).

Table A.I. Powder properties of alloy#1-11[1)].

Alloy#	Compositions (at.%)	Particle size distribution (μm)			True density (g/cm³)
		D_{10}	D_{50}	D_{90}	
1	$Fe_{70}Si_{15}B_{15}$	4.1	16.4	65.5	6.89
2	$Fe_{70}Si_{18}B_{12}$[2)]	4.1	14.0	48.2	6.84
3	$Fe_{72.5}Si_{12.5}B_{15}$[3)]	4.5	14.9	48.7	6.96
4	$Fe_{75}Si_5B_{20}$	5.7	18.9	62.9	7.20
5	$Fe_{75}Si_{7.5}B_{17.5}$	4.7	20.9	92.9	7.07
6	$Fe_{75}Si_{10}B_{15}$	3.9	16.5	68.7	7.05
7	$Fe_{75}Si_{12.5}B_{12.5}$	4.7	20.0	86.1	7.02
8	$Fe_{75}Si_{15}B_{10}$[2)]	4.2	17.2	70.9	7.04
9	$Fe_{77.50}Si_{7.5}B_{15}$	5.3	21.0	84.2	7.13
10	$Fe_{80}Si_5B_{15}$	5.2	18.1	62.9	7.26
11	$Fe_{80}Si_{12}B_8$[2)]	4.1	17.5	75.5	7.26

[1)] D_{10}: 10th percentile of the particle size distribution; D_{50}: median particle size, D_{90}: 90th percentile of particle size distribution.
[2)] Values obtained from Ref. [39].
[3)] Values obtained from Ref. [36].

References

[1] P. Duwez, R.H. Willens, W. Klement, Continuous series of metastable solid solutions in silver-copper alloys, J. Appl. Phys. 31 (1960) 1136–1137.

[2] H.X. Li, Z.C. Lu, S.L. Wang, Y. Wu, Z.P. Lu, Fe-based bulk metallic glasses: Glass formation, fabrication, properties and applications, Prog. Mater. Sci. 103 (2019) 235–318.

[3] C.A. Queiroz, J. Šesták, Aspects of the non-crystalline state, Phys. Chem. Glas. Eur. J. Glas. Sci. Technol. Part B. 51 (2010) 165–172.

[4] P.K. Gupta, Non-crystalline solids: glasses and amorphous solids, J. Non. Cryst. Solids. 195 (1996) 158–164.

[5] I.-R. Lu, G. Wilde, G.P. Görler, R. Willnecker, Thermodynamic properties of Pd-based glass-forming alloys, J. Non. Cryst. Solids. 250–252 (1999) 577–581.

[6] A. Masood, V. Ström, L. Belova, K. V. Rao, J. Ågren, Effect of Ni-substitution on glass forming ability, mechanical, and magnetic properties of FeBNbY bulk metallic glasses, J. Appl. Phys. 113 (2013) 013505.

[7] A. Masood, L. Belova, V. Ström, On the correlation between glass forming ability (GFA) and soft magnetism of Ni-substituted Fe-based metallic glassy alloys, J. Magn. Magn. Mater. 504 (2020) 166667.

In preparation

[8] E. Dastanpour, M.H. Enayati, A. Masood, V. Ström, On the glass forming ability (GFA), crystallization behavior and soft magnetic properties of nanomet-substituted alloys, J. Non. Cryst. Solids. 529 (2020) 119774.

[9] D. Turnbull, Under What Conditions Can A Glass Be Formed?, Contemp. Phys. 10 (1969) 473–488.

[10] Z.P. Lu, Y. Li, S.C. Ng, Reduced glass transition temperature and glass forming ability of bulk glass forming alloys, J. Non. Cryst. Solids. 270 (2000) 103–114.

[11] I.W. Donald, H.A. Davies, Prediction of glass-forming ability for metallic systems, J. Non. Cryst. Solids. 30 (1978) 77–85.

[12] A. Takeuchi, A. Inoue, Classification of bulk metallic glasses by atomic size difference, heat of mixing and period of constituent elements and its application to characterization of the main alloying element, Mater. Trans. 46 (2005) 2817–2829.

[13] C. Suryanarayana, A. Inoue, Bulk Metallic Glasses, CRC/Taylor & Francis, US, 2011.

[14] A. Inoue, T. Zhang, T. Masumoto, Glass-forming ability of alloys, J. Non. Cryst. Solids. 156–158 (1993) 473–480.

[15] M. Saad, M. Poulain, Glass forming ability criterion, Mater. Sci. Forum. 19–20 (1987) 11–18.

[16] Z.P. Lu, C.T. Liu, A new glass-forming ability criterion for bulk metallic glasses, Acta Mater. 50 (2002) 3501–3512.

[17] Q. Chen, J. Shen, D. Zhang, H. Fan, J. Sun, D.G. McCartney, A new criterion for evaluating the glass-forming ability of bulk metallic glasses, Mater. Sci. Eng. A. 433 (2006) 155–160.

[18] G.J. Fan, H. Choo, P.K. Liaw, A new criterion for the glass-forming ability of liquids, J. Non. Cryst. Solids. 353 (2007) 102–107.

[19] X.H. Du, J.C. Huang, C.T. Liu, Z.P. Lu, New criterion of glass forming ability for bulk metallic glasses, J. Appl. Phys. 101 (2007) 23–25.

[20] Z. Long, H. Wei, Y. Ding, P. Zhang, G. Xie, A. Inoue, A new criterion for predicting the glass-forming ability of bulk metallic glasses, J. Alloys Compd. 475 (2009) 207–219.

[21] Z.Z. Yuan, S.L. Bao, Y. Lu, D.P. Zhang, L. Yao, A new criterion for evaluating the glass-forming ability of bulk glass forming alloys, J. Alloys Compd. 459 (2008) 251–260.

[22] E.S. Park, W.T. Kim, D.H. Kim, A simple model for determining alloy composition with large glass forming ability in ternary alloys, Metall. Mater. Trans. A Phys. Metall. Mater. Sci. 32 (2001) 200–202.

In preparation

[23] E.S. Park, D.H. Kim, W.T. Kim, Parameter for glass forming ability of ternary alloy systems, Appl. Phys. Lett. 86 (2005) 061907.

[24] T. Egami, Y. Waseda, Atomic size effect on the glass forming ability of metallic alloys, J. Non. Cryst. Solids. 64 (1984) 113–134.

[25] K. Mondal, B.S. Murty, On the parameters to assess the glass forming ability of liquids, J. Non. Cryst. Solids. 351 (2005) 1366–1371.

[26] K. Ackland, A. Masood, S. Kulkarni, P. Stamenov, Ultra-soft magnetic Co-Fe-B-Si-Nb amorphous alloys for high frequency power applications, AIP Adv. 8 (2018).

[27] H. Ahmadian, A. Masood, Z. Pavlovic, K.L. Alvarez, C. Ómathúna, P. McCloskey, P. Stamenov, On the mechanisms limiting power loss in amorphous CoFeB-based melt-spun ribbons, J. Magn. Magn. Mater. 502 (2020) 166535.

[28] M. Hagiwara, A. Inoue, T. Masumoto, Mechanical properties of Fe-Si-B amorphous wires produced by in-rotating-water spinning method, Metall. Trans. A. 13 (1982) 373–382.

[29] G. Herzer, Modern soft magnets: Amorphous and nanocrystalline materials, Acta Mater. 61 (2013) 718–734.

[30] R.M. German, Powder Metallurgy and Particulate Materials Processing, Metal Powder Industries Federation (MPIF), Princeton, NJ, USA, 2005.

[31] K.L. Alvarez, H.A. Baghbaderani, J.M. Martín, N. Burgos, M. Ipatov, Z. Pavlovic, P. Mccloskey, A. Masood, J. Gonzalez, Novel Fe-based amorphous and nanocrystalline powder cores for high- frequency power conversion, J. Magn. Magn. Mater. 501 (2020) 166457.

[32] A.J. Yule, J.J. Dunkley, Atomization of Melts for Powder Production and Spray Deposition, Oxford University Press, UK Oxford, 1994.

[33] T. Sato, Study on powder properties of Fe-P-C and Fe-B-Si alloy powders prepared by water atomization, J. Mater. Sci. 26 (1991) 2329–2336.

[34] M. Hagiwara, A. Inoue, T. Masumoto, The critical thickness for the formation of Fe-, Ni- and Co-based amorphous alloys with metalloids, Sci. Reports Res. Institutes Tohoku Univ. Ser. a-Physics Chem. Metall. 29 (1981) 351–358.

[35] F.E. Luborsky, I. Reeve, H.A. Davies, H.H. Liebermann, Effect of Fe-B-Si composition on maximum thickness for casting amorphous metals, IEEE Trans. Magn. 18 (1982) 1385–1387.

[36] K.L. Alvarez, J.M. Martin, M. Ipatov, L. Dominguez, J. Gonzalez, Magnetic Properties of Annealed Amorphous $Fe_{72.5}Si_{12.5}B_{15}$ Alloy Obtained by Gas Atomization Technique, IEEE Trans. Magn. 54 (2018) 2002405.

In preparation

[37] K.L. Alvarez, J.M. Martín, M. Ipatov, L. Dominguez, J. Gonzalez, Effect of Composition and Particle Size on the Soft Magnetic Character of Fe-Rich Amorphous Alloys Obtained by Gas Atomization, in: Euro PM2019, European Powder Metallurgy Association (EPMA), Maastricht, The Netherlands, 2019: pp. 1–6.

[38] A. Załuska, H. Matyja, Crystallization characteristics of amorphous Fe-Si-B alloys, J. Mater. Sci. 18 (1983) 2163–2172.

[39] K.L. Alvarez, J.M. Martín, M. Ipatov, J. Gonzalez, Soft magnetic amorphous alloys (Fe-rich) obtained by gas atomisation technique, J. Alloys Compd. 735 (2018) 2646–2652.

[40] A.P. Shpak, A.G. Il'inskii, A. V. Marunyak, O.I. Slukhovskyy, Y. V. Lepeeva, A. Dekhtyar, I. Kaban, N. Mattern, J. Eckert, Crystallization of $Fe_{82}Si_2B_{16}$ and $Fe_{82}Si_4B_{14}$ metallic glasses upon isothermal and non-isothermal annealing, EPJ Web Conf. 15 (2011) 01008 (4 pages).

[41] J.L. Walter, A.E. Berkowitz, E.F. Koch, Crystallization of amorphous $Fe_{75}Si_{15}B_{10}$ ribbon and powder, Mater. Sci. Eng. 60 (1983) 31–44.

[42] K. Chrissafis, M.I. Maragakis, K.G. Efthimiadis, E.K. Polychroniadis, Detailed study of the crystallization behaviour of the metallic glass $Fe_{75}Si_9B_{16}$, J. Alloys Compd. 386 (2005) 165–173.

[43] E. Illekova, I. Mat'ko, P. Duhaj, F.A. Kuhnast, The complex characteristics of crystallization of the $Fe_{75}Si_{15}B_{10}$ glassy ribbon, J. Mater. Sci. 32 (1997) 4645–4654.

[44] M.E. Brown, Introduction to Thermal Analysis: Techniques and Applications, 2001.

[45] M. Hagiwara, A. Inoue, T. Masumoto, Production of amorphous CoSiB and CoMSiB (M ≡ Group IV - VIII transition metals) wires by a method employing melt spinning into rotating water and some properties of the wires, Mater. Sci. Eng. 54 (1982) 197–207.

[46] U. Carow-Watamura, D.V. Louzguine, A. Takeuchi, B-Fe-Si (144), in: Y. Kawazoe, U. Carow-Watamura, J.Z. Yu (Eds.), Phys. Prop. Ternary Amorph. Alloy. Part 2 Syst. from B-Be-Fe to Co-W-Zr. Landolt-Börnstein - Gr. III Condens. Matter (Numerical Data Funct. Relationships Sci. Technol., Springer, Berlin, Heidelberg, 2011: pp. 200–253.

[47] A. Takeuchi, A. Inoue, Calculations of mixing enthalpy and mismatch entropy for ternary amorphous alloys, Mater. Trans. JIM. 41 (2000) 1372–1378.

[48] Z.J. Yan, J.F. Li, S.R. He, Y.H. Zhou, Evaluation of the optimum solute concentration for good glass forming ability in multicomponent metallic glasses, Mater. Res. Bull. 38 (2003) 681–689.

[49] A. Tabeshian, H. Mao, L. Arnberg, R.E. Aune, Investigation of glass forming ability in the Zr-rich part of the Zr-Fe-Al ternary system, J. Appl. Phys. 125 (2019) 065101.

[50] D.D.E. Brennhaugen, H. Mao, D. V. Louzguine-Luzgin, L. Arnberg, R.E. Aune, Predictive

modeling of glass forming ability in the Fe-Nb-B system using the CALPHAD approach, J. Alloys Compd. 707 (2017) 120–125.

[51] H. Shiwen, L. Yong, G. Sheng, Cooling rate calculation of non-equilibrium aluminum alloy powders prepared by gas atomization, Rare Met. Mater. Eng. 38 (2009) 353–356.

[52] A. Inoue, Light-metal based amorphous alloys, in: Curr. Top. Amorph. Mater., Elsevier B.V., 1993: pp. 159–166.

[53] N. Ciftci, N. Ellendt, R. Von Bargen, H. Henein, L. Mädler, V. Uhlenwinkel, Atomization and characterization of a glass forming alloy $\{(Fe_{0.6}Co_{0.4})_{0.75}B_{0.2}Si_{0.05}\}_{96}Nb_4$, J. Non. Cryst. Solids. 394–395 (2014) 36–42.

[54] J. Zhang, H. Fujimori, A. Inoue, T. Masumoto, Specific heat behaviour on soft magnetic thick amorphous ribbons of an Fe-B-Si alloy, Mater. Sci. Eng. 99 (1988) 35–38.

Appendix II

Contribution to other Papers

Journal of Magnetism and Magnetic Materials 502 (2020) 166535

Contents lists available at ScienceDirect

Journal of Magnetism and Magnetic Materials

journal homepage: www.elsevier.com/locate/jmmm

On the mechanisms limiting power loss in amorphous CoFeB-based melt-spun ribbons

Hasan Ahmadian Baghbaderani [a, b,*], Ansar Masood [a], Zoran Pavlovic [a], Kenny L. Alvarez [c, d], Cian ÓMathúna [a, e], Paul McCloskey [a], Plamen Stamenov [a, b]

[a] *Microsystems Centre, Tyndall National Institute, University College Cork, Cork, Ireland*
[b] *School of Physics and CRANN, Trinity College, Dublin 2, Ireland*
[c] *CEIT-IK4 and Tecnun (University of Navarra), San Sebastián, Spain*
[d] *Escuela de Ingeniería Mecánica, Pontificia Universidad Católica de Valparaíso, Valparaíso, Chile*
[e] *School of Electrical and electronic Engineering, University College Cork, Cork, Ireland*

Abstract

The mechanisms that limit the power loss performance in melt-spun amorphous ribbons have been investigated through DC and AC magnetic characterization methods. The measured total power loss is resolved into hysteresis, eddy current, and anomalous losses. The anomalous loss is found to account for more than 90 % of the total loss, which significantly reduced by annealing in a transverse magnetic field. This is attributed to the reorientation of preferred magnetisation axis perpendicular to the length of ribbons. Transverse magnetic annealing promotes the relative contribution of domain rotation over domain wall motion during magnetisation reversal process. Magnetic annealing also causes a measurable decrease in the domain width, which promotes pinning and inhibits domain wall motion, thus further favoring coherent domain rotation as the primary mechanism of magnetization. This combination accounts for a 75 % decrease in the total power loss in the so-processed ribbons and renders them attractive for applications in mid- and high-frequency power supplies and inverters.

Keywords: Amorphous alloy, magnetic properties, magnetization process, magnetostructural transformations

* Corresponding author Tel.: + 353 87 175 0385
Email address: hasan.baghbaderani@tyndall.ie (H. A. Baghbaderani).
https://doi.org/10.1016/j.jmmm.2020.166535

1. Introduction

Power loss during electrical conversion accounts for a large percentage of the total dissipation (primarily heat) during power transmission and distribution. This is not only felt close to the enduser, resulting in a decreased efficiency of consumer-grade power electronic components [1]; but also in high-power applications such as power inverters used within photovoltaic installations [2]. The overall power loss can be attributed broadly to three different mechanisms, namely, hysteresis loss, eddy current loss, and anomalous loss. It is well understood that as the operating frequency f increases, the eddy current and anomalous losses become dominant at $f > 100$ kHz, for metallic, high polarisation materials. On the other hand, recent advances in power conversion circuits have pushed their switching frequencies to 100 s of kHz and even into the megahertz range [3, 4]. The utilization of these benefits is more readily attainable using ferrite-based low-moment materials, which are insulating. However, the low flux density typical to ferrites (0.3-0.4 T) requires considerable cross-sectional area, which is massive in many deployments [5]. Thus, to put conducting and insulating core materials on a level playing field, a key metric has to be used, say for transformer applications, which work as a direct indication of the overall efficiency of the end device. One such choice is material power loss performance. Presently, ferrites, iron powder [6] and tape wound cores [7, 8] are primarily used for relatively low-power applications, where only grams of material are required per installation. An affordable, yet efficient, high-moment magnetic material, allowing for operation beyond 100 kHz, would enable mass application in higher power export-to-grid invertors (in the kW range), which are expected to become prolific in the near future as many countries are adopting new regulations with respect to renewable energy sources.

Based on related parameters to calculate the as-mentioned different kinds of losses [5], the next generation of miniaturised power electronic devices requires cores with high magnetic flux density, high resistivity, and ultra-low coercivity along with ease of manufacturability [9]. All of these characteristics are documented in amorphous materials. Furthermore, good high-frequency permeability can be observed in this type of material which is due to the combination of low coercive resulting from the homogeneous glassy structure and low eddy current loss resulting from relatively high electrical resistivity [10]. Therefore, due to the variety of applications for these materials, the largest volume usage, by far, both in dollars and tonnage, is in cores of electrical distribution transformers [11].

Since 1995, a number of Fe- and Co-based amorphous alloys with T_C well above room temperature have been developed by different rapid cooling methods, such as copper mold casting or water quenching. The formation and properties of multicomponent Fe-based Bulk Metallic Glasses (BMGs) have attracted increasing attention because of the fundamental interests in their properties and the high industrial application potential [10]. For Co-based amorphous alloys, it is known that CoFeSiB alloys with zero magnetostriction exhibit high permeability and have been subsequently developed as ultra-low coercivity sensor materials. However, as a result of the poor glass-forming ability (GFA), high cooling rates are required, in order to obtain an amorphous phase directly from the liquid state, causing limitations in the shape and dimensions of the resulting material – limiting it to either a ribbon or a wire form [12]. One notable practical advantage of thin melt-spun ribbons is their lower eddy current loss, as compared to their crystalline counterparts, when utilized in tape wound magnetic cores.

Anomalous loss dominates the total dynamic loss in most soft magnets with a uniaxial anisotropy oriented longitudinally to the applied magnetic field. It originates from localized eddy currents around moving domain walls under the driving action of an external magnetic field. The anomalous loss can be decreased through changing the mechanism of magnetization from predominantly domain wall motion to the coherent rotation of domains, which can be done using transverse magnetic annealing [6]. The mechanisms of inducing magnetic anisotropy by magnetic annealing include atomic pair ordering resulting in directional order in the sample, structural relaxation, and rearrangement of free volume in amorphous materials [8].

In present work, the effect of transverse magnetic annealing on the magnetisation reversal process and power loss mechanisms in amorphous melt-spun CoFeB-based ribbons is studied. To clarify and understand the loss-limiting mechanisms and guide a decrement in anomalous loss, MagnetoOptic Kerr Effect (MOKE) microscopy is used in parallel to bulk magnetisation measurements and model-based evaluations.

2. Experimental Methods

Melt-spun ribbons of 20 μm thickness and 1 mm width, with the composition of $Co_{65.88}Fe_{4.2}B_{24}Si_{1.92}Nb_4$, are obtained using fabrication conditions explained in reference [13]. X-ray powder diffraction (XRD) data of the melt-spun ribbons are collected using a Phillips PANalytical X'pert Pro

diffractometer, with an operational wavelength of 1.5405 Å (Cu-Kα anode). The thermal behavior of the ribbons before any annealing treatment is evaluated by Differential Scanning Calorimetry (DSC) in TA Instrument DSC 2920. DSC experiments are performed on 20 mg of ribbons, at the heating rate of 10 K/min in Ar atmosphere. The ribbons are thermally annealed and magnetically annealed at 5 Tesla for one hour at three different temperatures (450, 475, and 500 °C) in a magnetic annealing oven (Model: TEL MRT5000) provided by Tokyo Electron Magnetic Solutions, Ltd. The small coercivity (< 3 A/m) and anisotropic field of the ribbons, along its length, is accurately measured by a B-H loop tracer running at 10 Hz with a maximum applied magnetic field up to 0.1 T and with the resolvable magnetic field of 0.01 A/ m. The initial relative permeability of ribbons is calculated based on the slope of the hysteresis loop linear part. In addition, Evico Magnetics Kerr Microscope & Magnetometer is used for the visualisation of magnetic domains at μ0H = 0 T when the ribbons are in the remanent state of the magnetization.

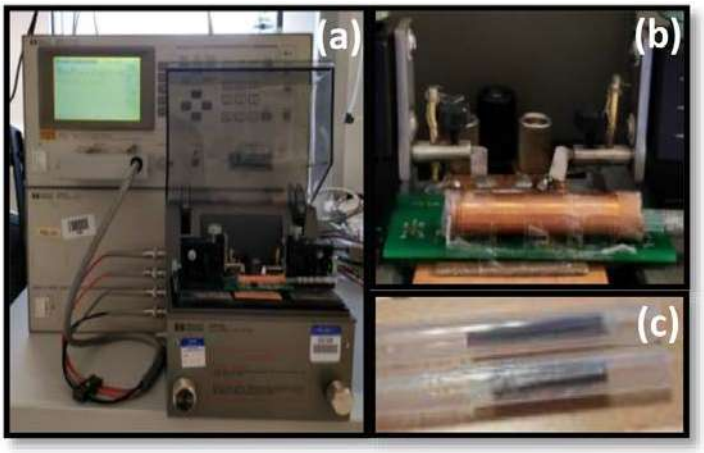

Fig. 1. Power loss measurement set-up; (a) complete set-up, (b) solonoid with 150 turns of wire of guage 28 to produce coherent magnetic field at the center, and (c) sample holders.

The power loss characterisation of the ribbons is performed using a custom design air-core solenoid inductor. 150 turns of 28 gauge Cu wire are wound on a 5 cm long hollow cylinder of 5 mm outer radius with near-zero spacing between the turns to create a uniform excitation field inside the solenoid. The impedance of the air core solenoid, Z_a, is measured using an LCR meter (HP4284A) at various excitation current levels. Three ribbon pices (20 mm × 1 mm × 0.02 mm) are fixed on a sample holder and inserted inside the solenoid, along its axis, where the uniformity of the field is best

(see Fig. 1). Without moving the probes from the test fixture, the ribbons are centered inside the solenoid, to be at the same distance from both open ends, where the field lines are no longer parallel to the axis. In this way, the magnetic core material is exposed to a uniform excitation field along its length. The Cu turns are at a sufficient distance from the solenoid axis so that the demagnetisation field does not alter the field lines around the turns maintaining the same AC winding resistance as in the case of air-core solenoid measurement. Therefore, the difference between the impedance measurement with and without magnetic core material, Z_c and Z_a, respectively, at different frequencies, represents the contribution of the magnetic core to the inductance and power loss at each frequency. As the cross-sectional area of the ribbons is significantly smaller than that of the solenoid, the effect of the insertion of the magnetic core on the real part of the inductance is negligible. Thus, the magnetic material power loss is calculated as;

$$P_{loss} = Re(Z_c - Z_a)I^2 \tag{1}$$

where Re(Z_c–Z_a) is the real part of the complex impedance difference and I is the excitation current measured using the LCR meter. The induction field inside the ribbon samples is calculated by

$$B = \frac{lm(Z_c - Z_a)I}{(2\pi fS)}\pi r^2 \tag{2}$$

where f and S are the measurement frequency and the total cross-sectional area of the ribbons, and r is the radius of the coils. The power loss measurement method has been tested with commercial samples, and the results are in good agreement with the reported power loss in standard datasheets.

Furthermore, high-frequency permeability is derived from the inductance measurement of the single turn closed core toroidal inductor using the following equation:

$$\mu = \frac{lL_e}{\mu_0 N^2 S} \tag{3}$$

where L_e is the measured inductance, l is the magnetic path length of the toroidal core, S is the cross-sectional area of the toroidal core, N is the number of copper turns, and μ_0 is the free space permeability.

3. Results and discussion

3.1 DC magnetic properties

The evolution of hysteresis loops measured along the length of the ribbons as a function of magnetic annealing temperature is shown in Fig. 2. As can be seen, an increase in magnetic annealing temperature causes more sheared-over loops, which suggests that the mechanism of magnetisation reversal process is changing from domain wall motion to rotation. Based on the DSC trace (Fig. 3) and XRD patterns (Fig. 4), up to magnetic annealing temperatures of 500 °C, the microstructure of the ribbons is still amorphous. Additionally, the important features distinguishing the hysteresis loops from each other in Fig. 2 can be explained using different parameters. First, when the field is growing from zero (Fig. 2, arrow 1), the permeability would decrease due to an increase in transverse induced anisotropy (Fig. 5), which is moving easy axis from the length to the width of the ribbons. In addition, saturation is not achieved until $H = H_k$; this parameter, the induced anisotropy field (H_k), is increased when the annealing temperature is increased. It also represents the induced anisotropy energy (K_u) (Fig. 6) which is calculated based on:

$$K_u = \frac{H_k \mu_0 M_s}{2} \tag{4}$$

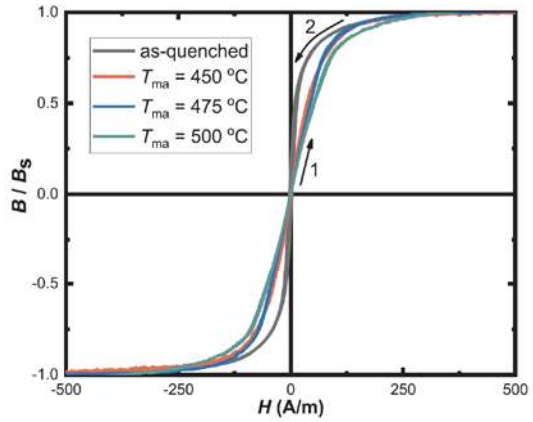

Fig. 2. Hysteretic loops of as-quenched and magnetically annealed amorphous ribbons.

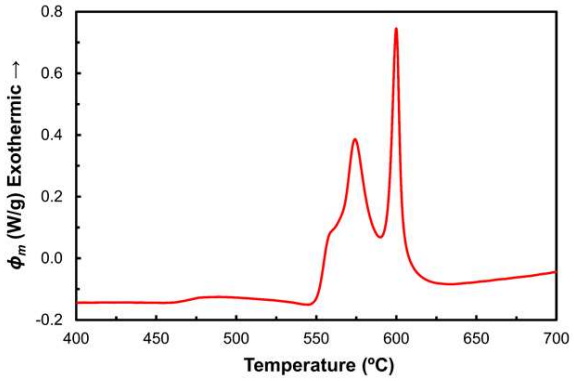

Fig. 3. DSC trace of CoFeB-based melt-spun ribbons.

The high induced anisotropy at elevated temperatures could be due to larger atomic mobility, leading to a microstructure in which atomic pairs of magnetic elements are ordered [14]. By increasing the annealing temperature, as H is decreased from saturation (Fig. 2, arrow 2), the system tends to demagnetise itself more completely, which results in a decline in B_r/B_s (Fig. 5). In other words, induced anisotropy takes over as H approaches zero and rotates the magnetisation toward the nearest easy direction. As can be seen in the diminishing trend of coercivity (see Fig. 7), the magnetisation becomes more reversible as the induced anisotropy is increased [6]. This trend can also be due to the structural relaxation and rearrangement of free volume, as well as other mechanisms of inducing anisotropy [8].

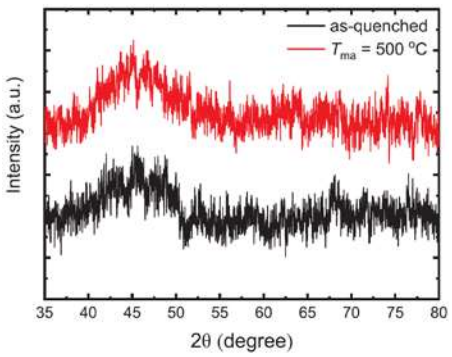

Fig. 4. XRD patterns of as-quenched and magnetic annealed ribbons at 500 °C.

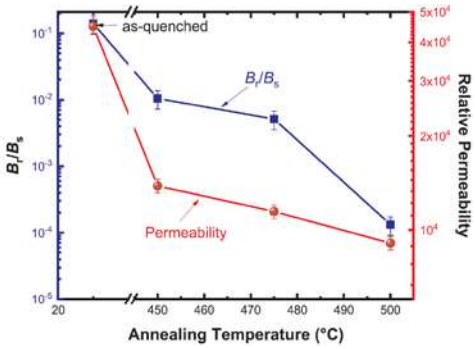

Fig. 5. Relative permeability and the ratio between remnant magnetisation and saturation flux density (B_r/B_s) of the as-quenched and magnetically annealed samples at different temperatures.

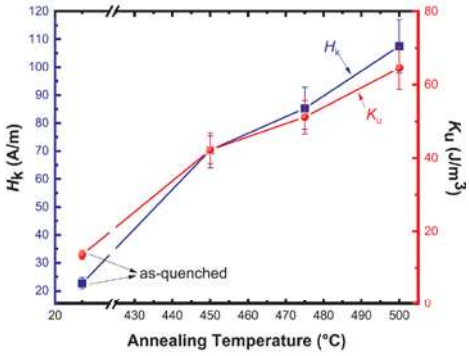

Fig.6. Magnetic anisotropy field (H_k) and field-induced anisotropy (K_u) of the CoFeB-based ribbons annealed in a transverse magnetic field at different temperatures.

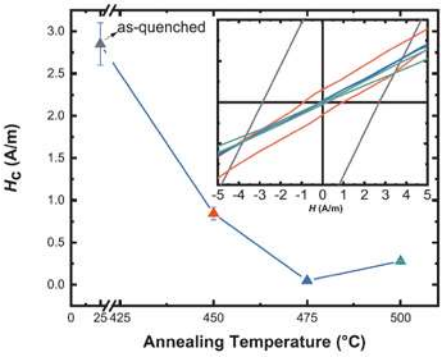

Fig. 7. Coercivity of ribbons as a function of magnetic annealing temperature.

3.2 AC magnetic properties

Total power loss density increases with AC magnetic induction (B_{AC}) and frequency (Fig. 8). Samples, which have been magnetically annealed at higher temperatures, show a lower amount of power loss, a decrease of 75% after magnetic annealing at 500 °C, although the same cannot be eliminated entirely. In other words, by inducing anisotropy of an equivalent remagnetisation power density ($K_u.f$), the power loss density is decreasing. A linear relationship between the induced anisotropy power and the power loss holds in the system in a broad range of frequency (Fig. 9). Furthermore, the power loss is just a small fraction of the induced anisotropy power (p_{loss} ~ 80 W/m^3, and p_{trans} ~ 540 kW/m^3), both evaluated in a transformer circuit at 100 kHz. However, at higher levels of magnetic induction, this fraction is increasing (Fig. 9). To evaluate the effect of field annealing compared to simple annealing, ribbons are annealed in vacuum at 450, 475 and 500 °C. The power loss of the as-quenched sample is increased after simple annealing as can be seen in Fig. 8 at three different frequencies. This effect can be attributed to the more relaxed microstructure of the ribbons, which makes domain wall motion easier and as a consequence the power loss bigger, likely due to the micro-induction currents associated with the domain wall motion i.e. the anomalous loss, which will be addressed accordingly.

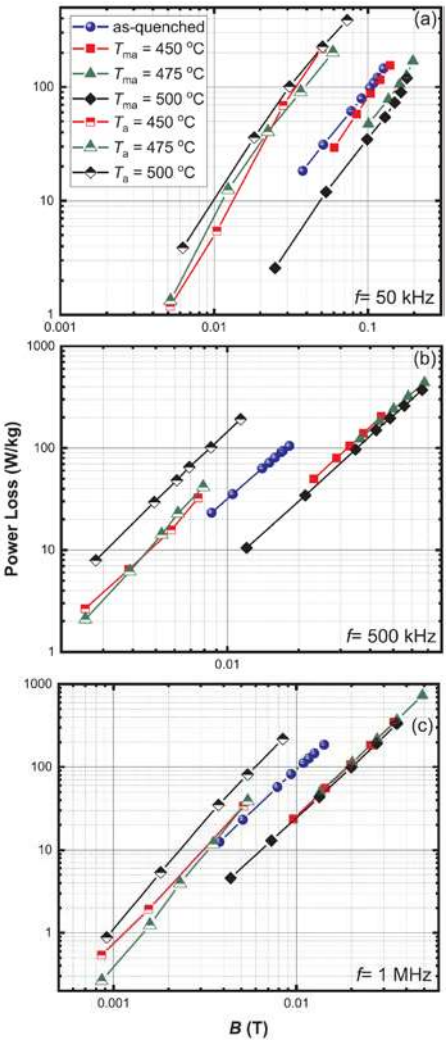

Figure 8. Power loss density of as-quenched, magnetically annealed, at T_{ma} = 450, 475 and 500 °C, and simply annealed at T_a = 450, 475 and 500 °C, ribbons as a function of the intensity of the applied magnetic induction at different frequencies; (a) 50 kHz, (b) 500 kHz and (c) 1 MHz.

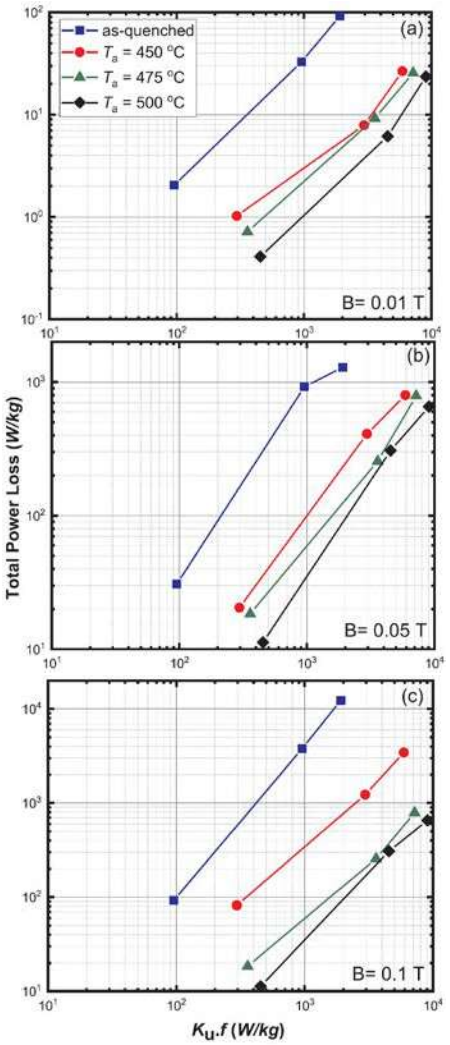

Figure 9. Total power loss as a function of induced anisotropy power for three different intensities of the magnetic induction.

To evaluate the contribution of different kinds of losses and their relations to microstructural and magnetic parameters, a power loss decomposition based on the analysis borrowed from reference [5] has been

carried out. According to these estimates, more than 90% of total power loss is due to anomalous loss, which is in agreement with previous studies [15–17]. This contribution can be due to the low amount of hysteresis and the high permeability in the ultra-soft magnetic ribbons, which means that the primary mechanism of magnetization is domain wall motion, instead of magnetisation rotation, which itself is mainly responsible for the anomalous part of the losses. Due to the excessiveness of this kind of loss, the relevant strategies for its minimization are discussed below in more details.

3.2.1 *Anomalous loss*

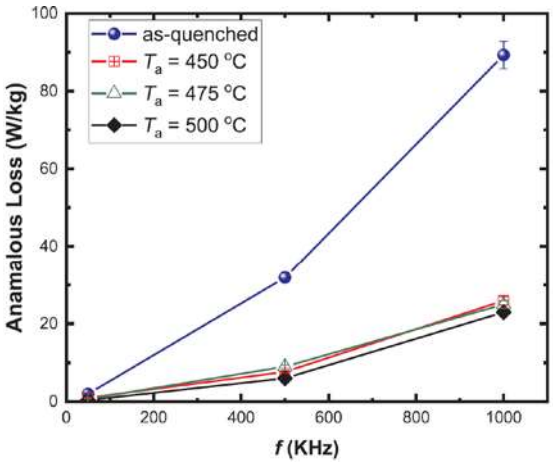

Fig. 10. Anomalous loss of different magnetic annealed samples as a function of frequency in 0.01 T magnetic induction.

The anomalous loss measured at 10 mT and the frequencies of 50, 500 kHz, and 1 MHz are shown in Fig. 10. It can be seen that inducing uniaxial anisotropy causes a substantial decline in the amount of anomalous loss. In other words, field annealing changes the magnetisation easy axis by inducing a transverse anisotropy, which also results in a domain size refinement, which in turn reduces the stray field energy (Fig. 11). To verify this observation, the average domain width w is estimated as [15]:

$$w \approx \sqrt{\frac{2\gamma_w t}{K_u(N_{zz}sin^2\beta + N_{yy}cos^2\beta)}} \tag{5}$$

where γ_w is the domain wall energy, t is the ribbon thickness, β is the out-of-plane angle of the magnetization vector, N_{zz} ($\approx$1) is the demagnetising factor normal to the ribbon plane, while along the long axis $N_{xx} \sim 0$, and N_{yy} ($\approx$ 0.004) is the demagnetising factor across the ribbon width. For the ribbon with transverse anisotropy β =0. The domain wall energy (γ_w) can be calculated based on $\gamma_w = 2\pi\sqrt{AK_u}$ [18]. It can be noticed that as magnetic annealing temperature is increasing, the average domain width would decrease (Figs. 11 and 12) and the domain wall energy would increase (Fig. 12), indicating that the induced anisotropy is changing the mechanism of magnetization, by making the domain wall motion harder as the domain wall energy is increasing [15]. Additionally, as can be seen in Fig. 11, the domain walls are getting smoother with increasing the magnetic annealing temperature that confirms incremental induced uniaxial anisotropy.

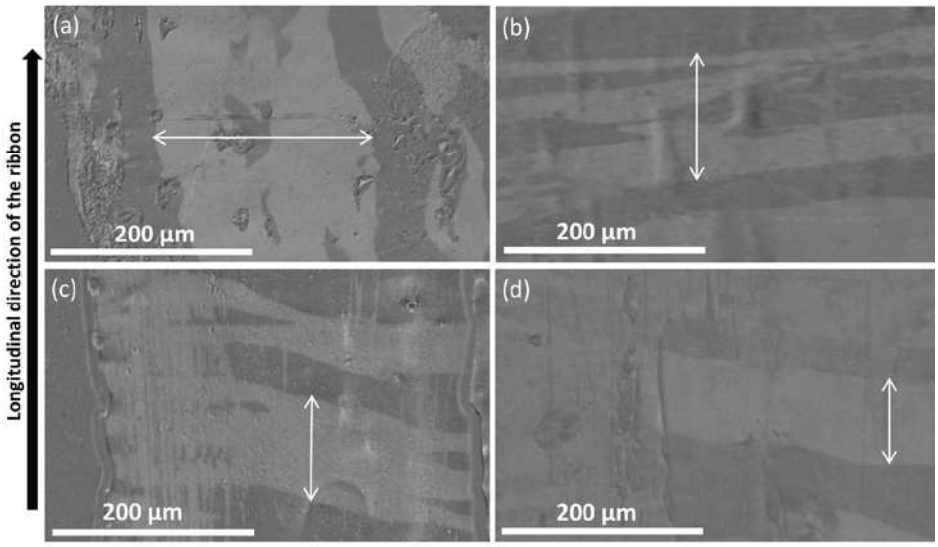

Figure 11. MOKE domain images of the (a) as-quenched, and thermomagnetic annealed ribbons at (b) 450 °C, (c) 475 °C and (d) 500 °C. The domain imaging were carried out at the remanent state of magnetization.

In addition, according to Herzer's theory [19], the relationship between total power loss and the total eddy current loss (P_{ec}), which includes classic eddy current loss and excess eddy current loss or anomalous loss, has the form as formulated in Eq. (6):

$$P_t \approx P_{ec}\left[1 + \frac{w^2}{(w\,cos\beta + t)^2}\frac{m^2}{1-m^2}\right] \quad (6)$$

where *m* denotes the average magnetisation component along the ribbon axis normalised to the saturation magnetisation. Thus, by decreasing the domain width (*w*) as a result of magnetic annealing, the total eddy current loss will decrease, which can be seen in Fig. 13 [15]. As it can be noticed in this figure, there is a reasonably good agreement between the measured and the calculated total eddy current loss based on Eq. (6).

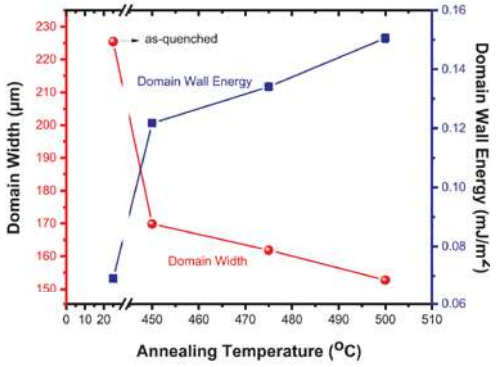

Fig. 12. Calculated domain width and domain wall energy in magnetic annealed samples at different temperatures.

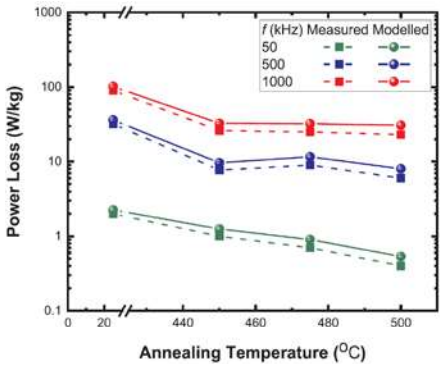

Fig. 13. Measured and estimated total power loss of magnetic annealed samples in 0.01 T magnetic induction.

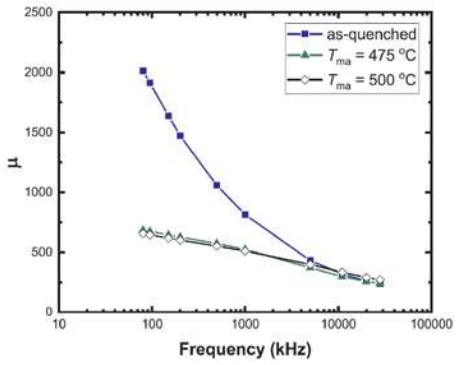

Fig. 14. Frequency dependence of the effective permeability of as-quenched and magnetic annealed ribbons in the frequency range of 50 kHz-28 MHz.

Additionally, to evaluate the application potential of the amorphous ribbons, the frequency spectrum of effective permeability, μ, is measured and shown in Fig. 14. The effective permeability of the as-quenched ribbons decreases steadily from 2000 to 240 in the frequency range from 50 kHz to 28 MHz, which is about 88% decrement. The permeability of the magnetic annealed samples at 50 kHz is less than one-third of as-quenched ones, while the reduction rate of permeability for magnetic annealed samples in the as-

mentioned frequency range is about 60%. At 50 kHz, the permeability of the as-quenched sample is much higher than the magnetic annealed samples because the primary mechanism of magnetization is domain wall motion in this sample, while in the magnetic annealed samples, the dominant mechanism of magnetization reversal is magnetisation rotation. Hence, the effective permeability in this frequency region is associated with the initial permeability of the material. Further increase in f causes a significant reduction in μ, which can be ascribed to a relaxation-type dispersion of the reversible bulging mechanism for which the domain walls are no longer able to follow the AC magnetic variations. Beyond the relaxation frequency, μ becomes small, reflecting the contribution of the domain rotation as the dominant magnetization process. Therefore, the abrupt change in the permeability of the as-quenched sample is due to change in the mechanism of magnetization reversal, while this change is much smaller for the magnetically-annealed samples, in which the primary mechanism of magnetization is domain rotation, in the whole range of frequency.

4. Conclusions

Melt-spun ribbons have been annealed in a transverse magnetic field of 5 T, at varying temperatures of up to 500 °C. The effect of field-induced anisotropy on DC and AC magnetic properties are reported. Magnetic annealing results in ribbons with lower longitudinal coercivity and permeability (μ' from 5000 down to 1450, μ'' from 100 down to 25 at 50 kHz) due to structural relaxation and a change in the easy axis of magnetization of the ribbons, from along their length, to along their width, respectively. The latter results in consequence pre-dominance of domain rotation as the mechanism of magnetization reversal. Therefore, the material-specific Q-factor (μ'/μ'') has improved from ~50 to ~58 at 50 kHz. Total power loss within the ribbons has been decomposed into hysteresis, eddy current, and anomalous losses. Based on this analysis, anomalous loss accounts for about 90% of total power loss, and through magnetic annealing and the associated decrease in the domain width, it can be reduced substantially. This mechanism is explained and verified using MOKE imaging and domain wall energy calculations, based on magnetization data. The measured behavior of the total power loss is dominated by total eddy current loss, including eddy current and anomalous losses, and is in good agreement with Herzer's theory. Soft magnetic ribbons, of low thickness (< 20 μm), of CoFeB-based metallic compositions, heat-treated in transverse magnetic field of above 5 T, at a temperature in the range 450–500 °C,

therefore, hold great promise for power applications at frequencies in the range 10–500 kHz, as a higher-permeability alternative to ferrites.

CRediT authorship contribution statement

Hasan Ahmadian Baghbaderani: Methodology, Validation, Formal analysis, Investigation, Data curation, Writing - original draft, Visualization. **Ansar Masood:** Conceptualization, Methodology, Validation, Formal analysis, Investigation, Resources, Data curation, Writing - review & editing, Project administration, Funding acquisition. **Zoran Pavlovic:** Investigation, Data curation, Formal analysis. **Kenny L. Alvarez:** Investigation, Writing - review & editing. **Cian Ó Mathúna:** Supervision. **Paul McCloskey:** Conceptualization, Validation, Project administration, Writing - review & editing. **Plamen Stamenov:** Conceptualization, Validation, Project administration, Writing - review & editing, Formal analysis, Visualization, Funding acquisition.

Declaration of Competing Interest

The authors declare that they have no known competing financial interests or personal relationships that could have appeared to influence the work reported in this paper.

Acknowledgment

The authors would like to thank the Science Foundation of Ireland (SFI) for the financial support to perform the research work under the grant number of 2015/SIRG/3569, Starting Investigator Research Grant (SIRG). The authors would like to acknowledge Niclas Teichert and TEL Magnetic Solutions Company for helping in MOKE imaging and magnetic annealing.

References

[1] A.M. Leary, P.R. Ohodnicki, M.E. McHenry, Soft magnetic materials in high-frequency high-power conversion applications, JOM 64 (2012) 772–781.

[2] S.B. Kjaer, J.K. Pedersen, F. Blaabjerg, A review of single-phase grid-connected inverters for photovoltaic modules, IEEE Trans. Ind. Appl. 41 (2005) 1292–1306.

[3] J.S. Glaser, J.M. Rivas, A 500 W push-pull dc-dc power converter with a 30 MHz switching frequency, in: 2010 Twenty-Fifth Annual IEEE Applied Power Electronics Conference and Exposition (APEC), 2010, pp. 654–661.

[4] D.J. Perreault, J. Hu, J.M. Rivas, Y. Han, O. Leitermann, R.C.N. Pilawa-Podgurski, A. Sagneri, C.R. Sullivan, Opportunities and Challenges in Very High Frequency Power

Conversion, in: 2009 Twenty-Fourth Annual IEEE Applied Power Electronics Conference and Exposition, 2009, pp. 1–14.

[5] S. Kulkarni, D. Li, N. Wang, S. Roy, C.Ó. Mathúna, G. Young, P. McCloskey, Low Loss magnetic thin films for off-line power conversion, IEEE Trans. Magn. 50 (2014) 1–4.

[6] R.C. O'Handley, Modern magnetic materials: principles and applications, Wiley, 1999.

[7] G. Herzer, Amorphous and nanocrystalline soft magnets, in: G.C. Hadjipanayis (Ed.), Magnetic Hysteresis in Novel Magnetic Materials, Springer, Netherlands, Dordrecht, 1997, pp. 711–730.

[8] M.E. McHenry, M.A. Willard, D.E. Laughlin, Amorphous and nanocrystalline materials for applications as soft magnets, Prog. Mater Sci. 44 (1999) 291–433.

[9] M. Ansar, M. Paul, M. Cian Ó, K. Santosh, Tailoring the ultra-soft magnetic properties of sputtered Finemet thin films for high-frequency power applications, J. Phys. Conf. Ser. 903 (2017) 012050.

[10] W.H. Wang, C. Dong, C.H. Shek, Bulk metallic glasses, Mater. Sci. Eng. R: Rep. 44 (2004) 45–89.

[11] V.R.V. Ramanan, Metallic glasses in distribution transformer applications: an update, J. Mater. Eng. 13 (1991) 119–127.

[12] Q.K. Man, Y.Q. Dong, C.T. Chang, X.M. Wang, R.W. Li, Co-Based bulk metallic glasses with good soft-magnetic properties and high strength, Mater. Sci. Forum 898 (2017) 703–708.

[13] K. Ackland, A. Masood, S. Kulkarni, P. Stamenov, Ultra-soft magnetic Co-Fe-B-Si-Nb amorphous alloys for high frequency power applications, AIP Adv. 8 (2018) 056129.

[14] F. Johnson, C.Y. Um, M.E. McHenry, H. Garmestani, The influence of composition and field annealing on magnetic properties of FeCo-based amorphous and nanocrystalline alloys, J. Magn. Magn. Mater. 297 (2006) 93–98.

[15] Z. Li, K. Yao, D. Li, X. Ni, Z. Lu, Core loss analysis of finemet type nanocrystalline alloy ribbon with different thickness, Prog. Nat. Sci. Mater. Int. 27 (2017) 588–592.

[16] K.J. Overshott, The causes of the anomalous loss in amorphous ribbon materials, IEEE Trans. Magn. 17 (1981) 2698–2700.

[17] M.A. Willard, T. Francavilla, V.G. Harris, Core-loss analysis of an (Fe Co, Ni)-based nanocrystalline soft magnetic alloy, J. Appl. Phys. 97 (2005) 10F502.

[18] L. Yue, S.-H. Liou, Magnetic force microscopy studies of magnetic features and nanostructures, in: B. Bhushan (Ed.), Scanning Probe Microscopy in Nanoscience and Nanotechnology 2, Springer, Berlin, Heidelberg, 2011, pp. 287–319.

[19] G. Herzer, Magnetic materials for electronic article surveillance, J. Magn. Magn. Mater. 254–255 (2003) 598–602.

Journal of Magnetism and Magnetic Materials 50X (2020) (Under Review)

Contents lists available at ScienceDirect

Journal of Magnetism and Magnetic Materials

journal homepage: www.elsevier.com/locate/jmmm

High-frequency power loss mechanisms in ultra-thin amorphous ribbons

Ansar Masood [a,*], H. A. Baghbaderani [a], K. L. Alvarez [b], J. M. Blanco [c], Z. Pavlovic [a], V. Ström [d], P. Stamenov [e], C. O. Mathuna [a], Paul McCloskey [a]

[a] *Nano-microsystems Centre, Tyndall National Institute, University College Cork, Lee Maltings, Dyke Parade, T12 R5CP, Cork, Ireland*

[b] *Escuela de Ingeniería Mecánica, Pontificia Universidad Católica de Valparaíso, Av. Brasil 2950, Valparaíso, Chile*

[c] *Department of Applied Physics I, Faculty of Engineering Gipuzkoa, University of the Basque Country, San Sebastián, Spain*

[c] *Materials Science and Eng, Dept., KTH-Royal Institue of Thechnology, Brinellvägen 23, S100 44, Stockholm, Sweden*

[b] *School of Physics and CRANN, Trinity College Dublin, 43 Pears street, Dublin 2, Ireland*

Abstract

Soft magnetic amorphous materials with ultra-low power loss are highly desirable for high-frequency drive applications. The present work demonstrates the high-frequency power loss performance and underlying loss mechanisms in ultrathin amorphous alloys. This is achieved by rapid-quenching amorphous alloys of different thickness from Co-, CoFe and Fe-rich alloy systems, investigating their amorphous atomic structure, quantifying the saturation magnetostriction constants (λ_s), magnetic domains imaging at remanence magnetization, analyzing magnetization reversal from various magnetization levels, and finally, investigating the material loss performance over a broad frequency range (f=50 kHz-2 MHz) at various excitation levels (B_m=25-100 mT). The ultra-high performance of ultra-thin Co-rich amorphous ribbons, as compared to CoFe- and Fe-rich alloys, was attributed to the significantly low eddy current loss, due to the reduced ribbon thickness, and a minimal amount of excess loss, due to magnetization reversal by rotation, instead of domain wall motion. The underlying loss mechanisms have been analyzed by decomposing material loss into primary components and by identifying the magnetization reversal using minor hysteresis loops. In the Co-rich amorphous alloys, we suggest that magnetization reversal by rotation dominates, at least at low excitations, while in CoFe- and Fe-rich alloys domain wall motion prevails and contributes significantly to the excess loss up to the MHz frequency range. Magnetization reversal by rotation in Co-rich alloys could be attributed to the low residual stress and zero/nearzero λ_s leading to a homogeneous magnetic domain structure, as compared to the inhomogeneous,

* Corresponding author Tel.: + 353 21 234 6692
Email address: ansar.masood@tyndall.ie (A. Masood).
https://doi.org/XXXX/j.jmmm.2020.XXXX

"fingerprint-like", complex domains in highly magnetostrictive CoFe-rich alloys together with the high residual stress induced during the quenching process.

Keywords: Soft magnetic amorphous alloys, ultra-thin ribbons, high-frequency material loss, material loss mechanisms, eddy current loss, excess loss

1. Introduction

Recent advances in power conversion circuits have pushed their switching frequencies to100s of kHz and even into the megahertz range [1-3]. The size of passive components, which occupy almost 30% volume fraction, is the main challenge in the miniaturization of power converters [4]. As a case in point, despite having ultra-low loss performance, the low magnetic flux density ($\leqslant$ 0.5 T) of ferrites is a critical roadblock in miniaturizing the passive component technology [5]. Thus, the development of high-flux density low-loss soft magnetic materials to replace the best-in-class bulky ferrite passive components is a significant challenge to attain the miniaturized power converters at high frequencies [6].

The high-flux density (B_s>1.8 T), high-permeability (μ>105), ultra-low coercivity (H_c<10 A/m), and high electrical resistivity (>100 μΩ cm) of amorphous metals make them a potential soft magnetic material for device miniaturization in high-frequency applications [6-9]. The single largest example of commercially available amorphous alloys is melt-spun ribbons that have a thickness in the range of 20-30 μm and are widely used in low-frequency (50-60 Hz) power distribution transformers [6]. However, as the operating frequency (f) of device approaches kHz range, the eddy-current losses ($P_{eddy} \propto f^2$) sharply increase as compared to the hysteresis loss ($P_{hys} \propto f$) and the total core loss is dominated by P_{eddy} for f>100 kHz [4, 7]. At high frequencies, the eddy current loss generates a tremendous amount of Joule heat and, consequently, complicates the engineering of the energy storage/conversion devices. Eddy current losses can be dramatically reduced by eliminating the electrically conducting path using high resistivity magnetic materials. The electrical resistivity of amorphous alloys materials is significantly higher than their crystalline counterparts, but at the same time, is substantially lower than the best-in-class ferrites. To demonstrate an advantage of high-flux density amorphous alloys at high frequencies, the authors have investigated two different approaches to produce ultra-thin soft magnetic ribbons for high-frequency applications [6, 10]. The in-situ thinning of melt-spun amorphous ribbons has significant economic advantages, over the post-processing route of chemical etching, for high-frequency power applications. However, the fundamental mechanisms

responsible for material loss at high frequencies in ultra-thin ribbons produced by in-situ rapid quenching still need to be explored [6].

Fundamental mechanisms responsible for material losses at high frequencies depend on the type of domain walls and the nature of the magnetization reversal through domain wall displacement or magnetization rotation. In the present work, we demonstrate the highfrequency materials performance and underlying loss mechanisms in rapidly quenched ultrathin amorphous ribbons of Co-, CoFe-, and Fe-rich amorphous alloys. The advantage of zero/near-zero magnetostrictive ultra-thin Co-rich amorphous alloys for high-frequency applications, over Fe-rich amorphous alloys, has been demonstrated and discussed in relation to low magnetostriction constants, λ_s, the nature of magnetic domains, and their magnetization reversal through the magnetization rotation, using minor hysteresis loops as an instrument.

2. Experimental Methods

Arc-melting using high-purity (at least 99.99%) elements in an argon-flow atmosphere was used to produce 20-30 g ingots of $Co_{67}Fe_4Mo_2Si_{16}B_{11}$ (Co-rich), $Co_{47.6}Fe_{20.4}Nb_5Si_{5.1}B_{21.9}$ (CoFe-rich), and $Fe_{71}Ni_{14}B_{23}Nb_4$ (Fe-rich) alloys. All alloy compositions are in atomic %. From now on, for simplicity, the name of alloys is used as Co-rich, CoFe-rich, and Fe-rich alloys. In order to avoid oxidation of ingots, one arc was fixed to melt titanium, which was used as a getter material. The ingots were melted at least ten times (5-times each side) to achieve a homogeneous composition of the alloys. In the second step, the ingots were crushed into small pieces and remelted by induction before the rapid quenching process. A single roller melt spinner was used to quench the amorphous ribbons of different thicknesses (5-18 μm), which were produced by varying the speed of the copper wheel in an inert atmosphere. The detailed procedure for the production process of ultra-thin ribbons is reported elsewhere [6]. The ultra-thin (~5 μm) and 18 μm ribbons were only used for the high-frequency performance comparison.

The structural analysis of the samples was carried out using X-ray diffraction (XRD) technique using Cu-Kα radiation of λ=1.54 Å (Siemens 5000). Thermal properties of the amorphous ribbons were characterized using differential scanning calorimetry (TA Instruments, DSC 2920) at the heating rate of 10 K/min. The temperature dependence of magnetic properties, *M(T)*, of ribbons was performed using a magneto-thermo-gravimetry (MTG). The Curie temperature (T_c) of the alloys was measured at

the steepest temperature derivative, $dM(T)/dT$, of the $M(T)$ curve, the detailed procedure is published elsewhere [11].

Saturation magnetostriction (λ_s) was measured using a small-angle magnetization rotation (SAMR) process; the detailed procedure is published elsewhere [12]. Magnetic domains were imaged using a magneto-optical Kerr effect microscope (Evico Magnetics Kerr Microscope & Magnetometer) after polishing the ribbon samples to a high level of smoothness. The magnetization reversal of the ribbons was studied using a BH-loop tracer (SHB Mesa-200) at the sample length of 2.5 cm at room temperature.

The power loss characterization of the ribbons was performed using a custom design air-core solenoid inductor. The inductor was constructed from 150 turns of 28 gauge Cu wire wound onto a 5 cm long hollow cylinder of 5 mm outer radius with near-zero spacing between the turns to create a uniform excitation field inside the solenoid. The impedance of the air core solenoid, Z_a, was measured using an LCR meter (HP4284A) at various excitation current levels. The ribbon samples of 20 mm length were fixed on a sample holder and inserted inside the solenoid, along its axis, where the uniformity of the field is best. Without moving the probes from the test fixture, the ribbons were centered inside the solenoid, to be at the same distance from both open ends, where the field lines are no longer parallel to the axis. In this way, the magnetic core material was exposed to a uniform excitation field along its length. The Cu turns are at a sufficient distance from the solenoid axis so that the demagnetization field does not alter the field lines around the turns, maintaining the same AC winding resistance as in the case of air-core solenoid measurement. Therefore, the difference between the impedance measurement with and without magnetic core material, Z_c, and Z_a, respectively represents the contribution of the magnetic core to the inductance and power loss at each particular frequency. As the cross-sectional area of the ribbons is significantly smaller than that of the solenoid, the effect of the insertion of the magnetic core on the real part of the inductance is negligible. Thus, the magnetic material power loss is calculated as;

$$P_{loss} = Re(Z_c - Z_a)I^2 \quad (1)$$

where Re(Z_c-Z_a) is the real part of the complex impedance difference, and I is the excitation current measured using the LCR meter. The induction field inside the ribbon samples is calculated by;

$$B = \frac{lm(Z_c - Z_a)I}{(2\pi fS)}\pi r^2 \quad (2)$$

where f and S are the measurement frequency and the total cross-sectional area of the ribbons, and r is the radius of the coils. The power loss measurement method was tested with commercial amorphous and nanocrystalline alloys, and the results were in good agreement with the reported power loss in the standard datasheets.

3. Results and discussion

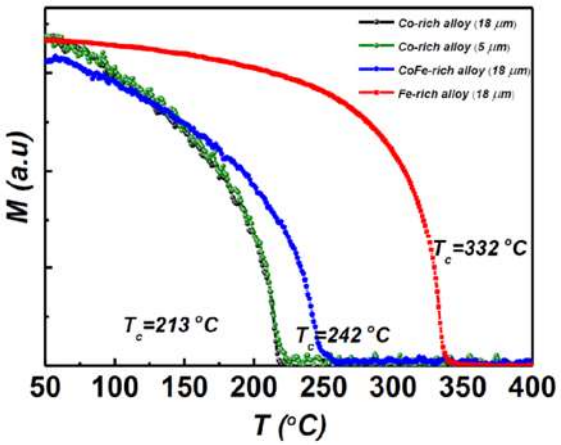

Fig. 1. The monotonic temperature dependence of magnetization, *M(T)*, shows the amorphous nature of the melt-spun Co-rich alloys (T_c=213 °C), (b) CoFe-rich alloys (T_c=242 °C), (c) Fe-rich alloys (T_c=332 °C). The *Tc* of alloys was measured at the steepest temperature derivative, *dM/dT*, of the *M(T)*.

The microscopic structural analysis of the Co-, CoFe- and Fe-rich alloys was investigated using X-ray diffraction analysis (not shown here). A broad-maxima in the range of 2θ=40-50° and the absence of Bragg's peak in XRD pattern of ultra-thin and 20 μm ribbons confirmed the disorder amorphous atomic structure of the as-quenched alloys. Further, the atomic structure of the amorphous ribbons was investigated using magnetothermo-gravimetry (MTG). Fig. 1 presents the temperature dependence of magnetization, *M(T)*, of the melt-spun amorphous ribbons. All ribbons revealed a single-phase *M(T)* behavior, instead of showing any multi-phase "kink", until reaching the Curie point. The single-phase *M(T)* response confirms that investigated alloys were monolithic amorphous materials with a crystallization temperature above T_c of the amorphous phase. The *M(T)* of

Co-rich ultra-thin ribbons is shown for comparison. The overlapped *M(T)* curves of ultrathin ~5 μm and ~18 μm ribbons confirms the uniform homogenous amorphous atomic structure of ribbons produced under different experimental conditions (i.e., speed of Cu wheel=3500-5100 rpm) [6]. The Curie point, shape, and area under the *M(T)* curve depend on the nature and quantity of the phase and have been found to be useful to trace small structural changes in amorphous materials [6, 13].

Fig. 2 represents the DSC traces of the Co-, CoFe-, and Fe-rich amorphous alloys. The glass transition temperature (T_g), crystallization temperature (T_x), supercooled region (ΔT_x=T_x-T_g), peak temperatures (T_p) and crystallization enthalpy (ΔH_C) were measured using DSC traces, and summarized in Table I. The CoFe-rich alloy revealed the highest T_g, T_x, and T_p as compared to Co-rich alloy. However, the ΔT_x of Co-rich alloy was found to be broader than the other investigated alloys. The different nature of crystallization behaviors as a function of temperature is evident from the DSC patterns (Fig. 2). The CoFe-rich alloy showed a two-stage crystallization behavior before complete melting. The two-stage crystallization behavior started to vanish by showing a small exothermic peak, along with a narrow temperature range between the exothermic events, when Co-rich alloys were substituted with a high concentration of Fe (~20 at. %). Finally, the crystallization mechanism transformed into a single stage for Fe-rich glassy alloys, which suggests a eutectic crystallization is taking place [14].

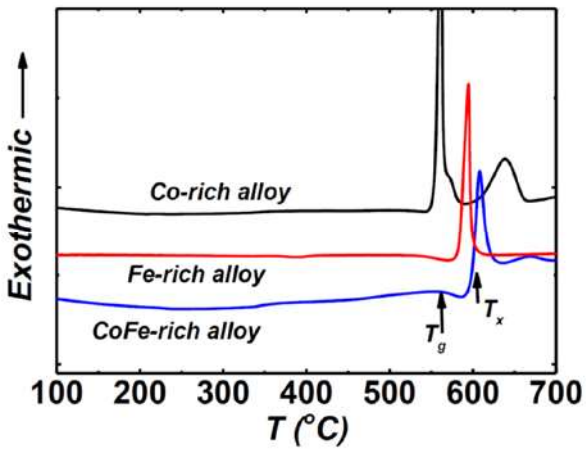

Fig. 2. The differential scanning calorimetry (DSC) trace of as-quenched ribbons of Co-, CoFe-, and Fe-rich alloys. The glass transition temperature (T_g), crystallization temperature (T_x), and supercooled region (ΔT_x= T_x-T_g) are marked on the traces.

The presence of ΔT_x in the DSC patterns of all investigated alloys reveals the glassy nature and hence confirms the highly stable amorphous atomic structure as compared to conventional amorphous alloys. The large ΔT_x (=47.11 K) of Co-rich ribbons, as compared to CoFe- and Fe-rich alloys, shows higher glass forming ability (GFA), which is considered another instrument to measure the soft magnetic properties of amorphous materials [7]. The glassy alloys with large ΔT_x are expected to show enhanced soft magnetic properties as compared to conventional amorphous alloys [15]. The enhanced soft magnetic properties are due to the small number of quasidislocation dipole (QDDs)-type defects in glassy alloys, as compared to conventional amorphous alloys, which were originally considered sources of elastic stress or pinning sites for the domain walls during displacement [15]. Piccino et al., [16] investigated the frequency dependence of materials loss performance of the glassy alloys with different GFA and revealed the better performance of high GFA alloys. To conclude, the structural, thermal, and magneto-thermal analysis of ribbons confirms the highly stable disordered atomic structure of the investigated alloys in the as-quenched state.

Table I: The glass transition temperature (T_g), crystallization temperature (T_x), supercooled region (ΔT_x=T_x-T_g), peak temperature (T_p), and crystallization enthalpy (ΔH_c) of Co-, CoFe-, and Fe-rich alloys measured using the differential scanning calorimetry (DSC).

Sample	T_g (°C)	T_x (°C)	ΔT_x (T_x-T_g)	T_p (°C)	ΔH_c (J/g)
Co-Fe-Mo-B-Si (Co-rich alloy)	508.71	555.82	47.11	561.69	144.00
Co-Fe-Nb-B-Si (CoFe-rich alloy)	563.40	597.33	33.92	603.01	67.77
Fe-Ni-B-Nb (Fe-rich alloys)	538.01	581.02	43.01	594.80	6.44

Fig. 3 presents the power loss density (P) of Co-, CoFe-, and Fe-rich melt-spun glassy alloys over a broad frequency spectrum (f=50 kHz-2 MHz) and excitation fields (B_m=25-100 mT). The power loss density of Co-rich alloys was significantly improved by reducing the ribbon thickness from 18 to 5 µm. For Co-rich melt-spun alloys, for example, the P reduced from 2591 to 253 W/kg at f=300 kHz (B_m=100 mT), revealing ~10x improvement in material loss performance. Similarly, the P reduced from 253 to 42 W/kg at f=2 MHz (B_m=10 mT) by reducing the ribbon thickness, which represents a ~6x improvement in materials loss performance. However, the improvement in P after thinning the amorphous ribbons for CoFe- and Fe-rich alloys was not as significant. For example, for CoFe-rich amorphous alloys, the power loss density reduced from 2271 to 1245 W/kg on thickness reduction from 18 µm to 5 µm at f=300 kHz (B_m=100 mT), which is only ~1.8x improvement in the material loss performance. Similarly, the P of the

amorphous ribbons was reduced from 236 to 98 W/kg at f=2 MHz (B_m=10 mT) on thickness reduction by revealing ~2x improvement. Similar trends in the improvement of P of Fe-rich amorphous alloys were observed, showing the ~1.5x improvement at f=300 kHz (100 mT) and ~1.6x improvement at 2 MHz (10 mT) after thinning the ribbons.

The less significant improvement in the power loss density of CoFe- and Fe-rich amorphous alloys, as compared to Co-rich alloy, by thinning the ribbons to 5 μm is surprising, and points to an interesting question to explore in relation to the fundamental loss mechanisms in soft magnetic amorphous alloys of different systems.

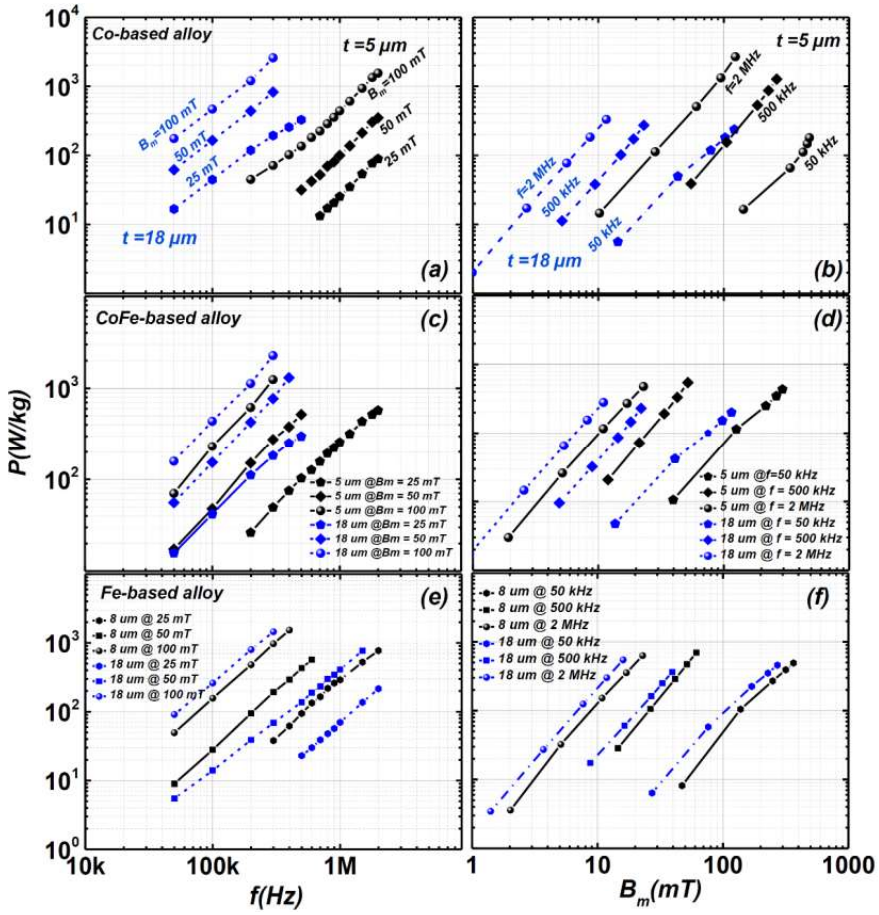

Fig. 3. (a) Power loss density (P) of in-situ thinned amorphous ribbons over a broad frequency (f) spectrum and excitation fields (B_m). (a)-(b) Co-rich alloy, (c)-(d) CoFe-rich alloy, (e)-(f) Fe-rich alloy.

According to the statistical theory of material loss separation, the total power loss (P) of magnetic materials can be broadly divided into three different mechanisms, such as hysteresis loss (P_{hys}), eddy current loss (P_{eddy}), and excess loss (P_{exc}) [10, 17]. The P of the materials can be expressed as:

$$P = P_{hys} + P_{eddy} + P_{exc} \tag{3}$$

The area of the hysteresis loop, which originates due to short-range magnetization reversal mechanisms, such as magnetic moment reversal modes, pinning of magnetic domain walls, effective magnetic anisotropies, and size distribution of grains, governs the P_{hys} of the materials [16, 17]. The P_{hys} becomes independent of frequency due to the short response time of the mechanisms discussed earlier [17]. On the other hand, P_{eddy} is a dynamic macroscopic loss and is independent of the magnetic domain structure [17]. Contrary to P_{eddy}, P_{exc} strongly relates to the intermediate length scales of magnetic domains [16, 17]. Considering the sinusoidal waveform and rectangular dimensions of ribbons, P_{eddy} can be described by the following equation [16].

$$P_{eddy} = (\pi^2/6)\sigma t^2 B_m^2 f^2 \tag{4}$$

where t is the thickness of the ribbons, and σ is the conductivity of the material. Under the same assumptions as mentioned above, the analytical expression for the P_{exc} can be expressed as [18-20]:

$$P_{exc} = 8.76(\sigma G A \delta)^{1/2} B_m^{3/2} f^{3/2} \tag{5}$$

where G=0.1356 is a dimensionless coefficient, A is the cross-sectional area, and δ is a field constant which directly depends on domain wall pinning. For magnetic cores, the P is frequency-dependent and largely depends on the hysteresis and eddy current losses at low frequencies ($\leqslant$ 100 kHz). However, the excess loss, which is due to localized eddy currents around the moving domain walls, dominates at > kHz frequency range in amorphous materials [21]. Core loss per cycle (P/f) of ultra-thin ribbons was analyzed (see Fig. 4) to understand the material's loss mechanism over a broad frequency range. The behavior of P/f verses f should be linear if eddy current loss is dominant, and the slope of the curve should give its magnitude [22]. The nonlinear behavior of P/f of the ultra-thin alloys (see Fig. 4) shows a change in the material loss mechanism at higher frequencies. The inflection

point in the P/f verses f is strictly dependent on the B_m of the alloys. Interestingly, the infection point for Co-rich alloys appeared at significantly higher frequencies as compared to CoFe- and Ferich alloys at all excitation fields (B_m=10-100 mT). For example, Co-rich alloy showed the transition at 1 MHz (B_m=50 mT), while CoFe- and Fe-rich alloys revealed the same transition in the range of 200 kHz.

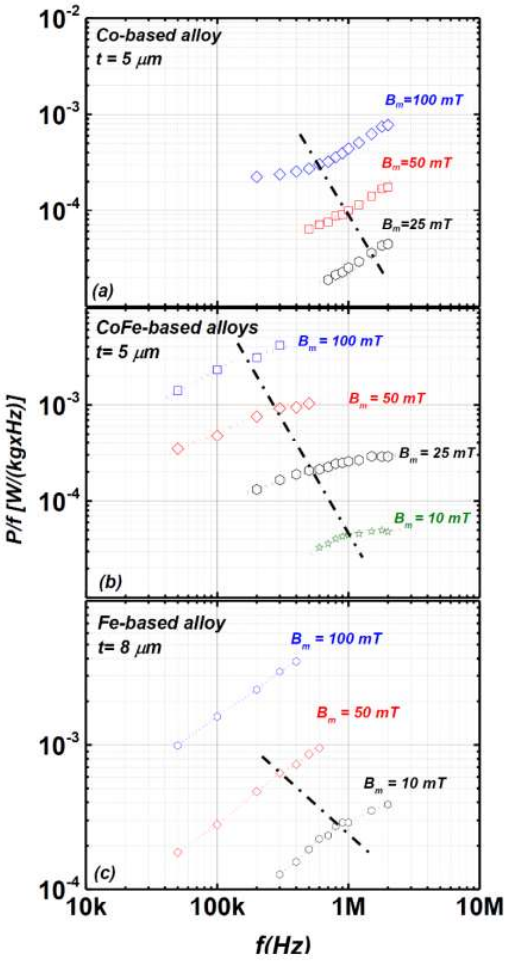

Fig. 4. Core loss per cycle (P/f) versus f of 5 μm as-quenched amorphous ribbons of (a) Corich alloy, (b) CoFe-rich alloy, and 8 μm as-quenched amorphous ribbon of (c) Fe-rich alloy at different excitation fields (B_m). The dash-dotted line is used as a guide to show the eddy-excess transition frequency for the investigated alloys.

Furthermore, the slope of the first linear section of the P/f verses f curve of Co-rich alloy is significantly lower, as compared to other investigated alloys, which confirm the existence of small eddy current loss in the material. The change in the slope of P/f (shown as the dashed line in Fig. 4) indicates a significant contribution of excess loss in the investigated alloys when frequency approaches the high kHz to MHz range for different alloy systems. Alvarez et al. [13] and Suzuki et al. [22], separately, observed a similar transition in the material loss of amorphous cores and correlated it to the domination of excess loss at particular frequencies. We believe the sharp transition in P/f of the ultra-thin ribbons at high frequencies is due to the remarkable increase in the excess loss of the alloys. The transition behavior of Co-rich alloys at higher frequencies, as compared to CoFe- and Fe-rich alloys, is of significant importance for high-frequency drive applications.

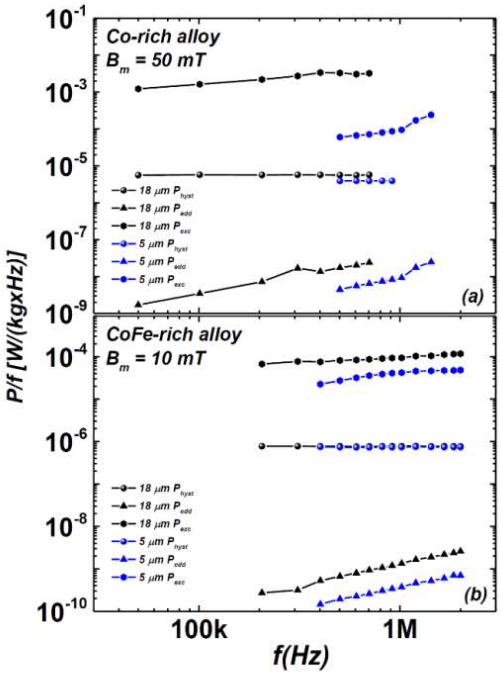

Fig. 5. Material loss decomposition of total loss (P) into Hysteresis loss (P_{hys}), Eddy-current loss (P_{eddy}), and Excess loss (P_{exc}) for (a) Co-rich alloys, (b) CoFe-rich alloys.

Detailed information on the frequency dependence of materials loss performance and microstructural parameters can be extracted using the theory of magnetic loss separation without a precise description of the magnetization reversal process for a broadband frequency spectrum [16, 17,

19]. The material's loss of Co-rich and CoFe-rich alloys (5 and 18 μm ribbons) was decomposed into the primary loss components (see Fig. 5). The eddy current and excess loss in Co-rich alloys reduced significantly on thickness reduction, while a minimal reduction in the eddy and excess loss was observed in the CoFe-rich alloys. A sharp transition in the excess loss of Co-based alloys was observed at 1 MHz, while a similar transition was observed in CeFe-rich alloys at much lower frequencies. Interestingly, the slope after the inflection point for CoFe-rich alloys is lower than the Co-rich alloys. It is wellknown that the frequency dependence of the excess loss component per cycle follows a power law close to $f^{½}$ [20]. However, specific anomalies can deviate the power-law dependence at high frequencies [20]. The difference in the slopes of the investigated alloys can be explained as a change in the balance between magnetization rotation and domain wall motion, frequency-dependent skin effects, and magnetic resonance phenomenon [20].

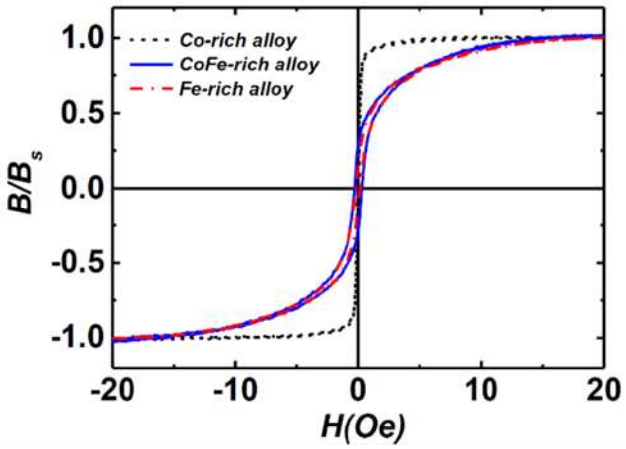

Fig. 6. Major hysteresis loops of as-quenched Co-, CoFe- and Fe-rich amorphous alloys measured using ribbons of length 25 mm at the maximum field of 1000 Oe.

In order to understand the material's loss mechanisms, a precise description of the magnetization reversal of each alloy was investigated using hysteresis loops. Fig. 6 presents the typical quasistatic hysteresis loops of the investigated alloys. It is well-known that the balance between the domain wall motion and moment rotation governs the shape and area of the hysteresis loop [23]. The different shape of hysteresis loops (Fig. 6) suggests that the magnetization reversal is fundamentally different between the investigated alloys. In addition, a significant difference in the H_c of the Co-rich (~0.04 Oe) and CoFe- (~0.3) and Fe-rich (~0.2 Oe) was measured,

which could be attributed to the different levels of residual stress, owning to different magnetostriction constants of alloys, produced during the quenching process of the alloys.

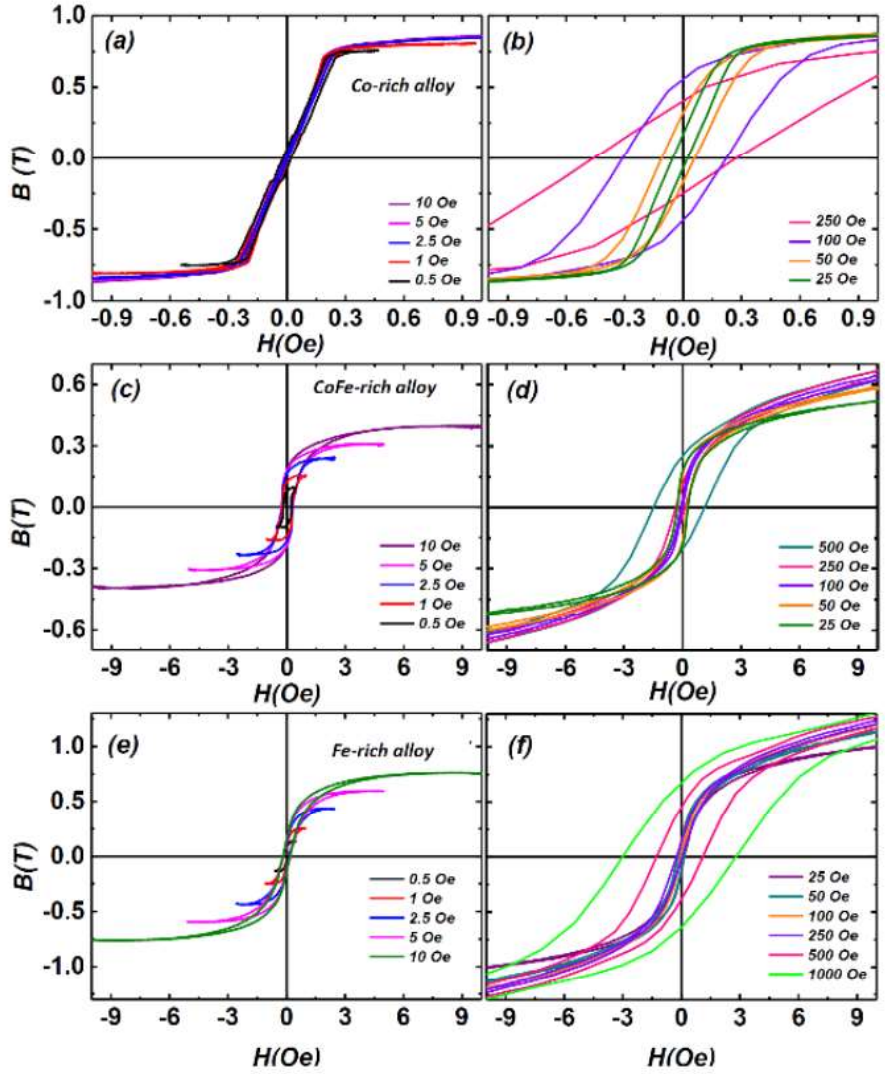

Fig. 7. Minor hysteresis loops of amorphous ribbons of (a)-(b) Co-rich alloy, (c)-(d) CoFerich alloys, (e)-(f) Fe-rich alloys.

Magnetization reversal modes are crucial to understanding the fundamental mechanisms responsible for material losses at high frequencies. The magnetization reversal modes inside the bulk samples can

be determined by the shape of the hysteresis loops and the dependence of the remanence magnetization (B_r), based on minor hysteresis loops on the maximum induction B_{max} [4]. Fig. 7 presents the detailed minor hysteresis loops of the investigated alloys at various magnetization levels. Varga et al. [24] extracted the domain wall movement and magnetization rotation process using a magnetization reversal process of an ultra-soft magnetic alloy and concluded that the domain wall displacement generates a square-type hysteresis loop similar to the major loop, while domain rotation reveals a flat loop. A similar explanation can be put forward in the present case. The minor flat loops of the Co-rich alloy suggest that the magnetization reversal was based on magnetization rotation while the square shape of the minor hysteresis loops of the CeFe-rich, and Fe-rich alloys confirms the magnetization reversal by domain wall displacement. The difference in the magnetization processes of the Co-, and CoFe- and Fe-rich amorphous ribbons might be related to differences in local and average anisotropies resulting from different magnetostriction constant (λ_s) of the materials. In order to confirm this hypothesis, the λ_s of the alloys was measured and summarized in Table II. The λ_s of CoFe- and Fe-rich alloys was found to be two orders of magnitude higher than the Co-rich alloy. In CoFe- and Fe-rich amorphous alloys, the local magnetostrictive anisotropies, predominate due to the large λ_s of the alloys, and consequently, extend over larger length scales than the exchange length and, as a result, are not balanced by the exchange interaction [25]. The magnetization reversal process takes place as a domain wall motion against these local anisotropies. Contrary to the CoFe- and Fe-rich alloys, Co-rich alloys reveal very small magnetostrictive anisotropies due to small λ_s=0.02x10^{-6}, and consequently, the magnetization reversal is much easier at low fields, as shown in Fig 7.

Table II: The magnetostriction constant (λ_s) of the as-quenched amorphous Co-, CoFe-, and Fe-rich alloys measured by a small-angle magnetization rotation (SAMR) process.

Sample	λ_s (10^{-6})
Co-rich alloy	0.02
CoFe-rich alloy	1.27
Fe-rich alloys	9.34

The type of domain walls and nature of domain wall motion in a magnetic field determines the magnetization and magnetization reversal in the magnetic material. However, the observation of magnetic domains in amorphous materials is rather challenging, especially at high frequencies [4]. Another difficulty appears from the absence of magnetocrystalline

anisotropy in amorphous materials and, consequently, magnetic domains can only be observed in as-quenched amorphous alloys either with ultra-low residual stress or after inducing uniaxial magnetic anisotropy by magnetic annealing[4]. Fig. 8 shows the magnetic domain images measured at low frequency using Kerr microscopy, under zero DC magnetic field. Wide and uniform magnetic domains with 180° walls were observed for the Co-rich alloys, while a very complex, fingerprint-like, inhomogeneous domain was observed in CoFe-rich alloys. Despite our best efforts, magnetic domains in Fe-rich alloys were not apparent under the same experimental conditions. The orientation of magnetic domains in ferromagnetic systems results from the minimization of magnetic Gibb's free energy, which consists of magnetostatic stray field energy (E_S), anisotropy energy (E_A), and domain wall energy (E_D) [23]. A wide magnetic domain structure appears when the E_S and E_A components are at their lowest levels, and spontaneous magnetization tends to emerge in the in-plane orientation. Contrarily, a complex domain structure, like closure domains, emerges by minimizing the E_S component when the anisotropy axis is perpendicular to the ribbon axis [23]. Residual stress in the amorphous alloys can be a source of strong magnetic anisotropy, especially when λ_s is remarkably high [23]. The high λ_s of CoFe- and Fe-rich amorphous alloys, as compared to Co-rich alloys (see Table II), makes the alloys highly compressive, and hence leads to the formation of fingerprint-like intricate domain patterns, while the 180° domain walls observed in Co-based alloys are the result of comparatively small residual stress due to zero/near-zero λ_s [23]. The high level of residual stress in Fe-rich alloys, induced due to the highest λs among the investigated alloys, might be the reason for orienting magnetic domains into a scale below the instrumental limits.

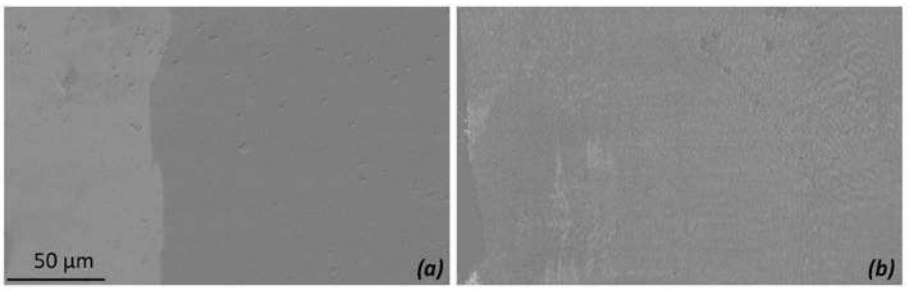

Fig. 8. Magnetic domains imaged by the magneto-optical Kerr effect (MOKE) microscope along the longitudinal ribbon axis of (a) Co-rich amorphous alloy, (b) CoFe-rich amorphous alloy.

Direct observation of magnetic domains with the evolution of frequency is quite challenging and mostly observed up to the kHz frequency

range in amorphous and nanocrystalline materials [26]. Most recently, Magni et al. [27] imaged the magnetic domains up to the MHz range and found the exciting fact that domain wall displacement was progressively damped and eventually halted on approaching the MHz range; and consequently, the only dissipation mechanisms emerge from the rotational process [28]. However, at low frequencies, the magnetization process is a combined effect of magnetization rotation and domain wall displacement [26]. As the dominant mechanism of magnetization reversal in CoFe- and Fe-rich amorphous alloys is domain wall displacement, as shown by minor hysteresis loops and magnetic domain imaging, it seems that the excess loss prevails over the eddy current loss in the investigated frequency range. Therefore, no remarkable improvement in the material performance was observed even after reducing the thickness of alloys to 5 μm. Contrary to that, the contribution of excess loss in Co-rich alloy is significantly small, due to the magnetization reversal by rotation and so the eddy current loss prevails in this alloy system. As thinning of the ribbons mainly affects the eddy current loss, so the total power loss performance of Co-rich alloys is substantially improved by in-situ thinning the alloys.

4. Conclusions

The high-frequency performance and underlying loss mechanisms in rapidly quenched ultra-thin amorphous ribbons of Co-rich, CoFe-rich, and Fe-rich alloys were investigated in order to understand the potential of high-flux density soft magnetic amorphous alloys for device miniaturization. The ultra-high performance of Co-rich amorphous alloys at high-frequencies, as compared to the CoFe- and Fe-rich alloys, was attributed to the significantly reduced eddy current losses due to the reduced thickness of the alloys achieved by in-situ rapid quenching process and domain rotation magnetization reversal process, instead of domain wall motion. The advantage of ultra-thin Co-rich amorphous alloys over the CoFe- and Fe-rich alloys was discussed in relation to their magnetization reversal through the domain rotation process using minor hysteresis loops.

CRediT authorship contribution statement

Ansar Masood, Conceptualization; Data curation; Formal analysis; Investigation; Methodology; Validation; Visualization; Roles/Writing – original draft; Writing – review & editing. **H. A. Baghbaderani**, Data curation; Formal analysis; Methodology; Validation; Visualization; Roles/Writing; Writing – review & editing. **K. L. Alvarez**, Data curation; Formal analysis; Investigation; Methodology; Validation; Visualization;

Writing – review & editing. **J. M. Blanco**, Data curation; Formal analysis; Investigation; Methodology; Resources; Validation. **Z. Pavlovic**, Data curation; Formal analysis; Investigation; Methodology; Validation; Visualization. **V. Ström**, Methodology; Resources; Supervision. **P. Stamenov**, Funding acquisition; Project administration; Resources. **C. O. Mathuna**, Funding acquisition; Project administration; Resources. **P. McCloskey**, Funding acquisition; Project administration; Resources; Validation; Writing – review & editing.

Declaration of Competing Interest

The authors declare that they have no known competing financial interests or personal relationships that could have appeared to influence the work reported in this paper.

Acknowledgment

The authors would like to thank Science Foundation of Ireland (SFI) for the financial support to perform the research work under the grant number of 2015/SIRG/3569, Starting Investigator Research Grant (SIRG).

References

[1] J.S. Glaser, J.M. Rivas, A 500 W push-pull dc-dc power converter with a 30 MHz switching frequency, in: 2010 Twenty-Fifth Annual IEEE Applied Power Electronics Conference and Exposition (APEC) (2010) 654–661.

[2] D.J. Perreault, J. Hu, J.M. Rivas, Y. Han, O. Leitermann, R.C.N. Pilawa-Pdgurski, A. Sagneri, C.R. Sullivan, Opportunities and Challenges in Very High Frequency Power Conversion," 2009 Twenty-Fourth Annual IEEE Applied Power Electronics Conference and Exposition, Washington, DC, (2009) 1-14.

[3] W. Li, Y. Zheng, Y. Kang, A. Masood, Y. Ying, J. Yu, J. Zheng, L. Qiao, J. Li, S. Che, Magnetic behavior of soft magnetic composites constructed by rapidly quenched flake-like FeSiAl alloy, J. Alloys Compd. 819 (2020) 153028.

[4] N.A. Skulkina, O.A. Ivanov, A.K. Mazeeva, P.A. Kuznetsov, E.A. Stepanova, O.V. Blinova, E.A. Mikhalitsyna, Magnetization processes in ribbons of soft magnetic amorphous alloys, Phys. Metals Metallogr. 119 (2018) 127-133.

[5] H.A. Baghhaderani, D.J. Cronin, P. McCloskey, S. Kulkarni, Z. Pavlovic, A. Masood, K. Ackland, P. Stamenov, C. O'Mathuna, Fabrication and development of miniaturized efficient power converters using ultra-soft magnetic ribbons. 2018 IEEE International Magnetic Conference (INTERMAG), Singapore (2018) 1-1.

[6] A. Masood, H.A. Baghbaderani, V. Ström, P. Stamenov, P. McCloskey, C. Mathúna, S. Kulkarni, Fabrication and soft magnetic properties of rapidly quenched Co-Fe-B- Si-Nb ultra-thin amorphous ribbons, J. Magn. Magn. Mater. 483 (2019) 54–58.

[7] A. Masood, V. Ström, L. Belova, K.V. Rao, J. Ågren, Effect of Ni-substitution on glass forming ability, mechanical, and magnetic properties of FeBNbY bulk metallic glasses, J. Appl. Phys. 113 (2013) 013505.

[8] K. Ackland, A. Masood, S. Kulkarni, P. Stamenov, Ultra-soft magnetic Co-Fe-B-Si-Nb amorphous alloys for high frequency power applications, AIP Adv. 8 (2018) 056129.

[9] E. Dastanpour, M.H. Enayati, A. Masood, V. Ström, On the glass forming ability (GFA), crystallization behavior and soft magnetic properties of nanomet-substituted alloys. J. Non. Cryst. Solids, 529 (2020) 119774.

[10] S. Kulkarni, D. Li, N. Wang, S. Roy, C. O'Mathuna, G. Young, P. McCloskey, Low loss magnetic hin Fiflms for off-line ower Cocnversion, IEEE Trans. Magn. 50 (2014) 2004404.

[11] S. Lee, A. Masood, T. Tamaki, S. Valter, K.V. Rao, A. Makino, A. Inoue, Magneto-thermo-gravimetric technique to investigate the structural and magnetic properties of Fe-B-Nb-Y Bulk Metallic Glass, J. Phys. Conf. Ser. 144 (2009) 8–12.

[12] K. Narita, J. Yamasaki, H. Fukunaga, Measurement of saturation magnetostriction of a hin Aamorphous ribbon by means of small-angle magnetization rotation, IEEE Trans. Magn. 16 (1980) 435-439.

[13] K.L. Alvarez, H.A. Baghbaderani, J.M. Martín, N. Burgos, M. Ipatov, Z. Pavlovic, P. MacCloskey, A. Masood, J. Gonzalez, Novel Fe-based amorphous and nanocrystalline powder cores for high-frequency power conversion, J. Magn. Magn. Mater. 501 (2020) 166457.

[14] K.L. Alvarez, J.M. Martín, N. Burgos, M. Ipatov, L. Dominguez, J. Gonzalez, Structural and magnetic properties of amorphous and nanocrystalline Fe–Si–B–P–Nb–Cu alloys produced by gas atomization, J. Alloys Compd. 810 (2019) 151754.

[15] T. Bitoh, A. Makino, A. Inoue, Origin of low coercivity of Fe-(Al, Ga)-(P, C, B, Si, Ge) bulk glassy alloys, Mater. Trans. 44 (2003) 2020-2024.

[16] R. Piccin, P. Tiberto, H. Chiriac, M. Baricco, Magnetic properties and power losses in Fe-Co-based bulk metallic glasses, J. Magn. Magn. Mater. 320 (2008) e806-e809.

[17] G. Bertotti, Hysteresis in magnetism, Academic Press, USA, 1998.

[18] E. Barbisio, F. Fiorillo, C. Ragusa, Predicting loss in magnetic steels under arbitrary induction waveform and with minor hysteresis loops, IEEE Trans. Magn. 40 (2004) 1810-1819.

[19] G. Bertotti, V. Basso, C. Beatrice, M. LoBue, A. Magni, P. Tiberto, Hysteresis in magnetic materials: the role of structural disorder, thermal relaxation, and dynamic effects, J. Magn. Magn. Mater. 226 (2001) 1206-1212.

[20] C. Appino, C. Beatrice, E. Ferrara, Magnetization process and magnetic losses in field-annealed amorphous and nanocrystalline ribbons, J. Opto. Adv. Mater. 6 (2004) 511-521.

[21] W.A. Roshen, Thin amorphous films for power magnetic components, in: 2007 Twenty-Second Annual IEEE Applied Power Electronics Conference and Exposition (APEC), 2007, 63-70.

[22] T. Suzuki, P. Sharma, A. Makino, Extending the operational frequency range of high B_s – FeSiBP amorphous alloy to GHz by coating the powder surface with silicon oxide, J. Magn. Magn. Mater. 491 (2019) 165641

[23] S. Mallick, P. Sharma, K. Takenaka, A. Makino, S. Bedanta, Static and dynamic behavior of domain walls in high B_S soft magnetic ribbons tuned by the annealing temperature, J.Phys. D: Applied Phys. 51 (2018) 065007.

[24] L.K. Varga, G. Kovacs, Separation of magnetization loop in domain wall movement and domain rotation contributions for soft magnetic materials, Acta Phys. Polon. A 113 (2008) 159-162.

[25] J. Kovac, L. Novak, L.K. Varga, Study of the magnetization processes in amorphous and nanocrystalline FINEMET by the numerical decomposition of the hysteresis loops. Acta Phys. Polon. A 131 (2017) 732-734.

[26] S. Flohrer, R. Schäfer, J. McCord, S. Roth, L. Schultz, F. Fiorillo, W. Günther, G. Herzer, Dynamic magnetization process of nanocrystalline tape wound cores with transverse field-induced anisotropy, Acta Mater. 54 (2006) 4693-4698.

[27] A. Magni, F. Fiorillo, A. Caprile, E. Ferrara, L. Martino, Fluxmetric-magnetooptical approach to broadband energy losses in amorphous ribbons, J, Applied Phys. 109 (2011) 07A322.

[28] A. Magni, A., C. Beatrice, O. Bottauscio, A. Caprile, E. Ferrara, F Fiorillo, Magnetization process in thin laminations up to 1 GHz, IEEE Trans. Magn. 48 (2012) 1363-1366.